

MICROPOROUS VANADOSILICATE AM-6 FILMS FOR PHOTOCATALYTIC  
APPLICATIONS

A THESIS SUBMITTED TO  
THE GRADUATE SCHOOL OF NATURAL AND APPLIED SCIENCES  
OF  
MIDDLE EAST TECHNICAL UNIVERSITY

BY

DUYGU KUZYAKA

IN PARTIAL FULFILLMENT OF THE REQUIREMENTS  
FOR  
THE DEGREE OF DOCTOR OF PHILOSOPHY  
IN  
MICRO AND NANOTECHNOLOGY

NOVEMBER 2019



Approval of the thesis:

**MICROPOROUS VANADOSILICATE AM-6 FILMS FOR  
PHOTOCATALYTIC APPLICATIONS**

submitted by **DUYGU KUZYAKA** in partial fulfillment of the requirements for the degree of **Doctor of Philosophy in Micro and Nanotechnology Department, Middle East Technical University** by,

Prof. Dr. Halil Kalıpçılar  
Dean, Graduate School of **Natural and Applied Sciences**

\_\_\_\_\_

Prof. Dr. Almıla Güvenç Yazıcıoğlu  
Head of Department, **Micro and Nanotechnology**

\_\_\_\_\_

Prof. Dr. Burcu Akata Kurç  
Supervisor, **Micro and Nanotechnology, METU**

\_\_\_\_\_

Prof. Dr. Ahmet Macit Özenbaş  
Co-Supervisor, **Metallurgical and Mat. Eng., METU**

\_\_\_\_\_

**Examining Committee Members:**

Prof. Dr. Münevver Sökmen  
Bioengineering, Konya Food and Agriculture University

\_\_\_\_\_

Prof. Dr. Burcu Akata Kurç  
Micro and Nanotechnology, METU

\_\_\_\_\_

Prof. Dr. Ali Çırpan  
Department of Chemistry, METU

\_\_\_\_\_

Assoc. Prof. Dr. Selis Önel  
Chemical Engineering, Hacettepe University

\_\_\_\_\_

Assist. Prof. Dr. Bilge İmer  
Metallurgical and Mat. Eng., METU

\_\_\_\_\_

Date: 18.11.2019

**I hereby declare that all information in this document has been obtained and presented in accordance with academic rules and ethical conduct. I also declare that, as required by these rules and conduct, I have fully cited and referenced all material and results that are not original to this work.**

Name, Surname: Duygu Kuzyaka

Signature:

## ABSTRACT

### MICROPOROUS VANADOSILICATE AM-6 FILMS FOR PHOTOCATALYTIC APPLICATIONS

Kuzyaka, Duygu

Doctor of Philosophy, Micro and Nanotechnology

Supervisor: Prof. Dr. Burcu Akata Kurç

Co-Supervisor: Prof. Dr. Ahmet Macit Özenbaş

November 2019, 174 pages

There is an increasing attention on the photocatalysis experimentations providing removal of organic contaminants from water under visible and UV radiation. The role of semiconductor materials as photocatalysts is to degrade highly toxic pollutants. Pore regularity, control of defects, and the presence of stoichiometric amounts of vanadium in the silicate framework allows one to create alternative materials in advanced applications such as photocatalysis. Vanadium, present in specific form within the structure of SiO<sub>2</sub> matrix could open up the gateway to investigate and tailor the defects created for specific catalytic applications. For that reason, vanadosilicate AM-6 containing 1-dimensional, semiconducting, and quantum-confined ...V-O-V-O-V... chains can be a very interesting material with tailorable defect sites in photocatalysis.

Accordingly, vanadosilicate AM-6 thin films with controlled defect sites were produced by tailoring the ratio of V<sup>4+</sup>/V<sup>5+</sup> ratio within the thin film structure. It was shown that the quality of seed crystals (morphology and thickness) affects the quality of thin films grown by secondary growth approach, leading to alterations in the V<sup>4+</sup>/V<sup>5+</sup> ratio. The effect of changing molar composition and vanadium source used for the secondary growth solution was also investigated systematically.

Furthermore, it was observed that altering the molar water content of the secondary growth gel also affects the film growth causing differences in the  $V^{4+}/V^{5+}$  ratio. It was found that vanadosilicate AM-6 films with higher amount of  $V^{5+}$  ions arising from seed layer or different synthesis conditions possess better photocatalytic activity under visible light irradiation for the degradation of methylene blue, which can be attributed to the presence of  $V^{5+}$  cation within the framework of AM-6.

Photocatalysts production in thin form provides integration of the material to device-oriented applications, hinders the agglomeration originated from the powder form of the photocatalyst, and also accelerates the degradation kinetics due to the increase of the contact surface area between the pollutant and the photocatalyst increasing the photocatalytic activity.

Keywords: Photocatalysis, Vanadosilicates, AM-6, Thin-Films, Zeo-type Materials

## ÖZ

### FOTOKATALİTİK UYGULAMALAR İÇİN MİKRO GÖZENEKLİ VANADYUM SİLİKAT AM-6 FİMLERİ

Kuzyaka, Duygu  
Doktora, Mikro ve Nanoteknoloji  
Tez Danışmanı: Prof. Dr. Burcu Akata Kurç  
Ortak Tez Danışmanı: Prof. Dr. Ahmet Macit Özenbaş

Kasım 2019, 174 sayfa

Görünür ışık ve UV aydınlatma altında organik kirleticilerin uzaklaştırılmasını sağlayan fotokataliz deneylerine ilgi her geçen gün artmaktadır. Yarı iletken malzemelerin fotokatalizör olarak rolü, oldukça toksik kirleticileri indirgemektir. Kusur oluşumunun kontrol edilebildiği, düzenli gözenek yapısına sahip ve sitokiyometrik miktarlarda vanadyum içeren malzemeler, fotokataliz gibi gelişmiş uygulamalarda tercih edilebilir. SiO<sub>2</sub> matrisinde vanadyumun spesifik şekillerde bulunması, spesifik katalitik uygulamaların araştırılmasını ve kusur oluşumunun ayarlanmasını kolaylaştırır. Bu sebeple, 1-boyutlu, yarı iletken ve kuantum özellikli ...V-O-V-O-V... zincirleri içeren vanadyum silikat AM-6, ayarlanabilir kusur oranlarıyla fotokatalitik uygulamalar için çok ilginç bir malzeme olma potansiyeline sahiptir. Buna göre, control edilebilen kusur bölgelerine sahip vanadyum silikat AM-6 filmleri, film yapısındaki V<sup>4+</sup>/V<sup>5+</sup> oranı ayarlanarak üretilmiştir. İkincil büyütme yaklaşımında tohum (seed) kristallerinin kalitesinin (morfoloji ve kalınlık) V<sup>4+</sup>/V<sup>5+</sup> oranında değişiklik yaratarak ince filmlerin kalitesini de etkilediği tespit edilmiştir. İkincil büyütme solüsyonunun molar kompozisyonunu ve kullanılan vanadyum kaynağını değiştirmenin etkileri de sistematik olarak araştırılmıştır. Hatta, ikincil büyütme jelinin içerisindeki molar su miktarının değişiminin de V<sup>4+</sup>/V<sup>5+</sup> oranında

farklılıklar yaratarak film büyümesini etkilediği gözlemlenmiştir. Tohum (seed) tabakasındaki farklılıklar ya da farklı sentez koşulları sebebiyle oluşan, daha yüksek  $V^{5+}$  iyonuna sahip vanadium silikat AM-6 filmlerinin görünür aydınlatma altında metilen mavisinin fotokatalitik gideriminde daha iyi performans sergilediği tespit edilmiştir. Bu durum vanadium silikat yapısında bulunan  $V^{5+}$  iyonlarının varlığıyla açıklanabilir.

İnce film formunda fotokatalizör üretimi malzemelerin cihaz uygulamalarında kullanılmasına olanak sağlar ve toz formundaki fotokatalizörlerin sebep olduğu aglomerasyon problemlerini de engeller. Ayrıca kirlenici ve fotokatalizör arasındaki temas yüzeyi ince film formundaki fotokatalizörlerde daha fazla olduğundan metilen mavisinin giderim kinetikleri artar ve böylelikle fotokatalitik aktivitede de artış gözlemlenir.

Anahtar Kelimeler: Fotokataliz, Vanadyum silikatlar, AM-6, İnce Filmler, Zeo-tip Malzemeler



Dedicated to my dear son, Başar

## ACKNOWLEDGEMENTS

I would like to express my sincere gratitude to my supervisor Prof. Dr. Burcu Akata Kurç for her support, inspiration and excellent guidance during my Ph.D. study.

I would like to thank the thesis monitoring committee members Prof. Dr. Ali Çırpan and Assoc. Prof. Dr. Selis Önel for their precious comments and valuable comments.

I would like to thank our group members; Berna Ozansoy Kasap, Melda İşler Binay, Ramona Davoudnezhad, Salih Kaan Kirdeciler, Sezin Galioğlu Özaltuğ and Temel Burak Kutlu for their friendship and help during my study. They cooled me down and lifted my spirit when I was having difficult times and stressed during the process of writing my thesis.

I owe my gratitude to Prof. Dr. Münevver Sökmen for giving me the opportunity to study in her laboratory and encouraging me for studying photocatalysis. I would also like to thank Assoc. Prof. Dr. İlknur Tatlıdil Altın and Dr. Melek Koç Keşir for their help in the first part of photocatalysis experiments.

I would like to thank Assoc. Prof. Dr. Murat Kaya for giving me the opportunity to study in his laboratory and use the photocatalysis system. I would also like to thank to Dr. Ceren Uzun for her help during the photocatalysis experimentations.

I would like to thank Ali Güzel, Dr. Elif Ünsal, İlker Yılmaz for their help during the analyses. I would also thank to Levent Yıldız, Merve Cengiz, Merve Kaplan, Salar Habibpur Sedani, Seçkin Öztürk, Sedat Canlı, and Uğur Özgürgil for their friendship and support during my thesis study.

I owe my gratitude to Prof. Dr. Abdelhamid Errachid and Prof. Dr. Maryam Tabrizian for giving me the opportunity to study in their laboratory in Institut des Sciences Analytiques in Lyon and in Biological Engineering in McGill University in Montreal.

I am also appreciative of the financial support that I received for this study through Scientific and Technical Research Council of Turkey (TUBITAK) with the project code 118M631 and European Union project with the project number FP7-PEOPLE-2012-IRSES, 318524, Integrated Nanodevices-NANODEV.

Special thanks to my mother Naile Uzmay for her never-ending love, patience, and support. Furthermore, I am also grateful to my sisters Serap Kozanođlu Őah, Utkum Kozanođlu Kol, and Őzlem Karakoç for their love, patience, caring and support. I owe them my deepest gratitude.

Last but not least, I would like to give my endless gratitude to my husband Guluhan Kuzyaka, who supported and motivated me with his love and understanding during the whole period of my study. My little baby boy BaŐar Kuzyaka also deserves praise for everything that he brings in my life.

## TABLE OF CONTENTS

ABSTRACT .....	v
ÖZ .....	vii
ACKNOWLEDGEMENTS.....	x
TABLE OF CONTENTS .....	xii
LIST OF TABLES.....	xvi
LIST OF FIGURES .....	xviii
LIST OF ABBREVIATIONS.....	xxiii
LIST OF SYMBOLS .....	xxiv
CHAPTERS	
1. INTRODUCTION.....	1
1.1. Semiconductor Photocatalysis .....	2
1.1.1. Semiconductors .....	3
1.1.2. Principals of Photocatalysis Mechanism.....	6
1.1.3. Methods for Enhancing Photocatalytic Activity .....	13
1.2. Zeolites and Zeo-Type Materials .....	16
1.2.1. Microporous Titanosilicate ETS-10 .....	17
1.2.2. Microporous Vanadosilicate AM-6.....	20
1.3. Thin Film Preparation of Zeolites and Zeo-type Materials: In situ and Secondary Growth Method .....	24
2. LITERATURE REVIEW.....	27
2.1. Photocatalytic Materials.....	27
2.1.1. Photocatalytic Decomposition of Methylene Blue.....	28

2.1.2. Porous Materials as Photocatalysts.....	29
2.2. Thin Film Preparation of Zeolites and Zeo-type Materials.....	31
2.2.1. Controlling the Crystal Orientation in Zeolite and Zeo-type Materials....	32
2.2.2. Effect of the Seed Layer Morphology and Seed Crystal Population on Film Formation .....	39
2.2.3. Effect of Molar Water Content on Film Formation.....	44
2.2.4. Effect of Ion Doping on Photocatalysis.....	45
2.3. Photocatalytic Performance of Microporous Titanosilicate ETS-10 and Microporous Vanadosilicate AM-6.....	46
2.4. Defects: Creation and Performance.....	49
2.5. Goal and Objectives .....	52
3. EXPERIMENTAL PROCEDURES.....	55
3.1. Synthesis of Submicrometer-Sized ETS-10 with Different Morphologies (i.e., bipyramidal and cubic).....	55
3.2. Thin Film Preparation of Microporous Titanosilicate ETS-10 and Microporous Vanadosilicate AM-6.....	58
3.2.1. Effect of Chemical Formula of the Secondary Growth Gel .....	58
3.2.2. Effect of Seed Crystal Morphology .....	60
3.2.3. Effect of Seed Layer Coating Technique.....	61
3.2.4. Effect of Molar Water Content of the Secondary Growth Gel .....	61
3.3. Evaluation of the Photocatalytic Activity.....	62
3.3.1. Photocatalytic Performances of Microporous Titanosilicate ETS-10 and Microporous Vanadosilicate AM-6 Films under UV and Visible Light Irradiation.....	62
3.3.1.1. Reuse of AM-6 Thin Films .....	64

3.3.2. Photocatalysis under Solar Light.....	64
3.4. Characterization Techniques.....	66
3.4.1. Field Emmision Scanning Electron Microscopy.....	66
3.4.2. X-ray Diffraction.....	66
3.4.3. Raman Spectroscopy.....	67
3.4.4. Electron Micro Probe Analaysis (EPMA).....	67
3.4.5. X-ray Photoelectron Spectroscopy.....	67
3.4.6. Diffuse Reflectance UV-Vis Spectroscopy.....	67
4. RESULTS AND DISCUSSION.....	69
4.1. Secondary Growth of Microporous Vanadosilicate AM-6 Films.....	69
4.1.1. The Effect of the Composition of Secondary Growth Gel on Film Formation.....	69
4.1.1.1. Sample Characterization.....	69
4.2. The Effect of Microporous Vanadosilicate AM-6 Films as Photocatalysts for the Degradation of MB under UV and Visible Light Irradiation.....	83
4.2.1. Sample Characterization.....	83
4.2.2. Evaluation of Photocatalytic Activity.....	95
4.2.2.1. Dark Experiments.....	96
4.2.2.2. Under UV Irradiation.....	97
4.2.2.3. Under Visible Light Irradiation.....	98
4.2.2.4. The Photocatalytic Reusability Efficiency of As-Prepared Materials .....	100
4.3. Investigation of the Parameters Affecting Film Formation and Photocatalytic Performance of AM-6 Films.....	102

4.3.1. The Effect of Seed Crystal Morphology on the Formation and Photocatalytic Activity of AM-6 Films .....	102
4.3.1.1. Sample Characterization .....	102
4.3.1.2. Evaluation of the Photocatalytic Activity .....	111
4.3.2. The Effect of Seed Layer Coating Technique on the Formation and Photocatalytic Activity of AM-6 Films .....	114
4.3.2.1. Sample Characterization .....	115
4.3.2.2. Evaluation of the Photocatalytic Activity .....	125
4.3.3. The Effect of Molar Water Content of the Secondary Growth Gel on the Formation and Photocatalytic Activity of AM-6 Films.....	129
4.3.3.1. Sample Characterization .....	129
4.3.3.2. Evaluation of the Photocatalytic Activity .....	140
5. SUMMARY, CONCLUSION, AND FURTHER SUGGESTIONS.....	151
REFERENCES.....	155
APPENDICES .....	167
A. Calculation of the Energy Bandgap .....	167
B. Calculation of the Degradation Kinetics of MB Without Using any Photocatalayst .....	169
C. Calculation of the Degradation Kinetics of MB for S1-F3 and S2-F3 as Photocatalayst .....	170
CURRICULUM VITAE .....	171

## LIST OF TABLES

### TABLES

Table 1.1. A comparison between microporous titanosilicate ETS-10 and microporous vanadosilicate AM-6 .....	23
Table 2.1. The angle between the crystallographic planes .....	38
Table 3.1. Interpretation of the experimental procedure for the preparation of AM-6 films .....	57
Table 4.1. Si/V ratios, thicknesses, and CPO values of S1-F1, S1-F2, S1-F3, S1-F1-W1, S1-F1-W2, and S1-F1-T1 .....	76
Table 4.2. Raman shift and FWHM (full-width half-maximum) values belonging to V-O stretching of AM-6 and Ti-O stretching of ETS-10 .....	79
Table 4.3. XPS spectral parameters for V 2p <sub>3/2</sub> : Binding energy (eV), and the ratio of V <sup>4+</sup> /V <sup>5+</sup> .....	88
Table 4.4. Thickness and CPO values of S1-F3 and S2-F3 films .....	105
Table 4.5. Raman shift and FWHM (full-width half-maximum) values belonging to V-O stretching of S1-F3 and S2-F3 .....	106
Table 4.6. XPS spectral parameters for V 2p <sub>3/2</sub> for S1-F3 and S2-F3: Binding energy (eV), and the ratio of V <sup>4+</sup> /V <sup>5+</sup> .....	110
Table 4.7. Thickness and CPO values of S1-F3, S1-dip1-F3, and S1-dip2-F3 films .....	118
Table 4.8. Raman shift and FWHM (full-width half-maximum) values belonging to V-O stretching of S1-F3, S1-dip1-F3, and S1-dip2-F3 films .....	120
Table 4.9. XPS spectral parameters for V 2p <sub>3/2</sub> for S1-F3, S1-dip1-F3, and S1-dip2-F3: Binding energy (eV), and the ratio of V <sup>4+</sup> /V <sup>5+</sup> .....	124
Table 4.10. Thickness and CPO values of S1-F3, S1-F3-W1, S1-F3-W2, and S1-F3-W3.....	133



Table 4.11. Raman shift and FWHM (full-width half-maximum) values belonging to V-O stretching of S1-F3, S1-F3-W1, S1-F3-W2, and S1-F3-W3 .....	135
Table 4.12. XPS spectral parameters for V 2p <sub>3/2</sub> for S1-F3, S1-F3-W1, S1-F3-W2, and S1-F3-W3: Binding energy (eV), and the ratio of V <sup>4+</sup> /V <sup>5+</sup> .....	139
Table 4.13. CPO, FWHM, V <sup>4+</sup> /V <sup>5+</sup> , and k values of AM-6 films.....	146

## LIST OF FIGURES

### FIGURES

Figure 1.1. Band model for insulator, conductors, and semiconductors .....	4
Figure 1.2. Energy band structures of intrinsic, n-type and p-type semiconductor.....	5
Figure 1.3. Stick representation of ETS-10 structure along the b direction (a). Si, Ti, and O atoms are represented as yellow, gray, and red sticks, respectively. -Ti-O-Ti-O-Ti- chains, running along with the a and b directions, are visible. Stick and ball representation, zoomed in on a fraction of the -Ti-O-Ti-O-Ti- chain showing also the charge-balancing monovalent cations (violet balls) (b) [37] .....	18
Figure 1.4. The framework structure of ETS-10 showing chains of corner-sharing TiO <sub>6</sub> octahedra which run along with two perpendicular directions, and which are isolated by corner-sharing SiO <sub>4</sub> tetrahedra: single element of the chain (a); single chain (b); three-dimensional view (c) [44] .....	19
Figure 1.5. A structural model for AM-6 structure [47].....	21
Figure 1.6. The model for AM-6 using DFT calculations [41] .....	21
Figure 1.7. Two chemical environments for the Si atoms in vanadosilicate AM-6 [25].....	22
Figure 2.1. XRD patterns of ETS-10 in powder form and ETS-10 membrane [91] .	35
Figure 2.2. XRD patterns of bare ITO glass substrate (a), ETS-10 powder (b), seed layers deposited on the ITO glass substrate using 1 (c), 2 (d), and 3 (e) dip coating steps, and films after secondary growth of seed layers deposited via single (f), double (g), and triple (h) dip coating [54] .....	36
Figure 2.3. A sketch for crystallographic planes .....	37
Figure 2.4. FE-SEM images of the silicalite-1 membranes grown on substrates seeded with (a and b) 100 nm, (c and d) 600 nm, (e and f) 1.5 μm, (g and h) 3.0 μm, and (i and j) 7.5 μm seed crystals [58] .....	41
Figure 3.1. Schematical view of the experimental procedure .....	56

Figure 3.2. Illustration for the preparation of microporous vanadosilicate AM-6 films .....	58
Figure 3.3. Illustration for microporous vanadosilicate AM-6 film formation using seeds with different morphologies .....	60
Figure 3.4. The system used for investigation of the photocatalytic activity of the samples under visible light irradiation .....	62
Figure 3.5. The solar simulator system used for the investigation of the photocatalytic activities of microporous vanadosilicate AM-6 films .....	65
Figure 4.1. Top view and cross-sectional images of S1-F1 (a), (b); S1-F2 (c), (d); S1-F3 (e), (f), respectively .....	70
Figure 4.2. XRD patterns of AM-6 samples in powder form F1(a), F2(b), F3(c). * indicates quartz impurity; * and * refer the peaks belonging to AM-6 and VSH, respectively .....	71
Figure 4.3. Growth directions of ETS-10 crystals as seed (a), S1-F1 (b), and S1-F3 (c) .....	72
Figure 4.4. Composition diagram of 3 molar compositions: .....	73
Figure 4.5. XRD patterns of ETS-10 (a), S1-F1 (b), S1-F2 (c), and S1-F3 (d) .....	74
Figure 4.6. Raman spectroscopy of ETS-10 seed layer (a), S1-F1 (b), S1-F2 (c), and S1-F3 (d) .....	77
Figure 4.7. FE-SEM images of the samples; S1-F1 (a), S1-F1-W1 (b), S1-F1-W2 (c), and S1-F1-T1 (d) .....	80
Figure 4.8. XRD patterns of the samples S1-F1 (a), S1-F1-150 (b), S1-F1-300 (5 h crystallization) (c), S1-F1-300 (8 h crystallization) (d), and S1-F1-528K (e). * indicates the quartz impurity .....	82
Figure 4.9. Top view FE-SEM images of ETS-10 (a), S1-F2 (b), Ag <sup>0</sup> -S1-F2 (c), and S1-F3 (d) thin films .....	84
Figure 4.10. X-ray diffraction patterns of ETS-10 (a), S1-F2 (b), Ag <sup>0</sup> -S1-F2 (c), and S1-F3 (d) thin films .....	85

Figure 4.11. XPS high resolution V 2p spectra of S1-F2 and S1-F3, deconvolution of V2p <sub>3/2</sub> XPS peak of S1-F2 ( $V^{4+}/V^{5+}=1.12$ ) (a), and deconvolution of V 2p <sub>3/2</sub> XPS peak of S1-F3 ( $V^{4+}/V^{5+}=1.68$ ) (b).....	87
Figure 4.12. XPS survey scan spectrum of Ag <sup>0</sup> -S1-F2 (a), and XPS high-resolution Ag 3d spectra of Ag <sup>0</sup> -S1-F2 (b).....	90
Figure 4.13. Raman spectroscopic analysis of ETS-10 (a), S1-F2 (b), Ag <sup>0</sup> -S1-F2 (c), and S1-F3 (d) thin films.....	91
Figure 4.14. UV-Vis absorption spectra and Tauc plot for bandgap calculations for the samples S1-F2 (a) and S1-F3 (b) .....	94
Figure 4.15. The adsorption of MB of the ETS-10, S1-F2, Ag <sup>0</sup> -S1-F2, and S1-F3 thin films in dark ( $[M] = 3.2 \text{ mg L}^{-1}$ , pH 6, $V_{MB} = 4 \text{ mL}$ ).....	96
Figure 4.16. The photocatalytic removal of MB of the S1-F3, S1-F2, and Ag <sup>0</sup> -S1-F2 thin films under UV light irradiation ( $[MB] = 3.2 \text{ mg L}^{-1}$ , pH 6, $V_{MB} = 4 \text{ mL}$ ).....	98
Figure 4.17. The photocatalytic removal of MB of the samples ETS-10, S1-F3, S1-F2, and Ag <sup>0</sup> -S1-F2 thin films under visible light irradiation ( $[MB] = 3.2 \text{ mg L}^{-1}$ , pH 6, $V_{MB} = 4 \text{ mL}$ ).....	99
Figure 4.18. The photocatalytic removal of MB of the ETS-10, S1-F2, Ag <sup>0</sup> -S1-F2 and S1-F3 thin films after 5-time usage under UV light irradiation ( $[MB] = 3.2 \text{ mg L}^{-1}$ , pH 6, $V_{MB} = 4 \text{ mL}$ ).....	101
Figure 4.19. Top view and cross-sectional images of S1-F3 (a), (b) and S2-F3 (c), (d), respectively .....	103
Figure 4.20. X-ray diffraction patterns of S1-F3 (a) and S2-F3 films (b).....	104
Figure 4.21. Raman spectroscopic analysis of the samples S1-F3 (a) and S2-F3 (b) .....	105
Figure 4.22. UV-Vis absorption spectra and Tauc plot for bandgap calculations for the samples (a) S1-F3 and (b) S2-F3 .....	107
Figure 4.23. XPS high resolution V 2p spectra of S1-F3 and S2-F3, (a) deconvolution of V2p <sub>3/2</sub> XPS peak of S1-F3 ( $V^{4+}/V^{5+}=1.68$ ), and (b) deconvolution of V 2p <sub>3/2</sub> XPS peak of S2-F3 ( $V^{4+}/V^{5+}=1.17$ ) .....	109

Figure 4.24. Absorbance of MB for S1-F3 in dark (a) and under illumination (b); S2-F3 in dark (c) and under illumination (d).....	111
Figure 4.25. The photocatalytic removal (a), and the degradation kinetics (b) of MB for S1-F3 and S2-F3 films under solar simulator (1 Abs. MB, pH 6, $V_{MB}= 10$ mL) .....	113
Figure 4.26. The photocatalytic removal (a), and the degradation kinetics (b) of MB without using any photocatalysts under solar light (1 Abs. MB, pH 6, $V_{MB}= 10$ mL) .....	114
Figure 4.27. Top view and cross-sectional images of S1-F3 (a), (b); S1-dip1-F3 (c), (d); S1-dip2-F3 (e), (f), respectively .....	116
Figure 4.28. X-ray diffraction pattern of the samples S1-F3 (a), S1-dip1-F3 (b), and S1-dip2-F3 (c) .....	117
Figure 4.29. Raman spectroscopic analysis of the samples S1-F3 (a), S1-dip1-F3 (b), and S1-dip2-F3 (c) .....	119
Figure 4.30. UV-Vis absorption spectra and Tauc plot for bandgap calculations for the samples (a) S1-F3, (b) S1-dip1-F3, and (c) S1-dip2-F3 .....	121
Figure 4.31. XPS high resolution V 2p spectra of S1-F3, S1-dip1-F3, and S1-dip2-F3 (a) deconvolution of $V_{2p_{3/2}}$ XPS peak of S1-F3 ( $V^{4+}/V^{5+}=1.68$ ), (b) deconvolution of V $2p_{3/2}$ XPS peak of S1-dip1-F3 ( $V^{4+}/V^{5+}=1.108$ ) and (c) deconvolution of V $2p_{3/2}$ XPS peak of S1-dip2-F3 ( $V^{4+}/V^{5+}=1.101$ ) .....	123
Figure 4.32. Absorbance of MB for S1-F3 in dark (a) and under illumination (b); S1-dip1-F3 in dark (c) and under illumination (d); S1-dip2-F3 in dark (e) and under illumination (f) .....	126
Figure 4.33. The photocatalytic removal (a), and the degradation kinetics (b) of MB for S1-F3, S1-dip1-F3, and S1-dip2-F3 films under solar simulator (1 Abs. MB, pH 6, $V_{MB}= 10$ mL).....	128
Figure 4.34. Top view and cross-sectional images of S1-F3 (a), (b); S1-F3-W1 (c), (d); S1-F3-W2 (e), (f); S1-F3-W3 (g), (h), respectively .....	130
Figure 4.35. X-ray diffraction spectroscopy of the samples S1-F3 (a), S1-F3-W1 (b), S1-F3-W2 (c), and S1-F3-W3 (d) .....	132

Figure 4.36. Raman spectroscopic analysis of the samples S1-F3 (a), S1-F3-W1 (b), S1-F3-W2 (c), and S1-F3-W3 (d).....	134
Figure 4.37. UV-Vis absorption spectra and Tauc plot for bandgap calculations for the samples (a) S1-F3, (b) S1-F3-W1, (c) S1-F3-W2, and (c) S1-F3-W3 .....	136
Figure 4.38. XPS high resolution V 2p spectra of S1-F3, S1-F3-W1, S1-F3-W2, and S1-F3-W3. deconvolution of V2p <sub>3/2</sub> XPS peak of S1-F3 ( $V^{4+}/V^{5+}=1.68$ ) (a), deconvolution of V 2p <sub>3/2</sub> XPS peak of S1-F3-W1 ( $V^{4+}/V^{5+}=2.06$ ) (b), and deconvolution of V 2p <sub>3/2</sub> XPS peak of S1-F3-W2 ( $V^{4+}/V^{5+}=1.06$ ) (c).....	138
Figure 4.39. Absorbance of MB for S1-F3 in dark (a) and under illumination (b); S1-F3-W2 in dark (c) and under illumination (d); S1-F3-W3 in dark (e) and under illumination (f).....	141
Figure 4.40. The photocatalytic removal (a), and the degradation kinetics (b) of MB for S1-F3, S1-F3-W2, and S1-F3-W3 films under solar simulator (1 Abs. MB, pH 6, VMB= 10 mL).....	143
Figure 4.41. Absorbance (a), and percent degradation (b) of MB for S2-F3 film as photocatalyst under solar light (1 Abs. MB, pH 6, VMB= 10 mL).....	145
Figure 4.42. CPO vs $V^{4+}/V^{5+}$ ratio for the samples .....	148

## LIST OF ABBREVIATIONS

### ABBREVIATIONS

FE-SEM	Field Emission Scanning Electron Microscopy
XRD	X-ray Diffraction
XPS	X-ray Photoelectron Spectroscopy
EPMA	Electron Microprobe Analysis
UV-Vis	Ultraviolet-Visible Spectroscopy
ITO	Indium Tin Oxide
TMAOH	Tetramethylammonium hydroxide
CPO	Crystallographic Preferred Orientation
ETS-10	Engelhard Titanosilicate-10
ETS-4	Engelhard Titanosilicate-4
AM-6	Aveiro-Manchester-6
VOSO <sub>4</sub>	Vanadium Sulfate
V <sub>2</sub> O <sub>5</sub>	Vanadium Pentoxide
AgNO <sub>3</sub>	Silver Nitrate
NaBH <sub>4</sub>	Sodium Borohydrate
P25	Degussa Titanium Dioxide
MB	Methylene Blue

## LIST OF SYMBOLS

### SYMBOLS

BE	Binding Energy
CB	Conduction band
VB	Valence band
k	Pseudo-first-order reaction rate constant
C	Concentration of MB
•OH	Hydroxyl radical



## CHAPTER 1

### INTRODUCTION

Water is the most important requirement for the continuity of the biological activity on earth. However, it is exposed to get more and more polluted due to plenty of factors such as industrialization and increasing population. Developing and less developed countries have difficulties to get clean water. The contaminated water can be cleaned by methods such as reverse osmosis and chemical degradation. Still, all of these processes are extremely expensive and not sufficiently effective for lowering rate of pollutant formation. Besides, traditional cleaning processes may cause the pollutants to transfer from one phase to another or secondary pollutants to arise. Thus, there is increasing attention on the photocatalysis experimentations providing removal of organic contaminants such as textile dyes from water under visible and UV radiation. Semiconductor photocatalyst has become a very attractive topic of research not only for researchers but also for water purifications companies mostly due to its harmless approach to the environment.

Titanium dioxide ( $\text{TiO}_2$ ) is the most frequently used semiconductor material as photocatalyst due to its high photocatalytic activity, chemical, and biological stability and low cost. However, its use as a photocatalyst is confronted by some issues. The first problem is that  $\text{TiO}_2$  is only activated by UV light which is 4-5% of the sunlight. This limits the use of solar energy and it is necessary to modify the material in order to increase its photoreactivity. The low electron transfer rate to oxygen and the high electron-hole recombination rate are other problems causing low photoreactivity. Besides, the use of nanocrystalline  $\text{TiO}_2$  as photocatalyst may induce agglomeration of nanoparticles such as clustering. This may hinder the homogeneous dispersion of the photocatalyst in the suspension causing low photocatalytic activity. Therefore, it is necessary to find a material with a low energy

band gap which is photocatalytically active in the visible light range and prone to agglomeration. Using photocatalysts in powder form requires filtration of photoactive particles which is an expensive and time-consuming procedure. Thin film production provides integration of the material to device-oriented applications and also accelerates the degradation kinetics due to the increase of the contact surface area between the pollutant and the photocatalyst. Therefore, the production of the materials with a low energy band gap in thin film form and photocatalytically active in the visible light range is very important. Based on this gap in the literature, the current thesis focusses on the production of microporous vanadosilicate AM-6 that is isostructural with ETS-10 in thin form for the first time.

The framework of AM-6 contains monatomic, one-directional, and quantum-confined ...V-O-V-O-V... chains, which extend in two orthogonal directions and are surrounded by the insulating SiO<sub>2</sub> matrix. Microporosity, pore regularity, and the presence of stoichiometric amounts of vanadium in the silicate framework make AM-6 a promising material in the traditional and also advanced applications. For that purpose, thin film making techniques from vanadosilicate AM-6 crystals were deeply investigated for the aim of obtaining photocatalytic activity in the visible region for the first time. It is believed that this study will open a new door for possible applications of these types of materials containing one-dimensional quantum wires.

### **1.1. Semiconductor Photocatalysis**

Water pollution is one of the key issues getting considerable attention especially due to factors such as global industrialization and increasing population. Among various pollutants, dyes are one of the most dangerous organic contaminants in industrial wastewater that need to be eliminated, since their presence in aquatic ecosystems can cause serious damage to human health and living creatures [1,2]. There are two important factors to take into consideration for the removal of synthetic dyes which are adsorption and the photocatalytic processes. Adsorption process is less feasible

with respect to the photocatalytic process due to the reasons such as its low effectiveness at low pollutant concentrations [3,4]. In the photocatalysis process, dye molecules are decomposed into inorganic species or by-products that are readily biodegradable when irradiated by light [5–9]. For that purpose, heterogeneous photocatalytic oxidation processes have been discussed widely in the literature [6,8–10]. These processes are governed by highly reactive oxygen species such as  $\text{HO}^\bullet$ ,  $\text{HO}_2^\bullet$ , and  $\text{H}_2\text{O}_2$ , which play an important role in the photocatalytic oxidation of organic dye molecules [11–14]. Photocatalysis is one of the methods to remove MB from wastewaters, which has been accepted as a model chemical and a representative of organic dyes in various studies [2,9,15–17].

Semiconductors have been shown to be good candidates as photocatalysts through the advantageous positioning of valence band and conduction band, enhancing their light absorption capability and thereby photocatalytic activity [6,18]. Among various semiconductors, visible-light-driven photocatalysts have gained much attention due to less energy consumption [19].

### **1.1.1. Semiconductors**

Photocatalysis starts with the absorption of a photon by a photocatalyst. If the photocatalyst is a semiconductor, information on its band structure is very important for understanding the photocatalysis mechanism [20].

The classification of the materials upon their electrical conductivity is carried out by splitting them into three categories: the insulator, conductor and semiconductor. Insulators do not have the ability to conduct electricity because of the inability of electrons to move. The ability of electrons to move freely brings conductors to conduct electricity whereas the ability to conduct electricity of semiconductor materials is intermediate and expressed by their bandgap [21]. While allowed energetic states are defined as bands, the term band gap indicates forbidden energetic states. One can get information about the electronic state of material through band structures. Conduction and valence bands are the terms for the lowest unoccupied

band and the highest occupied band by electrons, respectively. The bandgap is defined as the difference between the highest occupied molecular orbital and the lowest unoccupied molecular orbital [20]. A large band gap separates the conduction band and the valence band in an insulator. Molecular orbitals overlap in conductors resulting in the lack of bandgap between the conduction band and the valence band. Bandgap size gives information on whether a material is an insulator or a semiconductor because semiconductors have a bandgap between the conduction band and the valence band as insulators (Figure 1.1) [21].

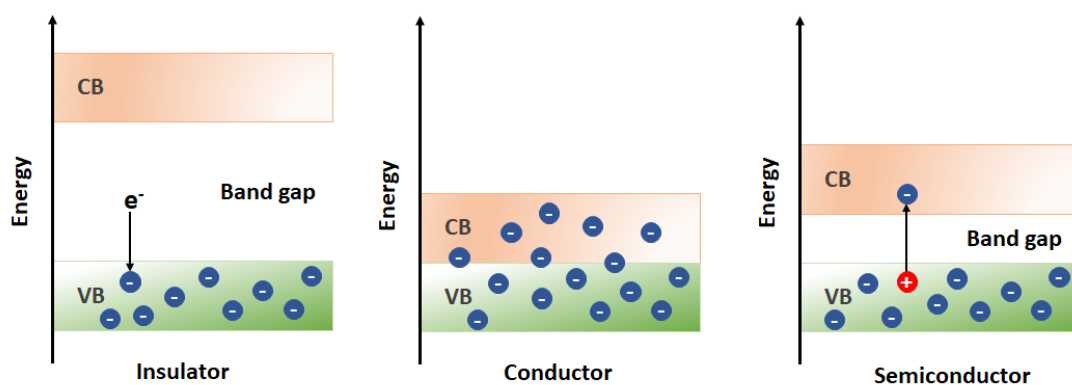


Figure 1.1. Band model for insulator, conductors, and semiconductors

Semiconductors can be classified in three ways in terms of their impurity as shown in Figure 1.2. Intrinsic semiconductors contain no impurity, whereas crystal lattice of n-type and p-type semiconductors (extrinsic semiconductors) encapsulates impurity or dopants. Electrical conductivity is provided thermally in intrinsic semiconductors. Electrical conduction occurs by impurities (i.e., electron donors or electrons acceptors) in extrinsic semiconductors. Electrons can easily excite to conduction band without leaving a hole in the valence band in the presence of an electron donor creating an n-type semiconductor. However, the possibility of electrons in the valence band to excite to the conduction band is less likely when an electron

acceptor is incorporated into the lattice structure of a semiconductor creating a p-type semiconductor. For p-type semiconductors, minority carriers are electrons whereas majority carriers are holes. Excitation of electrons from valence band is provided thermally [21].

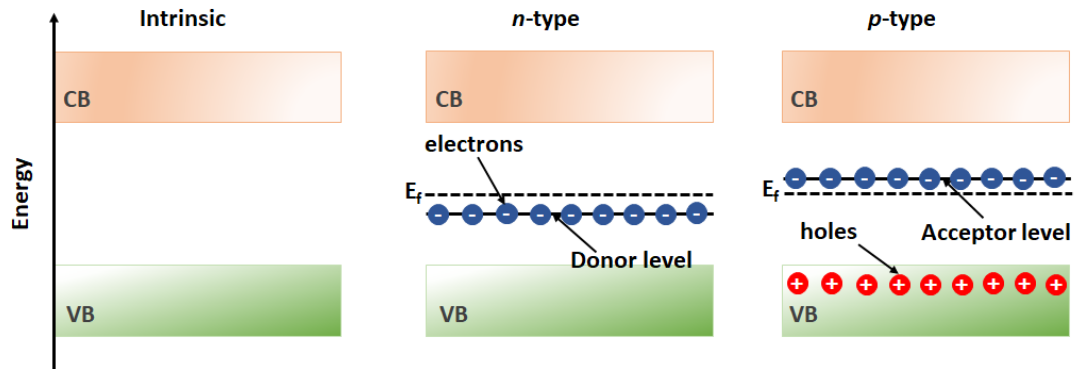
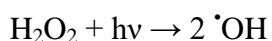
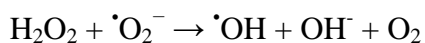
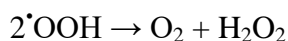
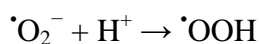
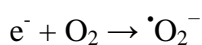
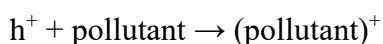
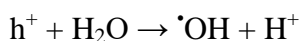
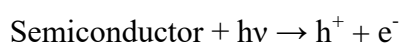


Figure 1.2. Energy band structures of intrinsic, n-type and p-type semiconductor

Fermi level is present between the conduction band and valence band as shown in Figure 1.2. The possibility of electrons to occupy this level is 0.5. For an n-type semiconductor, Fermi level exists above the donor level, whereas it lies below the acceptor level for a p-type semiconductor. Fermi level is close to the conduction band and electrons excite from donor level to conduction band in n-type semiconductors making them electron conductors. Conversely, Fermi level is close to the valence band and electrons excite from valence band to acceptor level in p-type semiconductors making them hole conductors [21]. At zero Kelvin, energetic states below the Fermi level are occupied by electrons. Energetic states above the Fermi level are empty. At finite temperatures, a few electrons can excite to the conduction band. This situation is defined as Fermi-Dirac statistics. Fermi level acts as a virtual electronic state and locates in the middle of the bandgap (Figure 1.2) [20].

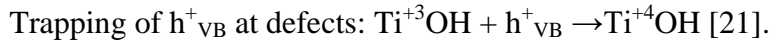
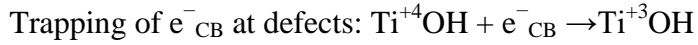
### 1.1.2. Principals of Photocatalysis Mechanism

Photocatalysis is used for decomposition of water from pollutants such that the coverage of the photocatalyst by water molecules is expected. Therefore, water oxidation is a very important part of the photocatalysis mechanism [22]. Photocatalytic oxidation and reduction reactions are used to define the reactions of a photocatalytic process [21]. In a photocatalysis system, pollutant degradation process involves many steps (vide infra) including  $\cdot\text{OH}$  generation, which is a powerful oxidizing agent for the degradation of organic contaminants [23]. Photocatalysis starts with the absorption of photon energy ( $h\nu$ ) by a semiconductor.

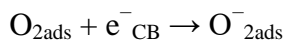


First, photons with energy higher than the bandgap energy of a semiconductor excite electrons from valence band to conduction leaving holes in the valence band in photocatalysis mechanism. These electrons and holes could be separated from each other or recombine resulting from the random migration of electrons and holes [24]. Physiosorbed water molecules, surface oxygen vacancies or defects, and surface

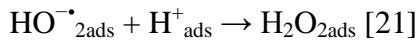
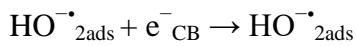
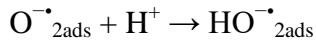
hydroxyl groups can trap these charge carriers. Trapping of charge carriers represented by the equations is exemplified below:



Oxygen is crucial for photocatalytic applications due to the fact that organic pollutants need oxygen to degrade. Photoreaction starts with the adsorbed oxygen on the surface of the photocatalysts occurring superoxide radicals.



These superoxide radicals cause the formation of hydrogen peroxide.



Among other oxidizing species, hydroxyl radical is the most effective due to its high oxidation potential. Figure 1.3 shows the possible ways to oxidize organic pollutant caused by hydroxyl radical.

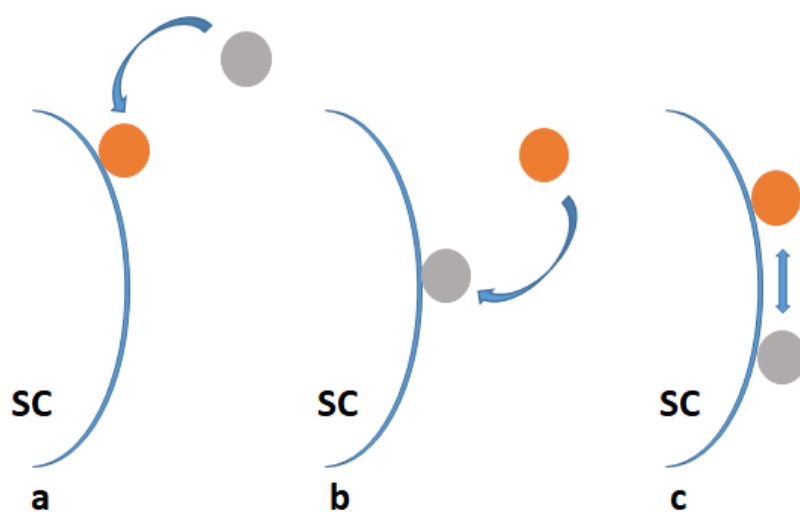


*Figure 1.3.* Schematic view of the pollutant molecule reacting with the hydroxyl radical. Hydroxyl radical adsorbed on the surface of the semiconductor is attacking the pollutant (a), pollutant is oxidizing at the surface of the semiconductor by the hydroxyl radical present in the solution (b), hydroxyl radical and the pollutant are adsorbed on the surface of the semiconductor (c). Oxidation reaction occurs (grey and orange balls represent target molecule and hydroxyl radical, respectively) [21]

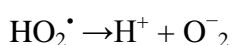
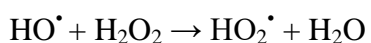
Hydroxyl radical adsorbed on the surface of the semiconductor might cause an oxidation reaction to degrade pollutant molecules existing near the semiconductor. Organic molecules adsorbed on the surface of the semiconductor might be degraded by the hydroxyl radical moving freely. Hydroxyl radical and the pollutant might be adsorbed on the surface of the semiconductor and oxidation reaction occurs. Hydroxyl radical moving freely might attack the pollutant molecules existing in the solution. However, it is acceptable that this reaction does not take place in photocatalytic systems due to the fact that the photocatalytic reactions occur at the adsorbed phase. Organic molecules can also be degraded by holes as well as hydroxyl radicals. The nature of the substrate might play an important role to choose the pathway for the degradation process [21].

Superoxide radicals ( $\text{HO}^\bullet$  and  $\text{O}_2^{\bullet-}$ ) play an important role in photooxidation reactions. It has been shown that superoxide radicals may reduce recombination rate



as electrons transfer to oxygen molecule during the formation of superoxide radicals. The photocatalytic reaction rate can also be controlled by superoxide radicals.

The formation of hydrogen peroxide can cause positive or negative effects in terms of photocatalysis. Photocatalytic degradation rate might be increased with the optimum level of hydrogen peroxide. Photooxidation rate may decrease with the increasing level of hydrogen peroxide.



The rate of the photocatalytic reaction is increased by scavenging electrons from superoxide through oxygen which is the safest, cheapest and the most reliable electron acceptor. Singlet oxygen ( $\text{O}_2^{-\bullet}$ ) is imported as the lowest excited state of molecular oxygen. It is a powerful oxidizing agent [21].

The semiconductors can participate in photocatalysis process in two ways: they can capture electrons from the substrate as an oxidizing agent; they can transfer electrons to substrates as reducing agent (Figure 1.4) [24].

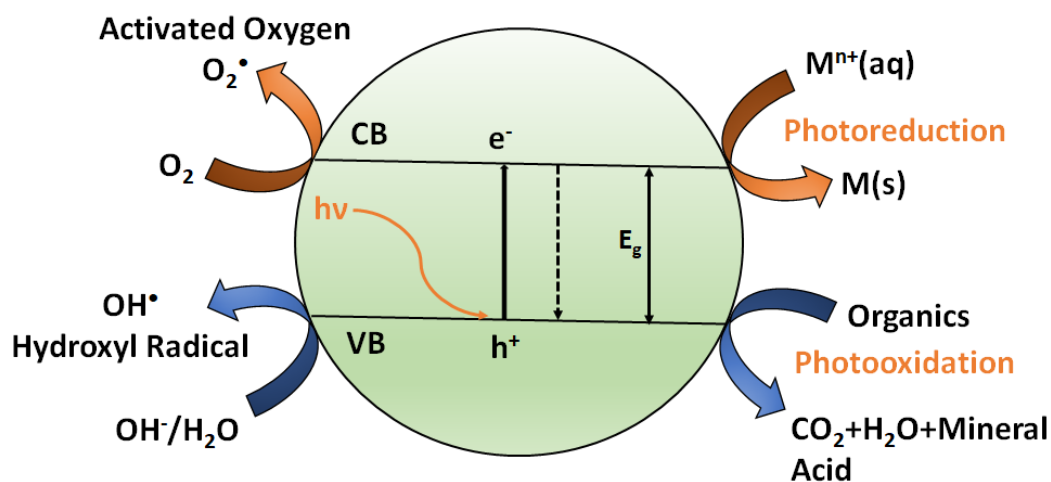


Figure 1.4. Schematic view of the photocatalysis mechanism [25]

Various conditions might occur for electrons and holes en route to the surface of a semiconductor. Hole traps are present near the valence band, whereas electron traps are present at the center of the energy bandgap or near the conduction band. Figure 1.5 demonstrates the schematic view of electron-hole recombination and their trapping mechanism. Hole trapping triangle indicates the movement of the hole into a shallow trap, then deep trap or directly to a deep trap. The chemistry of deeply trapped holes and surface bound hydroxyl radicals are similar to each other. Therefore, it is important to understand the mechanism of hole trapping [21].

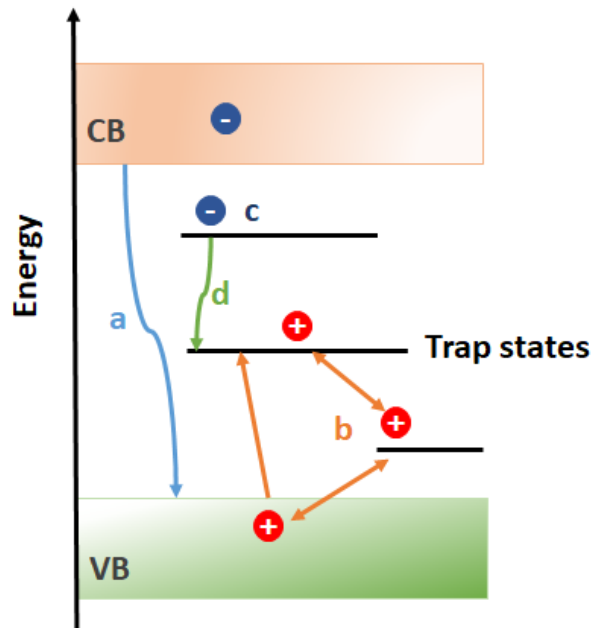


Figure 1.5. Schematic view of band-band recombination (a), hole trapping triangle (b), shallowly trapped electron (c), trapped-assisted recombination (d) [21]

When a semiconductor is irradiated by light with photon energy greater than the bandgap energy, photons can excite electrons from the valence band to conduction band. This excitation can occur in two ways: for direct bandgap, the energy of the electron changes but its momentum remains the same during the excitation process. In the indirect bandgap, both energy and momentum of the electron change. Electrons interact with photon and a lattice vibration (i.e., phonons) to change its energy and momentum. Indirect bandgap transitions are relatively slow and less effective in terms of photocatalysis mechanism. After the excitation process, the electron-hole pair should have a particular lifetime without recombination for a good photocatalytic performance of a semiconductor. The energy on the system resulting from the excitation can be lost in two ways: recombination of the electron-hole pair or photocatalytic reduction and oxidation processes. For an enhanced photocatalytic activity, charge separation and conduction are crucial. Crystal impurities and defects are known as trapping sites for electrons and holes hindering recombination [20].

The use of a photocatalyst for practical applications, visible light activity is very important in terms of the effective use of solar energy. Some photocatalysts effective under visible light irradiation are shown in Figure 1.6.

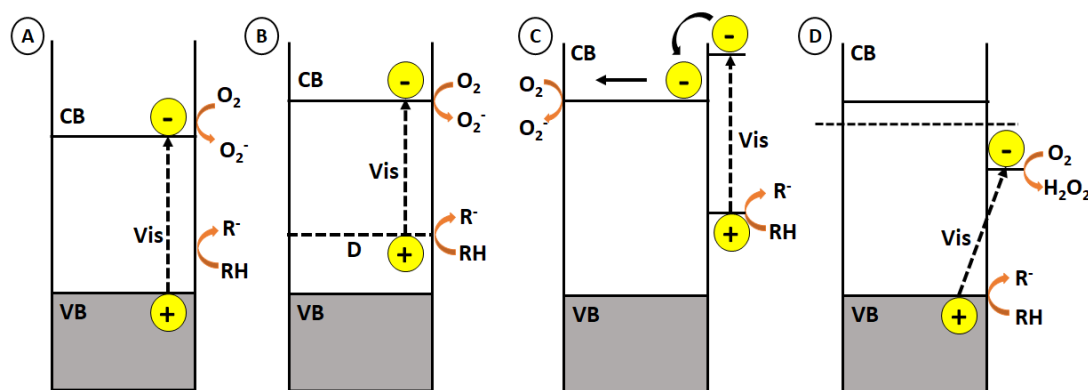


Figure 1.6. Photocatalysts under visible light irradiation by means of the reaction mechanism. Narrow-band-gap semiconductor such as  $\text{WO}_3$  (a), anion-doped  $\text{TiO}_2$  such as nitrogen-doped  $\text{TiO}_2$  (b), sensitizer deposited  $\text{TiO}_2$  such as  $\text{PtCl}_6^{2-}$ -deposited  $\text{TiO}_2$  (c), and interfacial-charge-transfer-type  $\text{TiO}_2$  such as  $\text{Cu(II)}$ -grafted  $\text{TiO}_2$  (d) [22]

O-2p orbital determines the energy level of valence band resulting in narrower bandgap energy for metal oxide semiconductors such as  $\text{WO}_3$  (Figure 1.6-A). For a better photocatalytic activity, doping the anions such as N or S can be applied to  $\text{TiO}_2$  resulting in a shift in the valence band. The holes left by the excited electrons on the donor level have the same oxidation ability as in the undoped  $\text{TiO}_2$  (Figure 1.6-B). A sensitizer can be deposited on a photocatalyst such as  $\text{TiO}_2$ . After visible light absorption by the sensitizer, excited electrons are transferred resulting in the production of radicals which are going to be used to oxidize organic molecules (Figure 1.6-C). Metal ions with good photocatalytic performance can be deposited. These types of absorption are denoted as interfacial charge transfer (IFCT) type absorption. Therefore, photoelectrons are excited to the valence band of the metal ions (Figure 1.7-D). If metal compound has the catalytic ability for the reduction of  $\text{O}_2$ , an enhanced photocatalytic activity is expected [22].

### **1.1.3. Methods for Enhancing Photocatalytic Activity**

When a photon is absorbed by a semiconductor, electrons in the occupied valence band excite to conduction band leaving positive holes in the valence band. These electrons and holes either recombine or induce redox reactions for the chemical species absorbed on the photocatalyst surface [22].

The wide bandgap of many semiconductors limits their photocatalytic effectiveness to UV light irradiation and makes them insensitive to visible light which is 42 % of sunlight. Therefore, production of photocatalysts effective under natural sunlight is gaining so much attention. Photocatalysis capturing the whole solar spectrum is desirable for the maximum performance of the system.

A few requirements are needed for an enhanced photocatalytic activity. The first and the most important one is energy bandgap of a semiconductor. Semiconductors with energy bandgap in the visible range show enhanced photocatalytic activity. The second requirement is the positions of CB and VB. The position of VB should be lower than the oxidation potential of oxygen and CB should be higher than the reduction potential of hydrogen (Figure 1.7) [23].

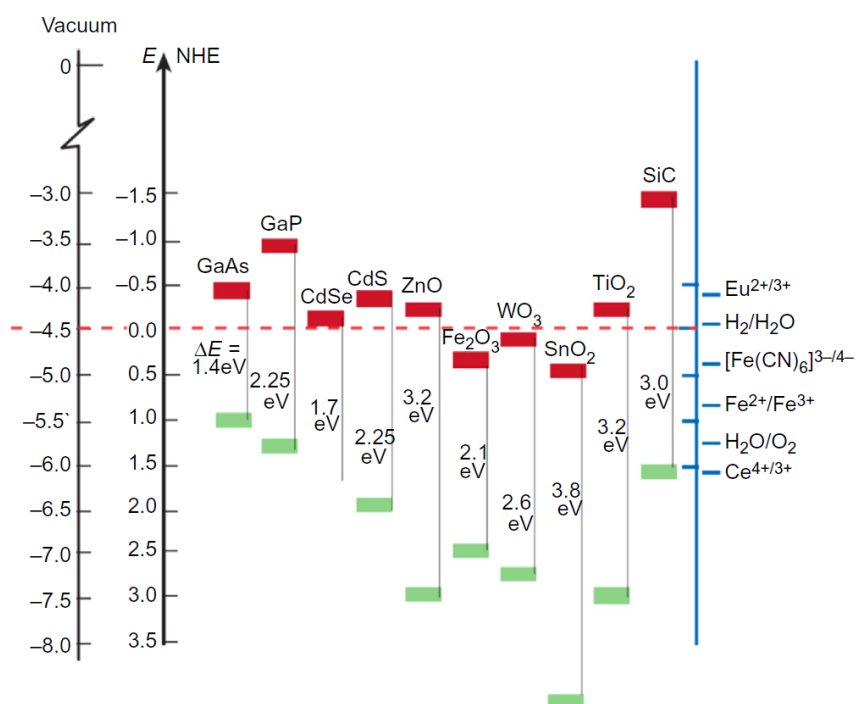


Figure 1.7. Bandgap positions of several semiconductors [23]

Most of the toxic chemicals dissolve in the water and the energy for water splitting is 1.23 eV. Therefore, bandgap of semiconductors should be higher than the energy needed for water splitting in order to produce high amounts of photoelectrons. The third requirement is related to the production and separation of charge carriers. Electrons are transferred to the semiconductor surface through diffusion and participate in the redox reaction. For an efficient photocatalysts, the absorption coefficient of the semiconductor should be large and diffusion length should be high. The fourth requirement is related to the presence of grain boundaries and surface states. Electron-hole pairs should reach the pollutant for an enhanced photocatalytic activity. Surface states on the surface of a semiconductor capture the charge carriers and increase their lifetimes. The fifth requirement is the stability against photocorrosion and dissolution of the photocatalysts. Accumulation of Photogenerated charge carriers on the surface of the semiconductor surface or pollutant can be observed under illumination. This may cause photocorrosion and

dissolution of the semiconductor. A minimum contact of the pollutant and the photocatalysts can hinder this situation. The sixth requirement is a high specific surface area of the semiconductor to adsorb more pollutant molecules. Nano-sized materials have a great amount of volume/surface ratio, these types of materials are preferable for enhance photocatalytic activity. Along with all these sixth requirements, other parameters such as electronic structure or geometry of the semiconductor affect the photocatalytic activity [23].

In order to produce semiconducting materials sensitive to visible light, they can be doped with metal ions (noble metals, rare earth ions or transition ions) or nonmetals resulting in a decrease in their bandgap. Metal-ion doping reduces the possibility of recombination of electron-hole pairs and alters the optical absorption edge [20,23].

Surface morphology of a semiconductor affected by particle size has a great impact on its photocatalytic properties. A more effective photocatalytic activity can be obtained by modifying surface morphology of a semiconductor [20,21]. When a smaller particle is used as a photocatalyst, redox potential is increased making it more effective to sunlight activation. The possibility of recombination also decreases with particle size. Particle size affects the number of adsorbed photons on the semiconductor surface [20].

The concentration of the photocatalyst is another parameter affecting the photocatalytic activity. For efficient photocatalytic activity and less light scattering, optimum concentration should be investigated. If semiconductor photocatalyst agglomerates, the photocatalytic reaction rate decreases [21].

Zeolite-based catalysts, one of the most promising systems for photocatalysis, are gaining attention due to their unique properties for photocatalytic applications. Zeolites with reversible structural and surface properties are able to be used in various catalytic applications. They could be modified with active metal ions in their cavities or outer surfaces. Different pore size may result in the formation of metal clusters of different sizes in the cavities. Therefore, it is important to select the

zeolite with the optimum pore size for photocatalysis. Ion exchange capacity is also affected by the pore size. Specific molecules may enter into the cavities and there react with the encapsulated catalysts. Metal ion doped zeolites may serve as photocatalyst for the photocatalytic systems operating under visible light [26].

Zeolites are famous now with their high surface area and adsorption capacity along with other parameters making them favorable for photocatalytic applications [27].

## **1.2. Zeolites and Zeo-Type Materials**

Zeolites are crystalline aluminosilicates consisting of  $\text{SiO}_4$  and  $\text{AlO}_4$  tetrahedra with a three-dimensional framework structure forming uniformly sized pores of molecular dimensions. Zeolites act as molecular sieves through the semipermeable property of the pores allowing to absorb molecules fitting inside the pores and exclude the large ones [28,29]. The framework of zeolites is negatively charged due to the replacement of  $\text{Al}^{3+}$  with  $\text{Si}^{4+}$  at some places. However, the extra framework cations in the cavities of the zeolite cause electroneutrality in the framework. Some of those cations are responsible for cation exchange and are able to reversibly interact with polar molecules. These properties have contributed significantly to the commercial use of zeolites [28].

The unique properties of zeolites such as ion-exchange, catalytic activity, and sorption capacity can be tailored by controlling the zeolite structure. That is, the size of the pores affect the sorption property, the number of extra framework cations and pore openings affect the ion-exchange capability, and Si/Al ratio affects the acidity and catalytic activity [30,31].

The framework types provide zeolites to be categorized upon their framework types [30]. FAU, LTA, MFI, etc. are codes representing the framework types as published in *Atlas of Zeolite Framework Types* [32]. The information about the pores,



connection of the tetrahedral atoms, and the channel system can be obtained from the framework type [30].

Zeolites consist of  $TO_4$  tetrahedra (T represents any tetrahedral coordination cation) and mostly have a 3-dimensional structure with channels and cavities. The size of the pore openings in zeolite structure is defined by the number of T-atoms enclosing these pores, for instance, an 8-ring structure is a small pore opening [30]. The pores of zeolite are flexible and pore and cavity dimensions are affected by the type of cation. In order to measure the dimensions of zeolites, it would be more accurate to mention the "effective" pore size, which could be 110 % of the crystallographic dimensions of zeolites [33,34]. Moreover, it is possible to modify the catalytic and ion-exchange characteristics of zeolites by changing the framework composition or type and/or the number of extra framework cations [34].

Extra framework cations originated from the synthesis mixture or post-synthesis treatments present in the channels and cages of the zeolite framework balance the electronegativity [30].

Zeolites have been widely used in chemical and petroleum industries as catalysts, adsorbents, animal feed additives, separators, etc. With the emerging technologies in nano-dimensions, zeolites became an interest as potential materials in nanotechnological applications such as medicine, and optoelectronics [34].

Materials with T atoms other than Al, but Ga, B, Ti, Cr, V, and P in their structures are called zeo-types. These materials have microporous or mesoporous structure consisting of hexagonal, elliptical, spherical, or parallel channels. They have some advantages over traditional zeolites such as their ability to be used in photocatalysis or quantum wire applications [33].

### **1.2.1. Microporous Titanosilicate ETS-10**

ETS-10, first synthesized by Engelhard in 1989, is an important microporous titanosilicate material with a 3-dimensional network consisting of corner-sharing

TiO<sub>6</sub> and SiO<sub>4</sub> and interconnecting channels and cavities. ETS-10 has a 12-membered ring pore system with dimensions 7.6 Å × 4.9 Å [15,35–39]. ETS-10 has unique properties such as pore uniformity, the presence of non-framework cations balancing the net negative charge of the framework. Thanks to these unique properties, ETS-10 is a promising material for catalytic, ion-exchange, adsorption and separation applications. Moreover, ETS-10 has monatomic, semiconductor, quantum-confined ...Ti-O-Ti-O-Ti... chains running along both *a* and *b* directions separated from each other by a silica matrix [15,37].

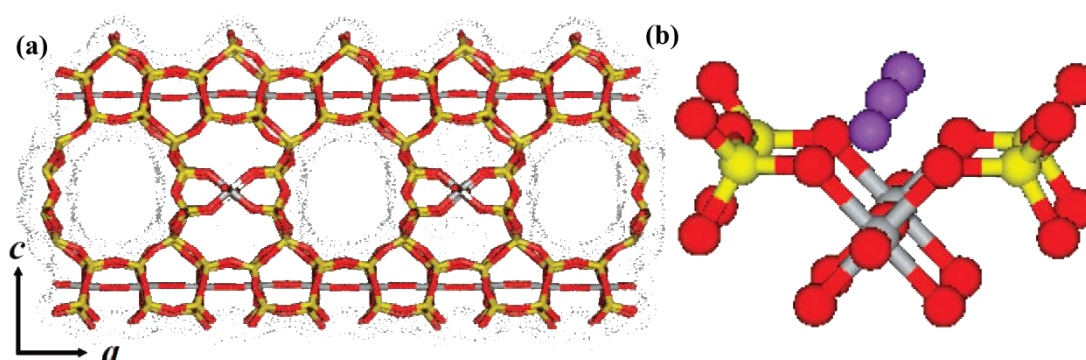
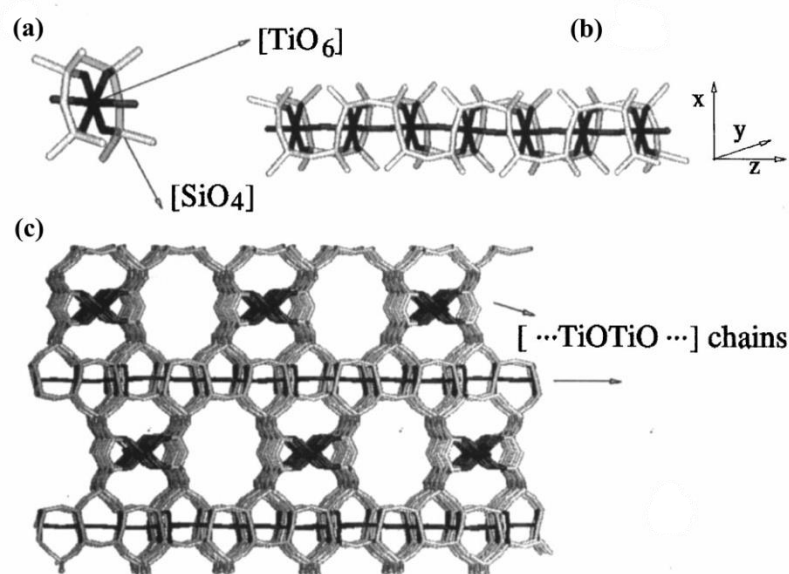


Figure 1.3. Stick representation of ETS-10 structure along the *b* direction (a). Si, Ti, and O atoms are represented as yellow, gray, and red sticks, respectively. -Ti-O-Ti-O-Ti- chains, running along with the *a* and *b* directions, are visible. Stick and ball representation, zoomed in on a fraction of the -Ti-O-Ti-O-Ti- chain showing also the charge-balancing monovalent cations (violet balls) (b) [37]

One-dimensional (1D) semiconductor quantum-confined materials are promising for nanoscale electronic devices and applications. Quantum wires are the thinnest 1D quantum-confined material. ...Ti-O-Ti-O-Ti... quantum wires are examples for these quantum wires (Figure 1.10) [40]. These chains act as one dimensional analog of the TiO<sub>2</sub> which is a photocatalyst. However, ETS-10 has a more flexible structure which readily allows for transition metal and main group [25,41].

Each Ti atom in the titanium chain carries two negative charges balanced by extra-framework, exchangeable cations (Na<sup>+</sup> and K<sup>+</sup>); this leads to high cation-exchange capacity (Figure 1.9) [35,42]. These quantum wires with a bandgap energy of 4.03 eV in ETS-10 structure act as semiconductors in photocatalysis [42,43]. When

radiation greater than the bandgap energy, electron-hole pairs are created. These electron-hole pairs travel down the chain and initiate reactions with molecules at structural defects along the chains [43]. Thus, ETS-10 is a suitable material for photocatalytic and semiconducting applications such as solar cells. However, high band-gap energy limits the photocatalytic activity [15].



*Figure 1.4.* The framework structure of ETS-10 showing chains of corner-sharing TiO<sub>6</sub> octahedra which run along with two perpendicular directions, and which are isolated by corner-sharing SiO<sub>4</sub> tetrahedra: single element of the chain (a); single chain (b); three-dimensional view (c) [44]

Many studies have been reported on ETS-10 structure and its applications up to now. Valtchev and coworkers reported the synthesis of ETS-10 from titanosilicate gels in the presence of an organic template [31]. Zhao and coworkers studied the synthesis of microporous titanosilicate ETS-10 by using TiF<sub>4</sub> as the Ti source and the adsorption properties of heavy metal ion Pb<sup>2+</sup> on the ETS-10 sample [45], Magnowski and coworkers reported the separation of ethane from methane in a synthetic natural gas mixture by adsorption on cation-exchanged ETS-10 at ambient temperature and pressure [46]. Agostini and coworkers applied many types of treatments (thermal-, chemical-, and UV-photo-) and accomplished the ETS-10 light absorption to shift down to the visible region [37]. Philippou and coworkers

investigated the catalytic performance of the ETS-10 for the aldol condensation of acetone [36]. Ji and coworkers investigated the role of ionic silver ( $\text{Ag}^+$ ) and metallic silver ( $\text{Ag}^0$ ) on the photocatalytic activity of ETS-10. They aimed at hindering the recombination of electrons and holes produced in semiconductors when irradiated [15].

### **1.2.2. Microporous Vanadosilicate AM-6**

Microporous vanadosilicate AM-6, isostructural with ETS-10, is another type of zeo-type material. ETS-10 and AM-6 have identical structures, thus it can be predicted that AM-6 might be used as a semiconductor or optoelectronic material as ETS-10. The manipulation of the properties of these zeo-type materials is possible by adding other atoms into the structure [42]. It wouldn't be a surprise that novel electronic and magnetic properties will be observed when paramagnetic V (IV) is added into the structure instead of Ti (IV) [47].

Vanadosilicate AM-6 (Aveiro/Manchester no. 6), isostructural with ETS-10, has 12-membered ring channels and contains monatomic semiconductor ...O-V-O-V-O... chains separated from each other by a silica matrix [48,49]. AM-6 is a microporous material with unit cell composition of  $(\text{Na}, \text{K})_2\text{VSi}_5\text{O}_{13}\cdot 3\text{H}_2\text{O}$  and pore openings of approximately  $4.9 \times 7.6 \text{ \AA}$  [50]. The structure of AM-6 consists of corner-sharing  $\text{VO}_6$  octahedra and  $\text{SiO}_4$  tetrahedra. AM-6 is a promising material for the catalysis, gas separation, and sorption applications due to its unique properties such as microporosity, pore regularity, and the presence of vanadium [48,49]. The framework of AM-6 has a net negative charge which is neutralized by  $\text{Na}^+$  and  $\text{K}^+$  extra-framework cations occupying the pores with water molecules [47,50]. Vanadosilicate AM-6 has a 3-dimensional pore system consisting of 12-, 7-, 5-, and 3-membered rings. 12-membered rings form minimal pore diameter. The unit cell composition is  $(\text{Na}, \text{K})_2\text{VSi}_5\text{O}_{13}\cdot 3\text{H}_2\text{O}$  [47].

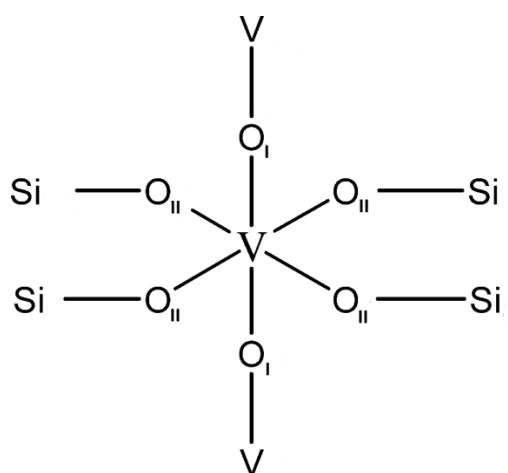


Figure 1.5. A structural model for AM-6 structure [47]

V ions are octahedrally coordinated by four Si-O bonds and two V-O in the AM-6 structure (Figures 1.11 and 1.12). V atoms do not substitute the Si atoms in the SiO<sub>2</sub> matrix [41].

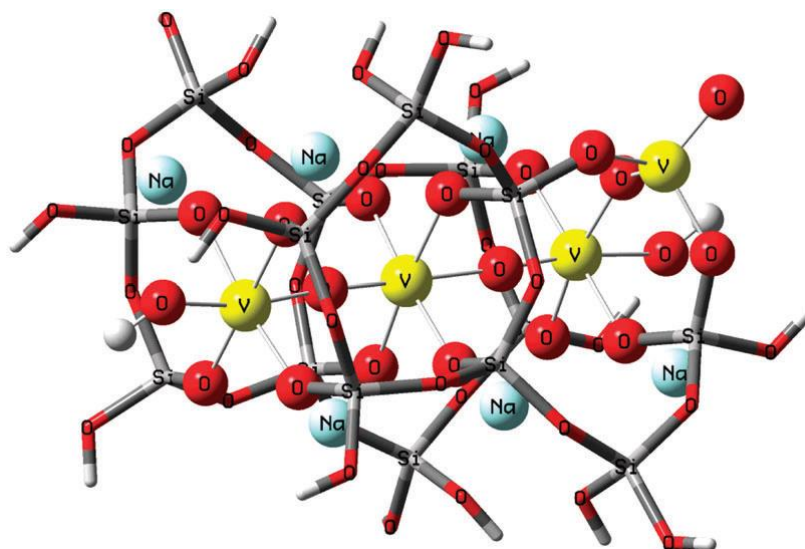


Figure 1.6. The model for AM-6 using DFT calculations [41]

There are two types of oxygen atoms in the structure: Type I and type II. Type I bridging the V atoms along the ...V-O<sub>I</sub>-V-O<sub>I</sub>-V... chains is also termed as axial oxygen atoms (O<sub>a</sub>). Type II bridging each vanadium atom with the silicon (Si) atom is also termed as equatorial oxygen atoms (O<sub>eq</sub>) (Figure 1.11). Si atoms have two types of chemical environment: Si linked via O bridges to four Si atoms (4 Si, 0V); and Si linked via OII bridges to three Si atoms and one V atom (Figure 1.13). The intensity ratio of the Si (4Si, 0V) sites to Si (3Si, 1V) sites is 1:4 [25].

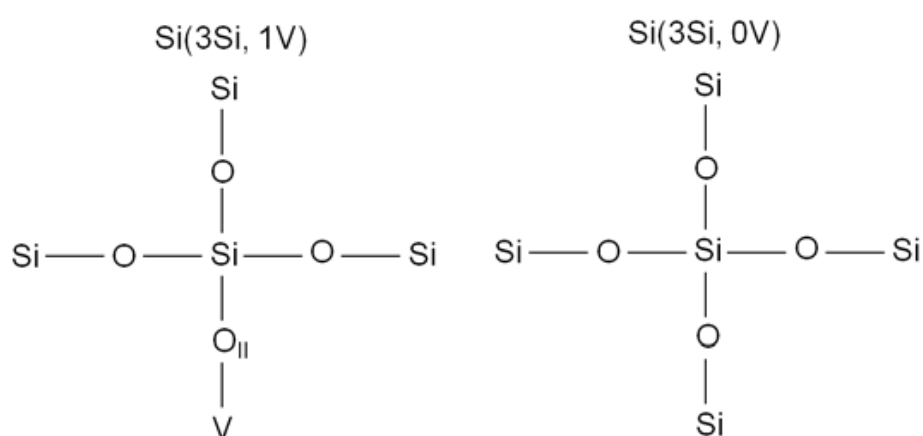


Figure 1.7. Two chemical environments for the Si atoms in vanadosilicate AM-6 [25]

Inorganic materials have the possibility to be used as photocatalysts and in photovoltaic applications due to their ability to harvest the light. Semiconductors can be modified by incorporating elements into them to enhance their photocatalytic activity in the visible light region [41]. AM-6 crystals are photocatalytically active under visible light irradiation, thus they can be used as natural sunlight photocatalysts [48]. The V<sup>5+</sup> and V<sup>4+</sup> sites along the ...V-O-V-O-V... act as electron and hole traps, respectively. If these two sites are close to each other, then electron-hole recombination may be promoted and photocatalytic activity may be lower consequently. Thus, Ismail and coworkers proposed the incorporation of transition metal ions into the AM-6 framework. They estimated that incorporation of transition

metal ions may provide separation of  $V^{5+}$  and  $V^{4+}$  sites and enhancement photocatalytic activity [50]. The ...O-V-O-V-O... chains also show ferromagnetic ordering at temperatures below 50 K. This makes AM-6 crystals potential porous magnets with the incorporation of magnetic guest molecules [48].

The microporous structure of AM-6 has a large surface area. However, only a small portion of the surface is reactive in both catalytic and photocatalytic reactions due to the isolation of the chains from adsorbed molecules by silica matrix. Post-treatments or usage of organic mesoscale templates is possible ways to enhance the mass transfer [51].

AM-6 was first synthesized by Rocha and coworkers by using ETS-10 as seed crystals. They produced an ETS-10/AM-6 core-shell structure. However, AM-6 crystals were containing quartz as impurity [49]. The modification of optical properties and the advanced applications were limited and the characterization was complicated due to the presence of ETS-10 in the AM-6 structure. Therefore, an unseeded synthesis method was in need [25,48]. This was achieved by Ismail and coworkers and they synthesized AM-6 crystals without using ETS-10 as a seed crystal [48].

Table 1.1 demonstrates the structural differences of microporous ETS-10 and microporous vanadosilicate AM-6.

Table 1.1. A comparison between microporous titanosilicate ETS-10 and microporous vanadosilicate AM-6

Properties	ETS-10	AM-6
Structure	SiO <sub>4</sub> tetrahedra and TiO <sub>6</sub> octahedra	SiO <sub>4</sub> tetrahedra and VO <sub>6</sub> octahedra
Pore Dimensions	4.9 x 7.6 Å	4.9 x 7.6 Å
Quantum wires	....Ti-O-Ti-O-Ti....	....V-O-V-O-V....
Energy bandgap	4.03 eV	3.80 eV
Photoreactivity	UV region	Visible region

AM-6 crystals produced by using these methods contain  $V^{4+}$  and  $V^{5+}$  states in quantum wires [48,49]. In 2012, Jit Datta and coworkers succeeded to synthesize pure, monodisperse, and highly crystalline AM-6 crystals without using ETS-10 seeds and containing only  $V^{IV}$  in the quantum wires [52]. Vanadosilicate AM-6 crystals should be supported on a substrate to utilize the unique properties for device applications. To the best of our knowledge, only one paper was reported on the synthesis of vanadosilicate AM-6 membranes on  $\alpha$ -alumina substrate to use it as a gas separation membrane [53]. Improving thin film making procedures are necessary for increased use of these types of zeo-type materials in advanced applications [54].

### **1.3. Thin Film Preparation of Zeolites and Zeo-type Materials: In situ and Secondary Growth Method**

Preparation of zeolites and/or zeo-type materials on a substrate is crucial for their potential applications such as gas separation membranes, sensors, catalysts or microelectronic devices [55–58]. It is possible to prepare these type of materials on a substrate by using many methods such as in situ, secondary growth, vapor phase transport, etc [59].

Seed preparation or spin/dip-coating technique is not required for in situ method. The direct coating is possible on the surfaces of different shapes and structures in this method [55]. Wang and co-workers investigated the effect of reaction time and temperature, properties of the substrate such as roughness and chemistry, and aging time for synthesis on the formation of MFI monolayer films. They easily obtained b-oriented MFI type monolayers on metal substrates without voids or cracks by using in situ method [55]. Uniform orientations of nonlinear optical molecules and semiconducting quantum dots could be obtained by producing a zeolite monolayer. Ha et al. investigated the monolayer formation of large zeolite crystals on several substrates by using in situ method [60]. A disadvantage for in situ models is that the control of the orientation of the membrane is unlikely. The membranes produced by



in situ methods are generally randomly oriented affecting molecular sieving properties and the roughness of the film [56,61].

The preparation of the seed layer and the subsequent growth of the seed layer into a continuous film are two main steps of secondary growth method. In the first step, a suspension of pre-synthesized seed crystal is deposited on a substrate by one of the in-situ methods. Electrostatic forces between zeolite particles and the substrates enable the seed layer formation on the substrate. In the second step, seed layer crystals are intergrown forming a continuous film [62]. In the secondary growth method, the orientation of the membrane is dependent on the orientation of the seed layer. Generally, the seed layer is randomly oriented resulting in a non-uniform orientation of membrane according to the competitive growth model. However, if the seed layer has the tendency to grow in one direction during hydrothermal synthesis, an oriented membrane can be obtained [61]. Anisotropic seed crystals such as cubic-shaped zeolites tend to form oriented seed layers [62]. Altering the parameters such as size or morphology of the seed crystals or synthesis conditions can result in an oriented membrane upon secondary growth method [61]. The manipulation of the orientation of a zeolite film is desirable for different applications affecting the performance of the zeolite film [63,64]. Hu and co-workers have successfully synthesized highly c-oriented AFI membranes by using secondary growth method. First, they synthesized plate-like AFI seeds, and then they placed these seed crystals to form a c-oriented seed layer by fingerprinting. Afterward, they applied hydrothermal treatment to grow highly c-oriented membranes [61].

There are two conditions for the preparation of an oriented zeolite and/or zeo-type film: growth rate should be faster than the nucleation rate and crystal faces should grow anisotropically with the crystal face. This will result in the highest orientation rate in the desired direction [63]. The secondary growth approach provides reproducibility and eliminates the negative effects of the substrate surface on film formation due to the existence of the seed layer [58,64]. Seed layer plays an important role in the formation of zeolite and/or zeo-type films. When smaller

crystals in size are used as seed, better intergrowth of these seeds is obtained resulting in a smooth surface. The larger seed crystals cause rough surfaces and defects resulting in a worse intergrowth of seed crystals as compared to smaller seeds [58]. Zhang et al. produced zeolite film using different sized silicalite-1 seed crystals. They investigated the effect of the seed crystal size on the formation of zeolite film. They obtained well intergrown and smooth zeolite film without voids or cracks upon using smaller seed crystals [58].

## CHAPTER 2

### LITERATURE REVIEW

#### 2.1. Photocatalytic Materials

Titanium dioxide ( $\text{TiO}_2$ ) is the most frequently used semiconductor material as photocatalyst owing to its high photocatalytic activity, chemical and biological stability, ease of availability, and low cost [4,8,16,65–68]. However, utilization of  $\text{TiO}_2$  as photocatalyst induces some problems. These can be summarized as its requirement of UV light, which is 4-5% of the sunlight to get activated, low electron transfer rate, and high electron-hole recombination rate-limiting the usage of solar energy with decreased photoreactivity [6,16,69]. For these reasons, various methods have been developed to modify  $\text{TiO}_2$  photocatalyst by doping foreign elements [17,70]. Engelhard titanosilicate (ETS-10) is a class of crystalline titanosilicate including ...Ti-O-Ti-O-Ti... wires acting as a one-dimensional analog of  $\text{TiO}_2$  with increased flexibility for doping foreign metals with respect to  $\text{TiO}_2$  [41]. Unfortunately, one important disadvantage of ETS-10 is its large bandgap of  $\sim 4.03$  eV, which limits its photoresponse in the ultraviolet (UV) region [54]. To solve this problem, transition metals such as Fe, Cr, and V into the titanium wires can be incorporated to reduce the bandgap, which can extend the photoresponse of ETS-10 and make the photocatalyst sensitive to visible light. Among these transition metals, when titanium in the ETS-10 is replaced by vanadium, the resulting vanadosilicate structure is isostructural to ETS-10 producing AM-6 with 1D ...V-O-V-O-V... wires [71]. Until now, AM-6 that is only in its powder form had been investigated in terms of its photocatalytic activity [25,41,71,72]. It was shown that AM-6 with different F/V ratio demonstrated strong visible light absorption which can be attributed to the structural defects originated from the connection of  $\text{VO}_6$  octahedral wires and  $\text{VO}_4$  tetrahedral units [41].

While using photocatalysts in powder form requires filtration of photoactive particles, which is an expensive and time-consuming procedure, thin film production provides integration of the material to device-oriented applications and also accelerates the degradation kinetics increasing the contact area between the surfaces of the pollutant and the photocatalyst [54,65,73]. Therefore, the production of thin films with low energy bandgap and photocatalytic activity under visible light irradiation would be a significant improvement.

### **2.1.1. Photocatalytic Decomposition of Methylene Blue**

The textile industry is the main source of dyes resulting in severe water pollution. Around 20-30 % of the dyes cannot be adsorbed on the fabric and cause water to be colored and ultimately wastewater. This wastewater with high pH and temperature is highly toxic for animals and plants. Hardly any of the dyes are biodegradable and they are highly resistant to environmental conditions. Therefore, wastewater caused by the textile industry induces critical problems. Thus, various techniques such as membrane separation, ion exchange, chemical oxidation, electrochemical techniques, adsorption, and photocatalysis have been investigated to remove dyes from wastewaters. Methylene blue (MB) as a representative organic dye for dyes used in textile industry has been used in many studies [74,75]. In industry, MB is being utilized for coloring materials such as cotton or wood [75].

MB can cause eye burns as such that permanent eye damages may occur. Rapid and difficult breathing increases when MB is inhaled. Burning, sickness, vomiting, sweating, and mental instability are examples of symptoms when MB is consumed. Wastewater management containing such dyes are challenging due to these harmful effects [75,76].

Ghosh et al. investigated the parameters affecting the adsorption capacity of kaolin. In this study, the adsorption of MB on kaolin was studied. For adsorption experiments, they used six different kaolin samples. They claimed that purified and NaOH treated kaolin sample showed the best adsorption property [76]. Carvalho et

al. studied the effect of copper as metal dopant on the photocatalytic activity of TiO<sub>2</sub> for the photocatalytic decomposition of MB. They deposited a thin copper layer above a relatively thicker TiO<sub>2</sub> film on a glass substrate. The copper layer was etched followed by a thermal treatment in order to allow copper ions to migrate from the surface to a deeper region. Therefore, structural changes on the surface were obtained and high hydrophilicity was observed. The increased photocatalytic activity was also achieved by this mechanism [77]. Ji et al. utilized ETS-10 crystals as photocatalyst and MB as a model organic compound for photocatalytic activity investigations. They aimed ETS-10 crystals to be photocatalytically active under visible light irradiation and investigate the role of silver incorporation in photocatalysis. In this way, Ag<sup>0</sup> nanoparticles were formed in the structure of as-synthesized ETS-10 crystals followed by the ion-exchange procedure with Ag<sup>+</sup> ions. It is known that silver nanoparticles create a very strong electric field due to surface plasmon resonance (SPR) effect and role as electron traps. Silver nanoparticles are critical catalytic sites providing the formation of reactive radicals and the reactions of oxygen adsorption and reduction. Silver modified ETS-10 showed photocatalytic activity under visible light irradiation as compared to unmodified ETS-10 due to the reasons mentioned above [15].

### **2.1.2. Porous Materials as Photocatalysts**

High surface area, accessibility to active sites, enhanced mass transport and diffusion properties are the reasons why porous materials have proposed an area of research such as energy conversion and storage, catalysis, photocatalysis, adsorption, and separation. The indicative parameters for their performance in applications are porosity, morphological and content information. The adsorption of dye molecules could increase the optical path length enhancing light-harvesting efficiency. Besides, photogenerated electrons and holes occur due to enhanced light-harvesting efficiency. The porosity of the materials is an improving parameter for their performances [78]. Pollutants need to be adsorbed on the surface of the photocatalyst

for a redox reaction. High surface area and enhanced diffusibility of the pollutant resulting from the porosity increase photocatalytic activity [79].

The photocatalytic activity could be enhanced through porous structures. They facilitate the adsorption of reactant molecules and provide multiple accessible sites. Diffusion length of the reactant molecules decreases due to their high specific surface area. More isolated and more separated active sites could be formed after irradiation and special channels could be provided for charge transport. Thus, charge separation and transport are facilitated under illumination [80].

High thermal stability, low cost, and fewer damaging properties of titania is the most promising photocatalyst among other semiconductors. However, only the UV region of the solar radiation is allowed due to its relatively large bandgap. It has been proposed that porosity should be added to the structure of  $\text{TiO}_2$  to enhance the light-harvesting efficiency likewise photocatalytic activity [78].

Porous ZnO materials are gaining attention due to their enhanced photocatalytic activity considering ZnO particles [79]. Cho et al. synthesized porous ZnO-ZnSe nanocomposites for photocatalysis under visible light irradiation. Following the synthesis of porous ZnO nanostructures, they converted them into ZnO-ZnSe nanocomposites using a dissolution-recrystallization method. A comparison between the photocatalytic properties of ZnO nanostructure and ZnO-ZnSe nanocomposites were carried out. They obtained an enhanced photocatalytic activity when ZnO-ZnSe nanocomposites were used as photocatalyst. Electrons transfer to the conduction band of ZnO and holes remain in the valence band of ZnSe decreasing the possibility of electron-hole recombination. Holes in the valence band of ZnSe oxidize directly the dye molecules adsorbed on the ZnSe nanoparticles. Electrons in the conduction band of ZnO reduce the oxygen on the surface of ZnO generating a superoxide radical anion. The superoxide radical would create hydroxyl radicals to degrade dye molecules [81].

Jiang et al. synthesized porous TiO<sub>2</sub> in nanoscale and discussed the effect of size and preparation technics of the nanoparticles. They obtained enhanced photocatalytic activity when nano-sized porous TiO<sub>2</sub> was used as photocatalyst for the degradation of methyl orange [82].

Taha et al. prepared carbon nanofiber embedded in WO<sub>3</sub> structure with the ability of separation of electrons and holes. Their photocatalytic activities were investigated using different types of dyes under visible light irradiation and improved photocatalytic activity was observed. It was also demonstrated that these materials could be recycled without any change in their photocatalytic activity through their nanostructural properties [83].

Silver-containing complex oxide semiconductors are considerable for the enhancement of photocatalytic activity. In these materials, the top of the valence band could form a new valence band with higher energy-containing Ag 4d and O 2p hybrid orbitals resulting in a narrower bandgap. The utilization of Ag<sub>2</sub>NO<sub>3</sub> has been proposed for photocatalytic degradation processes due to its stability and electron acceptor behavior instead of Ag<sub>2</sub>CO<sub>3</sub> which has corrosion behavior. Guo et al. prepared porous Ag<sub>2</sub>CO<sub>3</sub> nanorod photocatalyst for the photocatalytic decomposition of RhB under visible light irradiation [80].

## **2.2. Thin Film Preparation of Zeolites and Zeo-type Materials**

Yoon et al. [40] synthesized seedless and template free AM-6 crystals for the first time in comparison with ETS-10 core/AM-6 shell crystals made by Rocha et al. [49] and ETS-10-free AM-6 crystals containing tetramethylammonium ion (TMA<sup>+</sup>) as structure-directing agent synthesized by Sacco, Jr. et al. [48]. AM-6 samples in powder form synthesized by Yoon et al., Sacco, Jr. et al., and Rocha et al. were denoted as AM-6-(Y), AM-6-(S) and AM-6-RA respectively. AM-6-(Y) samples were found to be the purest (i.e., vanadium has just one oxidation state -V<sup>IV</sup>- in the chain) having the cheapest production method. This founding was mainly based on the variations made in the growth solution, i.e., the vanadium source of V<sub>2</sub>O<sub>5</sub> in AM-

6-(Y) as opposed to  $\text{VOSO}_4$  in AM-6-(S) and AM-6-RA and the use of ethanol as a reducing agent.

In order to use these materials in advanced device-oriented applications, it can be of interest to support these materials on transparent conductive oxide substrates. Utilization of zeolite thin films using secondary growth has already attracted considerable interest as an alternative route in several device applications, such as zeolite membranes, sensors, and photochromic films [40,84–87]. Accordingly, the novel and interesting properties carried along with 1-D quantum confined materials can be extended to such applications in order to benefit from the catalytic, magnetic and electronic properties of vanadosilicate AM-6 if these materials are obtained in thin film form on different substrates. To the best of our knowledge, only one paper was reported on the synthesis of vanadosilicate AM-6 membranes, where  $\alpha$ -alumina substrates were used as support [53]. In the current study, the ETS-10 core/AM-6 shell methodology was applied in the original formation of AM-6 crystals in powder form by using ETS-10 as seeds [40,48,49].

### **2.2.1. Controlling the Crystal Orientation in Zeolite and Zeo-type Materials**

In order to produce high-quality zeolite films, microstructures of zeolite such as crystallographic preferred orientation (CPO) or thickness should be manipulated and optimized accurately. Device applications involving zeolite films are most likely affected by these microstructures. Among other types of microstructures, control of CPO is vital [64,88]. Out-of-plane crystallographic texture of the films highly affects their performance. Van der Drift proposed an evolutionary selection model to explain the formation of this texture in the 1960's. According to this model, grains have different crystal faces with different growth rates. Crystals with slighter growth rate disappear when they meet the boundaries of larger crystals. Crystals with growth rate in the perpendicular direction of the surface are preserved [88]. Zeolite films are most likely randomly oriented, but preferred orientation is required for particular applications [55]. There is a competition between the crystal growth rate and nucleation rate. Secondary growth mechanism should provide conditions such



that crystal growth rate overcomes the nucleation rate. Besides, crystals in the desired orientation should have the highest growth rate [89].

Secondary growth method is the most proper approach to obtain oriented zeolite film with respect to other methods due to the reasons such as higher reproducibility is possible and film formation is less affected by substrates. Liu et al. applied hydrothermal pretreatment to precursor solution in order to obtain highly *b*-oriented MFI films and to hinder twin growth using secondary growth approach [64].

Lee et al. prepared uniformly *b*-oriented monolayers of silicalite crystals on glass substrates by using fingerprinting. To strengthen the bonds between the substrates and zeolite crystals certain modification was applied to substrates or zeolite crystals. While silicalite-1 was modified Trimethylpropylammonium (TMP<sup>+</sup>) groups, glass substrates were modified with butyrate (Bu<sup>-</sup>) groups forming ionic bonding. Hydrogen bonding was formed between the surface hydroxyl groups of bare zeolite and bare glass. Another hydrogen bonding existed between the zeolite hydroxyl groups and poly(ethyleneimine) (PEI) and PEI and the hydroxyl groups of bare glass substrates. These ionic and hydrogen bonding were the most effective bonding types for monolayer formation [90].

Wang et al. produced *b*-oriented MFI monolayer films on metal substrates by using in-situ crystallization. Since MFI crystals have channels along *b*-axis, it was crucial to producing *b*-oriented MFI films. They investigated the parameters affecting film formation such as synthesis temperature, surface roughness, position and chemistry of the substrate, aging time. At lower crystallization temperature some *a*-oriented crystals were also obtained. Reaction time and temperature were optimized for *b*-oriented MFI film formation. They polished the substrate surface to investigate the effect of surface roughness on the orientation of the crystals and obtained *b*-oriented MFI monolayers with these two substrates. However, MFI monolayers had higher quality without curvature of the substrate. In order to investigate the position of the substrate, the substrates were placed vertically and horizontally resulting in the

formation of *b*-oriented MFI monolayer films for both positions. Aluminum alloy and gold substrates were utilized to see the effect of substrate chemistry on the film orientation. The only vertically placed aluminum substrate provided the formation of *b*-oriented MFI monolayer films. Aging time was another parameter affecting the crystal size. The more the aging time was, the larger the crystals were obtained. At an optimized aging time, *b*-oriented MFI monolayer films were obtained [55].

Yilmaz et al. obtained *b*-oriented ETS-4 films on alfa-alumina and titania substrates by using secondary growth approach. The pore channel system and ...Ti-O-Ti-O-Ti... chains in the structure of ETS-4 is in *b*-oriented. Therefore, it is important to prepare *b*-out-of plane ETS-4 films for applications. It was demonstrated that seed layer on alfa alumina is partially *b*-oriented; while seed layer on titania substrate is partially *a*- and *c*-oriented. After hydrothermal treatment of seed layers, *b*-oriented ETS-4 films were obtained on both alfa-alumina and titania substrates. They claimed that secondary growth conditions are more effective than seed layer orientation for the formation of ETS-4 films [89].

Lin et al. studied on the formation of ETS-10 membranes on different types of substrates for water/alcohol pervaporation experiments by using secondary growth approach. XRD patterns of pure ETS-10 powder and ETS-10 membrane were demonstrated in Figure 2.1 [91].

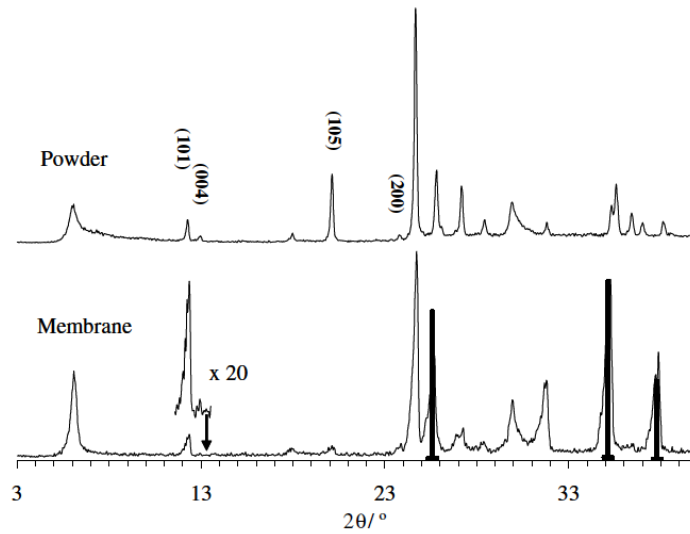


Figure 2.1. XRD patterns of ETS-10 in powder form and ETS-10 membrane [91]

Certain peaks with different intensities were obtained in the XRD pattern of ETS-10 membrane with respect to ETS-10 powder through preferred growth direction. The (004) reflection was almost insignificant which indicates c-orientation. CPO was calculated for a quantitative analysis for orientation. Accordingly,  $CPO_{x/y} = \frac{(I_x/I_y)_m - (I_x/I_y)_p}{(I_x/I_y)_p}$  was defined where I indicates the integrated intensity corresponding to x and y peaks; m and p represent membrane and powder form, respectively. a and b can be taken as equal due to the tetragonal structure of ETS-10.  $CPO_{200/105}$  was calculated as around 20 for ETS-10 indicating ETS-10 has a(or b)-out-of-plane preferred orientation. The main channels of ETS-10 is parallel to a or b orientation, a(or b)-out-of-plane preferred orientation can enhance membrane properties [91].

Galioglu et al. prepared oriented ETS-10 films on ITO-coated glass substrates by using secondary growth approach. They coated seed layer by 1-time, 2-times, and 3-times by dip-coating method and applied hydrothermal growth to seed crystals for ETS-10 formation. It was observed that the intensities of XRD peaks of ETS-10 powder have differences with respect to ETS-10 film (Figure 2.2) [54].

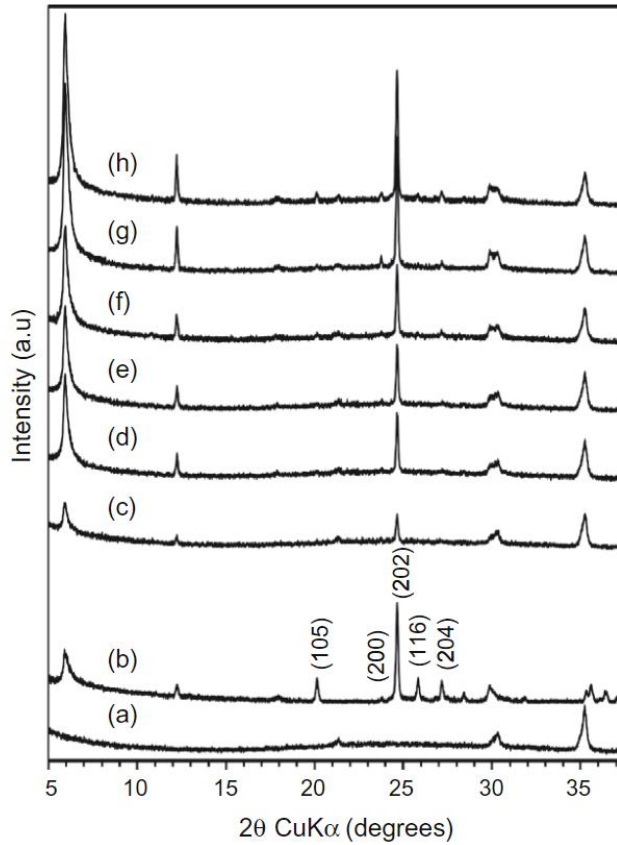


Figure 2.2. XRD patterns of bare ITO glass substrate (a), ETS-10 powder (b), seed layers deposited on the ITO glass substrate using 1 (c), 2 (d), and 3 (e) dip coating steps, and films after secondary growth of seed layers deposited via single (f), double (g), and triple (h) dip coating [54]

While the intensities of 105, 116, and 204 peaks decreased, the intensity of 200 peak increased indicating *a(b)*-out-of-plane orientation. CPO was also calculated for quantitative analysis of the degree of the *a(b)*-out-of-plane orientation. Accordingly,  $CPO_{200/105} = \frac{(I_{200}/I_{105})_f - (I_{200}/I_{105})_p}{(I_{200}/I_{105})_p}$  was defined. It was observed that CPO values decreased with the increasing number of dip-coating steps which is consistent with the literature [54].

CPO is calculated based on (200) and (105) reflections to determine the degree of *a(b)*-out-of-plane preferred orientation since ETS-10 has a tetragonal structure where *a* and *b* are equivalent. The intensity of (105) plane is used for the calculation of

CPO instead of (004) plane due to its very low intensity as shown in Figure 2.2. Therefore, the plane making the lowest angle with (004) plane is determined using the equation 2.1.

$$\cos \theta = \frac{\frac{h_1 h_2}{a^2} + \frac{k_1 k_2}{b^2} + \frac{l_1 l_2}{c^2}}{\sqrt{\left(\frac{h_1}{a}\right)^2 + \left(\frac{k_1}{b}\right)^2 + \left(\frac{l_1}{c}\right)^2} \sqrt{\left(\frac{h_2}{a}\right)^2 + \left(\frac{k_2}{b}\right)^2 + \left(\frac{l_2}{c}\right)^2}} \quad \text{Equation 2.1}$$

Figure 2.3 demonstrates a sketch for the positions of the crystallographic planes.

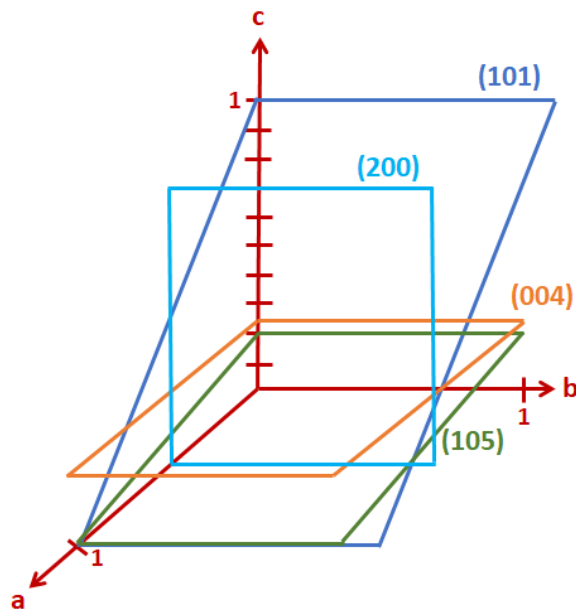


Figure 2.3. A sketch for crystallographic planes

Table 2.1 was also created to demonstrate the angle between the crystallographic planes.

Table 2.1. *The angle between the crystallographic planes*

Plane	Angle ( $\Phi$ )	Lowest Angle with (004) Plane
(200) and (004)	90°	
(109) and (004)	22°	1
(1110) and (004)	27.3°	2
(105) and (004)	36°	3
(116) and (004)	40.7°	4
(208) and (004)	42.4°	5
(217) and (004)	49.4°	6
(204) and (004)	61.2°	7
(224) and (004)	68.8°	8
(202) and (004)	74.7°	9

Accordingly, (105) plane was determined as the plane making the lowest angle with (004). Thus, CPO is calculated based on (200) and (105) reflections and defined as  $CPO_{200/105} = ((I_{200}/I_{105})_f - (I_{200}/I_{105})_p) / (I_{200}/I_{105})_p$ , where I depicts the intensity of the particular planes and f, and p depicts film and powder, respectively.

Photocatalytic activity is most likely dependent on the crystal growth direction of the crystal planes due to the fact that photocatalytic reactions occur at the interface between catalyst surface and organic pollutant [18]. Cations and anions might separate from each other through different surface orientations affecting surface chemistry, i.e. adsorption or reaction of molecules at the surface. Surface chemistry is crucial for heterogeneous photocatalysis. Different charge regions originate from different surface orientations. The possibility of recombination of electron-hole pairs decreases with large band bending at the surface. Different surface structures on the same material might give different photocatalytic activity. The change of charge transfer from the catalyst to the adsorbed molecule or the differences between charge separations may cause a difference in the photocatalytic activity. Electronic

anisotropy originated from the different orientations of different faces may induce photoexcited charge carriers to diffuse into desired crystallographic orientations. Thus, some faces might be photocatalytically more active [68]. Photocatalytic activity occurs at the interface between the catalyst surface and the pollutant. Therefore, photocatalytic activity was shown to be highly dependent upon the crystal orientation of the film produced for utilization as a photocatalyst. Accordingly, it is crucial to manipulate the crystal orientation for enhanced photocatalytic activity [18].

Jang et al. investigated the relationship between crystal growth orientation and their photocatalytic activity. They promoted a morphology-controlled system for the growth of ZnO crystals as they tend to grow anisotropically. They also demonstrated that photocatalytic activity is dependent upon particular crystal planes. In this way, they synthesized nanorod, nanoplane, microrod, and dumbbell-shaped of ZnO crystals and obtained different ratios of polar and nonpolar faces. Nanoplates with the highest amount of polar Zn (0001) face showed the best photocatalytic activity for the photocatalytic formation of H<sub>2</sub>O<sub>2</sub>. This was explained by facile adsorption of oxygen molecules on this face. Besides, Zn ions are coordinated with hydroxide ions which will be replaced with oxygen molecules to form H<sub>2</sub>O<sub>2</sub>. The hole formed at the onset of the photocatalytic reaction reacts with a hole scavenger such as acetate and consequently methyl radical is formed which will form organic peroxide [18].

### **2.2.2. Effect of the Seed Layer Morphology and Seed Crystal Population on Film Formation**

Seed layer added to the synthesis mixture gives smaller zeolite crystals, facilitate zeolite growth, and increases crystallization. Thin zeolite films and membranes are prepared by coating the pre-seeded substrates with zeolite nanocrystals. Afterward, a hydrothermal treatment is applied to the seeded substrates. In this way, perfect control on zeolite film orientation, morphology, and crystal growth is obtained. It is

known that the type, size, shape, and orientation of the seed crystal affect zeolite film growth [92]. Smaller seeds cause better-intergrown zeolite membranes to be obtained.

Crystal size and morphology affect the seed layer formation and consequently zeolite membrane. Seed layer becomes dense and homogenous with decreasing seed crystal size. Large or hexagonal-shaped seed crystals may cause a loose seed layer. It can be inferred that the quality of the seed layer is dependent on the size and morphology of seed crystals. Intergrowth of zeolite membranes grown from smaller seed crystals is better and smooth surfaces can be most likely obtained. Some defects and impurities come out during the formation of membranes using smaller seed crystals [58].

Qui et al. investigated the preparation, properties, and catalytic behavior of titanium silicalite-1 zeolites in powder and film form. They prepared titanium silicalite-1 in film form on alfa-alumina substrate without seeding and using two different seed crystals, i.e., titanium silicalite-1 and silicalite-1. While titanium silicalite-1 film with poor crystallization was obtained without seeding, well uniformly intergrown films were obtained after hydrothermal treatment of both seed crystals. The seeded films were demonstrated similar properties such as morphology, purity, etc. however, catalytic properties were different for styrene oxidation. Titanium silicalite-1 films obtained using silicalite-1 seed demonstrated almost two times selective behavior considering films obtained without seeding [92].

Zhang et al. prepared silicalite-1 membranes on alfa-alumina substrates using five different sized seed crystals. They investigated the effect of seed size on the formation of the zeolite membrane as shown in Figure 2.4 [58].



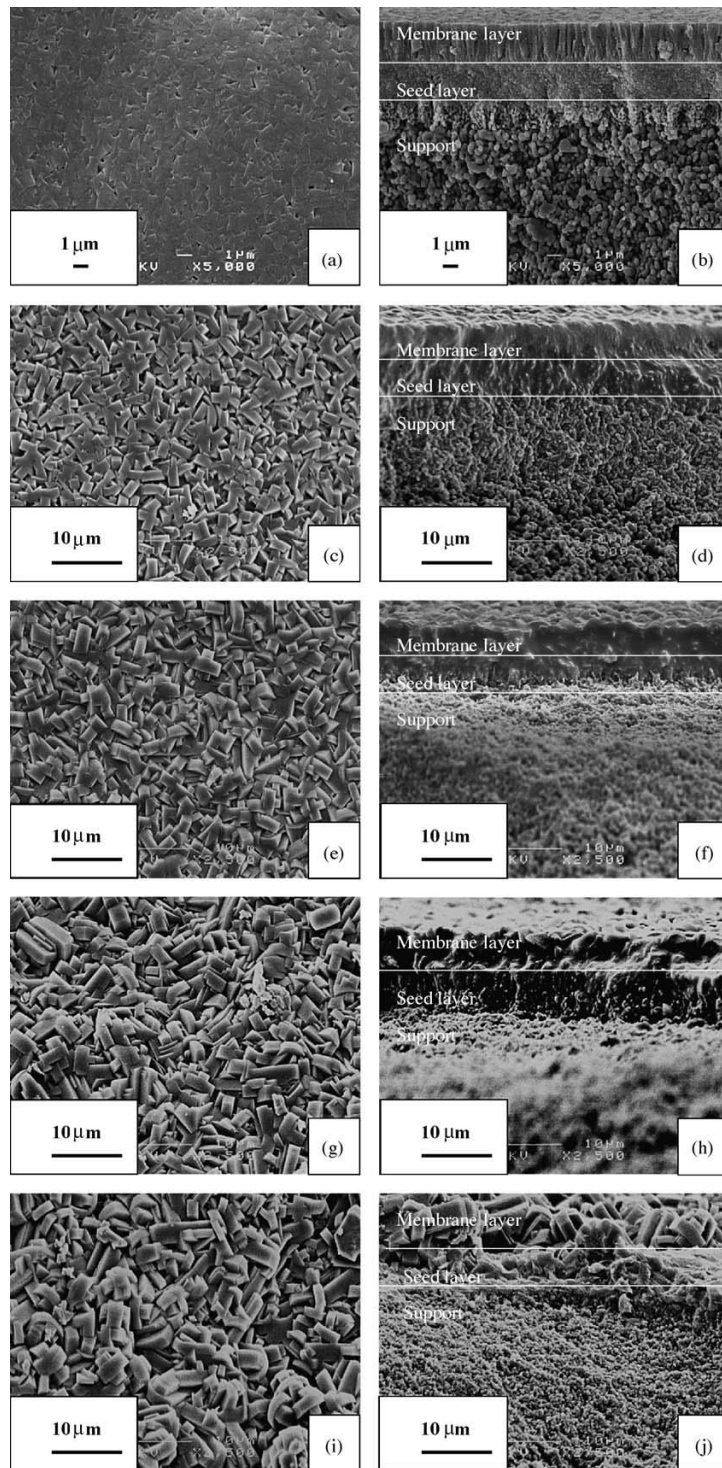


Figure 2.4. FE-SEM images of the silicalite-1 membranes grown on substrates seeded with (a and b) 100 nm, (c and d) 600 nm, (e and f) 1.5  $\mu\text{m}$ , (g and h) 3.0  $\mu\text{m}$ , and (i and j) 7.5  $\mu\text{m}$  seed crystals [58]

More uniform and smooth seed layers and consequently zeolite membrane surfaces were obtained using smaller seed crystals as shown in Figure 2.4. The use of oversized seed crystals caused zeolite membranes with voids and defects [58].

Li et al. investigated the seed layer concentration on the formation of silicalite-1 membranes. At low concentration rate, a loose structure of the zeolite membrane was obtained. With the increasing level of seed concentration, a denser seed layer and consequently thicker and more uniform zeolite membrane were obtained. Further increase of the seed concentration caused seed layer crystals to overlap with each other resulting in the formation of cracks on the zeolite membrane. They proposed that seed concentration affects the quality of the seed layer in parallel with the quality of zeolite membrane [93].

The performance of a zeolite film is affected by the orientation of the crystal constituting the zeolite film due to the fact that the pore system alters with the orientation of the crystals. Therefore, it is necessary to control the orientation of the crystal constituting the zeolite. Hedlund et al. succeeded to grow silicalite-1 films using silicalite-1 seed crystals with three different dimensions. Seed crystals were coated on a silicon wafer to form half-monolayer, monolayer or bilayer. Subsequently, hydrothermal treatment was applied to the seeded substrates. Thicker films were obtained as a result of the utilization of large seeds. When seed crystals with same dimensions were used, monolayer or half-monolayer coating of the seed layer could not change the thickness of the zeolite film. However, thicker films were obtained by using bilayer seed coating. The crystals constituting the zeolite films did not have characteristic silicalite-1 morphology due to the fact that crystal size was almost the same as the film thickness decreasing the possibility of lateral growth. The number of zeolite crystal per unit area decreases with increasing film thickness. This was clearly observed when the largest seed crystals were used. A continuous zeolite film could not be obtained when a half-monolayer seed layer was used. Besides, the growth of seed crystals was in every dimension and the characteristic morphology of seed crystals was no longer observed. In this study, it was identified

that the control of the amount and the orientation of seed crystals could provide control over the crystal constituting the zeolite film [94].

Wong et al. indicated that seed concentration along with the chemistry of synthesis and crystallization conditions is significant for the morphology and orientation of the crystals constituting zeolite film. That way, they synthesized TPA-silicalite-1 crystals as seed and coated the seed crystals on Si wafers such that each Si wafer has different concentration of seed crystals. Then, hydrothermal treatment was applied to seeded substrates. Crystal grains generally grow towards synthesis solution. According to competitive growth model, the competition between the neighboring grains determines the growth of each grain and the morphology and the orientation of the ultimate zeolite film. More growth center is formed with an increasing amount of seed causing a greater competition for nutrient and space affecting zeolite growth strongly. It was observed that crystal intergrowth is increased but crystal size is decreased due to competition. A change in the crystal morphology was also observed with increasing amount of seed crystals [95].

Xomeritakis et al. produced polycrystalline MFI films on porous alfa-alumina and non-porous glass substrates using secondary growth and in-situ approach. Microcrystalline MFI crystals were coated on the alfa-alumina substrates, and hydrothermal treatment was applied to the seeded substrates in secondary growth method. In situ method was applied on non-porous glass substrates without the use of seed crystals. A comparison between the films produced with or without seed layer was carried out for structural formation and permeability properties for butane isomers. The obtained films under secondary growth conditions revealed columnar grain structure and low surface roughness. The presence of seed layer affected strongly the film structure under secondary growth conditions. Crystals grew in solution and on the surface of the substrate in the absence of the seed layer. Characteristic imperfections arising from the gaps in the seed layer were obtained in the films obtained by using secondary growth method. Intergrown polycrystalline MFI films could not be observed in the absence of seed layer as seen in the

secondary growth method. The orientation of the MFI crystals constituting the film was different for secondary growth and in situ method. In the presence of seed layer, seed particles begin to grow as soon as they contact with the secondary growth solution skipping the nucleation step. The nutrient and precursor contribute to crystal growth without forming new grains. Seed layer provides crystal growth without the need for nucleation and restricts the formation of new crystals. The quality of the films is dependent on the seed layer. The permeability performance of the film is highly affected by the orientation of the crystals constituting the film [96].

### **2.2.3. Effect of Molar Water Content on Film Formation**

Increasing the water amount in the synthesis mixture also increases the reaction time and decreases the crystallization rate. Larger crystals are obtained from dilute synthesis solutions. Dilution causes fewer nuclei to be obtained considering the initial conditions. It can be inferred that dilution could restrict the crystal nucleation. The decrease in the supersaturation level over dilution may cause this condition. High level of pH gives a low supersaturation level [97]. Increasing the water content results in an increase in the crystallization time, decrease the crystallization rate, and lower the supersaturation level. In the primary nucleation step, fewer nuclei are formed causing larger crystals to grow. In addition, increasing the water content causes an increase in the pH level of the solution suggesting a lower supersaturation level. These are the evidence that the morphology and the growth rates of the crystals are strongly affected by the composition of the secondary growth gel [98].

Wong et al. synthesized MFI zeolite films on seeded alfa-alumina substrates and investigated various parameters affecting the thickness and the orientation of the film. Clarification of these parameters is crucial for possible applications of zeolite membranes such as gas permeability. Molecular permeability of a zeolite is directly dependent on its pore structure. The size of the molecule is limited to the pore size giving the zeolite molecular sieving property. Thus, Wong et al. investigated the parameters silica precursor, organic template, water amount, and synthesis

temperature. Dilution process was carried out to understand the effect of water amount on the thickness and the orientation of the film. The other parameters were kept constant. Crystal growth rate and crystallinity decreased with an increasing amount of water. Further increase in the water amount hindered zeolite growth and seed layer was partially peeled off the surface. Consequently, it was observed that crystallinity and orientation are dependent on the water amount in the synthesis solution [95].

#### **2.2.4. Effect of Ion Doping on Photocatalysis**

Doping enhances the adsorption of light in the visible region. A new energy state between the conduction band and valence band is formed and photogenerated electrons and holes are separated without recombination. Doping level plays an important role in the photocatalytic decomposition of various organic dyes as well as morphology, size, and defect concentration [79].

Achouri et al. synthesized porous Mn-doped ZnO nanoparticles and investigated the effect of  $Mn^{2+}$  doping on the structural, optical and photocatalytic properties of ZnO. The optical absorption was shifted to the visible range of solar radiation through  $Mn^{2+}$  doping. The porous structure of Mn-doped ZnO nanoparticles gave a high specific surface area of the photocatalyst. Besides, the possibility of electron-hole recombination decreased due to the role of  $Mn^{2+}$  dopant as electron donor. Ultimately, the number of  $\bullet OH$  radicals increased resulting in an enhancement in the photocatalytic activity [79].

Liu et al. investigated the vacuum activated method to obtain photocatalytically active  $TiO_2$  under visible light irradiation. According to this method,  $V^{4+}$  and  $Ti^{3+}$  were doped into the lattice structure of  $TiO_2$  to extend the wavelength over the visible range. It is known that vanadium is one of the most efficient elements to increase the photocatalytic effectiveness of  $TiO_2$ . While  $V^{4+}$  cation was doped into the structure of  $TiO_2$ ,  $Ti^{3+}$  cations were created reducing  $Ti^{4+}$  cations.  $Ti^{3+}$  cations could increase charge carrier mobility and alter the  $e^-/h^+$  recombination rate.

Therefore,  $V^{4+}$  and  $Ti^{3+}$  doped and photocatalytically active  $TiO_2$  under visible light irradiation was obtained using a vacuum activated method. No characteristic peaks pertained to vanadium were observed from XRD and Raman analyses indicating no deformation was formed originated from vanadium doping. However, absorption shifted to longer wavelengths and broadened with an increasing amount of dopant revealing impurity formation induced by doping [99].

### **2.3. Photocatalytic Performance of Microporous Titanosilicate ETS-10 and Microporous Vanadosilicate AM-6**

Microporous titanosilicate ETS-10 and microporous vanadosilicate AM-6 are gaining attention in photocatalysis thanks to their photo-excitabile titanium and vanadium units, respectively. Recently, photocatalytic activity under UV light irradiation was obtained when ETS-10 was used as photocatalyst due to its relatively large bandgap (i.e., 4.03 eV) in comparison with  $TiO_2$  (i.e., 3.2 eV) causing photocatalytic activity only under UV irradiation [100]. Tailoring AM-6 as a better candidate for photocatalytic applications would be more likely due to its relatively narrower bandgap and multiple oxidation states of vanadium in its structure [101]. The reason for the photocatalytic activity of vanadium silicate AM-6 under visible light is the amount of  $V^{5+}$  cations present in the ...V-O-V-O-V... wires in its structure [50]. Between the energy bandgap, a mid-gap state is formed, which is occupied by the extra electron produced due to the existence of a  $V^{4+}$  state in the structure. However, this mid-gap state is unoccupied and performs as an electron trap in the presence of  $V^{5+}$  cation. Moreover, the presence of  $V^{5+}$  causes a lower conduction band energy level resulting in enhanced photocatalytic activity in the visible region [25]. When a photocatalytic system with metal nanoparticles irradiated by light, photoexcited electrons are trapped by these nanoparticles leaving holes which then oxidize organic compounds. Extension of light absorption into the visible range and enhancement of the surface electron excitation due to the surface plasmon resonance effect are also possible through the incorporation of metal nanoparticles [25].

Uma et al. utilized ETS-10 and metal ion incorporated ETS-10 as photocatalyst for the photocatalytic decomposition of acetaldehyde under UV and visible light irradiation. While ETS-10 without incorporation of metal ion showed photocatalytic performance only under UV irradiation, photocatalytic activity was obtained under visible light irradiation when Cr or Co incorporated ETS-10 was used as photocatalyst [100].

Ji et al. investigated the photocatalytic activity of ionic and/or metallic silver incorporated ETS-10 under visible light irradiation for the decomposition of MB and tried to clarify the role of silver in this process. First, incorporation of  $\text{Ag}^+$  cation to as-synthesized ETS-10 was carried out and  $\text{Ag}^+$ -ETS-10 samples were obtained. Then,  $\text{Ag}^+$  cation was reduced to  $\text{Ag}^0$  and  $\text{Ag}^0$  nanoparticle incorporated samples were obtained. There was no significant morphological or crystallographic disruption of the samples in consequence of ion or nanoparticle incorporation. While as-synthesized ETS-10 showed no photocatalytic activity, an enhanced photocatalytic activity for the decomposition of MB under visible light irradiation was observed when  $\text{Ag}^+$  and  $\text{Ag}^0$  incorporated ETS-10 samples were used as photocatalysts. All of the  $\text{Ag}^+$  incorporated ETS-10 samples were photocatalytically active under visible light irradiation. Moreover, photocatalytic activity increased with an increasing amount of silver loading. It was observed that  $\text{Ag}^0$  nanoparticles were also formed during the decomposition of MB when  $\text{Ag}^+$  incorporated ETS-10 was used as photocatalyst. All of the  $\text{Ag}^0$  incorporated ETS-10 samples were also photocatalytically active under visible light irradiation. However, photocatalytic activity did not increase with an increasing amount of silver loading. An average silver loading provided the most efficient photocatalytic activity. The reason for the photocatalytic activity under visible light irradiation is that silver nanoparticles in metallic form act as an electron trap. The Schottky barrier is formed at the interface of metal-semiconductor and so, silver nanoparticles remove electrons from the irradiated semiconductor surface. Photoexcited electrons are introduced either to silver nanoparticles or the conduction band of ETS-10. These electrons reduce  $\text{Ag}^+$

to  $\text{Ag}^0$  and react with oxygen adsorbed on the surface of silver nanoparticles producing reactive oxygen radicals. Silver nanoparticles transfer the trapped electrons to adsorbed oxygen. A strong local electric field could be formed by silver nanoparticles through surface plasmon resonance effect [15].

Guo et al. synthesized AM-6 crystals with different concentrations of  $\text{VO}_4$  tetrahedral units in the presence of  $\text{F}^-$  ions. These crystals showed absorption property in the visible range which is unusual for AM-6 crystals. It was stated that unusual optical properties arising from the interactions between octahedral ...V-O-V-O-V... chains and tetrahedral  $\text{VO}_4$  units caused the absorption in the visible range. The presence of  $\text{VO}_4$  units and the optical properties of AM-6 were demonstrated using various characterization techniques and theoretical calculations. They observed that the intensity of Raman peak pertaining to V=O stretching vibration in the tetrahedral unit increased with an increased amount of  $\text{F}^-$  ions. Theoretical calculations revealed that the absorption in the visible range is originated from the electronic transition from octahedral ...V-O-V-O-V... chains to  $\text{VO}_4$  tetrahedral units [41].

Shough et al. investigated the properties of pure ETS-10 and vanadium incorporated ETS-10 using experimental data and theoretical calculations. Octahedrally coordinated  $\text{V}^{\text{IV}}$  and  $\text{V}^{\text{V}}$  were observed in the structure of vanadium incorporated ETS-10. This demonstrated that the change occurred only in the sites of  $\text{Ti}^{\text{IV}}$ . It was observed that vanadium incorporation induced major changes in the structure of ETS-10. There is a need for the presence of both  $\text{V}^{\text{IV}}$  and  $\text{V}^{\text{V}}$  sites due to the unstable nature of  $\text{V}^{\text{V}}\text{-O-V}^{\text{V}}\text{-O-V}^{\text{V}}$  chains.  $\text{V}^{\text{IV}}$  and  $\text{V}^{\text{V}}$  sites act as hole and electron trapping sites, respectively. The enhanced photocatalytic activity was expected at low vanadium concentrations due to the enhanced charge separation. At high vanadium concentrations, a decrease in the photocatalytic activity was expected due to the increase in the recombination rate. The presence of electron and hole trapping sites could decrease the possibility of recombination [72].



Nash et al. incorporated different amounts of vanadium into the structure of ETS-10. They investigated the photocatalytic performance of vanadium incorporated ETS-10 and identified the differences between their effectiveness and the performances of bare ETS-10 and TiO<sub>2</sub>. They obtained samples with various amounts of V<sup>4+</sup> and V<sup>5+</sup> cations having photocatalytic activity under visible light irradiation for the polymerization of ethylene. The structural damage created by the incorporation of vanadium into the structure of ETS-10 was demonstrated by several analyses such as Raman spectroscopy and UV-vis absorption spectroscopy. The stretching vibration peak observed assigned to Ti-O-V vibration in Raman spectroscopy was assumed as evidence for defect creation in the sample structure. They also observed a decrease in bandgap energy as a result of vanadium incorporation. These results had led to an enhanced photocatalytic performance of the samples under visible light irradiation [43].

#### **2.4. Defects: Creation and Performance**

The structure of the quantum wires (i.e., ...Ti-O-Ti-O-Ti... for ETS-10 or ...V-O-V-O-V... for AM-6) in the framework of a zeo-type material is noteworthy for particular applications and the qualification of a zeo-type material. In a defect-free crystal, the length of the quantum wires should have the same length of the crystal. However, defects cause discontinuities breaking these quantum wires at certain points [102,103].

Yilmaz et al. defined the perfection of the quantum wires of ETS-10 as the quality of these crystals. They compared the differences between the growth mechanism of the quantum wires and spectroscopic behavior of ETS-10 resulting from different synthesis conditions. They changed the amount of Na<sub>2</sub>O in the molar formula of ETS-10. The obtained crystals had different morphologies, aspect ratios, and surface roughness. Spectroscopic behavior of ETS-10 was investigated by using DR-UV-vis spectra and Raman analysis was performed to control the quality of titania chains in the structure of ETS-10 by Yilmaz et al (Figures 2.5 and 2.6) [102].

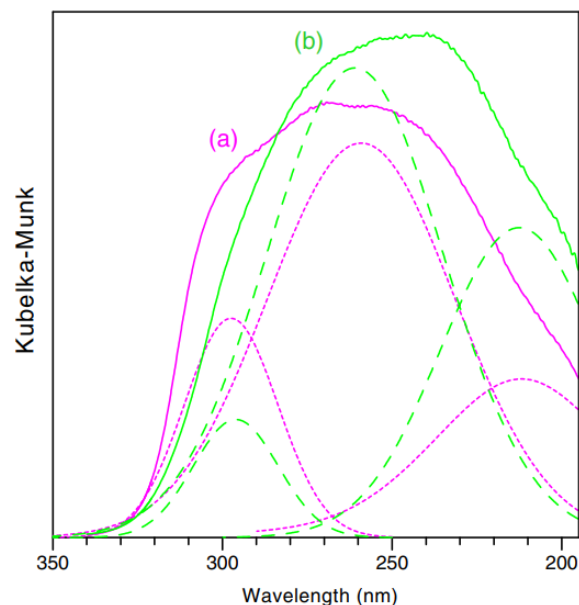


Figure 2.5. The DR-UV-vis spectra of the ETS-10 samples with molar composition  $5.5\text{SiO}_2:y\text{Na}_2\text{O}:1\text{TiO}_2:1.5\text{KF}:3.4\text{H}_2\text{SO}_4:300\text{H}_2\text{O}$ , where  $y = 4.4$  (a) and  $y = 5.1$  (b). Dotted and dashed lines represent deconvolution of the (a) and (b) spectra, respectively [102]

The DR-UV-vis spectra contain two overlapping peaks as shown in Figure 2.5. The absorption band centered at around 212 nm is related to charge transfer transitions in Ti-O-Si groups. The absorption band observed at shorter wavelength indicates delocalized charge transfer transitions in ...Ti-O-Ti-O-Ti... chains. This implies the differences in the length of quantum wires and interruption of the titania chains. The other absorption band observed at longer wavelength indicates localized charge transfer transitions caused by defects along titania chains. This band broadens with roughness and aspect ratio of the ETS-10 crystal. These two overlapping peaks increase by means of intensity and FWHM values when titania chains are interrupted and the number of defects increases [102].

Yilmaz et al. also performed Raman analysis to control the quality of titania chains as shown in Figure 2.6 [102].

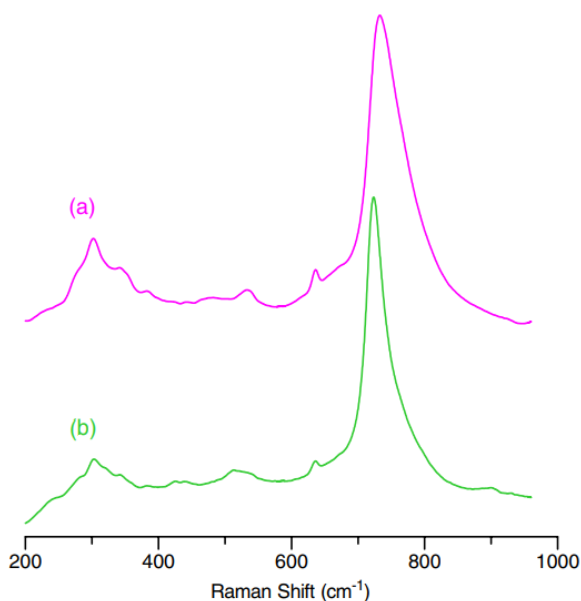


Figure 2.6. The Raman spectra of the ETS-10 samples with molar composition  $5.5\text{SiO}_2:y\text{Na}_2\text{O}:1\text{TiO}_2:1.5\text{KF}:3.4\text{H}_2\text{SO}_4:300\text{H}_2\text{O}$ , where  $y = 4.4$  (a) and  $y = 5.1$  (b) [102]

The Raman shift associated with Ti-O-Ti stretching vibration was observed in between  $710\text{-}750\text{ cm}^{-1}$ . The FWHM value of this stretching vibration band was also determined. This band got broader for ETS-10 crystals with higher roughness and aspect ratio [102].

Jit Datta et al. aimed to synthesize large ETS-10 crystals involving long titania chains without defects. They investigated the quality of titania chains using frequency, bandwidth, and intensity of Raman shift band arising from Ti-O-Ti-O-Ti stretching vibration. They claimed that frequency increases when the relative average length of the quantum wire decreases, bandwidth decreases with the inhomogeneity of the chains, and intensity increases with the density of the quantum wire. They synthesized ETS-10 crystals with different crystal size and chain length by changing the amount of KF in the synthesis mixture. They obtained that KF plays an important role in the formation of ETS-10 causing an increase in the crystal size upon decreasing KF concentration. However, crystal size decreases and the surface

becomes very rough when KF is completely removed from the synthesis solution [103].

Xamena et al. utilized ETS-10 for obtaining shape-selective heterogeneous photocatalysis. Excellent diffusion properties and regular pore structure endow ETS-10 to have shape-selective property. For molecules larger than the pore size of ETS-10, degradation becomes faster due to the reason that diffusion occurs at the internal surface of the material. Molecules smaller than the pore size of ETS-10 diffuse in the pores and cannot degrade due to the fact that degradation occurs at the external surface of the material. Thus, the pores of ETS-10 act as a protector for photocatalytic decomposition of small molecules enabling shape-selective behavior for ETS-10. Based upon this property of ETS-10, Xamena et al. investigated defect creation in the structure of ETS-10 in order to enhance their photocatalytic reactivity by post-synthesis modification of ETS-10 with hydrofluoric acid without damaging crystallinity. They observed an increase in the amount of TiOH at the external surface of ETS-10 with the increasing amount of defect. ETS-10 with defects showed enhanced photocatalytic activity with respect to pure ETS-10 for the decomposition of organic molecules. Besides, defect creation was assigned for the shape-selective behavior of the samples [104].

## **2.5. Goal and Objectives**

The goal of this study is first to successfully obtain microporous vanadosilicate AM-6 in thin film form and then tailor the concentration of defects in the structure of AM-6 films in order to investigate their performances as photocatalysts for photocatalytic decomposition of MB. The objectives to achieve this goal can be summarized as follows:

- To prepare microporous vanadosilicate AM-6 films on ITO coated glass substrates through secondary growth method without impurity,
  - To investigate the effects of water amount and reaction temperature on the formation of microporous vanadosilicate AM-6 films,

- To investigate the parameters affecting defect formation ( $V^{4+}/V^{5+}$ ) in the AM-6 films,
  - To change the chemistry of secondary growth gel and explore its effect on the formation of microporous vanadosilicate AM-6 films,  $V^{4+}/V^{5+}$  ratio, and its photocatalytic performances,
  - To investigate the parameters (i.e., the morphology of the seed crystals, seed layer coating technique, and water amount of the secondary growth solution) affecting  $V^{4+}/V^{5+}$  ratio in the structure of microporous vanadosilicate AM-6 films,
- To identify the photocatalytic performances of microporous vanadosilicate AM-6 films with different  $V^{4+}/V^{5+}$  ratio.



## CHAPTER 3

### EXPERIMENTAL PROCEDURES

The experimental procedure with prepared sample codes for the current thesis study is shown in Figure 3.1 and the abbreviations are summarized in Table 3.1.

#### **3.1. Synthesis of Submicrometer-Sized ETS-10 with Different Morphologies (i.e., bipyramidal and cubic)**

The synthesis of bipyramidal-shaped ETS-10 crystals was carried out according to the procedure stated by Lv et al. [35]. The molar formula  $3.4\text{Na}_2\text{O}:1.5\text{K}_2\text{O}:\text{TiO}_2:5.5\text{SiO}_2:150\text{H}_2\text{O}$  was used keeping the pH value at around 10.4. For the synthesis of ETS-10, no additional seeds or organic template were needed. For the preparation of silicon source, sodium silicate (27 wt. %  $\text{SiO}_2$ , 8 wt. %  $\text{Na}_2\text{O}$ , and 65 wt. %  $\text{H}_2\text{O}$ , Aldrich), NaOH and KOH were dissolved in DI water by hand-shaking. In another bottle, P25 (76wt% anatase and 24wt% rutile, Degussa) was dissolved in DI water by hand-shaking. These two solutions were combined and mixed to form a homogenous mixture. Following the hydrothermal treatment in the 10 mL Teflon-lined stainless-steel autoclaves at 503 K for 5 days, the precipitation was collected and washed with DI water and dried at 373 K in an oven. The molar formula  $5.3\text{SiO}_2:1\text{TIP}:8.5\text{NaOH}:1.46\text{KF}:2.3\text{H}_2\text{SO}_4:370\text{H}_2\text{O}$  stated by Jeong et al. [52] was used for the synthesis of cubic-shaped ETS-10 crystals.  $\text{Ti}(\text{iPrO})_4$ ,  $\text{H}_2\text{SO}_4$ , and DI water was added in an Erlenmeyer flask. The mixture was boiled for 60 minutes keeping the concentration constant. For the preparation of silicon source, NaOH was dissolved in DI water as a first step. Then, sodium silicate was added into this mixture. Titanium source was added into the silicon source. After aging for 18 h, hydrothermal treatment was applied to the gel at 473 K for 24 h. The solid was collected from the solution, washed with DI water, and dried at 373 K in an oven.

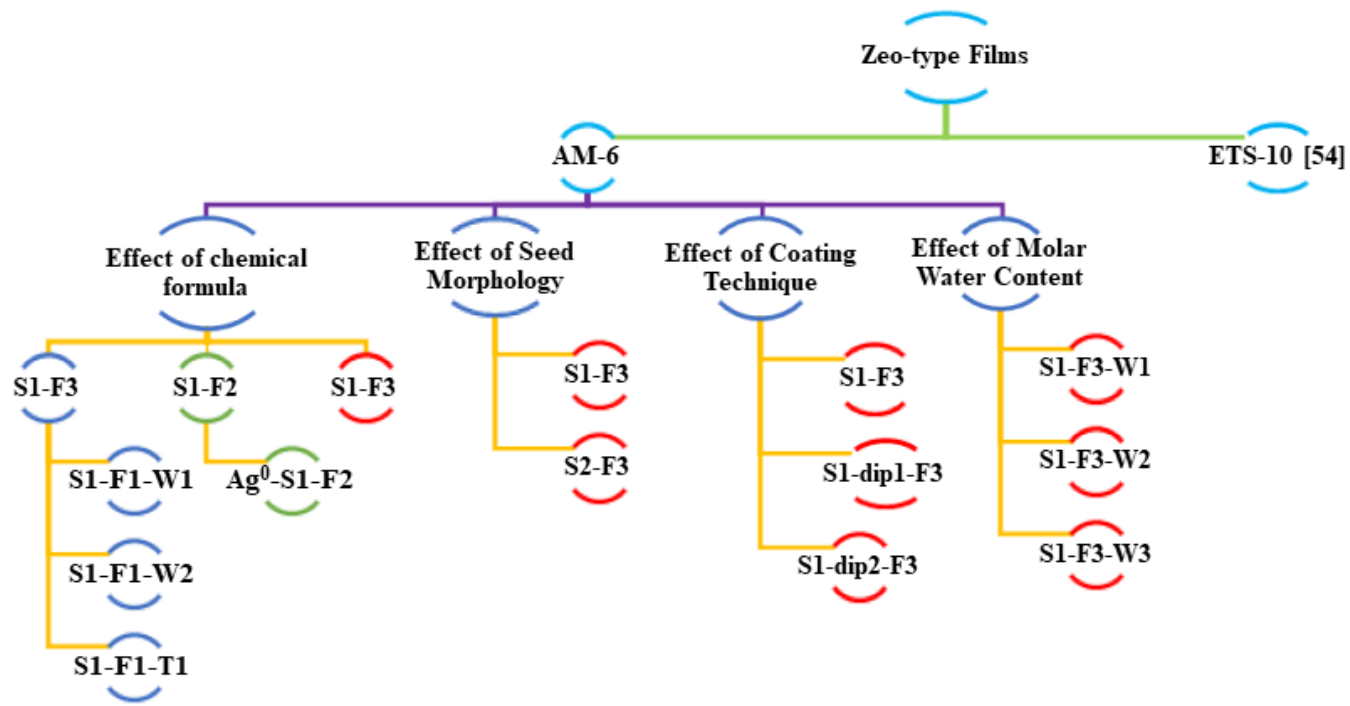


Figure 3.1. Schematical view of the experimental procedure

**Notation**    **Definiton**

- S** Seed Layer Morphology
- F** Secondary Growth Gel Formula
- T** Reaction Temperature
- W** Molar Water Content of the Secondary Growth Gel

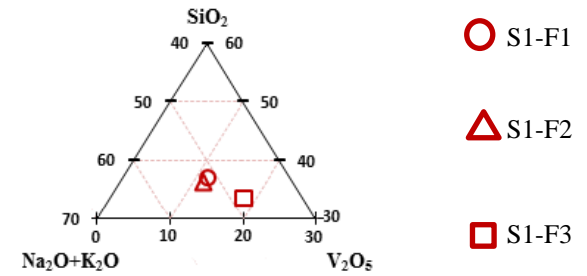




Table 3.1. Interpretation of the experimental procedure for the preparation of AM-6 films

Abbreviations	Molar Compositions	Type of seed crystal	Seed layer coating technique	Reaction Temp. (K)	Ref.
S1-F1	4.5Na <sub>2</sub> O:1.3K <sub>2</sub> O:4.85SiO <sub>2</sub> :0.5V <sub>2</sub> O <sub>5</sub> :2.2TMAOH:209H <sub>2</sub> O	Bipyramidal ETS-10	Spin-coating	503	[48]
S1-F1-W1	4.5Na <sub>2</sub> O:1.3K <sub>2</sub> O:4.85SiO <sub>2</sub> :0.5V <sub>2</sub> O <sub>5</sub> :2.2TMAOH:209H <sub>2</sub> O	Bipyramidal ETS-10	Spin-coating	503	[48]
S1-F1-W2	4.5Na <sub>2</sub> O:1.3K <sub>2</sub> O:4.85SiO <sub>2</sub> :0.5V <sub>2</sub> O <sub>5</sub> :2.2TMAOH:209H <sub>2</sub> O	Bipyramidal ETS-10	Spin-coating	503	[48]
S1-F1-T1	4.5Na <sub>2</sub> O:1.3K <sub>2</sub> O:4.85SiO <sub>2</sub> :0.5V <sub>2</sub> O <sub>5</sub> :2.2TMAOH:209H <sub>2</sub> O	Bipyramidal ETS-10	Spin-coating	528	[48]
S1-F2	Na <sub>2</sub> O:0.23K <sub>2</sub> O:0.97SiO <sub>2</sub> :0.1V <sub>2</sub> O <sub>5</sub> :30H <sub>2</sub> O	Bipyramidal ETS-10	Spin-coating	503	[49]
Ag <sup>0</sup> -S1-F2	Na <sub>2</sub> O:0.23K <sub>2</sub> O:0.97SiO <sub>2</sub> :0.1V <sub>2</sub> O <sub>5</sub> :30H <sub>2</sub> O	Bipyramidal ETS-10	Spin-coating	503	[49]
S1-F3	6.07SiO <sub>2</sub> :V <sub>2</sub> O <sub>5</sub> :3.37H <sub>2</sub> SO <sub>4</sub> :3.03Na <sub>2</sub> O:3.09K <sub>2</sub> O:7.22EtOH:415H <sub>2</sub> O	Bipyramidal ETS-10	Spin-coating	528	[41]
S2-F3	6.07SiO <sub>2</sub> :V <sub>2</sub> O <sub>5</sub> :3.37H <sub>2</sub> SO <sub>4</sub> :3.03Na <sub>2</sub> O:3.09K <sub>2</sub> O:7.22EtOH:415H <sub>2</sub> O	Cubic ETS-10	Spin-coating	528	[41]
S1-dip1-F3	6.07SiO <sub>2</sub> :V <sub>2</sub> O <sub>5</sub> :3.37H <sub>2</sub> SO <sub>4</sub> :3.03Na <sub>2</sub> O:3.09K <sub>2</sub> O:7.22EtOH:415H <sub>2</sub> O	Bipyramidal ETS-10	Dip-coating	528	[41]
S1-dip2-F3	6.07SiO <sub>2</sub> :V <sub>2</sub> O <sub>5</sub> :3.37H <sub>2</sub> SO <sub>4</sub> :3.03Na <sub>2</sub> O:3.09K <sub>2</sub> O:7.22EtOH:415H <sub>2</sub> O	Bipyramidal ETS-10	Dip-coating	528	[41]
S1-F3-W1	6.07SiO <sub>2</sub> :V <sub>2</sub> O <sub>5</sub> :3.37H <sub>2</sub> SO <sub>4</sub> :3.03Na <sub>2</sub> O:3.09K <sub>2</sub> O:7.22EtOH:300H <sub>2</sub> O	Bipyramidal ETS-10	Spin-coating	528	[41]
S1-F3-W2	6.07SiO <sub>2</sub> :V <sub>2</sub> O <sub>5</sub> :3.37H <sub>2</sub> SO <sub>4</sub> :3.03Na <sub>2</sub> O:3.09K <sub>2</sub> O:7.22EtOH:600H <sub>2</sub> O	Bipyramidal ETS-10	Spin-coating	528	[41]
S1-F3-W3	6.07SiO <sub>2</sub> :V <sub>2</sub> O <sub>5</sub> :3.37H <sub>2</sub> SO <sub>4</sub> :3.03Na <sub>2</sub> O:3.09K <sub>2</sub> O:7.22EtOH:700H <sub>2</sub> O	Bipyramidal ETS-10	Spin-coating	528	[41]
ETS-10	4.55Na <sub>2</sub> O:TiO <sub>2</sub> :5.50SiO <sub>2</sub> :1.5KF:300H <sub>2</sub> O	Bipyramidal ETS-10	Spin-coating	503	[40]

## 3.2. Thin Film Preparation of Microporous Titanosilicate ETS-10 and Microporous Vanadosilicate AM-6

### 3.2.1. Effect of Chemical Formula of the Secondary Growth Gel

In the secondary growth approach, two-step procedure was applied in the film production: seed layer formation (ETS-10 seeds; Section 3.1) and secondary growth of the seed crystals. The common procedure for every part of the study was the cleaning process of ITO coated glass substrates. The substrates (Aldrich, purity 99%, resistivity 10 ohm/sq,  $\sim 10 \text{ mm} \times \sim 25 \text{ mm}$ ) were cleaned ultrasonically in acetone, ethanol, and 2-propanol each for 15 minutes. Then, they were dried in an oven at 353 K for 20 minutes. The substrates were then coated with seed crystals and hydrothermal growth is applied for the growth of AM-6 films. Figure 3.2 shows an illustration for secondary growth approach.

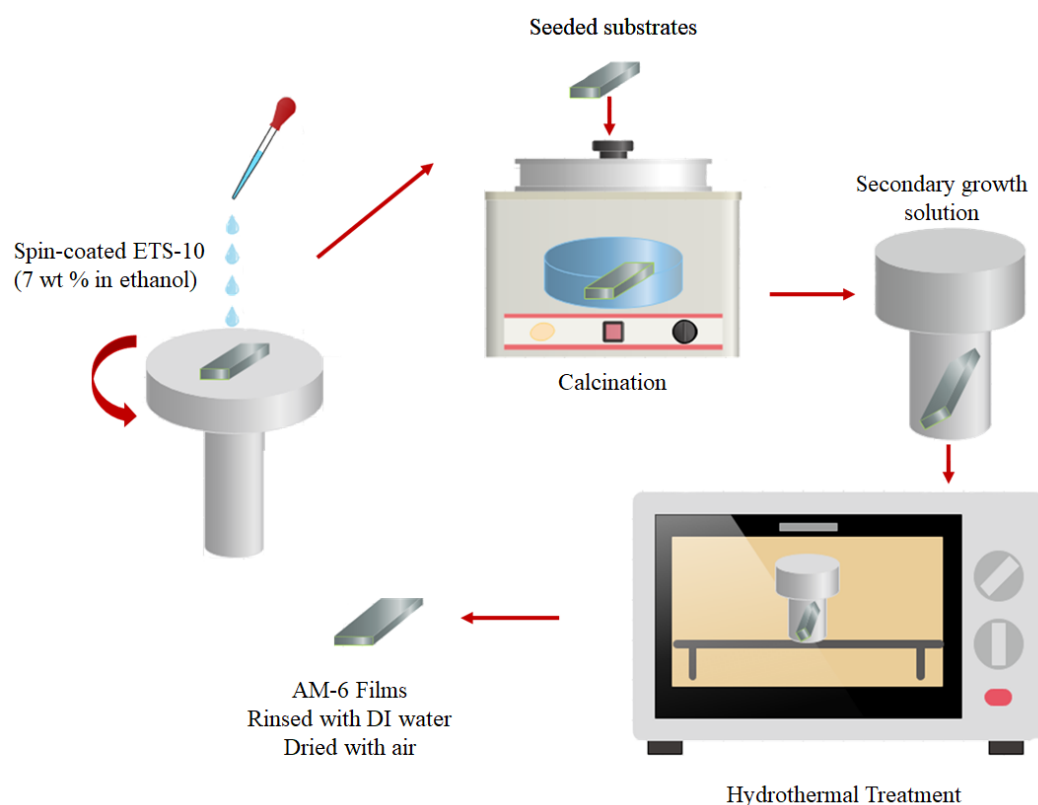


Figure 3.2. Illustration for the preparation of microporous vanadosilicate AM-6 films

First, a suspension of as-synthesized ETS-10 crystals with bipyramidal shape (7wt. % in ethanol) was used as seed solution and deposited by spin-coating on the pre-cleaned ITO coated glass substrates [35]. In the preparation method of ETS-10 seed crystals, the molar composition of  $3.4\text{Na}_2\text{O}:1.5\text{K}_2\text{O}:\text{TiO}_2:5.5\text{SiO}_2:150\text{H}_2\text{O}:0.3\text{H}_2\text{SO}_4$  was used [35]. After the spin-coating process, the seeded ITO coated glass substrates were heated isothermally in a calcination oven from 303 K to 673 K for 540 minutes. For AM-6 film preparation, the seeded ITO coated glass substrates were then placed in the reaction vessels of AM-6 growth solutions [40,48,49]. For this purpose, the seeded substrates facing downwards were placed diagonally in the 10 mL Teflon-lined stainless-steel autoclaves (Figure 3.2).

Three different secondary growth gels stated by Sacco, Jr. et al., Yoon et al., and Rocha et al. were prepared as explained in the literature and poured carefully into the autoclaves [40,48,49]. Then, hydrothermal treatments were applied at 528 K for 5 h, 503 K for 2 h, and 503 K for 48 h following the procedure of Yoon et al., Sacco, Jr. et al., and Rocha et al., respectively [40,48,49]. After cooling down the autoclaves to room temperature, the films on ITO coated glass substrates were removed from the secondary growth gel, rinsed with deionized water and dried using an air gun. Microporous vanadosilicate AM-6 films prepared by using bipyramidal-shaped ETS-10 crystals as seed and the adapted procedures of Sacco, Jr. et al., Rocha et al., and Yoon et al., were denoted as S1-F1, S1-F2, and S1-F3, respectively. Afterward, the reaction temperature and amount of water in the growth solution were altered to investigate their effect on film formation using S1-F1 due to its relative easiness of formation and short reaction time. The water amount in standard  $4.5\text{Na}_2\text{O}:1.3\text{K}_2\text{O}:4.85\text{SiO}_2:0.5\text{V}_2\text{O}_5:2.2\text{TMAOH}:209\text{H}_2\text{O}$  molar composition was decreased to 150 and increased to 300 for concentrated and diluted secondary growth gels, respectively. The diluted and concentrated S1-F1 films were denoted as S1-F1-W1 and S1-F1-W2, respectively. The reaction temperature was kept constant at 503 K for both S1-F1-W1 and S1-F1-W2. Then, the formation of S1-F1 was studied at lower and higher reaction temperatures of 473 and 528 K. There was no film

formation at 423 K in 2 h of reaction, so longer reaction periods were also tested at this temperature. At 528 K, it was possible to obtain the films, which were denoted as S1-F1-T1 after 1 h of reaction time (*vide infra*).

### 3.2.2. Effect of Seed Crystal Morphology

Cubic-shaped ETS-10 crystals were prepared following the procedure proposed by Jeong et al. [52]. A suspension of the ETS-10 crystals (7 wt % in ethanol) was prepared and spin-coated (2-times) on pre-cleaned ITO coated glass substrates. The seeded substrates were then dried in ambient air and afterward calcined at 673 K for 540 minutes. Then, the seeded substrates were placed vertically and facing downwards in 10 mL Teflon-lined stainless-steel autoclaves for hydrothermal growth of seed crystals. In this part of the study, only the secondary growth gel denoted as F3 was prepared to investigate the effect of seed morphology on film formation (Figure 3.3). Thus, the other parameters were kept constant. The microporous vanadosilicate AM-6 films produced in this part of the study was denoted as S2-F3 and compared with S1-F3 with regards to their structural differences and photocatalytic effectiveness.

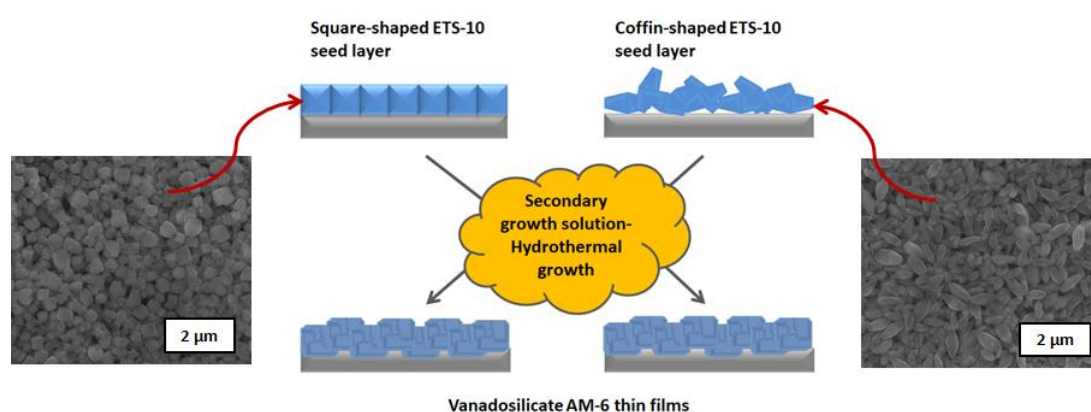


Figure 3.3. Illustration for microporous vanadosilicate AM-6 film formation using seeds with different morphologies

### **3.2.3. Effect of Seed Layer Coating Technique**

In the fourth part of the study, ETS-10 crystals with bipyramidal shape were used as seed layer [35]. A suspension of the ETS-10 crystals was coated on pre-cleaned ITO coated glass substrates by using spin-coating (2-times) and/or dip-coating (1-time and 2-times) method to see the effect of coating technique on film formation and their photocatalytic performances. The seeded substrates were then dried in ambient air and afterward calcined at 673 K for 540 minutes. Then, the seeded substrates were placed vertically and facing downwards in 10 mL Teflon-lined stainless-steel autoclaves for hydrothermal growth of seed crystals. The secondary growth gel denoted as F3 was prepared and poured into the autoclaves. Following the hydrothermal treatment at 528 K for 5 h, microporous vanadosilicate AM-6 films were rinsed with water and dried with air.

### **3.2.4. Effect of Molar Water Content of the Secondary Growth Gel**

ETS-10 crystals with bipyramidal shape were used as seed layer [35]. A suspension of the ETS-10 crystals was coated on pre-cleaned ITO coated glass substrates using the spin-coating method. Then, the seeded substrates were placed vertically and facing downwards in 10 mL Teflon-lined stainless-steel autoclaves for hydrothermal growth of seed crystals. Afterward, the amount of water in the growth solution was altered to investigate their effect on film formation using S1-F3. The water amount in standard  $6.07\text{SiO}_2:\text{V}_2\text{O}_5:3.37\text{H}_2\text{SO}_4:3.03\text{Na}_2\text{O}:3.09\text{K}_2\text{O}:7.22\text{EtOH}:415\text{H}_2\text{O}$  molar composition was decreased to 300 and increased to 600 and then 700 for concentrated and diluted secondary growth gels, respectively. The diluted and concentrated S1-F3 films were denoted as S1-F3-W1, S1-F3-W2, and S1-F3-W3 respectively. The reaction temperature was kept constant at 503 K for all of the samples.

### 3.3. Evaluation of the Photocatalytic Activity

#### 3.3.1. Photocatalytic Performances of Microporous Titanosilicate ETS-10 and Microporous Vanadosilicate AM-6 Films under UV and Visible Light Irradiation

The photocatalytic efficiencies of the synthesized materials were tested by measuring the removal percentage of an aqueous solution of MB as a model pollutant under both UV (6 W, 365 nm, Type Spectroline ENF-260, at a light intensity  $350 \mu\text{W}/\text{cm}^2$ ) and visible light ( $300 \mu\text{W}/\text{cm}^2$  light-emitting diode, LED) at dye's natural pH (pH=6) and room temperature (Figure 3.4).

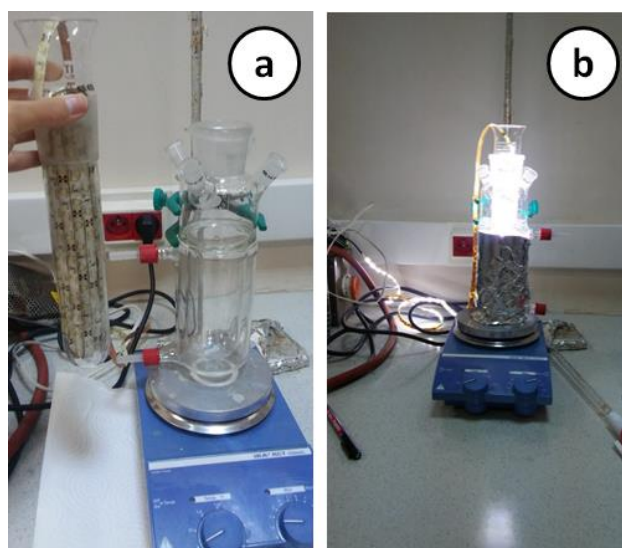


*Figure 3.4.* The system used for investigation of the photocatalytic activity of the samples under visible light irradiation

Microporous vanadosilicate AM-6 thin films (S1-F2 and S1-F3) were prepared using two different molar formula for secondary growth gels according to the procedure already represented by our group (Section 3.2.1) [98]. S1-F1 could not be utilized as photocatalyst due to its loose adsorption on the substrate surface. In order to

investigate the effect of noble metal nanoparticle incorporation on the photocatalytic activity, silver nanoparticles were incorporated into S1-F2 and this sample was denoted as Ag<sup>0</sup>-S1-F2. For the preparation of Ag<sup>0</sup>-S1-F2, S1-F2 film was inserted in a 1 mM aqueous solution of silver nitrate (AgNO<sub>3</sub>) at room temperature for 4 hours. Afterward, the sample was washed with water and dried at room temperature. Then, it was placed in a 0.1 M aqueous solution of sodium borohydride (NaBH<sub>4</sub>) for 30 seconds to reduce Ag<sup>+</sup> ions into Ag<sup>0</sup> nanoparticles. Finally, the sample was washed with 1 L ultra-pure deionized water and dried in ambient air.

ETS-10 films were also prepared as photocatalysts for the decomposition of MB to compare the photocatalytic effectiveness of ETS-10 and AM-6 films. For the preparation of ETS-10 thin films, the procedure represented by Galioglu et al. was followed [54]. According to their procedure, a suspension of ETS-10 crystals (7 wt % in ethanol) was used for the formation of ETS-10 thin films. The suspension was spin-coated on pre-cleaned ITO coated glass substrates which were placed vertically and facing downwards in 10 mL Teflon-lined stainless-steel autoclaves. Afterward, a secondary growth solution was prepared and poured into the autoclaves. Hydrothermal growth was applied at 503 K for 6 h for the formation of ETS-10 thin films.

The quartz vessel was illuminated with the lamp from 10 cm distance. Dark experiments were also carried out to know the degree of photodegradation upon adsorption of MB over the all photocatalyst thin films (ETS-10, S1-F3, S1-F2, and Ag<sup>0</sup>- S1-F2 thin films) under non-irradiation condition. The determined MB concentration after irradiation was compared with solutions kept during the dark experiments. 4 mL portion of 3.2 mg L<sup>-1</sup> MB was placed in a quartz cell containing material (2 pieces, approximately 1 cm × 1 cm). The concentration and the amount of MB were chosen according to the literature data [73]. Before the irradiation, the reaction solution was stirred in the dark for 30 min to reach adsorption-desorption equilibrium between the organic molecule and the catalyst surface. The decrease in the concentration of MB has monitored over 60 min spectrophotometrically at  $\lambda =$

668 nm (Hitachi-Ratio Beam Spectrophotometer U-5100) in the presence and absence of light. The remaining MB in the reaction mixture was determined at regular intervals of irradiation or dark experiments. Results are given as the mean of three replicates. Removal percentage of MB was calculated from equation 3.1:

$$\text{Degradation (\%)} = \frac{C_0 - C_t}{C_0} \times 100 \quad (\text{Equation 3.1})$$

Where;  $C_0$  is the initial concentration and  $C_t$  is the final concentration of dye after a certain treatment period (in the presence or absence of light).

### **3.3.1.1. Reuse of AM-6 Thin Films**

Reusability tests of S1-F2 films were investigated for the MB under UV light irradiation in the second part of the study. After the first 60 minutes of treatment, the thin films were simply washed with water and reused in a new treatment at the same pollutant concentration.

### **3.3.2. Photocatalysis under Solar Light**

In this part of the study, microporous vanadosilicate AM-6 films prepared in Sections 3.2.2, 3.2.3, and 3.2.4 were utilized as photocatalysts for the decomposition of MB. The photocatalytic performances of the films were investigated by evaluating the percent removals of MB dye at every 30 minutes up to 240 minutes under solar simulator at room temperature. Atlas solar simulator equipped with xenon arc lamp with 150 W power was utilized to investigate the photocatalytic effectiveness of the samples. The absorbance of methylene blue dye was measured after specified periods of time using a UV-Vis spectrophotometer SPECORD S600 in quartz cuvettes.

The beakers were filled with 10 mL of 1 Absorbance MB dye and placed 10 cm from the light source (Figure 3.5).



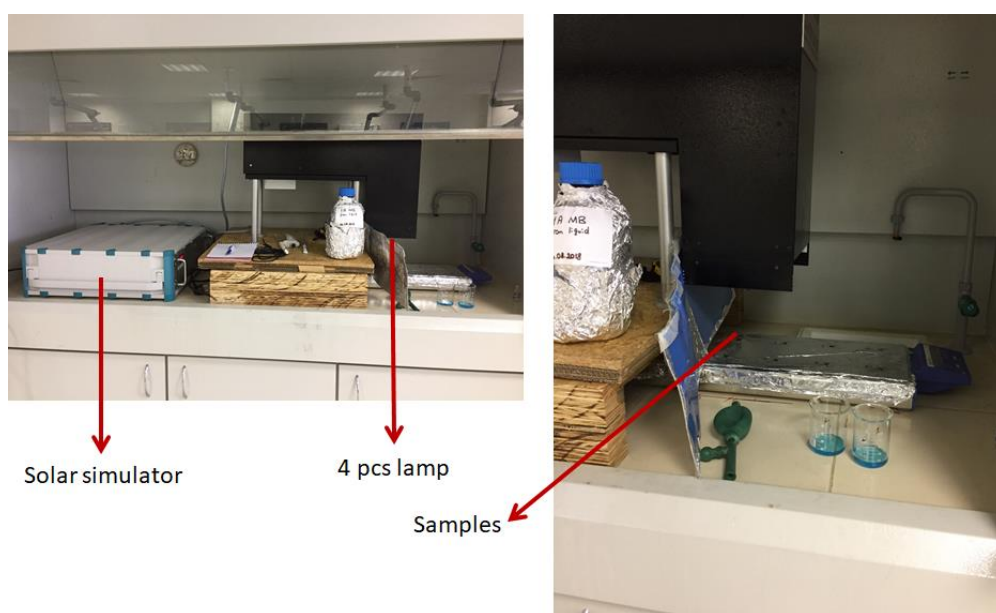


Figure 3.5. The solar simulator system used for the investigation of the photocatalytic activities of microporous vanadosilicate AM-6 films

The degradation of MB originated from the adsorption of dye over the film was also obtained at every 30 minutes up to 240 minutes through dark experiments. The percent removal of MB under irradiation and non-irradiation conditions was monitored by Spectrophotometer at a wavelength of 668 nm. The experiments were carried out by means of four replicates. The percent degradation of MB and degradation kinetics of MB on the photocatalysts was calculated using equations 3.1 and 3.2, respectively:

$$\ln\left(\frac{C_t}{C_0}\right) = k \times \text{time}(\text{min.}) \quad (\text{Equation 3.2})$$

Where;  $C_0$  is the initial concentration,  $C_t$  is the final concentration of dye after a certain treatment period, and  $k$  is the degradation kinetics of MB on photocatalysts.

### 3.4. Characterization Techniques

Microporous vanadosilicate AM-6 and microporous titanasilicate ETS-10 films were characterized by various techniques such as Field Emission Scanning Electron Microscopy (FE-SEM), X-ray Diffraction (XRD), Raman Spectroscopy, Electron Micro Probe Analysis (EPMA), X-ray Photoelectron Spectroscopy (XPS), and UV-Vis Absorption Spectroscopy. All characterization studies except UV-Vis Absorption Spectroscopy were carried out at METU central laboratory. UV-Vis Absorption Spectroscopy was done in our laboratory.

#### 3.4.1. Field Emission Scanning Electron Microscopy

The field emission scanning electron microscope (FE-SEM) images were acquired for AM-6 films using a Hitachi S-4700 FE-SEM (accelerating voltage 10 kV, beam current 10  $\mu$ A) in the secondary electron imaging mode. The film cross-sections were imaged on the broken edges after breaking the films on ITO coated glass substrates.

#### 3.4.2. X-ray Diffraction

The X-ray powder diffraction (XRD) analysis was carried out using Rigaku-Ultima IV XRD by using the thin-film attachment. The diffraction peaks were scanned between 5° and 40° with a scan speed of 1°/min. for phase identification. The degree of out-of-plane preferred orientation of AM-6 films were quantified by comparing the integrated intensities of (105) and (200) planes of AM-6 in the XRD patterns of the films and the powder sample. For orientation analysis, slow scan (i.e., 1°/8 min.) was carried out to obtain crystal preferred orientation (CPO) in XRD analyses. The CPO index based on (200) and (105) reflections was calculated using the definition of  $CPO_{200/105} = ((I_{200}/I_{105})_f - (I_{200}/I_{105})_p) / (I_{200}/I_{105})_p$  for quantitative analysis of the degree of *a(b)*-out-of-plane preferred orientation, where, *I* depicts the integrated intensity of the corresponding reflections, the subscripts *p* and *f* represent powder sample (randomly oriented) and films (preferentially oriented), respectively [54,91]. The integrated intensity of XRD peaks was determined using the Rigaku-Ultima IV XRD

software. The field emission scanning electron microscope (FE-SEM) images were acquired for AM-6 films using a Hitachi S-4700 FE-SEM (accelerating voltage 2 kV, beam current 10  $\mu$ A) in the secondary electron imaging mode. The film cross-sections were imaged on the broken edges after breaking the films on ITO coated glass substrates.

### **3.4.3. Raman Spectroscopy**

Renishaw type Raman micro-scope was utilized in the Raman spectroscopy analyses, where the excitation wavelength of 532 nm and a power of 0.5 - 1 mW were chosen for the acquisition.

### **3.4.4. Electron Micro Probe Analysis (EPMA)**

Si/V ratios of microporous vanadosilicate AM-6 films were determined via electron microprobe (EPMA) analysis using the wavelength-dispersive Cameca SX50 electron microprobe. Operating parameters were: 20 kV accelerating voltage, a 25 nA current, and a 5-micron spot size.

### **3.4.5. X-ray Photoelectron Spectroscopy**

X-ray photoelectron spectroscopy (XPS) analysis was carried out on a PHI 5000 VersaProbe spectrometer with an Al-K $\alpha$  radiation source. The binding energies were referenced to the internal standard C 1s binding energy at 284.5 eV. XPS peaks are referenced to the C 1s peak. The sub-peaks under the high-resolution silver, vanadium, and titanium spectra were identified by using PeakFit v4.12. Gaussian–Lorentzian functions fitted the high-resolution spectra of vanadium and silver after removal of the background by choosing two-point linear background function. The fitting percentages were adjusted to be 98.99% and 99.99% for high-resolution spectra of the vanadium and silver, respectively.

### **3.4.6. Diffuse Reflectance UV-Vis Spectroscopy**

UV-visible absorption spectra of the films were acquired for ETS-10 and AM-6 films by using an Agilent Technologies Cary 60 type UV-Vis spectrometer. The %

reflection values were collected for the wavelengths between 200-800 nm. Absorption spectra were obtained with Kubelka-Munk function transforming the reflection data to absorption data. The bandgaps of the films were calculated drawing Tauc plot for each sample [105]. Cut off wavelength of the absorption spectrum was also used to calculate the energy bandgap of the films using the equation 3.3.

$$E = \frac{hc}{\lambda} \quad (\text{Equation 3.3})$$

## CHAPTER 4

### RESULTS AND DISCUSSION

#### **4.1. Secondary Growth of Microporous Vanadosilicate AM-6 Films**

Although the synthesis of AM-6 in powder form is well known, the preparation of AM-6 in membrane form had only been studied for the purpose of measuring their single gas permeability by Tiscornia et al. [53]. In the current study, membranes were prepared by adapting three procedures described elsewhere as secondary growth gels [40,48,49]. Rocha et al. synthesized AM-6 crystals by adding titanosilicate ETS-10 as seeds, isostructural to AM-6, to the growth solution of AM-6 for the first time to obtain AM-6 crystals in the powder form [49]. Accordingly, relatively small-sized (i.e., 500 nm) titanosilicate ETS-10 crystals were attached on to the ITO coated glass substrates to prepare AM-6 films through secondary growth method. Samples with codes S1-F1, S1-F2, S1-F3, S1-F1-W1, S1-F1-W2, and S1-F1-T1 were prepared in this part of the study (Table 3.1).

##### **4.1.1. The Effect of the Composition of Secondary Growth Gel on Film Formation**

###### **4.1.1.1. Sample Characterization**

The prepared samples were first analyzed by FE-SEM and the obtained results are shown in Figure 4.1.

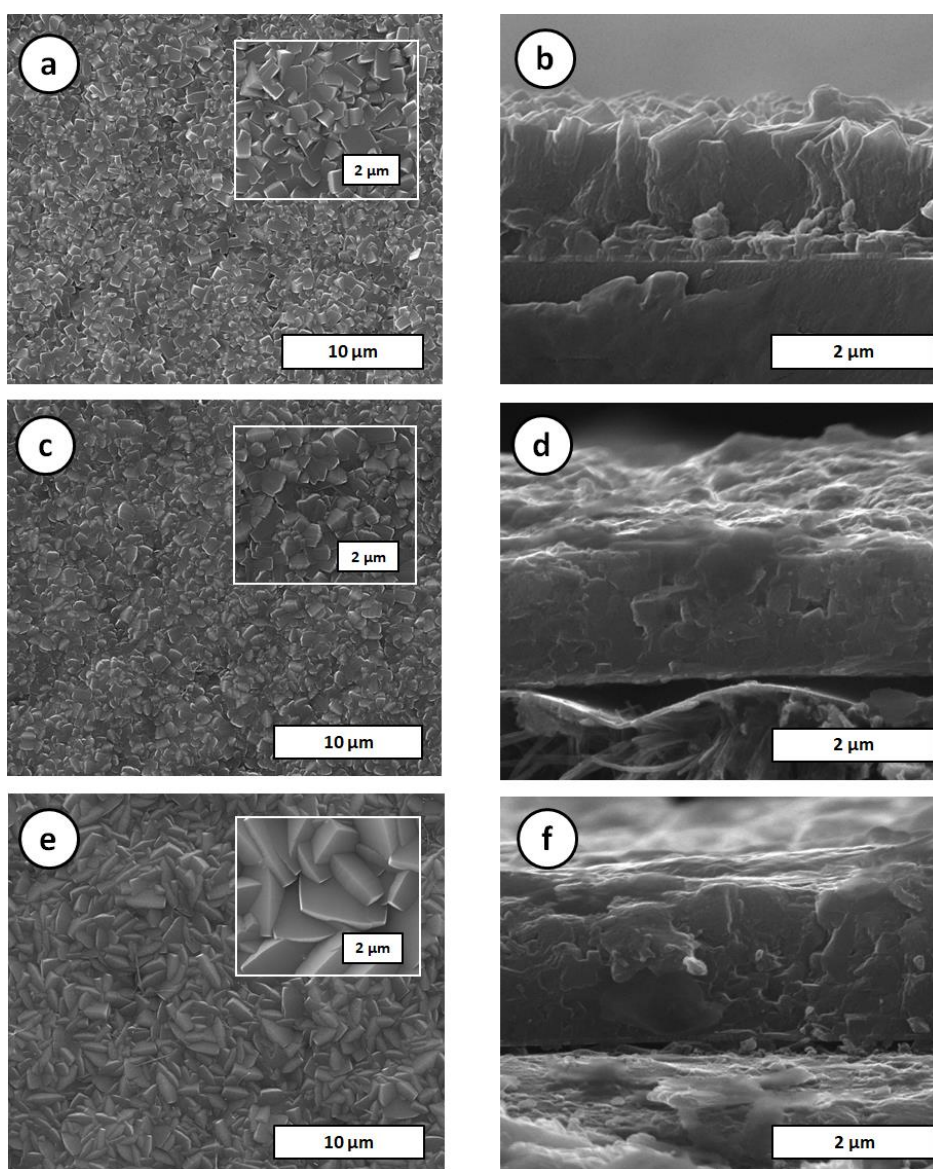


Figure 4.1. Top view and cross-sectional images of S1-F1 (a), (b); S1-F2 (c), (d); S1-F3 (e), (f), respectively

FE-SEM images revealed that the growth of titanasilicate ETS-10 seed crystals attached on the ITO coated glass substrates resulted in a continuous and uniformly dispersed vanadosilicate AM-6 films without intercrystalline gaps. AM-6 films, having no cracks and pinholes, were firmly adhered to the ITO coated glass substrates resisting repeated washing without peeling off the surface. The exact same

secondary growth solutions for films were also subjected to the synthesis of powder AM-6 to compare the obtained material. It is noteworthy that S1-F2 had no impurities (*vide infra*) while F2 in powder form contained a high amount of quartz (Figure 4.2-b) [49]. Likewise, F3 resulted in mostly VSH formation along with some AM-6 upon applying the procedures given by Yoon et al. (Figure 4.2-c) [40].

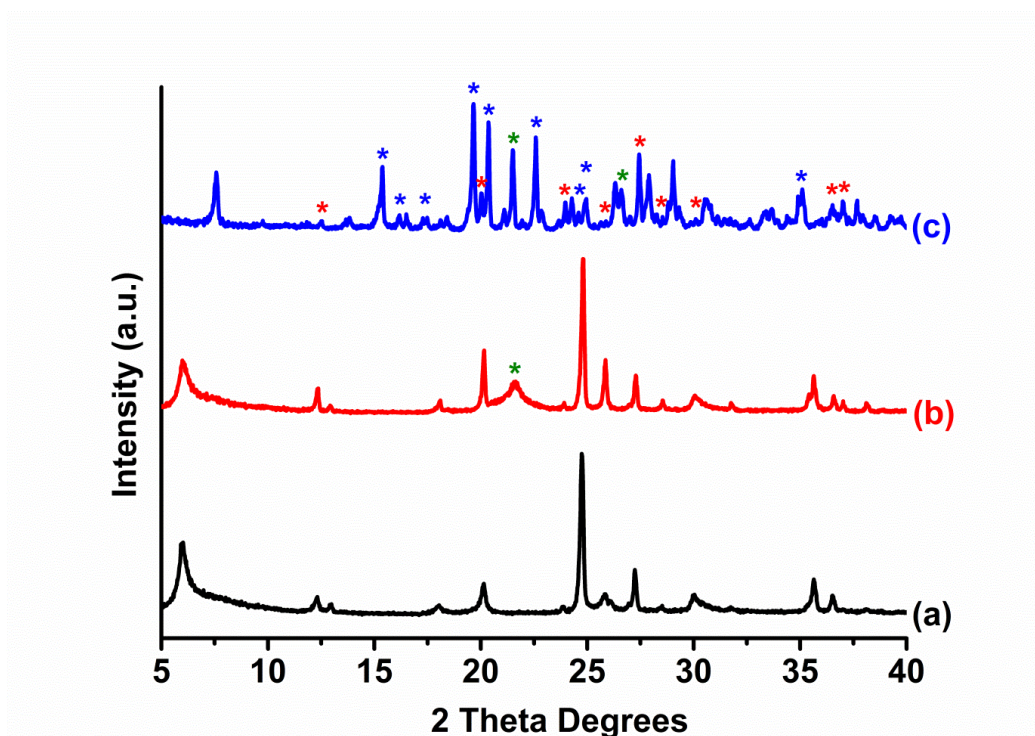


Figure 4.2. XRD patterns of AM-6 samples in powder form F1(a), F2(b), F3(c). \* indicates quartz impurity; \* and \* refer the peaks belonging to AM-6 and VSH, respectively

Nevertheless, S1-F3 resulted in pure AM-6 film formation. All of these results can be attributed to the fact that seeds played a major role in the relatively fast crystallization of the secondary growth solution in comparison with the production of the AM-6 crystals in powder form where no seed exists [98]. In film formation, crystals grow over the existing seeds which promote crystal growth and improve crystallization [92,106].

Top views of the S1-F1 and S1-F2 films were quite similar, truncated bipyramidal-shaped, with respect to S1-F3 (Figure 4.1), which can be attributed to the differences between the crystal growth rates in  $a$ -( $b$ )-out-of-plane orientations versus  $c$ -orientation. FE-SEM images (Figures 4.1 and 4.3) and CPO values proved that S1-F3 has a higher growth rate in  $c$ -orientation resulting in bipyramidal-shaped intergrown crystals.

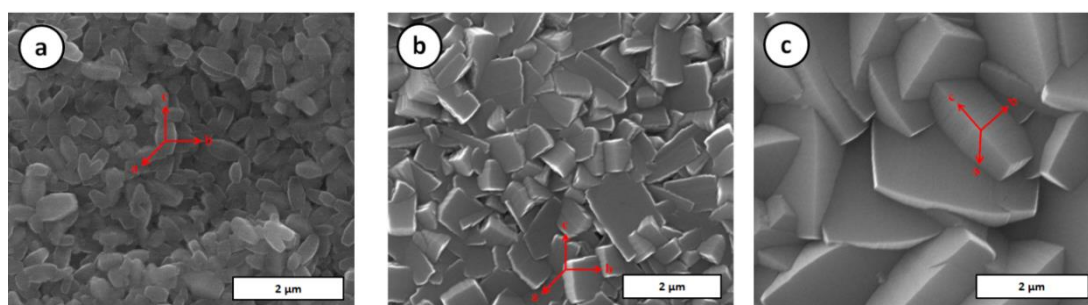


Figure 4.3. Growth directions of ETS-10 crystals as seed (a), S1-F1 (b), and S1-F3 (c)

It is well known that it is possible to control the direction and the rate of crystal growth by controlling the molar composition and concentration of the secondary growth gel. The molar compositions of secondary growth gels used in this section are shown in the composition diagram in Figure 4.4.



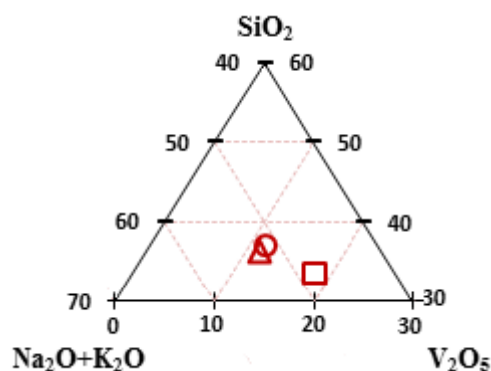


Figure 4.4. Composition diagram of 3 molar compositions:

○ S1-F1, △ S1-F2, and □ S1-F3 (Table 3.1)

The fact that samples S1-F1 and S1-F2 possess quite similar growth rates can arise from the close proximity of their gel compositions in the phase diagram as shown in Figure 4.4. However, the position representing S1-F3 is shifted, which means that the composition of  $V_2O_5$  and  $Na_2O + K_2O$  were higher while the content of  $SiO_2$  was lower. Different molar compositions as also shown in the phase diagram can be attributed to the differences in morphology and orientation of the intergrown crystals (i.e., films) prepared through three different adapted molar formulas since molar composition and concentration affect both the morphology and crystal growth rate [106].

Furthermore, the temperature is also a crucial parameter affecting not only the crystal growth rate but also the crystal morphology. The reaction temperatures were 503 K for S1-F1, S1-F2 while it was 528 K for S1-F3 films. Reaction time decreases with increasing temperature indicating that thermally activated reactions dominate crystallization [107].

The morphology and the molar composition of the S1-F1 and S1-F2 films were quite similar; however, the reaction time of former was only 2 h while the latter was 72 h. Crystallization in shorter time was attributed to the role of structure direction agent (SDA), tetramethylammonium hydroxide (TMAOH), used in the secondary growth gel of S1-F1 films, which involves ordering of water and silica. It is assumed that

these organic-inorganic composites structures participate in crystal growth and causes an increase in the crystal growth rate [107]. Further XRD analyses were carried out to figure out the morphological differences of AM-6 film growth.

To determine purity and crystal orientation, XRD patterns were collected from the AM-6 films. Figure 4.5 demonstrates the XRD patterns of vanadosilicate AM-6 films grown on the seeded substrates and the titanosilicate ETS-10 seed layer on ITO coated glass substrates.

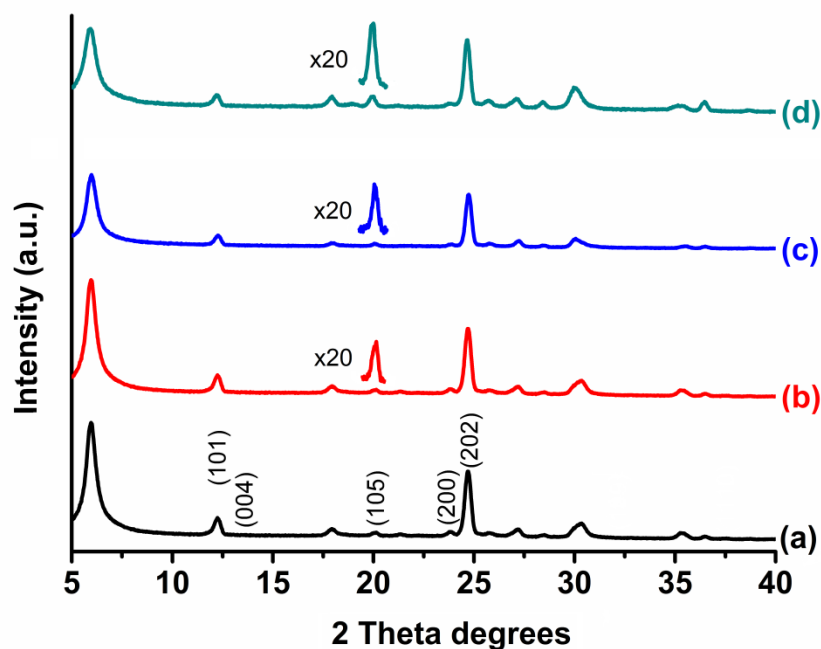


Figure 4.5. XRD patterns of ETS-10 (a), S1-F1 (b), S1-F2 (c), and S1-F3 (d)

The positions of the XRD peaks of the samples match well with that of the ETS-10 seed layer. The titanosilicate ETS-10 crystals in the seed layer were randomly oriented. The  $2\theta$  degree of  $\approx 20^\circ$  (i.e., (105) plane) observed in the AM-6 films relatively increased for S1-F3 film due to the tendency of crystals to grow in  $c$  direction (Figure 4.5-d). The intensity difference between the XRD patterns of the

samples is much more apparent when the peak belonging the (105) plane was magnified 20 times. The (004) plane makes an angle of  $90^\circ$  to the  $a$  and  $b$  axes, which are used to indicate growth in  $c$  direction [91]. However, as can be seen from the XRD patterns (Figure 4.5), the intensity of (004) plane is insignificant. Instead of using (004) plane, more intense (105) plane that makes a smaller angle with (004) plane can be used for examination of preferred orientation [91]. Thus, the increase of the peak intensity in (105) plane indicates the preferred orientation in the  $c$  direction. Accordingly, S1-F3 had the most intense (105) peak indicating the growth in S1-F3 is preferably in the  $c$  direction. In order to examine it further, CPO values were calculated for each sample.

CPO has been used for determination of the orientation qualitatively for several years. For instance, CPO values for ETS-10 membranes prepared on  $\alpha$ -alumina substrates and ITO coated glass substrates were calculated [54,91]. Yilmaz et al. compared the peak intensities of (110) and (001) planes instead of calculating CPO. They concluded that the increase in the ratio of (110)/(001) was an indication of partial  $b$ -out-of plane oriented membranes. Conversely, a decrease in this ratio indicated ( $a$ ,  $c$ )-out-of-plane orientation [89]. Hedlund et al. calculated CPO values to examine the changes in the orientation of the silicalite-1 membrane. They suggested that it is possible to control the orientation of the film by changing the seed size and the population of seed crystals [94]. It is desirable to choose the orientation of the layers, i.e. CPO axis, depending on the application [108].

In order to investigate  $a$ -( $b$ )-out-of-plane preferred orientation of the AM-6 films, the integrated intensity values of the (200) and (004) planes should have been compared since these two planes make an angle of  $90^\circ$  with each other. Instead, the CPO index was calculated based upon (200) and (105) planes, because the peak belonging to the plane (004) was inconvenient to use due to its very low intensity. Thus, the planes making the lowest angles with (004) plane were calculated and the most intense plane that makes the lowest angle with (004) plane was found to be (105) plane.

Thus, the integrated intensity values under the (200) and (105) planes were used for calculation of CPO values of AM-6 films.

In order to calculate CPO values, integrated intensities of selected planes were identified for each AM-6 films. The CPO index based on (200) and (105) reflections was calculated using the well-known definition of  $CPO_{200/105} = \frac{(I_{200}/I_{105})_f - (I_{200}/I_{105})_p}{(I_{200}/I_{105})_p}$  for quantitative analysis of the degree of  $a(b)$ -out-of-plane preferred orientation [54,109]. In this equation,  $I$  depict the integrated intensity of the corresponding reflections and the subscripts of  $p$  and  $f$  represent powder sample (randomly oriented) and films (preferentially oriented), respectively [54,109]. Accordingly, the obtained results are shown in Table 4.1.

Table 4.1. *Si/V ratios, thicknesses, and CPO values of S1-F1, S1-F2, S1-F3, S1-F1-W1, S1-F1-W2, and S1-F1-T1*

Sample	<i>Si/V</i>	<i>Thickness (μm)</i>	<i>CPO<sub>200/105</sub></i>
S1-F1	6.39 ± 0.02	2.03 ± 0.27	14.37
S1-F2	5.52 ± 0.09	1.67 ± 0.11	7.66
S1-F3	4.53 ± 0.07	1.29 ± 0.07	0.39
S1-F1-W1	6.37 ± 0.04	1.54 ± 0.06	10.27
S1-F1-W2	6.75 ± 0.10	1.31 ± 0.07	30.72
S1-F1-T1	6.23 ± 0.06	2.48 ± 0.25	9.07

As can be seen from the Table 4.1, the  $CPO_{200/105}$  value belonging to the S1-F1 film was the highest (i.e., 14.37) indicating the highest degree of  $a(b)$ -out-of-plane preferred crystal orientation while S1-F3 film has the lowest value (i.e., 0.39). The  $CPO_{200/105}$  values suggest that seed crystals grow much faster along  $a$  and  $b$  directions for the samples S1-F1 and S1-F2 films with respect to S1-F3 films.

The characteristic vibration band of the ...V-O-V-O-V... ( $\text{VO}_3^{-2}$ ) quantum wires of the AM-6 films were detected via Raman analyses and the results are shown in Figure 4.6.

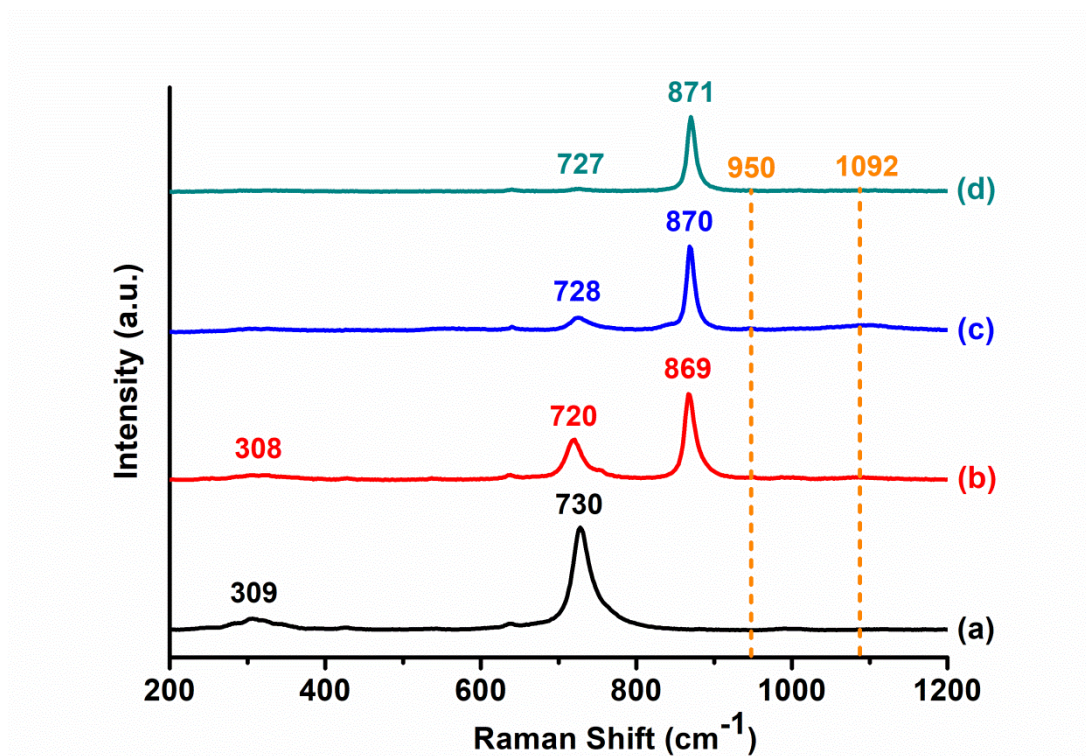


Figure 4.6. Raman spectroscopy of ETS-10 seed layer (a), S1-F1 (b), S1-F2 (c), and S1-F3 (d)

It is well known that  $\text{VO}_3^{-2}$  quantum wires are characterized by the Raman Shift centered at around  $870 \text{ cm}^{-1}$  giving an indication of quality (bandwidth) and length of the quantum wire (shift). Vanadium in the  $\text{VO}_3^{-2}$  quantum wires has two oxidation states:  $\text{V}^{4+}$  (hole traps) and  $\text{V}^{5+}$  (electron traps) [40]. The oxidation states in AM-6 crystals draw attention in catalysis due to the easy reduction process of oxidized  $\text{V}^{5+}$  state to  $\text{V}^{4+}$  state [110]. Synthesis of AM-6 crystals having pure oxidation state (i.e.,  $\text{V}^{4+}$  hole traps) was a subject of several studies in the literature [48,111]. Raman spectroscopy is a crucial tool to identify V-O stretching vibrations of  $\text{VO}_3^{-2}$  quantum wires in the AM-6 films accurately and find the purity of the films.

The Raman shift at around  $870 \text{ cm}^{-1}$  as shown in Figure 4.6 is attributed to the undistorted  $\text{VO}_6$  octahedra and associated with V-O stretching vibrations that involve octahedrally

coordinated  $V^{4+}$  in AM-6 structure [49]. The characteristic V-O stretching vibration of S1-F1, S1-F2, and S1-F3 films was observed at 870, 869 and 868  $\text{cm}^{-1}$ , respectively, which indicates that  $\text{VO}_3^{-2}$  quantum wires in the AM-6 films have  $V^{4+}$  oxidation state (Figure 4.6). The shoulder observed at 950  $\text{cm}^{-1}$  is the characteristic Raman shift of the  $V^{5+}$  oxidation state of  $\text{VO}_3^{-2}$  quantum wires in AM-6 crystals [50]. The Raman spectra of S1-F1 and S1-F2 films showed a slight shoulder at around  $\sim 950 \text{ cm}^{-1}$  indicating that these two films had two oxidation states of vanadium in the structure (i.e.,  $V^{4+}$  and  $V^{5+}$ ). However, the absence of the shoulder around  $\sim 950 \text{ cm}^{-1}$  in Raman spectra of S1-F3 film revealed that the film had only one oxidation state (i.e.,  $V^{4+}$ ) in its 1-D  $\text{VO}_3^{-2}$  quantum wires. The shoulder observed at 1092  $\text{cm}^{-1}$  for the sample S1-F2 was attributed to the  $V^{5+}=\text{O}$  stretching mode of terminal oxygen atoms [112]. The other noticeable Raman shift observed at around 309  $\text{cm}^{-1}$  and 730  $\text{cm}^{-1}$  was associated with the Ti-O stretching vibration indicating the presence of ETS-10 in the AM-6 films (Figure 4.6) [48,49].

The appearance of Ti-O stretching vibration peaks in the Raman spectrum of AM-6 is the evidence of that the ETS-10 crystals are present as nucleation cores in AM-6 structure [113]. The AM-6 formation mechanism using ETS-10 as a seed by Guo et al. is based on the dissolving of the external surfaces of ETS-10 into small pieces, which would serve as nucleation sites for AM-6 crystal synthesis [113]. It is known from the literature that the dissolution rates of vanadium sources (i.e.,  $\text{VO}_2$  and  $\text{V}_2\text{O}_5$ ) differ from each other during AM-6 synthesis. The variation in the relative intensities observed for ETS-10 peaks at 720-728  $\text{cm}^{-1}$  in Raman spectra and thus, the proposed three-membered ring species consumed as initiators during AM-6 formation could be attributed to different dissolution rates of V precursors (i.e.,  $\text{VO}_2$  and  $\text{V}_2\text{O}_5$ ) used in AM-6 film formation [40]. Since 720-728  $\text{cm}^{-1}$  Raman peaks are more intense in Figure 4.6-b and c, it can be hypothesized that ETS-10 seed crystals could not find sufficient time to dissolve for the transformation into vanadosilicate AM-6 structure due to the high dissolution rate of  $\text{VO}_2$  used for the preparation of S1-F1 and S1-F2.

The narrow width of vibration band pertaining to  $\text{VO}_6$  quantum wires in Raman spectra indicates the length homogeneity of the quantum wires in AM-6 crystals [111]. In order to show this, the full-width half-maximum (FWHM) was obtained for the main band of V-O stretching for each film and shown in Table 4.2. The maximum broadening was observed for the S1-F1 film (i.e.,  $15.23 \pm 0.09 \text{ cm}^{-1}$ ). S1-F2 and S1-F3 films revealed similar degrees of broadening with a slight increase of FWHM of S1-F3 (i.e.,  $12.17 \pm 0.02 \text{ cm}^{-1}$  for S1-F2;  $12.27 \pm 0.07 \text{ cm}^{-1}$  for S1-F3). These values were also comparable with the ones reported for the powder AM-6 crystals in the literature [40].

Table 4.2. Raman shift and FWHM (full-width half-maximum) values belonging to V-O stretching of AM-6 and Ti-O stretching of ETS-10

	Raman Shift ( $\text{cm}^{-1}$ )		FWHM of V-O stretching ( $\text{cm}^{-1}$ )
	V-O Stretching	Ti-O Stretching	
ETS-10	-	730	-
S1-F1	869	720	$15.23 \pm 0.09$
S1-F2	870	728	$12.17 \pm 0.02$
S1-F3	871	727	$12.27 \pm 0.07$

In order to gain a better understanding of the growth and orientation of vanadosilicate AM-6 films, the effect of reaction temperature and amount of water in secondary growth gel were investigated. The molar composition of S1-F1 film was selected as standard composition since its experimental procedure was easier and the reaction time was also shorter with respect to others. The effect of reaction temperature on morphology was also studied for S1-F1 films with a standard molar composition by increasing the temperature from 503 K to 528 K, which was normally used for S1-F3 film formation (Table 3.1). The FE-SEM images of the resulting morphology of the crystals were illustrated in Figure 4.7-c.

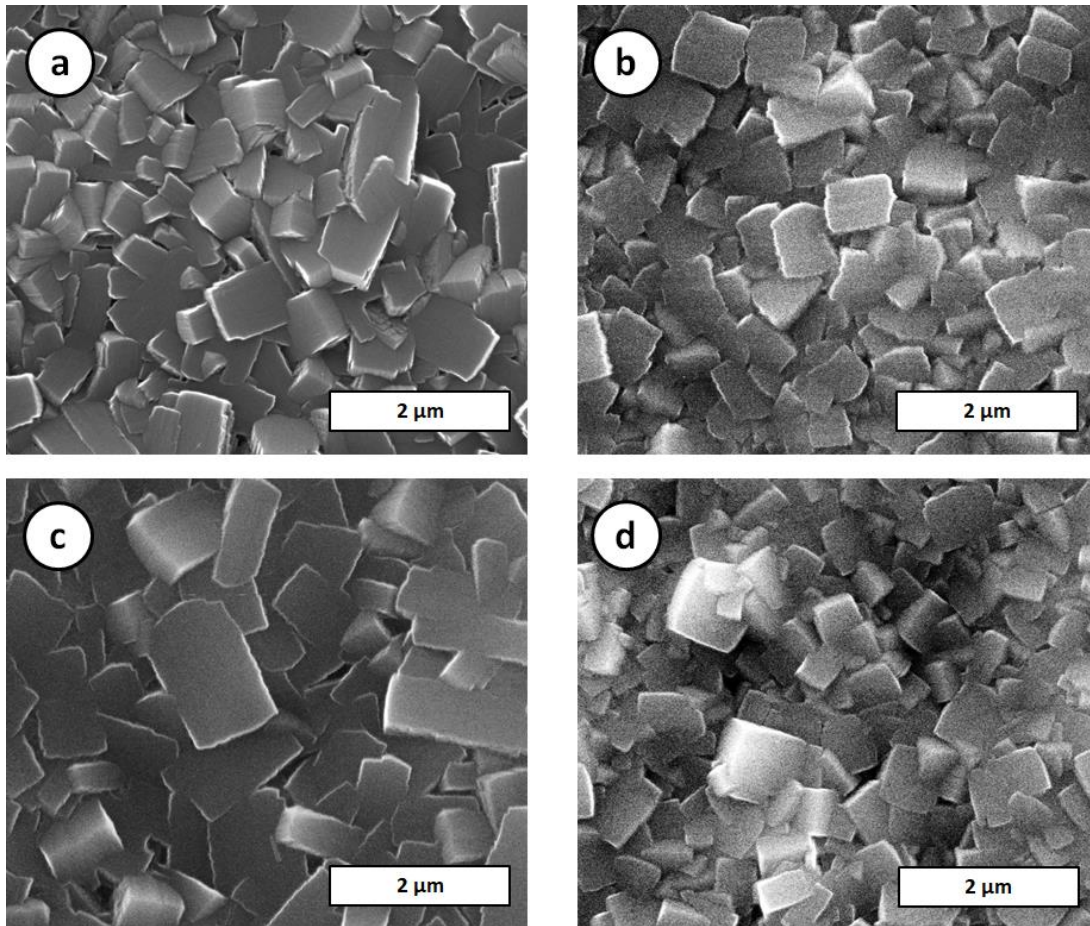


Figure 4.7. FE-SEM images of the samples; S1-F1 (a), S1-F1-W1 (b), S1-F1-W2 (c), and S1-F1-T1 (d)

The crystals of the synthesis mixture produced at 528 K (S1-F1-528K) formed more of a rectangular shape in comparison with S1-F1 that was synthesized at 503 K. Furthermore, increasing the temperature led to a decrease in the crystallization time in accordance with the thermodynamic expectations [114]. The crystallization time was 2 h for standard composition while 1 h was enough for crystallization at 528 K. This can be explained by triggering the acceleration of formation of primary nucleation at higher temperatures due to the enhanced interaction frequency of nutrients [35]. The effect of decreasing the temperature from 503 K to 473K was



also studied. However, the films were peeled off the surface and the FE-SEM and XRD analyses showed no significant film formation (results not shown).

The effect of water content in the secondary growth gel on morphology was also studied for vanadosilicate S1-F1 films by decreasing the molar water amount from 209 to 150 and by increasing it from 209 to 300. The FE-SEM images of the resulting morphology of the crystals were illustrated in Figure 4.7-a, b. The morphology of the resulting crystals of the synthesis mixture with different water content, i.e., S1-F1 and S1-F1-W1 were nearly identical. Decreasing the water content did not affect the crystallization time as well. The crystallization time was 2 h for both the standard and the concentrated compositions. This is because; the water content is in a similar range with the optimum concentration of water defined for standard composition.

Upon increasing the water content from 209 to 300 (S1-F1 versus S1-F1-W2), the morphology of the crystals was modified and formed more of a rectangular shape, suggesting the growth to be in preferably in c-direction in S1-F1-300. In addition to these, increasing the water content caused an increase in the crystallization time. The 2 h time frame used for standard composition used for the crystallization had to be extended at least to 5 h to achieve crystallization in the diluted solution, which is consistent with the results of Ji et al. [97,115]. Increasing the water content results in an increase in the crystallization time, decrease the crystallization rate, and lower the supersaturation level [114]. In the primary nucleation step, fewer nuclei are formed causing larger crystals to grow. In addition, increasing the water content causes an increase in the pH level (from 11.8 to 12.7) of the solution suggesting a lower supersaturation level [97]. These are the evidence that the morphology and the growth rates of the crystals are strongly affected by the composition of the secondary growth gel.

To determine the purity and crystal orientation of the samples, XRD patterns were collected. Figure 4.8 demonstrates XRD patterns of S1-F1, S1-F1-W1, S1-F1-W2,

and S1-F1-T1 (Table 3.1). The XRD patterns of the samples in Figure 4.8-b, c, and d match well with that of S1-F1 (Figure 4.8-a).

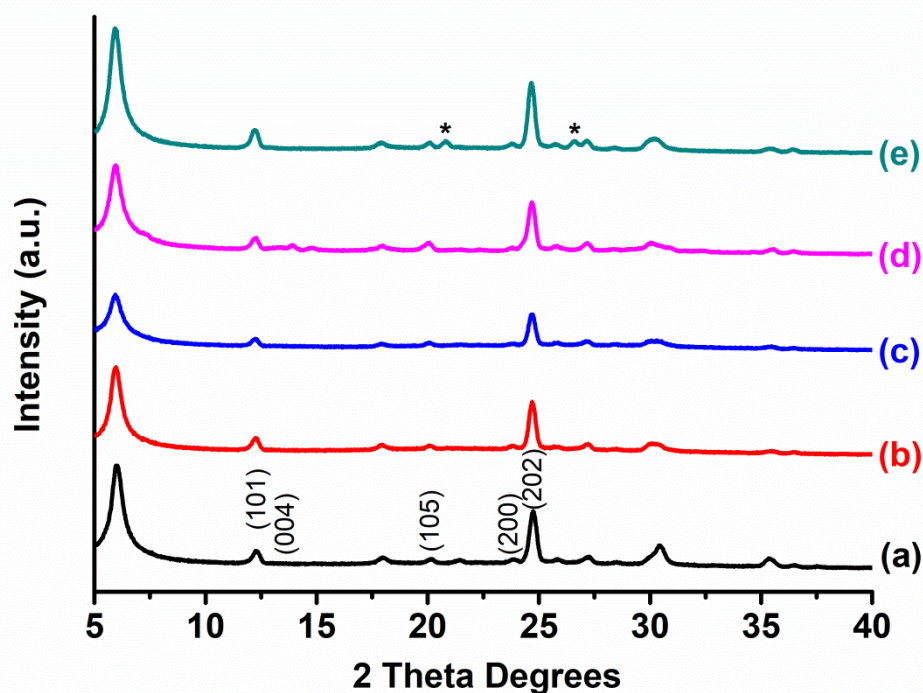


Figure 4.8. XRD patterns of the samples S1-F1 (a), S1-F1-150 (b), S1-F1-300 (5 h crystallization) (c), S1-F1-300 (8 h crystallization) (d), and S1-F1-528K (e). \* indicates the quartz impurity

However, XRD peak intensity of S1-F1-300 produced in 5 h was much lower than that of S1-F1 (Figure 4.8-c). Therefore, 8 h reaction (Figure 4.8-d) was more suitable to obtain high crystallinity. The positions of the XRD peaks of the samples produced at 528 K (Figure 4.8-e) match well with that of standard S1-F1 (Figure 4.8-a). However, there are some extra peaks (i.e., 20.8, 26.6) at the  $2\theta$  degree indicating quartz impurity.

The  $CPO_{200/105}$  values of S1-F1, S1-F1-W1, and S1-F1-W2 were demonstrated in Table 4.1. As can be seen from the Table 4.1, the  $CPO_{200/105}$  value belonging to S1-F1-W2 was the highest (i.e., 30.72) indicating the highest degree of  $a(b)$ -out-of-

plane preferred crystal orientation while the S1-F1-W1 film has the lowest (i.e., 10.20) value. The increase in the  $CPO_{200/105}$  values for the samples indicates an increasing degree of preferential crystal orientation [109]. According to the CPO results, alteration of the water content affects the degree of crystal orientation. The increase in water content led to an increase in the CPO value. Thus, manipulation of crystal orientation is possible by changing the amount of water in the secondary growth gel which is consistent with the suggestions given by Li et al. [116]. They stated that it was possible to manipulate the preferred orientation of mordenite membranes by changing the water content in the secondary growth mixture, which was attributed to the influence of synthesis parameters on the diffusion of the aluminosilicate species [116].

## **4.2. The Effect of Microporous Vanadosilicate AM-6 Films as Photocatalysts for the Degradation of MB under UV and Visible Light Irradiation**

In the second part of the study, ETS-10, S1-F3, S1-F2 and silver nanoparticle incorporated S1-F2 films were prepared for utilization as photocatalysts for the photocatalytic decomposition of MB. The samples coded as S1-F1 could not be utilized in this part of the study due to the loose adsorption of the AM-6 crystals on the substrate surface making this sample unsuitable for photocatalytic applications. Thus, the current study was carried out with the utilization of ETS-10, S1-F3, S1-F2 and  $Ag^0$ -S1-F2 as photocatalysts [117].

### **4.2.1. Sample Characterization**

Top view FE-SEM images demonstrate the morphological and spatial differences of ETS-10, S1-F2,  $Ag^0$ -S1-F2, and S1-F3 thin films resulting from different synthesis conditions as shown in Figure 4.9.

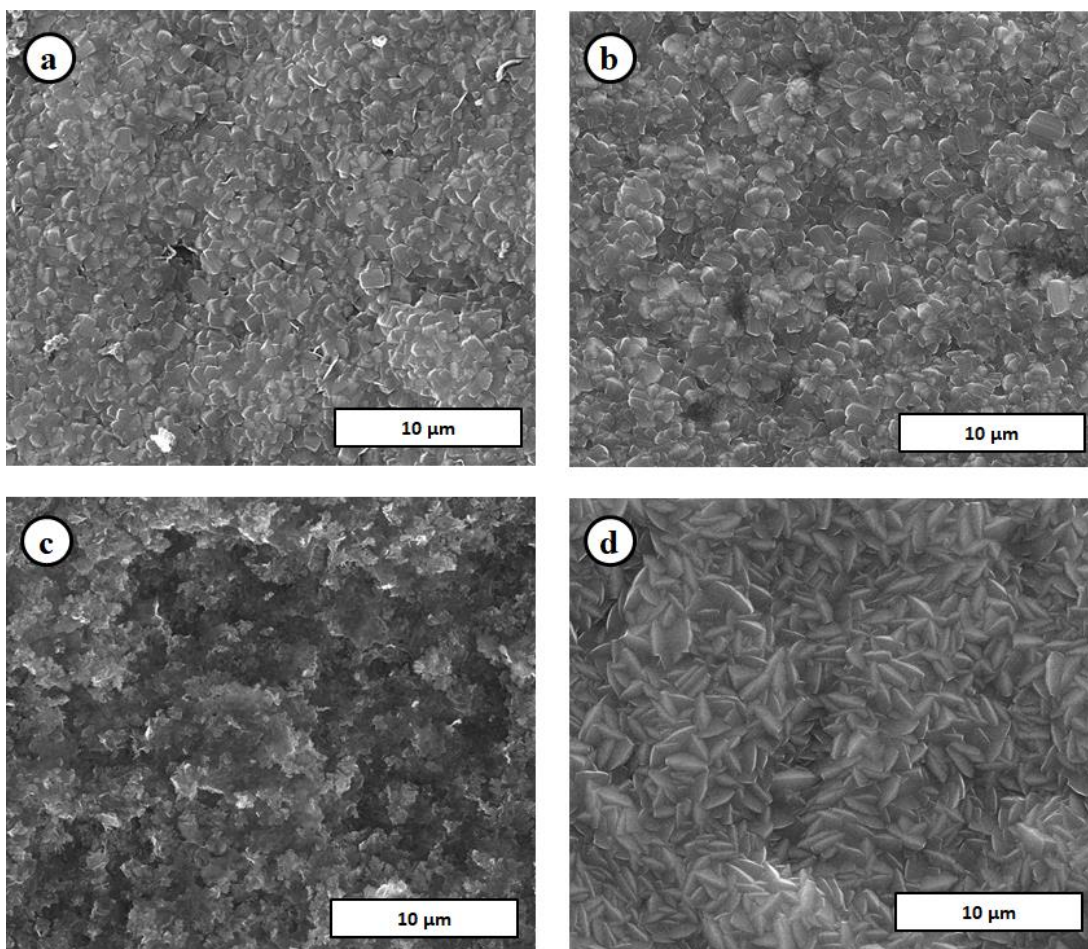


Figure 4.9. Top view FE-SEM images of ETS-10 (a), S1-F2 (b), Ag<sup>0</sup>-S1-F2 (c), and S1-F3 (d) thin films

FE-SEM images revealed that thin films have a bipyramidal structure for ETS-10 (Figure 4.9-a) and S1-F2 (Figure 4.9-b), respectively, while the crystals of S1-F3 thin film (Figure 4.9-d) have truncated bipyramidal structure. The crystals of the ETS-10 thin film tended to grow in truncated tetragonal bipyramidal shape, which was in agreement with previous studies [54]. The morphological differences between thin films of S1-F3 and S1-F2 could be attributed to the different crystal growth rates originated from the different molar compositions and concentrations of the secondary growth gels, specifically different vanadium sources, used for the formation of thin films. The reaction temperature (528 K for S1-F3, 503 K for S1-

F2) used for the formation of thin films is also a crucial parameter that affects both crystal growth rate and crystal morphology [98]. As a result, different synthesis conditions lead to two different AM-6 films with different morphologies, which are thought to affect the ...V-O-V-O-V... wires as also discussed for powder AM-6 samples [40].

Figure 4.10 shows the XRD patterns of ETS-10 and vanadosilicate AM-6 films in addition to silver nanoparticle modified S1-F2 film ( $\text{Ag}^0$ -S1-F2) grown on ITO coated glass substrates.

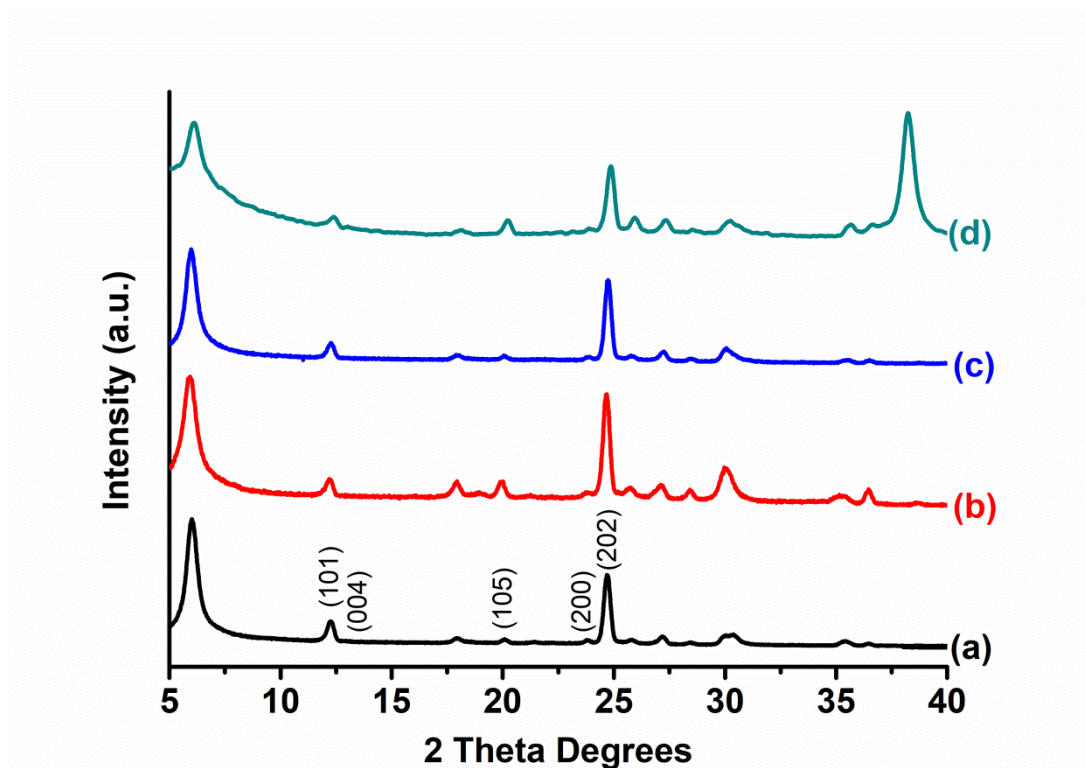


Figure 4.10. X-ray diffraction patterns of ETS-10 (a), S1-F2 (b),  $\text{Ag}^0$ -S1-F2 (c), and S1-F3 (d) thin films

As seen from the XRD data, there is neither noticeable changes in the peak positions nor a peak broadening. The results showed that thin films were crystalline and have no other typical impurity phases like ETS-4,  $\text{TiO}_2$ , and VSH resulting from the

synthesis of ETS-10 and AM-6 crystals. The XRD pattern of Ag<sup>0</sup>- S1-F2 indicates that ion-exchange with Ag<sup>+</sup> ions and reduction of Ag<sup>+</sup> ions to Ag<sup>0</sup> nanoparticles by NaBH<sub>4</sub> solution did not affect the crystal structure of thin film. Furthermore, the Bragg peak located at 2 theta degree of 38.2° is clearly observable in the XRD pattern of Ag<sup>0</sup>- S1-F2, which could be attributed to the existence of silver nanoparticles [84,118].

XPS analyses were conducted to investigate chemical states of the elements incorporated into structures of thin films (Figures 4.11 and 4.12). The existence of different oxidation states of vanadium cation could be detected through XPS analysis technique due to the dependence of binding energy (BE) of the Vp<sub>3/2</sub> core level to the oxidation state of V [119].

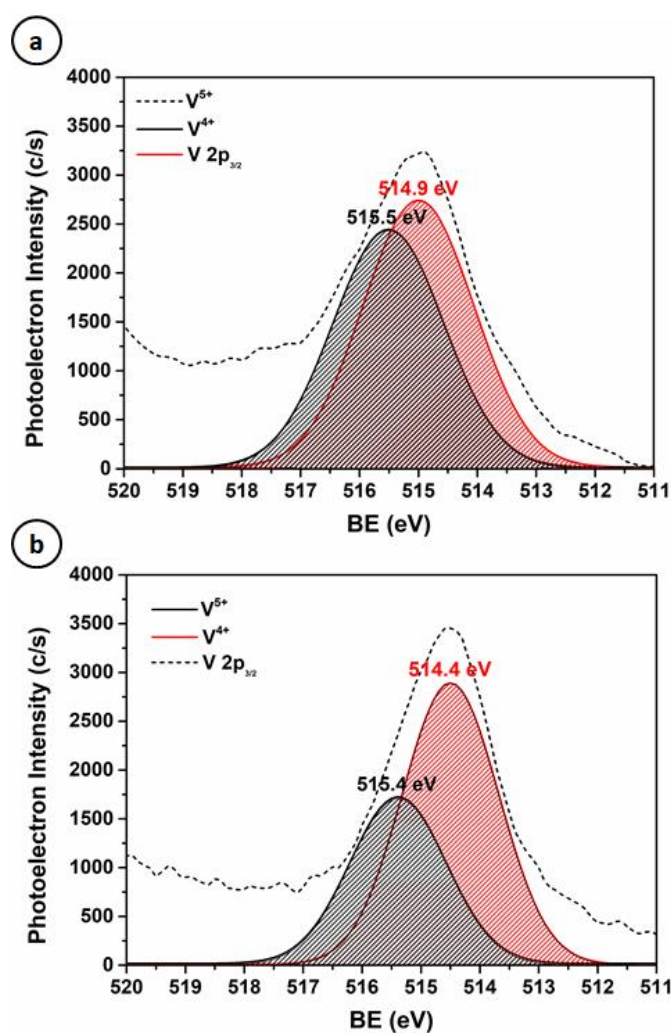


Figure 4.11. XPS high resolution V 2p spectra of S1-F2 and S1-F3, deconvolution of V2p<sub>3/2</sub> XPS peak of S1-F2 ( $V^{4+}/V^{5+}=1.12$ ) (a), and deconvolution of V 2p<sub>3/2</sub> XPS peak of S1-F3 ( $V^{4+}/V^{5+}=1.68$ ) (b)

The V2p<sub>3/2</sub> and V2p<sub>1/2</sub> of S1-F2 were found at 521.9 eV and 514.5 eV, respectively (not shown). These values are close to the binding energy values of Vp<sub>3/2</sub> and Vp<sub>1/2</sub> core level stated by Zhang et al., which are 524.9 eV and 517.2 eV, respectively [120]. Yeates et al. represented the XPS spectrum of AM-6 in the V2p region with a splitting of 7.3 eV which were found to be consistent with our results [47]. The BE values of V2p<sub>1/2</sub> and V2p<sub>3/2</sub> are also consistent with the spectral fitting parameters identified by Silversmith et al. for vanadium (III) oxide [119].

Different states of  $V^{5+}$  and  $V^{4+}$  are typically obtained by deconvolution of  $V2p_{3/2}$  level into two peaks [120,121]. In our case, the XPS spectrum of S1-F3 and S1-F2 thin films for  $V2p_{3/2}$  was deconvoluted into two peaks. These peaks with binding energies of 514.9 eV and 515.5 eV for S1-F2 have been attributed to  $V^{5+}$  and  $V^{4+}$ , respectively. The peaks centered at 514.4 eV and 515.4 eV for S1-F3 has been attributed to  $V^{5+}$  and  $V^{4+}$ , respectively [120]. These values are consistent with the binding energy values specified for  $V^{5+}$  and  $V^{4+}$  cations in the literature [99,119,122–124]. The XPS peaks indicating  $V^{4+}$  and  $V^{5+}$  were obtained following the deconvolution of  $V2p_{3/2}$  peak. In Figure 4.11, while the dotted lines represent the original XPS data, the straight lines represent the fitted data. XPS signals were fitted using mixed Gaussian-Lorentzian functions using Peak Fit v4.12 as deconvolution software.

Absolute area of the fitted  $V^{4+}$  and  $V^{5+}$  peaks were calculated. In accordance with this, the ratio of  $V^{4+}/V^{5+}$  was calculated as 1.12 and 1.68 for the samples S1-F2 and S1-F3, respectively. Table 4.3 was created using these data obtained from the calculation of the area under each curve.

Table 4.3. XPS spectral parameters for  $V 2p_{3/2}$ : Binding energy (eV), and the ratio of  $V^{4+}/V^{5+}$

Sample	$V2p_{3/2}$		$V^{4+}/V^{5+}$
	$V^{4+}$	$V^{5+}$	
	BE (eV)	BE (eV)	
S1-F2	514.9	515.5	1.12
S1-F3	514.4	515.4	1.68

The data in Table 4.3 indicates that the quantity of  $V^{5+}$  cations is greater in S1-F2 than the S1-F3. Table 4.3 demonstrates the calculated percentage of different oxidation states of vanadium ( $V^{4+}$  and  $V^{5+}$ ) based on the XPS results. These results indicate that vanadium exists in two oxidation states ( $V^{4+}$  and  $V^{5+}$ ) and the amount of these oxidation states is different for the samples.



In addition to the observed morphological differences between S1-F2 and S1-F3 results, it can be deduced that vanadium exists in two different oxidation states in the structure of these two films upon the changes induced with the synthesis route. According to these results, it is expected that S1-F2 is more sensitive to visible light when it is used as a photocatalyst under visible light irradiation due to the presumed dependence of visible light photocatalytic activity to the presence of  $V^{5+}$  cations [50].

XPS survey scan of  $Ag^0$ -S1-F2 thin film demonstrated in Figure 4.12-a possesses peaks at 571.2 eV (Ag 3p), 531.7 eV (O 1s), 515.1 eV (V 2p), 717.9 eV (Ag 3s), 154.3 eV (Si 2s) and 367.1 eV (Ag 3d). High-resolution Ag 3d spectrum was also obtained for the  $Ag^0$ -S1-F2 thin film through XPS analysis (Figure 4.12-b-black line).

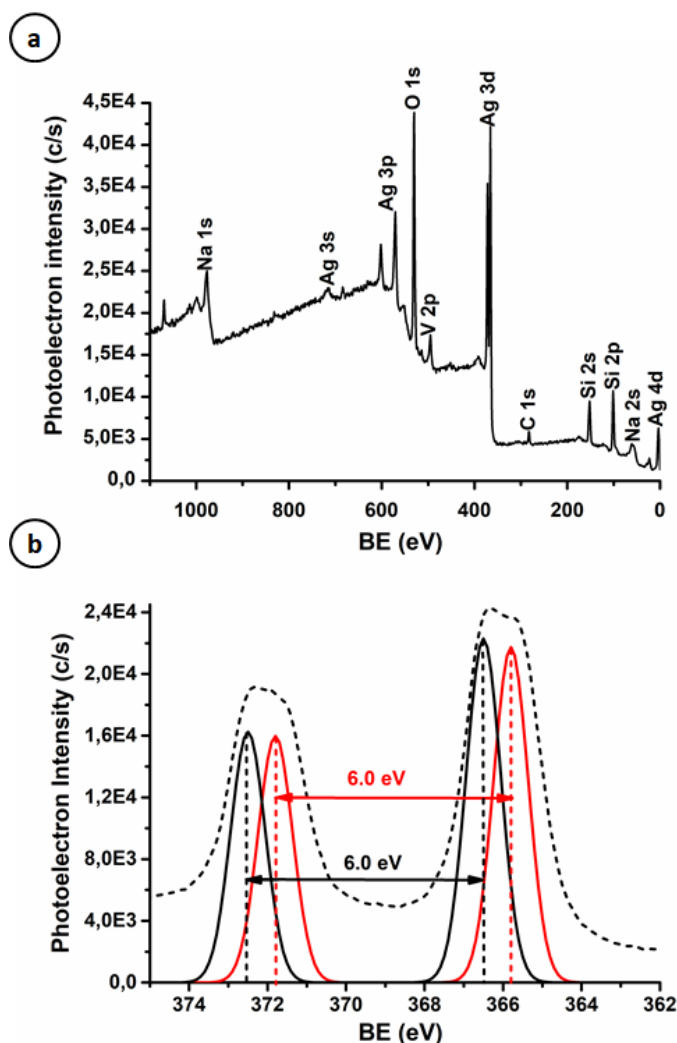


Figure 4.12. XPS survey scan spectrum of Ag<sup>0</sup>-S1-F2 (a), and XPS high-resolution Ag 3d spectra of Ag<sup>0</sup>-S1-F2 (b)

The peaks observed at 366.02 eV and 372.02 eV are assigned to the 3d<sub>5/2</sub> and 3d<sub>3/2</sub> respectively with a binding energy separation of 6.0 eV. This separation of 6.0 eV was also reported in the literature, suggesting the presence of Ag nanoparticles [84]. Therefore, it can be deduced that silver is present in metallic form in the structure of AM-6 which correlates the data obtained from XRD analysis of Ag<sup>0</sup>-S1-F2 thin film. The XPS analysis was repeated for the same sample after its utilization as photocatalyst under UV irradiation to indicate the possible structural change of the

films (Figure 4.12-b-red line). The binding energies of Ag 3d<sub>5/2</sub> (366.03 eV) and 3d<sub>3/2</sub> (372.03 eV) for the sample Ag<sup>0</sup>- S1-F2 after its utilization as photocatalyst under UV irradiation were lower than the binding energies of Ag 3d<sub>5/2</sub> (367.89 eV) and 3d<sub>3/2</sub> (373.89 eV) for the same sample before its utilization as photocatalyst. This might be due to the ionization of metallic silver during the photocatalytic cycle which is expected due to the interaction of Ag nanoparticles with light [84].

Raman analysis technique was used to determine the characteristic vibration peaks of ...V-O-V-O-V... and ...Ti-O-Ti-O-Ti... quantum wires in the structures of vanadosilicate AM-6 and titanosilicate ETS-10, respectively (Figure 4.13). Multiple oxidation states of the vanadium (V<sup>4+</sup> and V<sup>5+</sup>) present in the quantum wires of the vanadosilicate AM-6 could be identified by Raman analysis along with XPS [110].

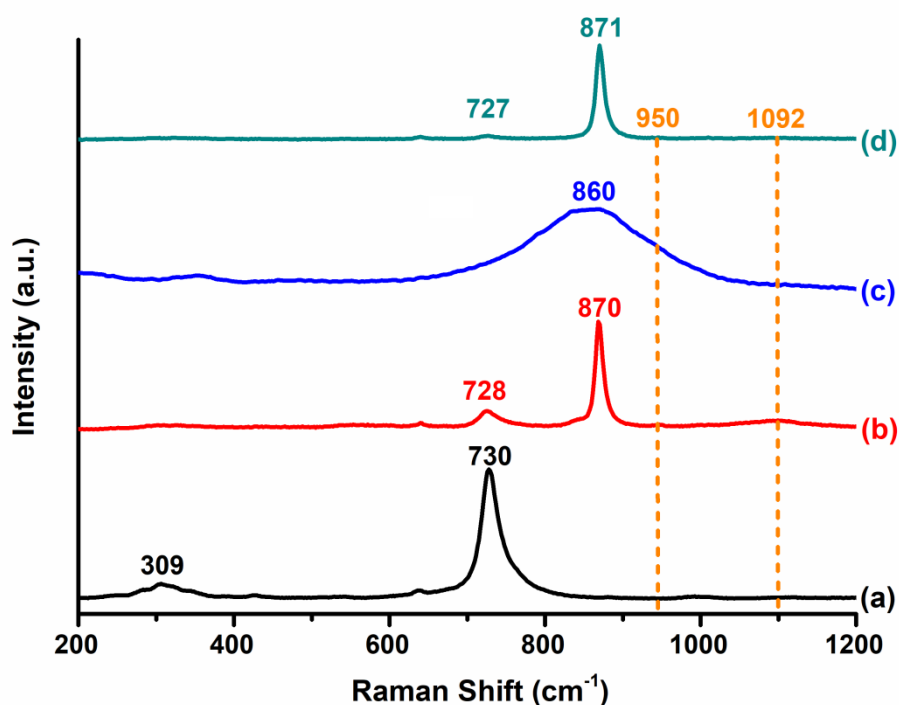


Figure 4.13. Raman spectroscopic analysis of ETS-10 (a), S1-F2 (b), Ag<sup>0</sup>-S1-F2 (c), and S1-F3 (d) thin films

The presence of the V-O wires that involve octahedrally coordinated V<sup>4+</sup> in the structure of vanadosilicate AM-6 causes a Raman shift at around 870 cm<sup>-1</sup> [49].

Raman shift at around  $720\text{ cm}^{-1}$  belonging to the Ti-O vibrations has the highest intensity for the ETS-10 containing only titanosilicate ETS-10. Although S1-F3 and S1-F2 thin films contain only vanadosilicate AM-6, there is a shoulder observed at around  $728\text{ cm}^{-1}$ , which is originated from the ETS-10 core/AM-6 shell structure of the thin films as also evidenced by Guo et al. [113]. According to this mechanism, ETS-10 seeds dissolve from their surfaces into small pieces which would serve as nucleation sites for the growth of vanadosilicate AM-6 [113]. The difference between the dissolution rates of the vanadium sources (i.e.,  $\text{V}_2\text{O}_5$  for the S1-F3,  $\text{VO}_2$  for the S1-F2) used for the secondary growth gels could be hypothesized to cause intensity differences of Ti-O vibration bands in Raman spectroscopy of S1-F3 and S1-F2 [40]. Due to the high dissolution rate of  $\text{VO}_2$  used to produce S1-F2 thin film, it is possible that ETS-10 seed crystals did not find sufficient time to dissolve for the transformation into vanadosilicate AM-6 structure. Thereby, Ti-O vibration bands representing the existence of ETS-10 crystals are more apparent in the Raman spectrum of S1-F2. The shoulders located around  $950\text{ cm}^{-1}$  and  $1092\text{ cm}^{-1}$  in the Raman spectrum of S1-F2 are the characteristic Raman shifts of the  $\text{V}^{5+}$  oxidation states of ...V-O-V-O-V... quantum wires [112]. The Raman spectrum of S1-F2 thin film demonstrates more apparent Raman shifts of the two oxidation states of vanadium ( $\text{V}^{4+}$  and  $\text{V}^{5+}$ ) with respect to S1-F3. Surprisingly, there is no visible peak or shoulder expressing the existence of  $\text{V}^{5+}$  cation in the structure of S1-F3 unlike the results obtained from XPS analysis. This is probably due to the fact that XPS analysis is more accurate than Raman analysis in the sense that XPS possesses high sensitivity to surface phenomena and maximum information can be gathered from the topmost few layers. This can be crucial for thin film analysis for the determination of chemical states of elements, which also allows the estimation of defects in high sensitivity.

The Raman spectrum of  $\text{Ag}^0$ -S1-F2 thin film is given in Figure 4.13-d, which shows that the V-O stretching band loses intensity, broadens, and shifts to a lower frequency. Although structural changes were not observed upon the incorporation of

silver within the S1-F2 thin film, which was demonstrated by XRD analysis (Figure 4.10), the procedure causes deterioration in the ...V-O-V-O-V... quantum wires of AM-6 structure as indicated by Raman analysis. In the Raman spectrum of Ag<sup>0</sup>-S1-F2 thin film, the broad and flattened V–O stretching band is evidence for this damaged vanadate quantum wires in Ag<sup>0</sup>-S1-F2 upon silver loading.

UV-vis absorption spectroscopy was used to investigate the optical properties of AM-6 films. The UV-vis absorption spectra of the samples demonstrate a strong absorption band in the UV region (Figure 4.14).

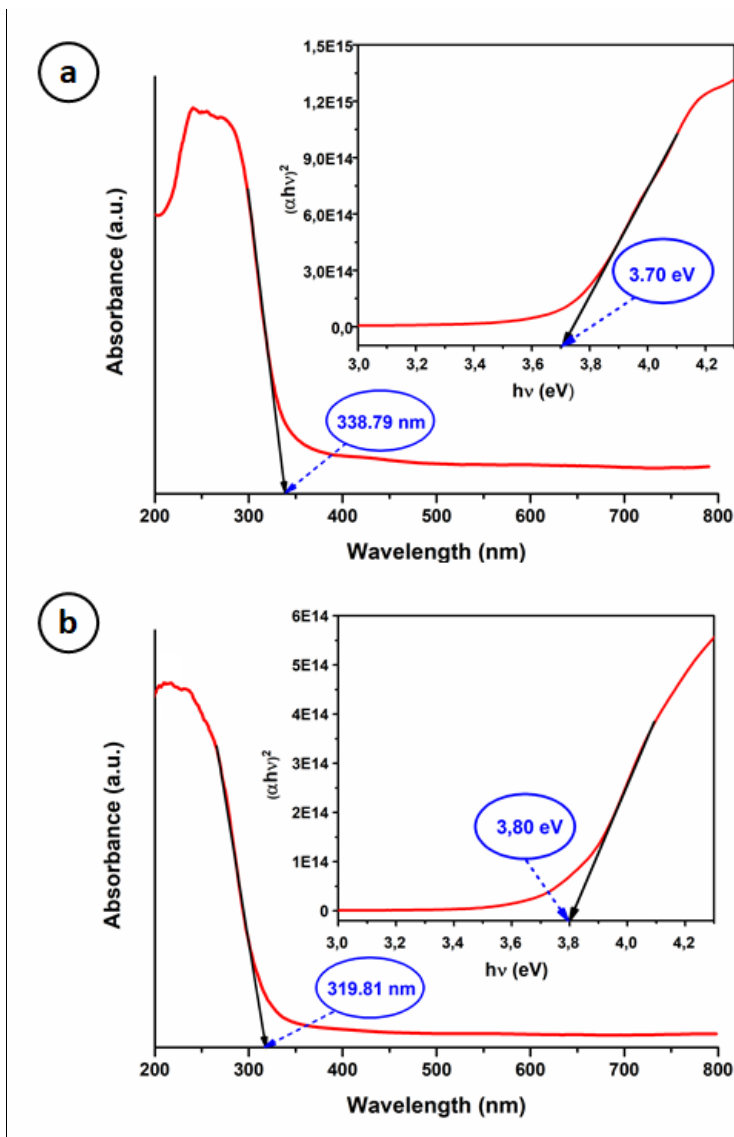


Figure 4.14. UV-Vis absorption spectra and Tauc plot for bandgap calculations for the samples S1-F2 (a) and S1-F3 (b)

The absorption maxima ( $\lambda_{\max}$ ) in the UV region are 260 nm and 210 nm for S1-F2 and S1-F3. The redshift observed in the UV-vis absorption spectroscopy of the sample S1-F2 could be attributed to the defect formation induced by different synthesis conditions [99]. These bands are similar to the UV-vis absorption spectrum observed in between 200-350 nm for powder AM-6 formation stated by Ismail et al. and assigned to  $O(2p) \rightarrow V(3d)$  charge-transfer transition [25]. While, the absorption

peak centered at around 450 nm indicates charge-transfer transition in  $V^{5+}$ , d-d transition in  $V^{4+}$  is indicated by the absorption band centered at around 590 nm [25,41]. However, these two absorption peaks are not distinctive for our samples. Therefore, further analysis should be carried out to elucidate the different oxidation states of vanadium.

The bandgap energies of the samples were calculated according to the procedure applied by López et al. (See Appendix A). As seen from Figure 4.14, S1-F2 has bandgap energy (3.70 eV) narrower with respect to S1-F3 (3.80 eV). The absorption spectra showed a cut off at 338.79 nm and 319.81 nm for S1-F2 and S1-F3, respectively as shown in Figure 4.14. These values of wavelength were also used for the calculation of energy band gap using the Equation of  $E = \frac{hc}{\lambda}$  [105]. According to this calculation energy band gap values were obtained as 3.66 eV and 3.87 eV for S1-F2 and S1-F3, respectively. The energy bandgap values are obtained similar to the ones indicated in the literature [25]. The difference between the energy bandgap values obtained using Tauc plot and/or wavelength cut off is originated from the differences between the techniques. Nevertheless, the energy bandgap of S1-F2 is lower with respect to that of S1-F3 using both techniques. The lower bandgap of S1-F2 would allow photons with lower energy to excite electrons from valence band to conduction band and create electron-hole pairs increasing photocatalytic activity [43]. Based on the data mentioned above and the results obtained from XPS and Raman analyses, it is expected that the S1-F2 could perform better photocatalytic activity under visible light irradiation.

#### **4.2.2. Evaluation of Photocatalytic Activity**

Photocatalytic activities of the ETS-10, S1-31, S1-F2, and  $Ag^0$ -S1-F3 thin films were tested under the following conditions for MB; (i) in the dark (Section 4.2.2.1), (ii) under UV light irradiation ( $\lambda=365$  nm) (Section 4.2.2.2), (iii) under visible light irradiation ( $\lambda>400$  nm) (Section 4.2.2.3).

#### 4.2.2.1. Dark Experiments

Before irradiation of the thin films with UV and visible light, dark experiments were carried out to know the degree of photodegradation upon adsorption of MB over the all photocatalyst thin films (ETS-10, S1-F2, Ag<sup>0</sup>-S1-F2, and S1-F3) under non-irradiation condition. It is clear that MB was adsorbed by ETS-10 (54.55 %), S1-F2 (59.54 %), Ag<sup>0</sup>-S1-F2 (55.94 %), and S1-F3 (56.73 %) after a 60 min period (Figure 4.15) with the highest adsorption occurring for S1-F2 thin film.

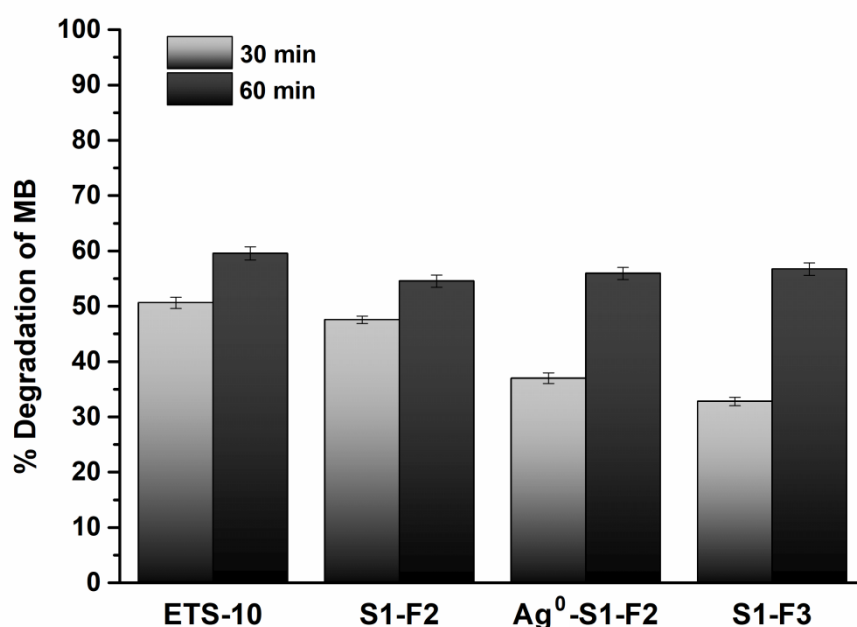


Figure 4.15. The adsorption of MB of the ETS-10, S1-F2, Ag<sup>0</sup>-S1-F2, and S1-F3 thin films in dark ([M] = 3.2 mg L<sup>-1</sup>, pH 6, V<sub>MB</sub> = 4 mL)

Photocatalytic reactions occur even in the dark when semiconducting TiO<sub>2</sub> is used as a photocatalyst. However, the effect of the photocatalyst requires longer periods of time [125]. In our case, the porous structure of the photocatalyst besides its semiconducting property allows absorption over 50 %. Nevertheless, there was no significant difference between % photocatalytic degradation of MB when samples



were used as a photocatalyst in the dark environment, which might be due to the highly porous structure of all samples [25]. More active sites for the adsorption of water and hydroxyl groups are formed due to the porous structure. These sites capture photogenerated holes resulting in the formation of hydroxyl radicals. The pores of the films are filled with the electrolyte solution and so diffusion length for photoexcited holes becomes shorter. These factors are crucial for photocatalytic activity [126].

#### **4.2.2.2. Under UV Irradiation**

For industrial applications, production of the photocatalysts which are effective under indoor conditions (i.e. under UV irradiation) is very important [127]. The contribution of electrons and holes to the photocurrent after they leave the electrode is much more possible under UV light irradiation as compared to visible light [125]. Figure 4.16 demonstrates the % photocatalytic degradation of MB when ETS-10, S1-F2, Ag<sup>0</sup>-S1-F2, and S1-F3 thin films were used as photocatalysts under the UV light irradiation ( $\lambda=365$  nm). No significant difference (67.14 % for ETS-10, 69.4 % for S1-F2, 70.57 % for Ag<sup>0</sup>-S1-F2, and 71.19 % for S1-F3 after 60 min illumination) between the percent removals of MB was observed among these films. However, the photocatalytic activity of titanosilicate ETS-10 film was slightly lower than that of vanadosilicate AM-6 film, which can be attributed to the relatively larger bandgap reported for ETS-10 (i.e.  $\sim 4.03$  eV for ETS-10 and  $\sim 3.8$  eV for AM-6) [54,98]. The photocatalytic activity is expected to be increased due to the factors such as more effective trapping of electrons and holes under UV light [127]. In our case, the photocatalytic performances of all samples are increased due to the factors mentioned above.

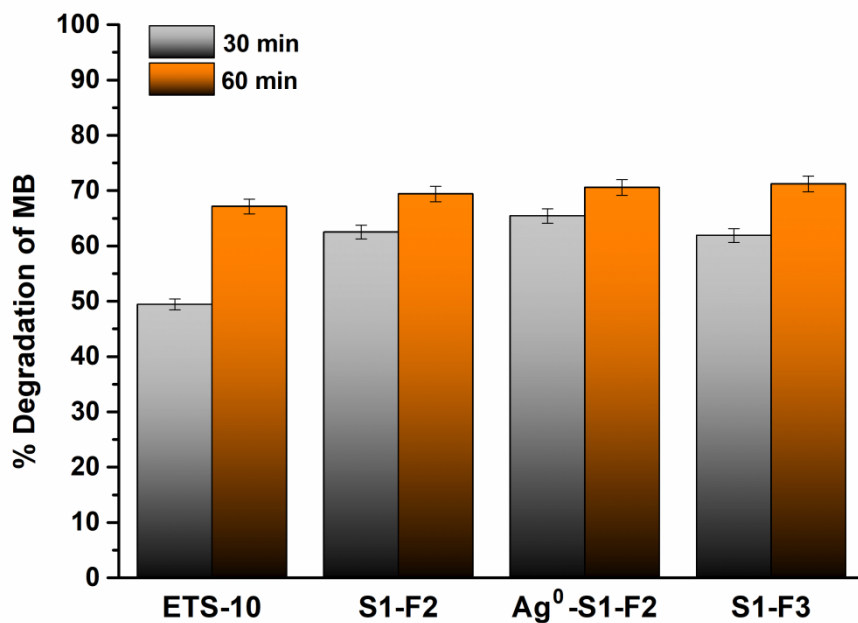


Figure 4.16. The photocatalytic removal of MB of the S1-F3, S1-F2, and Ag<sup>0</sup>-S1-F2 thin films under UV light irradiation ([MB] = 3.2 mg L<sup>-1</sup>, pH 6, V<sub>MB</sub> = 4 mL)

#### 4.2.2.3. Under Visible Light Irradiation

Figure 4.17 shows that vanadosilicate AM-6 thin films demonstrate higher photocatalytic activity under visible irradiation ( $\lambda > 400$  nm) with respect to the ETS-10 thin film. 65.53 % removal of MB was observed after 30 min visible light illumination when S1-F2 film was used as a photocatalyst. The percent removal of MB was 33.21 for S1-F3 film after 30 min illumination which is ~30% lower with respect to S1-F2. After 60 min illumination, the percent removal of MB was 44.92, 67.85, 68.74, and 58.12 for ETS-10, S1-F2, Ag<sup>0</sup>-S1-F2, and S1-F3 respectively.

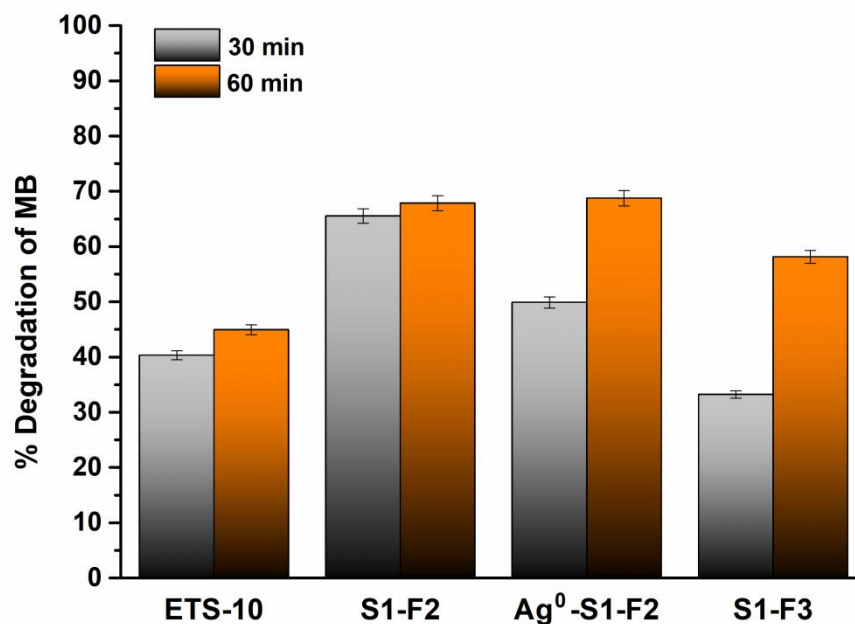


Figure 4.17. The photocatalytic removal of MB of the samples ETS-10, S1-F3, S1-F2, and Ag<sup>0</sup>-S1-F2 thin films under visible light irradiation ([MB]=3.2 mg L<sup>-1</sup>, pH 6, V<sub>MB</sub>= 4 mL).

These results suggest that AM-6 thin films are sensitive to visible light for photocatalytic decomposition of MB along with the performances obtained under UV irradiation. Another significant result was the increased photocatalytic activity of S1-F2 under visible light irradiation with respect to S1-F3 arising from different amounts of V<sup>5+</sup> cations in their structures due to their different synthesis conditions. It was shown that S1-F2 film possessed more V<sup>5+</sup> ions than S1-F3 film with reduced V<sup>4+</sup> ions. Thus, this photoactivity observed at visible light irradiation could be due to the higher V<sup>5+</sup> ions found in S1-F2 films, which is also in correlation with the literature data suggesting V<sup>5+</sup> ions to be responsible for the photocatalytic activity under visible light [16,68]. Accordingly, not only photocatalytic activity was obtained upon using AM-6 films under visible light irradiation, but also it was shown that chemical modifications (i.e. different synthesis conditions) during the

synthesis of these films also helped visible light photocatalytic activity. To enhance the photocatalytic activity of S1-F2 thin film, Ag<sup>0</sup> nanoparticle incorporation into S1-F2 film was carried out (i.e., Ag<sup>0</sup>-S1-F2 thin film). A slight improvement was obtained after 60 min. irradiation for the percent removal of MB which was 67.85 for S1-F2 and 68.74 for Ag<sup>0</sup>-S1-F2. It was expected that Ag<sup>0</sup> nanoparticle incorporation provides an increase for the photocatalytic activity under visible light irradiation since Ag<sup>0</sup> nanoparticle incorporation extends the light absorption spectrum into the visible region, hinders the recombination of electron/hole pairs through the electron transfer to the Ag sites, and the enhanced surface electron excitation occurs by incorporation of Ag<sup>0</sup> nanoparticle due to surface plasmon resonance effect [25]. However, the slight improvement observed for Ag<sup>0</sup>-S1-F2 may be attributed to the deterioration of the ...V-O-V-O-V... chain structure resulting from the silver incorporation as indicated by Raman analysis with broad, and flattened V-O stretching vibration band.

#### **4.2.2.4. The Photocatalytic Reusability Efficiency of As-Prepared Materials**

The reusability tests of the thin films were investigated for the MB under UV light irradiation as shown in Figure 4.18.

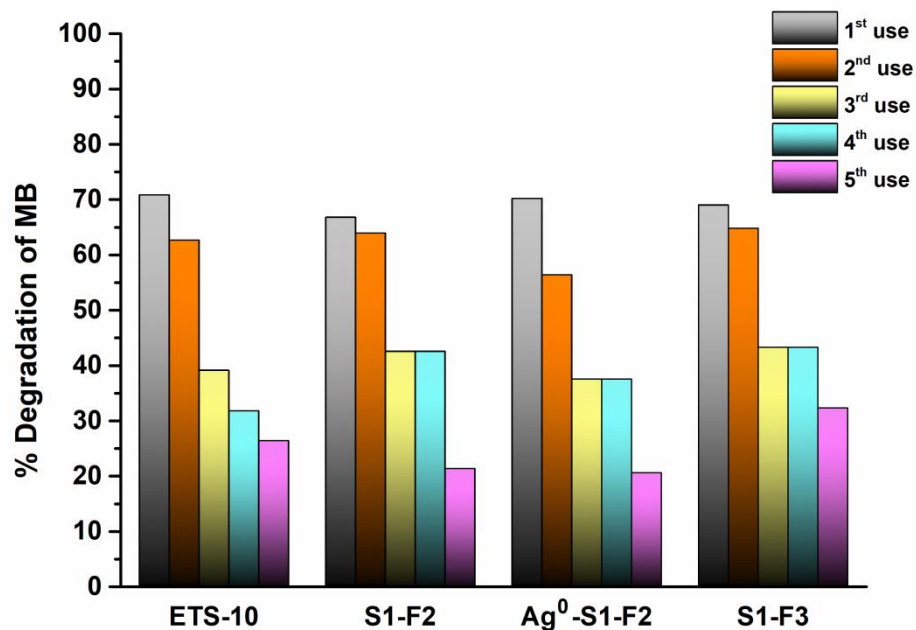


Figure 4.18. The photocatalytic removal of MB of the ETS-10, S1-F2, Ag<sup>0</sup>-S1-F2 and S1-F3 thin films after 5-time usage under UV light irradiation ( $[MB] = 3.2 \text{ mg L}^{-1}$ , pH 6,  $V_{MB} = 4 \text{ mL}$ )

After the first 60 minutes treatment, the thin films were simply washed with water and reused in a new treatment at the same pollutant concentration. The degradation percentages obtained after 5 times usage for MB are shown in Figure 4.18. It was clear that there is a significant decrease in the photocatalytic activity of thin films after the third use. The decrease may be due to the accumulation of the dye molecules on the porous surface of the thin films [117].

### **4.3. Investigation of the Parameters Affecting Film Formation and Photocatalytic Performance of AM-6 Films**

#### **4.3.1. The Effect of Seed Crystal Morphology on the Formation and Photocatalytic Activity of AM-6 Films**

In this part of the study, the effect of seed morphology on the formation and photocatalytic activity of the films were investigated. In this regard, two types of seed crystals with different morphologies (i.e., bipyramidal and cubic shaped) were utilized as seed layer keeping the other conditions such as reaction time and temperature and the secondary growth gel formula constant during the secondary growth procedure. Following the hydrothermal treatment procedure, different than previous catalytic experiments, the obtained films were used as photocatalysts for the decomposition of MB under the solar simulator. The obtained films were denoted as S1-F3 (bipyramidal-shaped ETS-10 as seed) and S2-F3 (cubic-shaped ETS-10 as seed) (Section 3.2.2.).

##### **4.3.1.1. Sample Characterization**

The morphological and spatial differences and the thicknesses of S1-F3 and S2-F3 were demonstrated through FE-SEM analysis. While, Figures 4.19-a and 4.19-c shows top view images of S1-F3 and S2-F3, respectively; cross-sectional images of S1-F3 and S2-F3 were shown in Figures 4.19-b and 4.19-d, respectively.

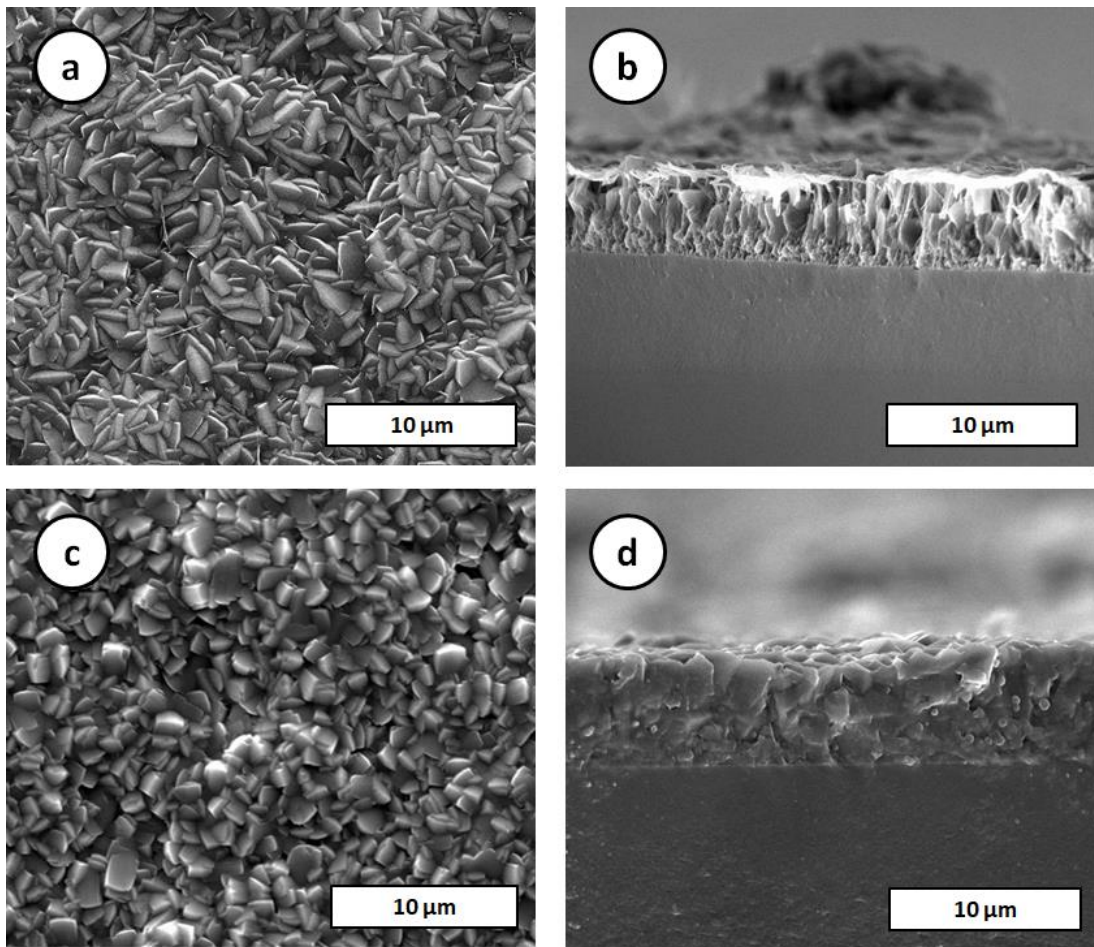


Figure 4.19. Top view and cross-sectional images of S1-F3 (a), (b) and S2-F3 (c), (d), respectively

FE-SEM images revealed that the crystals of S1-F3 have truncated bipyramidal structure (Figure 4.19-a), while the crystals of S2-F3 film (Figure 4.19-b) have bipyramidal structure. It is inevitable to attribute the morphological differences between S1-F3 and S2-F3 to different crystal growth rates originated from the different seed crystal morphologies used for the formation of the films. As a result, different seed crystal morphologies lead to two different AM-6 films with different morphologies, which are thought to affect the ...V-O-V-O-V... wires. The films with controlled morphologies, it can be demonstrated that photocatalytic activity is dependent upon a particular surface of the crystal [18]. To determine the

morphological differences of AM-6 film with seed crystals with different morphologies, further analyses were carried out.

XRD patterns were collected from the AM-6 films in order to determine the purity and the crystal orientation (Figure 4.20). The XRD peaks of AM-6 films are centered such that they are well-matched with XRD peaks identified for AM-6 [98].

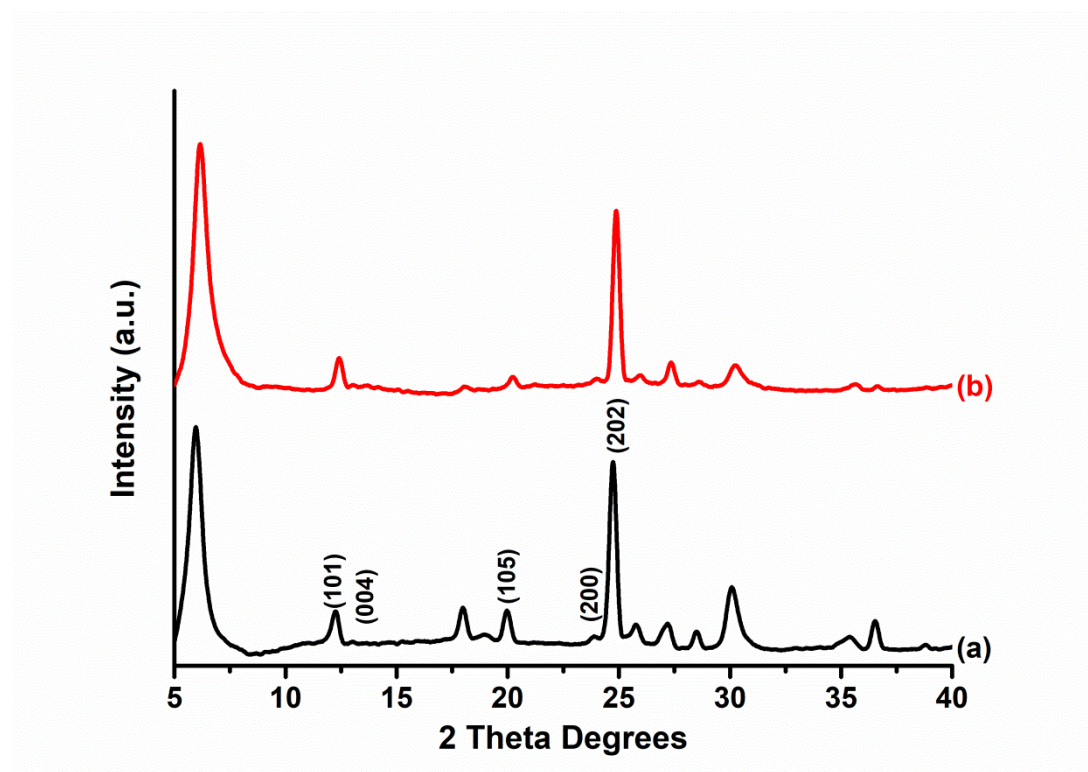


Figure 4.20. X-ray diffraction patterns of S1-F3 (a) and S2-F3 films (b)

The intensity of the peak incidental to (105) plane observed in the XRD pattern of S1-F3 is higher as compared to S2-F3 indicating the growth in S1-F3 is preferably in the  $c$  direction as shown in Figure 4.20. In order to examine the orientation of the crystals further, CPO values were calculated for each sample.

In order to calculate CPO values, integrated intensities of selected planes were identified for S1-F3 and S2-F3. Accordingly, the obtained results are shown in Table 4.4.



Table 4.4. Thickness and CPO values of S1-F3 and S2-F3 films

Sample	Thickness ( $\mu\text{m}$ )	CPO <sub>200/105</sub>
S1-F3	4.17 $\pm$ 0.08	0.39
S2-F3	5.95 $\pm$ 0.09	14.05

As can be seen from the Table 4.4, the CPO<sub>200/105</sub> value incidental to S2-F3 film is higher (i.e., 14.05) than that of S1-F3 (i.e., 0.39) indicating S2-F3 has a higher degree of *a(b)*-out-of-plane preferred crystal orientation. The CPO<sub>200/105</sub> values suggest that seed crystals grow much faster along with *a* and *b* directions for the samples S2-F3 with respect to S1-F3 films.

The films were further investigated by Raman spectroscopy and the results are shown in Figure 4.21.

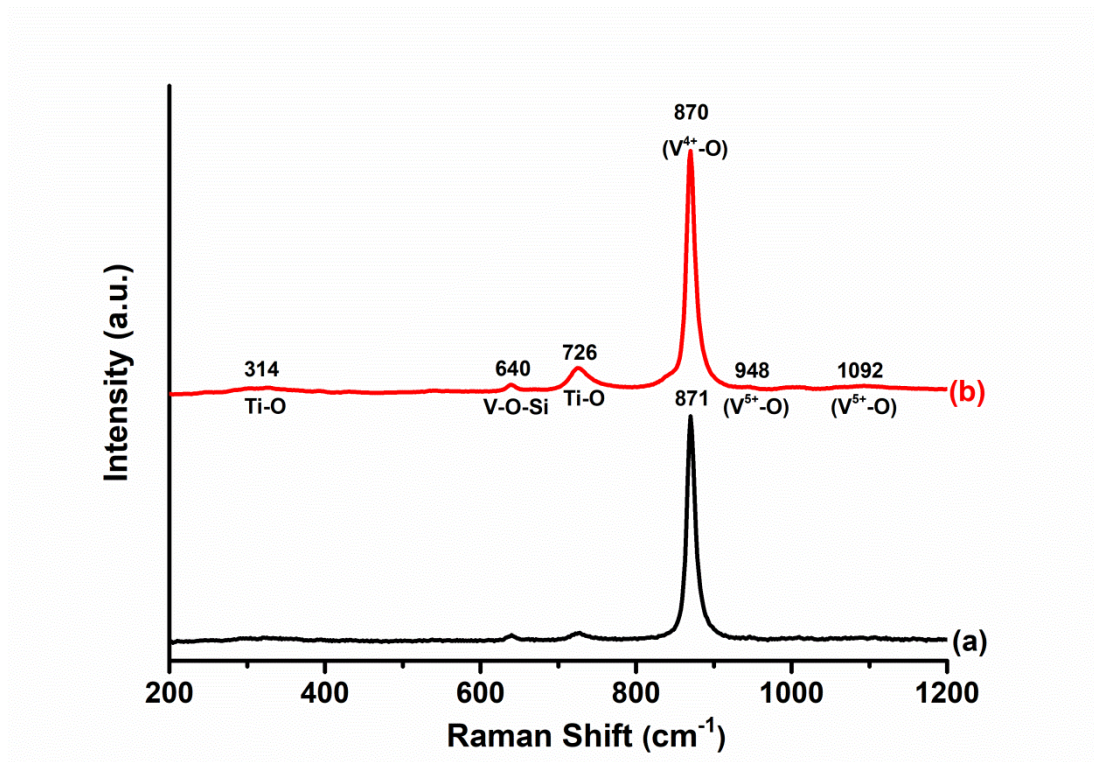


Figure 4.21. Raman spectroscopic analysis of the samples S1-F3 (a) and S2-F3 (b)

Raman shift centered at  $870\text{ cm}^{-1}$  indicates the undistorted  $\text{VO}_6$  octahedra and is associated with V-O stretching vibrations that involve octahedrally coordinated  $\text{V}^{4+}$  in AM-6 structure [49]. According to Figure 4.21, the characteristic V-O stretching vibration of S1-F3 and S2-F3 films was observed at  $871$  and  $870\text{ cm}^{-1}$ , respectively. The shoulder observed at  $950\text{ cm}^{-1}$  is the characteristic Raman shift of the  $\text{V}^{5+}$  oxidation state of  $\text{VO}_3^{-2}$  quantum wires in AM-6 crystals [50]. Due to its low intensity, the  $950\text{ cm}^{-1}$  peak was hard to compare between the two samples. Nevertheless, it was observed that Raman spectra of S1-F3 and S2-F3 films showed a slight shoulder at around  $\sim 948\text{ cm}^{-1}$  indicating that these two films had two oxidation states of vanadium in the structure (i.e.,  $\text{V}^{4+}$  and  $\text{V}^{5+}$ ). The shoulder observed at  $1092\text{ cm}^{-1}$  for the samples was attributed to the  $\text{V}^{5+}=\text{O}$  stretching mode of terminal oxygen atoms [112]. The other noticeable Raman shift observed at around  $314\text{ cm}^{-1}$  and  $723\text{ cm}^{-1}$  was associated with the Ti-O stretching vibration indicating the presence of ETS-10 in the AM-6 films (Figure 4.21) [48,49]. The peak centered at  $640\text{ cm}^{-1}$  is ascribed to the bridging vibration of V-O-Si [128].

The full-width half-maximum (FWHM) values were obtained for the main band of V-O stretching of  $870\text{ cm}^{-1}$  for each film and shown in Table 4.5.

Table 4.5. Raman shift and FWHM (full-width half-maximum) values belonging to V-O stretching of S1-F3 and S2-F3

Samples	Raman Shift ( $\text{cm}^{-1}$ )	
	V-O Stretching ( $\text{cm}^{-1}$ )	FWHM of V-O stretching
S1-F3	871	$12.27 \pm 0.07$
S2-F3	870	$12.66 \pm 0.07$

The narrow width of  $870\text{ cm}^{-1}$  vibration band in Raman spectra indicates the length homogeneity and the quality of the quantum wires in AM-6 crystals [111]. A deterioration in the  $\text{VO}_6$  chains originated from the use of seed crystals with different morphologies for the formation of AM-6 could be noticed by broadening of FWHM at around  $870\text{ cm}^{-1}$  vibration band, and has a tendency for enhanced

photocatalytic activity of S2-F3 film. The broadening of S2-F3 (i.e.,  $12.66 \pm 0.07$ ) was higher than S1-F3. It can be concluded that S2-F3 might be a better candidate for photocatalytic applications under visible light irradiation.

In order to attain more detailed information on the films and their optical properties along with the defects created, UV-Vis absorption spectroscopy was employed. The UV-vis absorption spectra of the samples demonstrate a strong absorption band in the UV region as shown in Figure 4.22.

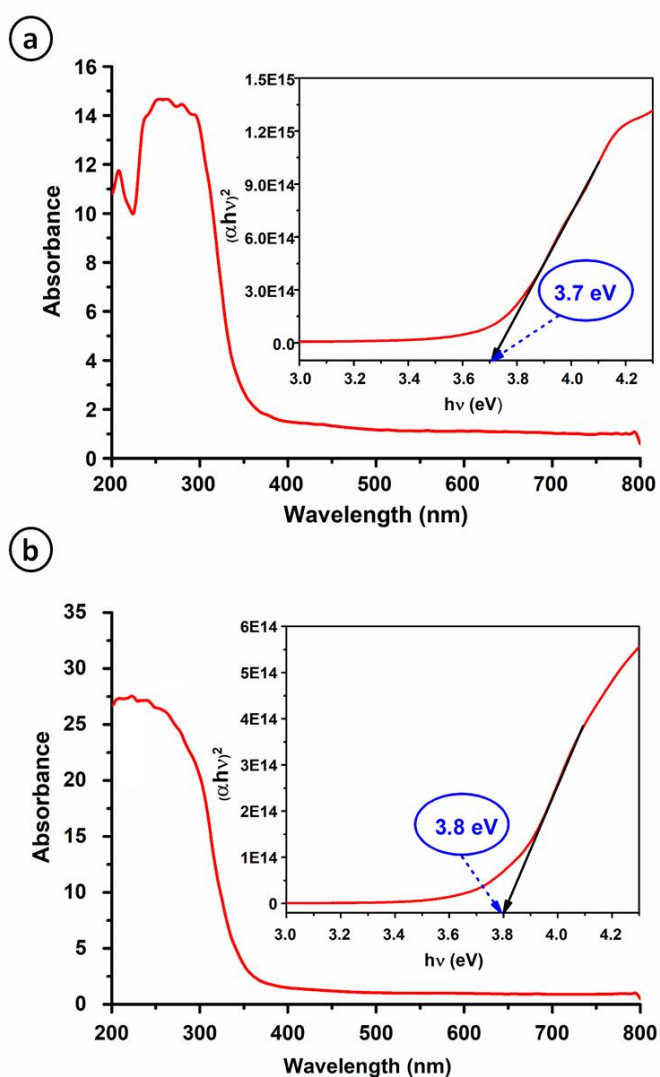


Figure 4.22. UV-Vis absorption spectra and Tauc plot for bandgap calculations for the samples (a) S1-F3 and (b) S2-F3

It was seen that, the absorption maxima ( $\lambda_{\max}$ ) in the UV region are 210 nm and 287 nm for S1-F3 and S2-F3, respectively. The redshift observed in the UV-vis absorption spectroscopy of the sample S2-F3 could be attributed to the defect formation induced by using seed crystal with different morphologies [99]. These bands are similar to the UV-vis absorption spectrum observed in between 200-350 nm for powder AM-6 formation stated by Ismail et al. and assigned to  $O(2p) \rightarrow V(3d)$  charge-transfer transition [25]. While, the absorption peak centered at around 450 nm indicates charge-transfer transition in  $V^{5+}$ , d-d transition in  $V^{4+}$  is indicated by the absorption band centered at around 590 nm [25,41]. However, these two absorption peaks are not distinctive for our samples. Therefore, further analysis should be carried out to elucidate the different oxidation states of vanadium.

The bandgap energies of the samples were calculated according to the procedure applied by López et al. [105]. As seen in Figure 4.22, S1-F3 and S2-F3 were found to have bandgap energy of 3.80 and 3.65 eV, respectively. Absorption edge of the UV-vis spectra was also obtained as 319.81 nm and 344.22 nm for the samples S1-F3 and S2-F3, respectively for the calculation of energy bandgap as shown in Figure 4.22. Accordingly, energy bandgap values were obtained as 3.87 eV and 3.60 eV for S1-F3 and S2-F3, respectively. The results obtained in the current study are similar to the ones obtained by Ismail et al. and Nash et al. [25,43]. The observed lower bandgap of S2-F3 suggest that photons with lower energy excite electrons from the valence band to conduction band and create electron-hole pairs increasing photocatalytic activity [43]. Based on the data mentioned above, S2-F3 is expected to perform better photocatalytic activity under visible light irradiation.

Another analysis method for the existence of different oxidation states of vanadium cation is through XPS analysis technique due to the dependence of binding energy (BE) of the  $Vp_{3/2}$  core level to the oxidation state of V [119]. Different states of  $V^{5+}$  and  $V^{4+}$  are typically obtained by deconvolution of  $V2p_{3/2}$  level into two peaks [120,121]. The XPS analysis results in the current study are shown in Figure 4.23. In Figure 4.11, while the dotted lines represent the original XPS data, the straight lines

represent the fitted data. XPS signals were fitted using mixed Gaussian-Lorentzian functions using Peak Fit v4.12 as deconvolution software.

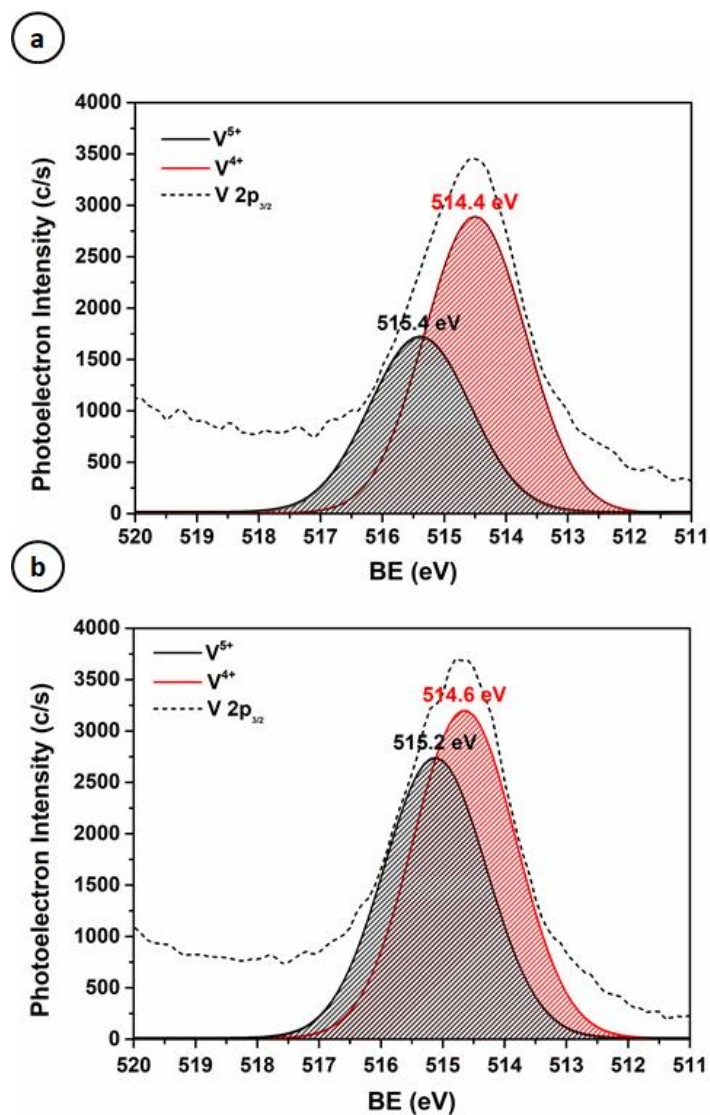


Figure 4.23. XPS high resolution V 2p spectra of S1-F3 and S2-F3, (a) deconvolution of  $V2p_{3/2}$  XPS peak of S1-F3 ( $V^{4+}/V^{5+}=1.68$ ), and (b) deconvolution of  $V\ 2p_{3/2}$  XPS peak of S2-F3 ( $V^{4+}/V^{5+}=1.17$ )

Accordingly, the XPS spectra of S1-F3 and S2-F3 films for  $V2p_{3/2}$  was deconvoluted into two peaks. The peaks with binding energies of  $\sim 514.4$  eV and  $\sim 515.4$  eV for S1-F2 have been attributed to  $V^{5+}$  and  $V^{4+}$ , respectively. The peaks centered at 514.6 eV

and 515.2 eV for S2-F3 has been attributed to  $V^{5+}$  and  $V^{4+}$ , respectively [120]. These values are consistent with the binding energy values specified for  $V^{5+}$  and  $V^{4+}$  cations in the literature [99,119,122–124].

The absolute areas of the XPS peaks of  $V^{4+}$  and  $V^{5+}$  were calculated and the ratio of  $V^{4+}/V^{5+}$  was obtained. Accordingly, the ratio of  $V^{4+}/V^{5+}$  was calculated as 1.68 and 1.17 for the samples S1-F3 and S2-F3, respectively. Table 4.6 was created using these data obtained from the calculation of the area under each curve.

Table 4.6. XPS spectral parameters for V 2p<sub>3/2</sub> for S1-F3 and S2-F3: Binding energy (eV), and the ratio of  $V^{4+}/V^{5+}$

Sample	V2p <sub>3/2</sub>		$V^{4+}/V^{5+}$
	$V^{4+}$ BE (eV)	$V^{5+}$ BE(eV)	
S1-F3	514.4	515.4	1.68
S2-F3	514.6	515.2	1.17

The calculated percentage of different oxidation states of vanadium (i.e.,  $V^{4+}$  and  $V^{5+}$ ) based on XPS results demonstrated in Table 4.6 indicates that the quantity of  $V^{5+}$  cations is greater in S2-F3 than S1-F3.

These results suggest that, in addition to the observed morphological differences between S1-F3 and S2-F3, vanadium exists in two different oxidation states ( $V^{4+}$  and  $V^{5+}$ ) in the structure of these two films upon the changes induced with the utilization of seed crystals with different morphologies. Based on the fact that a lower ratio of  $V^{4+}/V^{5+}$  was obtained for S2-F3, it is expected that S2-F3 is more sensitive to visible light when it is used as a photocatalyst under visible light irradiation due to the presumed dependence of visible light photocatalytic activity to the presence of  $V^{5+}$  cations [50].

### 4.3.1.2. Evaluation of the Photocatalytic Activity

The photocatalytic effectiveness of the proposed films (i.e., S1-F3 and S2-F3) was investigated for the decomposition of MB under solar light. Besides, dark experiments were also carried out to the degree of photodegradation upon adsorption of MB overall photocatalyst films under non-irradiation condition as shown in Figure 4.24.

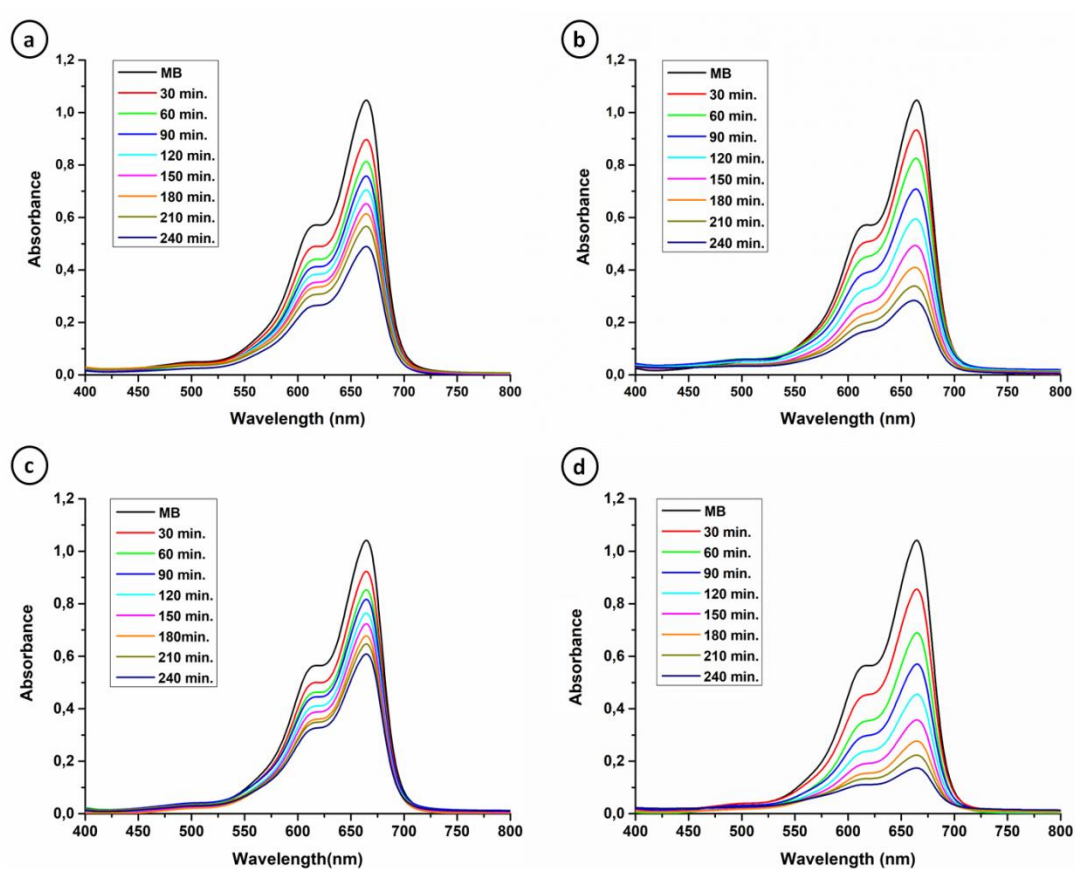


Figure 4.24. Absorbance of MB for S1-F3 in dark (a) and under illumination (b); S2-F3 in dark (c) and under illumination (d)

It is clear that MB was adsorbed by S1-F3 (50.49 %) and S2-F3 (41.53 %) after a 240 min period with the highest adsorption occurring for S1-F3 film which might be

due to the highly porous structure of the samples [25]. More active sites for the adsorption of water and hydroxyl groups are formed due to the porous structure. These sites capture photogenerated holes resulting in the formation of hydroxyl radicals. The pores of the films are filled with the electrolyte solution and so diffusion length for photoexcited holes becomes shorter. These factors are crucial for photocatalytic activity [126].

Figures 4.24 and 4.25-a indicate that S2-F3 demonstrates higher photocatalytic activity under the solar light with respect to S1-F3. 83.29 % removal of MB was observed after 240 min of solar light illumination when S2-F3 film was used as a photocatalyst. The percent removal of MB was 73.11 for S1-F3 film after 240 min illumination under solar light which is ~10% lower with respect to S2-F3. These results suggest that S2-F3 is more sensitive to solar light for photocatalytic decomposition with respect to S1-F3. Another significant result was the increased photocatalytic activity of S2-F3 under solar light irradiation in comparison with S1-F3 arising from different amounts of  $V^{5+}$  cations in their structures as predicted from various analysis techniques due to the seed crystals with different morphologies used for the formation of AM-6 films. It was shown that the S2-F3 film possessed more  $V^{5+}$  ions than S1-F3 film. Thus, this photoactivity observed at solar light irradiation could be due to the higher  $V^{5+}$  ions found in S2-F3 films, which is also in correlation with the literature data suggesting  $V^{5+}$  ions to be responsible for the photocatalytic activity under visible light [16,68]. Accordingly, not only photocatalytic activity was obtained upon using AM-6 films under solar light irradiation, but also it was shown that modifications (i.e. utilization of seed crystals with different morphologies) during the synthesis of these films also helped solar light photocatalytic activity.



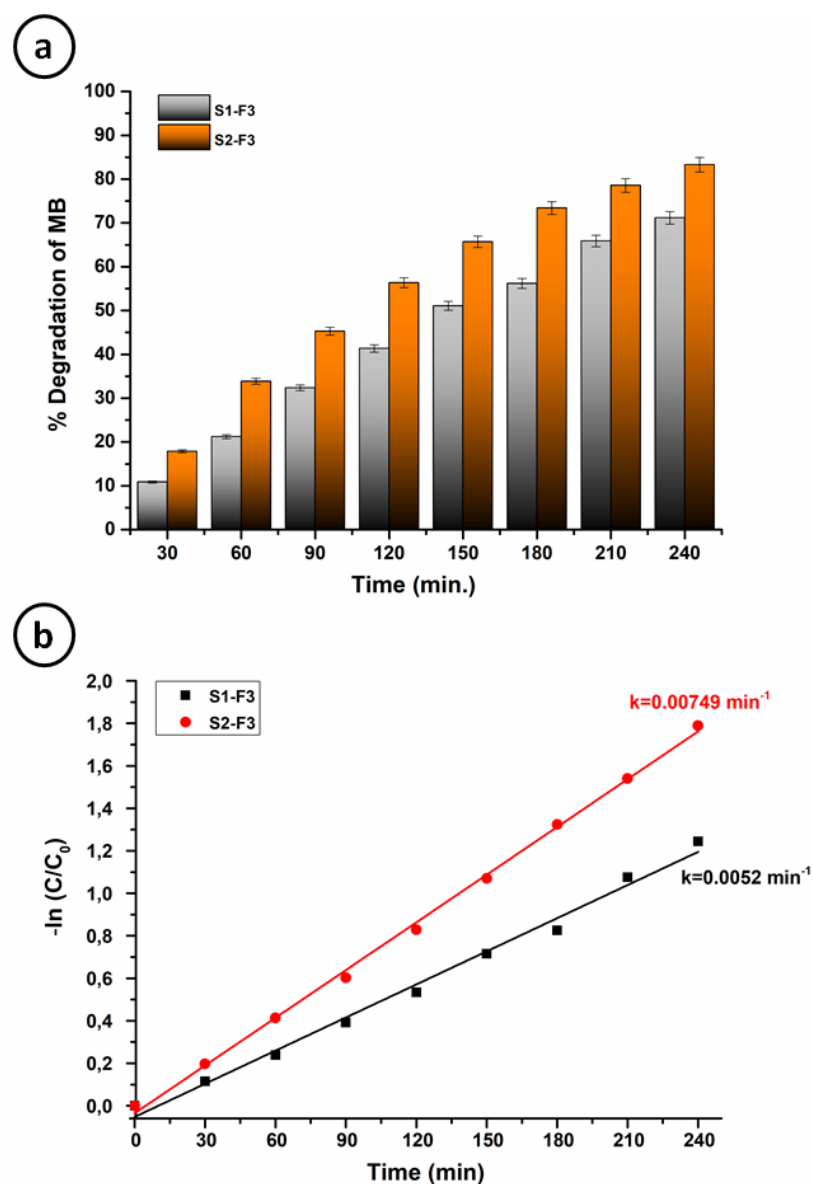


Figure 4.25. The photocatalytic removal (a), and the degradation kinetics (b) of MB for S1-F3 and S2-F3 films under solar simulator (1 Abs. MB, pH 6,  $V_{\text{MB}} = 10 \text{ mL}$ )

The pseudo-first-order reaction rate constants ( $k$ ) were calculated based on the photodegradation kinetics of S1-F3 and S2-F3 as shown in Figure 4.25-b. MB was also exposed to solar light for 240 minutes uninterruptedly to investigate its

photodegradation under solar light without using any photocatalyst (Figure 26-a and b).

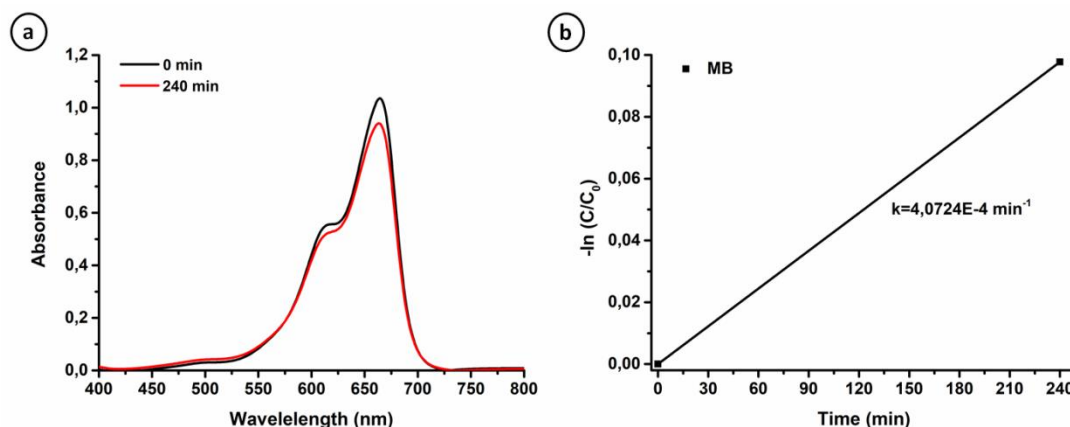


Figure 4.26. The photocatalytic removal (a), and the degradation kinetics (b) of MB without using any photocatalysts under solar light (1 Abs. MB, pH 6,  $V_{MB}= 10 \text{ mL}$ )

It was observed that only 9.3 % of MB was degraded after 240 min exposure to solar light. The  $k$  values calculated for S1-F3 ( $0.0052 \text{ min}^{-1}$ ) and S2-F3 ( $0.00749 \text{ min}^{-1}$ ) are much higher with respect to the  $k$  value ( $4.0724E-4 \text{ min}^{-1}$ ) calculated for the decomposition of MB without using any photocatalysts (See Appendix B and C). Accordingly, S1-F3 and S2-F3 show photocatalytic activity for the decomposition of MB under the solar light. Furthermore, the photocatalytic activity of S2-F3 was found to be higher with respect to S1-F3 as also predicted from various analysis techniques.

#### 4.3.2. The Effect of Seed Layer Coating Technique on the Formation and Photocatalytic Activity of AM-6 Films

The effect of seed layer coating technique on the formation and photocatalytic activity of the films was investigated. In this regard, bipyramidal seed crystals were coated on ITO coated glass substrates by using spin-coating and/or dip-coating method. In order to investigate the effect of the thickness of the seed layer on film

formation, the dip-coating method was applied 1-time and 2-times on substrates. The other parameters such as reaction time and temperature and secondary growth gel formula were kept constant. Following the hydrothermal treatment procedure, the obtained films were used as photocatalysts for the decomposition of MB under the solar simulator. The samples were denoted as S1-F3, S1-dip1-F3, and S1-dip2-F3 upon seed layer coating techniques which are spin-coating, 1-time dip-coating, and 2-times dip-coating, respectively.

#### **4.3.2.1. Sample Characterization**

The morphological and spatial differences and the thicknesses of S1-F3, S1-dip1-F3, and S1-dip2-F3 were shown in Figure 4.27. While, Figures 4.27-a, c, and e demonstrate the top view FE-SEM images of S1-F3, S1-dip1-F3, and S1-dip2-F3, respectively; cross-sectional images of S1-F3, S1-dip1-F3, and S1-dip2-F3 were demonstrated in Figure 4.27-b, d, and f, respectively.

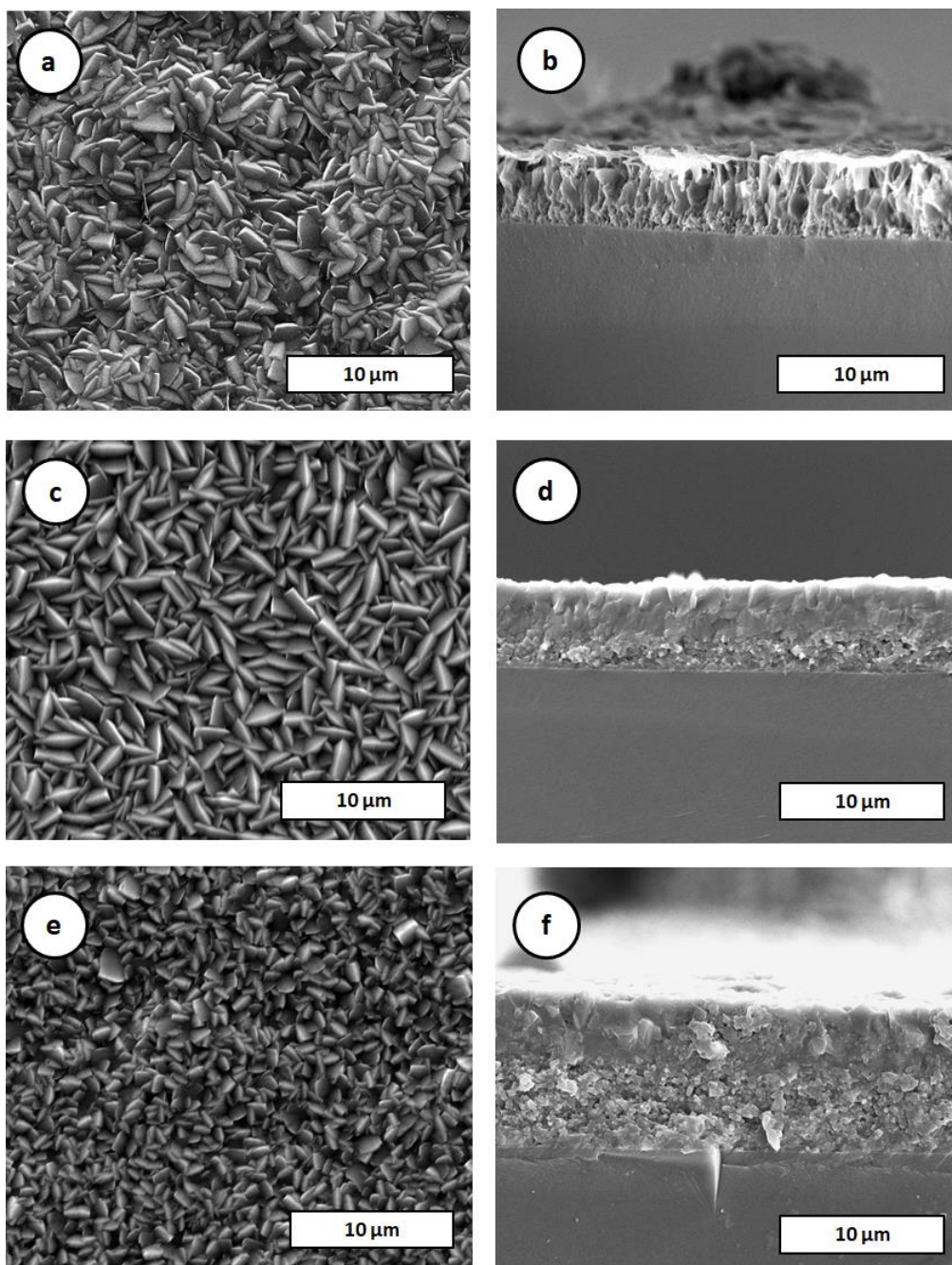


Figure 4.27. Top view and cross-sectional images of S1-F3 (a), (b); S1-dip1-F3 (c), (d); S1-dip2-F3 (e), (f), respectively

It was observed that the crystals of S1-F3, S1-dip1-F3, and S1-dip2-F3 have truncated bipyramidal structures as shown in Figure 4.27-a, c, and e. As seen from

Figure 4.27, crystals of S1-dip2-F3 are smaller than S1-dip1-F3 due to the close proximity of the seed crystals originated from the number of coating techniques [129]. The presence of the seed crystals very close to each other causes grains to strike and alter their orientations. When seed population increases, overlapping growth of grains are observed and size and orientation of the final crystal is altered [129].

Purity and the crystal orientation of AM-6 films were determined by the XRD analysis technique as shown in Figure 4.28. The XRD pattern of AM-6 films well matched with the XRD pattern stated for AM-6 formation [98].

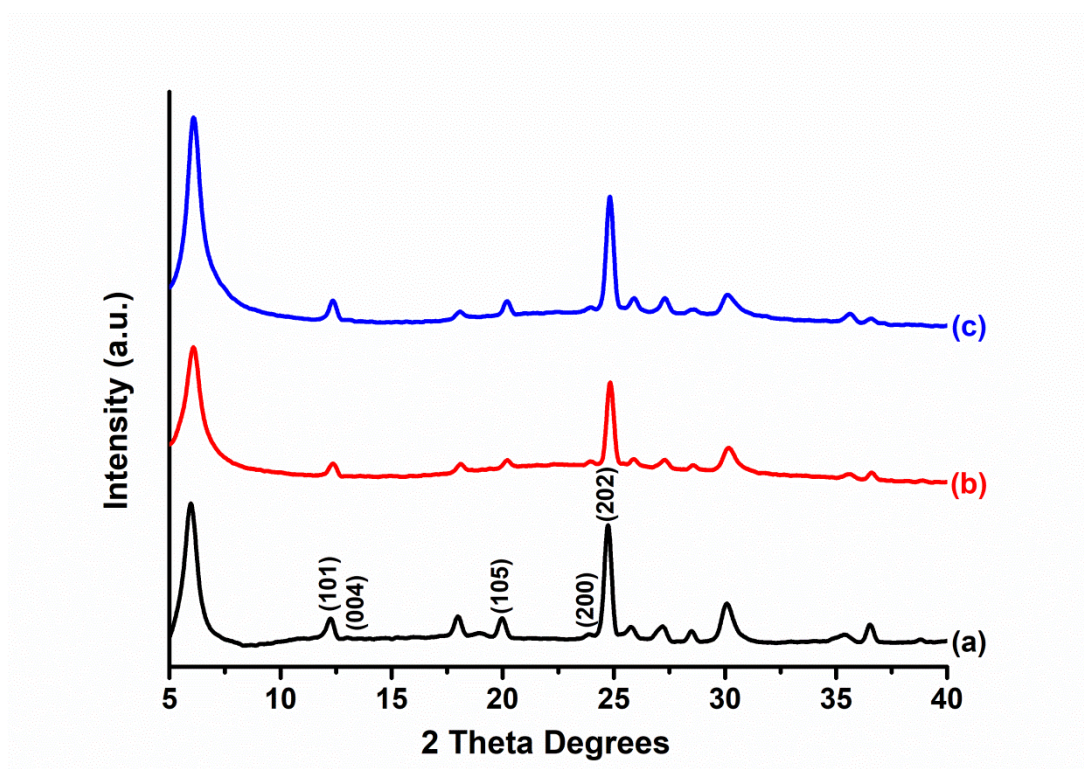


Figure 4.28. X-ray diffraction pattern of the samples S1-F3 (a), S1-dip1-F3 (b), and S1-dip2-F3 (c)

As seen from the XRD data, there is neither noticeable change in the peak positions nor a peak broadening with respect to AM-6 crystals obtained in powder form as shown in Figure 4.2. The results showed that films are crystalline and have no other

typical impurity phases resulting from the preparation of AM-6 films. The  $2\theta$  degree of  $\approx 20^\circ$  (i.e., (105) plane) was observable for AM-6 films produced by using seed crystals coated with spin-coating and dip-coating method indicating the tendency of crystals to grow in c direction (Figure 4.28).

In order to calculate CPO values, integrated intensities of (105) and (200) planes were identified for S1-F3, S1-dip1-F3, and S1-dip2-F3 and the results were shown in Table 4.7.

Table 4.7. Thickness and CPO values of S1-F3, S1-dip1-F3, and S1-dip2-F3 films

Sample	Thickness ( $\mu\text{m}$ )	$CPO_{200/105}$
S1-F3	$4.17 \pm 0.08$	0.39
S1-dip1-F3	$10.93 \pm 0.08$	3.15
S1-dip2-F3	$15.28 \pm 0.09$	3.17

As can be seen from Table 4.7, the  $CPO_{200/105}$  values of S1-dip1-F3 and S1-dip2-F3 are very close to each other indicating these samples have similar degrees of  $a(b)$ -out-of-plane preferred orientations. According to the CPO values of the samples S1-F3 (i.e., 0.39), S1-dip1-F3 (i.e., 3.15), and S1-dip2-F3 (i.e., 3.17), it can be implied that the tendency of S1-F3 to grow in c direction is higher with respect to S1-dip1-F3 and S1-dip2-F3. However, CPO values obtained for S1-dip1-F3 and S1-dip2-F3 were not high enough to claim that these samples have  $a(b)$ -out-of-plane preferred orientation.

The investigation of S1-F3, S1-dip1-F3, and S1-dip2-F3 films was carried out by Raman spectroscopy as shown in Figure 4.29.

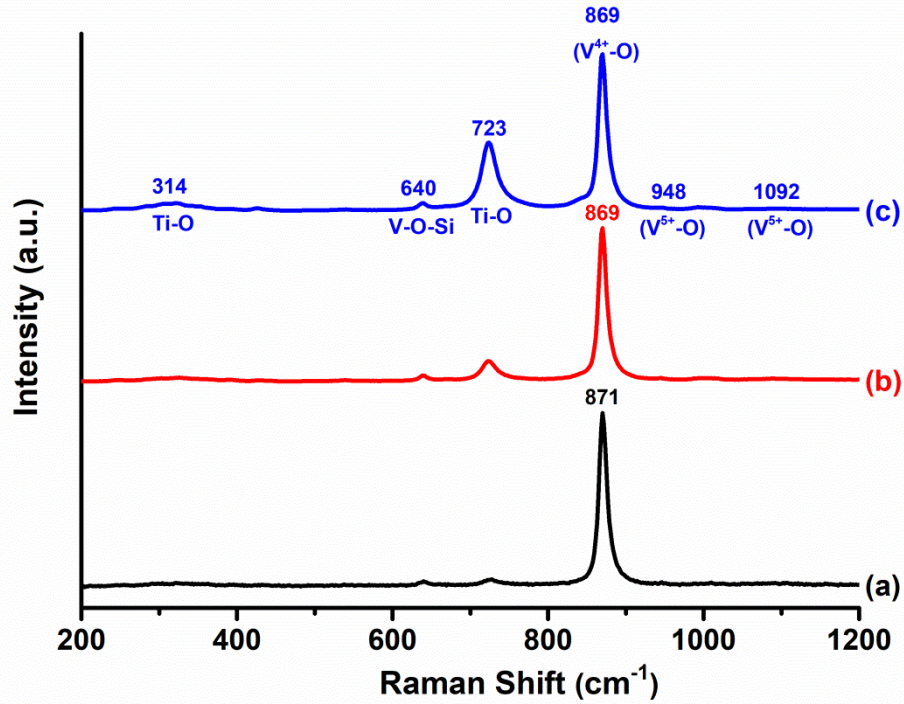


Figure 4.29. Raman spectroscopic analysis of the samples S1-F3 (a), S1-dip1-F3 (b), and S1-dip2-F3 (c)

According to Figure 4.29, the characteristic V-O stretching vibration of S1-F3, S1-dip1-F3, and S1-dip2-F3 films was observed at 871, 869, and 869  $\text{cm}^{-1}$ , respectively which are comparable with the Raman shift centered at 870  $\text{cm}^{-1}$  and stated by Rocha et al. [49].

The characteristic Raman shifts defined for the  $\text{V}^{5+}$  oxidation state of  $\text{VO}_3^{-2}$  quantum wires in AM-6 crystals and centered at 950  $\text{cm}^{-1}$  and 1092  $\text{cm}^{-1}$  are not comparable between the samples due to the low intensity of these peaks [50,112]. Ti-O stretching vibration showed the Raman shift at around 314  $\text{cm}^{-1}$  and 723  $\text{cm}^{-1}$  which indicates the presence of ETS-10 in the AM-6 films as shown in Figure 4.29 [48,49]. An intense Ti-O stretching vibration peak centered at 723  $\text{cm}^{-1}$  in the Raman spectra of S1-dip2-F3 indicates that the presence of ETS-10 crystals in the sample is the most apparent among other samples which is originated from the thick seed layer. The

bridging vibration of V-O-Si was determined by the Raman shift centered at  $640\text{ cm}^{-1}$  [128].

Broadening of FWHM at around  $870\text{ cm}^{-1}$  vibration band was calculated for the samples S1-F3, S1-dip1-F3, and S1-dip2-F3 in order to identify the length homogeneity and the quality of the quantum wires in AM-6 crystals originated from different seed layer coating techniques [111]. The obtained results were shown in Table 4.8.

Table 4.8. Raman shift and FWHM (full-width half-maximum) values belonging to V-O stretching of S1-F3, S1-dip1-F3, and S1-dip2-F3 films

Samples	V-O Stretching ( $\text{cm}^{-1}$ )	FWHM of V-O stretching
S1-F3	871	$12.27 \pm 0.07$
S1-dip1-F3	869	$12.54 \pm 0.05$
S1-dip2-F3	869	$12.66 \pm 0.04$

The maximum broadening was observed for the sample S1-dip2-F3 (i.e.,  $12.66 \pm 0.04$ ). FWHM value of S1-dip1-F3 (i.e.,  $12.54 \pm 0.05$ ) was higher than that of S1-F3 (i.e.,  $12.27 \pm 0.07$ ). It can be concluded that S1-dip2-F3 might be a better candidate for photocatalytic applications under visible light irradiation.

More detailed information on the films and their optical properties was obtained by UV-vis absorption spectroscopy. The UV-vis absorption spectra of the samples demonstrated a strong absorption band in the UV region as shown in Figure 4.30.



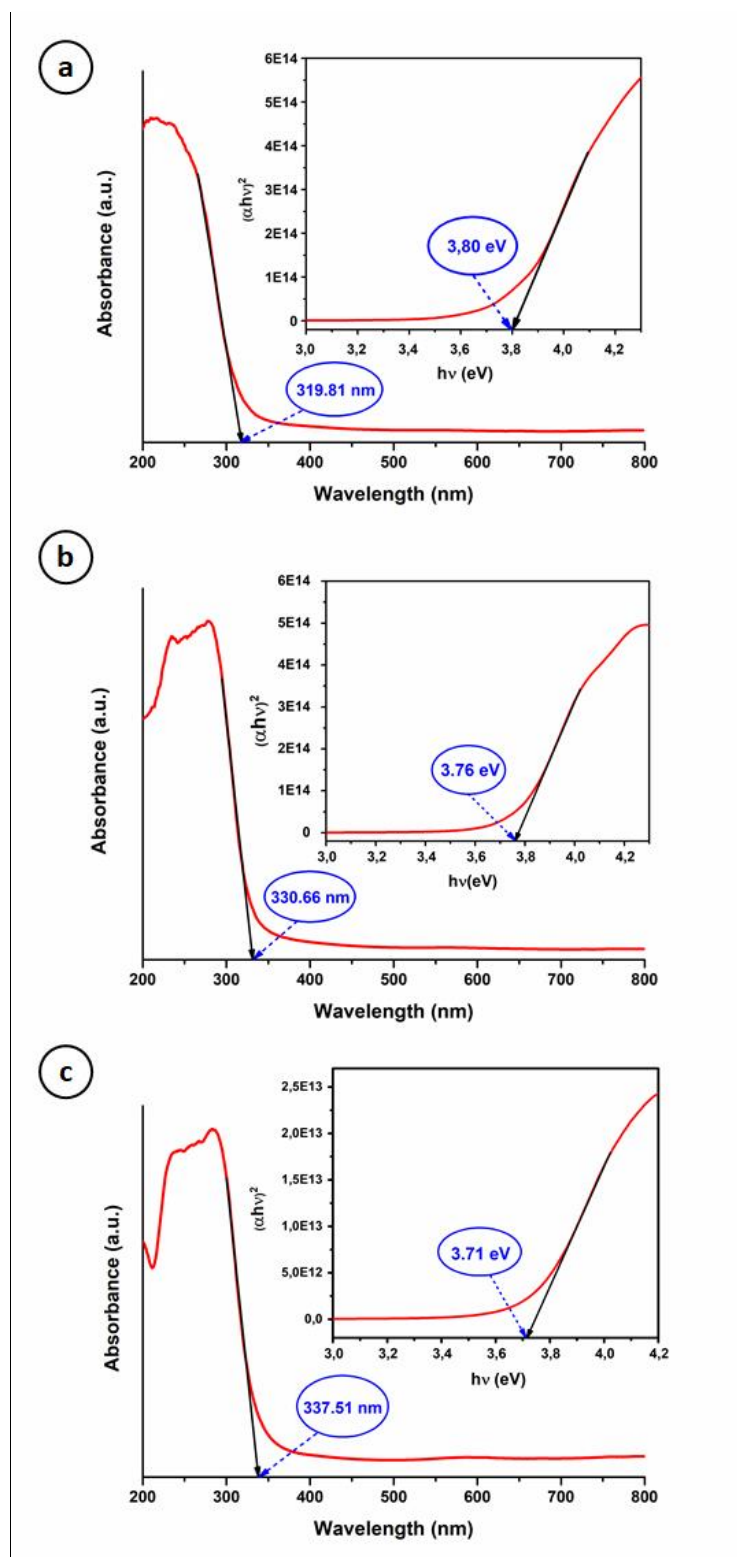


Figure 4.30. UV-Vis absorption spectra and Tauc plot for bandgap calculations for the samples (a) S1-F3, (b) S1-dip1-F3, and (c) S1-dip2-F3

S1-F3, S1-dip1-F3, and S1-dip2-F3 showed the absorption maxima ( $\lambda_{\max}$ ) at 210 nm, 288 nm and 289 nm, respectively. It was observed a redshift of  $\lambda_{\max}$  for the samples S1-dip1-F3 and S1-dip2-F3 with respect to S1-F3 which might be due to the defect formation originated from the utilization of different seed layer coating techniques [99]. These absorption maxima values are comparable with the UV-vis absorption bands centered in between 200-350 nm which are assigned to O(2p)  $\rightarrow$  V(3d) charge-transfer transition and identified for powder AM-6 crystals [25].

The bandgap energies were calculated as 3.80, 3.76 and 3.71 eV for the samples S1-F3, S1-dip1-F3, and S1-dip2-F3, respectively according to the procedure stated by López et al. [105]. The bandgap energies were also calculated using cut off wavelengths of absorption spectra which are found to be 319.81 nm, 330.66 nm, and 337.51 nm for S1-F3, S1-dip1-F3, and S1-dip2-F3, respectively as shown in Figure 4.30. Accordingly, the energy bandgap values were obtained as 3.87 eV, 3.75 eV, and 3.67 eV for S1-F3, S1-dip1-F3, and S1-dip2-F3, respectively. The calculated bandgap energies were found to be comparable with bandgap energies of AM-6 crystals imported by Ismail et al. and Nash et al. [25,43]. Photons with lower energy excite electrons from valence band to conduction band and electron-hole pairs are formed due to the observed lower bandgap of S1-dip2-F3 resulting an enhanced photocatalytic activity [43]. Based on the data mentioned above, S1-dip2-F3 is expected to perform better photocatalytic activity under visible light irradiation.

The chemical states of vanadium in the structures of S1-F3, S1-dip1-F3, and S1-dip2-F3 films were conducted by XPS analysis technique due to the dependence of binding energy (BE) of the Vp<sub>3/2</sub> core level to the oxidation state of V as shown in Figure 4.31 [119].

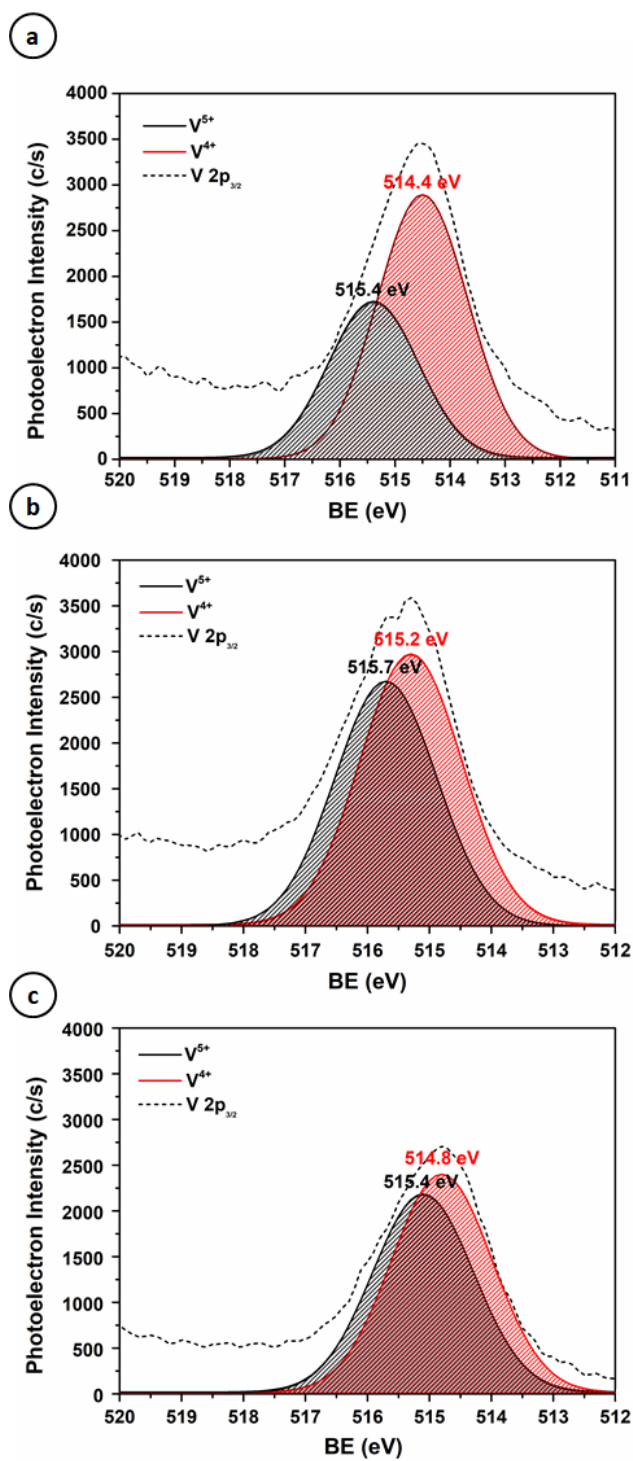


Figure 4.31. XPS high resolution V 2p spectra of S1-F3, S1-dip1-F3, and S1-dip2-F3 (a) deconvolution of V $2p_{3/2}$  XPS peak of S1-F3 ( $V^{4+}/V^{5+}=1.68$ ), (b) deconvolution of V $2p_{3/2}$  XPS peak of S1-dip1-F3 ( $V^{4+}/V^{5+}=1.108$ ) and (c) deconvolution of V $2p_{3/2}$  XPS peak of S1-dip2-F3 ( $V^{4+}/V^{5+}=1.101$ )

XPS spectra of S1-F3, S1-dip1-F3, and S1-dip2-F3 films for  $V2p_{3/2}$  were deconvoluted into two peaks. These peaks with binding energies of 514.4 eV and 515.4 eV for S1-F3 have been attributed to  $V^{5+}$  and  $V^{4+}$ , respectively. The peaks centered at 515.7 eV and 515.2 eV for S1-dip1-F3 has been attributed to  $V^{5+}$  and  $V^{4+}$ , respectively [120]. The peaks with binding energies of 515.4 eV and 514.8 eV for S1-dip2-F3 have been attributed to  $V^{5+}$  and  $V^{4+}$ , respectively. These values are comparable with the binding energy values identified for  $V^{5+}$  and  $V^{4+}$  cations in the literature [99,119,122–124].

The ratio of  $V^{4+}/V^{5+}$  was calculated for the samples S1-F3, S1-dip1-F3, and S1-dip2-F3 as 1.68, 1.108, and 1.101, respectively according to the calculated areas of XPS peaks of  $V^{4+}$  and  $V^{5+}$ . Surprisingly, close values of  $V^{4+}/V^{5+}$  were obtained for S1-dip1-F3 and S1-dip2-F3. The data obtained from the calculation of the area under each curve was shown in Table 4.9.

Table 4.9. XPS spectral parameters for  $V 2p_{3/2}$  for S1-F3, S1-dip1-F3, and S1-dip2-F3: Binding energy (eV), and the ratio of  $V^{4+}/V^{5+}$

Sample	$V2p_{3/2}$		$V^{4+}/V^{5+}$
	$V^{4+}$ BE (eV)	$V^{5+}$ BE(eV)	
S1-F3	514.4	515.4	1.68
S1-dip1-F3	515.2	515.7	1.108
S1-dip2-F3	514.8	515.4	1.101

According to Table 4.9, close values of the  $V^{4+}/V^{5+}$  ratio observed for the samples S1-dip1-F3 and S1-dip2-F3 indicate these samples contain more amounts of  $V^{5+}$  cations with respect to S1-F3. These results indicate that vanadium exists in two different oxidation states ( $V^{4+}$  and  $V^{5+}$ ) and the amount of these oxidation states is different for the samples originated from the different seed layer coating technique.

Based on the fact that the samples S1-dip1-F3 and S1-dip2-F3 have lower values of  $V^{4+}/V^{5+}$  ratio with respect to S1-F3, these samples are expected to be more sensitive to visible light due to the presumed dependence of visible light photocatalytic activity to the presence of  $V^{5+}$  cations [50].

#### **4.3.2.2. Evaluation of the Photocatalytic Activity**

In this part of the study, the samples S1-F3, S1-dip1-F3, and S1-dip2-F3 were used as photocatalysts for the photocatalytic decomposition of MB under the solar light. Dark experiment were also carried out to control the degree of photodegradation upon adsorption of MB overall photocatalyst films under non-irradiation condition as shown in Figure 4.32-a,c, and e.

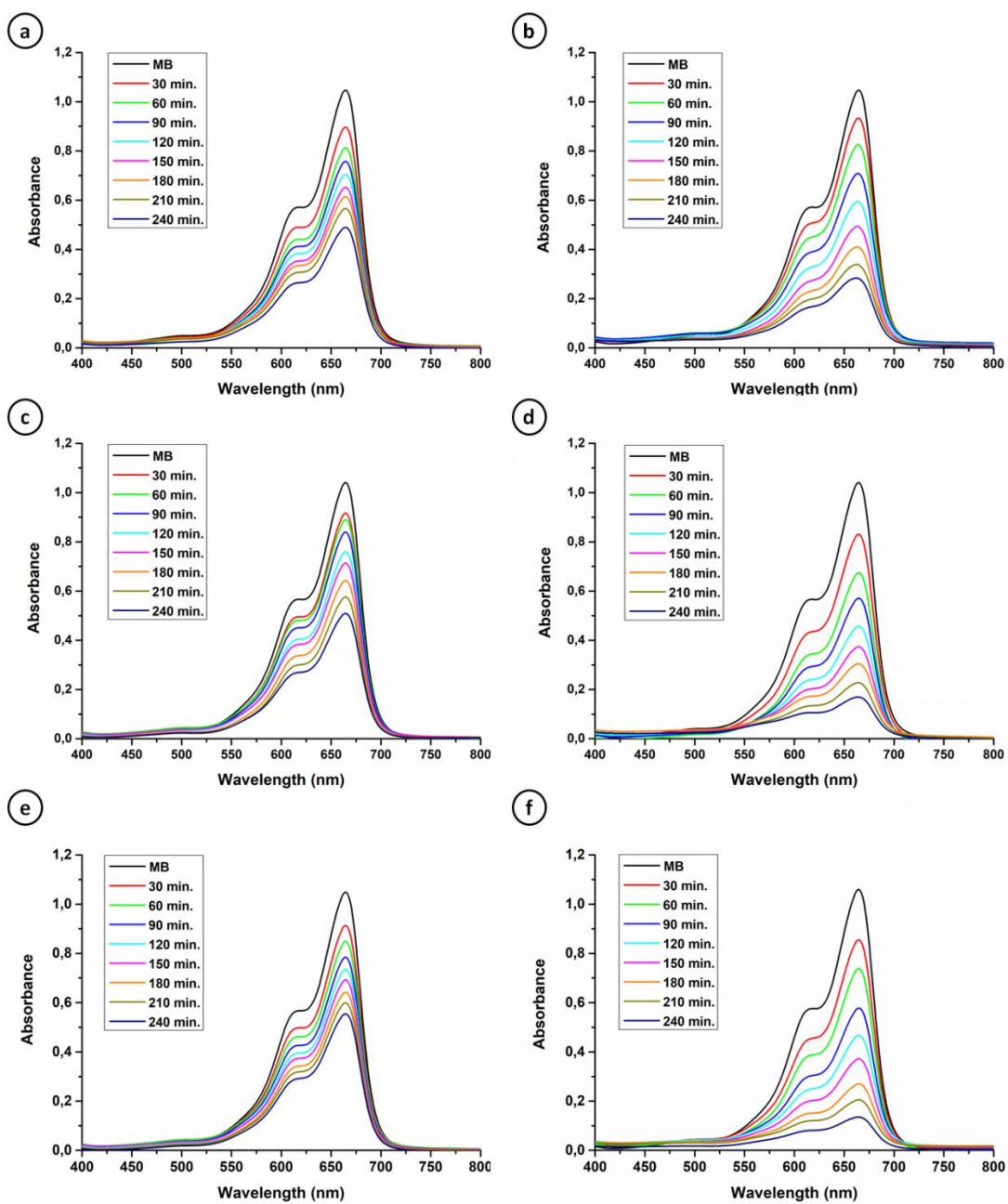


Figure 4.32. Absorbance of MB for S1-F3 in dark (a) and under illumination (b); S1-dip1-F3 in dark (c) and under illumination (d); S1-dip2-F3 in dark (e) and under illumination (f)

The adsorption of MB was 50.49 % for S1-F3, 51.16 % for S1-dip1-F3, and 47.19 % for S1-dip2-F3 after a 240 min period under non-irradiation condition with the highest adsorption occurring for S1-dip1-F3 film which might be due to the rough

surface of this film due to the fact that surface roughness increases the surface area increasing the adsorption of the pollutant to the surface of the photocatalyst [20]. The thickness of S1-dip2-F3 is higher with respect to other samples. Therefore, it is not surprising that S1-dip2-F3 has the highest adsorption of MB under non-irradiation condition.

According to Figures 4.32 and 4.33-a, S1-dip2-F3 demonstrates the highest photocatalytic activity under the solar light with respect to S1-F3 and S1-dip1-F3. 87.12 % removal of MB was observed after 240 min of solar light illumination when S1-dip2-F3 film was used as a photocatalyst. The percent removal of MB was 73.11 for S1-F3 film after 240 min illumination under solar light, which is ~14% lower with respect to S1-dip2-F3. MB decomposed 80.85 % when S1-dip1-F3 was used as photocatalyst which is ~7 % lower with respect to S1-dip2-F3. These results suggest that S1-dip2-F3 film shows the maximum sensitivity to the solar light for photocatalytic decomposition of MB with respect to S1-F3 and S1-dip1-F3. According to the values of  $V^{4+}/V^{5+}$  in Table 4.8, it is expected that S1-dip1-F3 and S1-dip2-F3 should have similar sensitivities to solar light. Interestingly, the enhanced photocatalytic activity of S1-dip2-F3 is induced by the thickness of the films and the adsorption of MB might play a crucial role in this reaction. Nevertheless, S1-dip1-F3 and S1-dip2-F3 showed significantly enhanced photocatalytic activity under the solar light irradiation in comparison with S1-F3. This might be due to the observed increased amount of  $V^{5+}$  cations in their structures as also predicted by different characterization techniques.

The photoactivity observed at solar light irradiation could be due to the higher  $V^{5+}$  ions found in S1-dip1-F3 and S1-dip2-F3 films, which is also in correlation with the literature data suggesting  $V^{5+}$  ions to be responsible for the photocatalytic activity under visible light [16,68]. However, the close proximity of the ratio  $V^{4+}/V^{5+}$  cations observed for the samples S1-dip1-F3 and S1-dip2-F3 suggest that, a more enhanced photocatalytic activity observed for the S1-dip2-F3 might be induced by the

adsorption of MB originated from the thickness of this film instead of the higher amount of  $V^{5+}$  cations.

The pseudo-first-order reaction rate constants ( $k$ ) were calculated based on the photodegradation kinetics as shown in Figure 4.33-b.

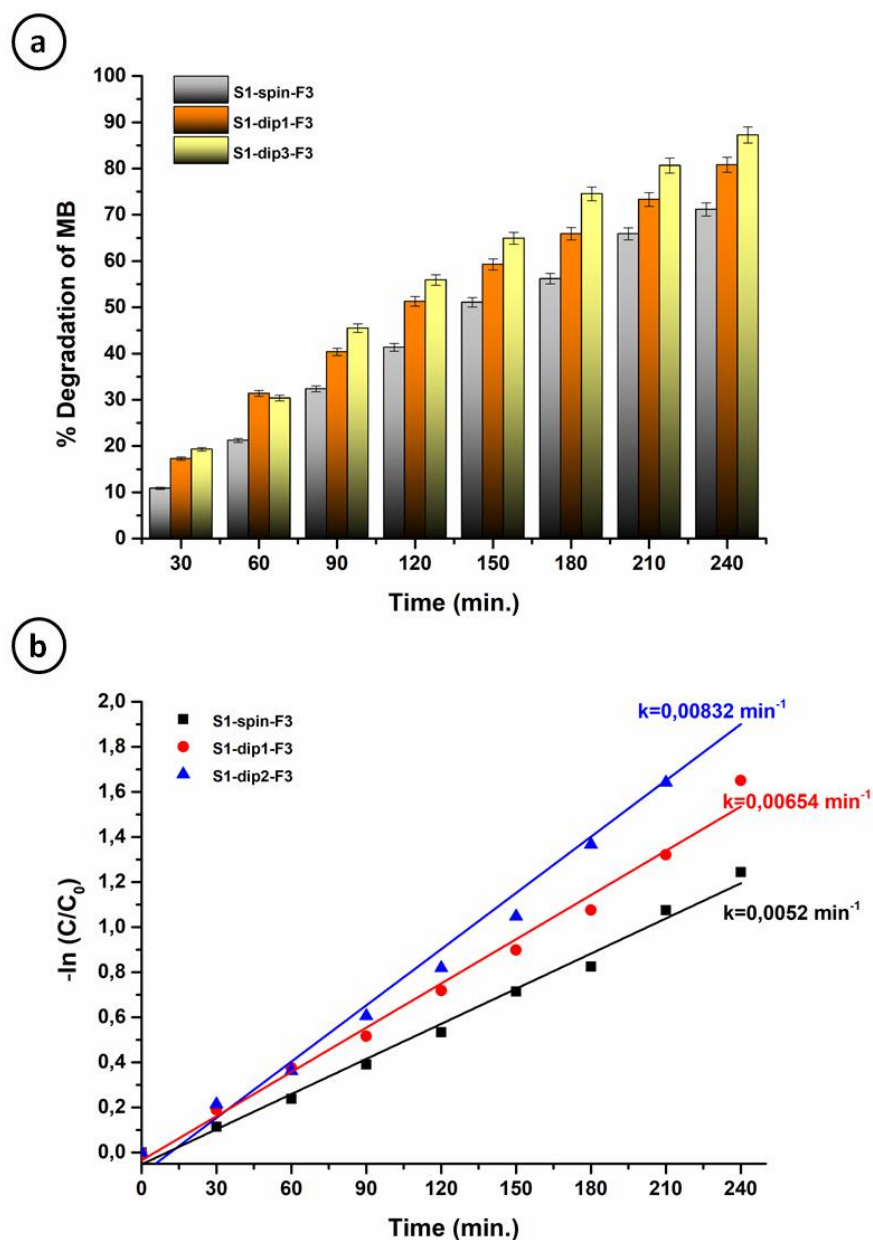


Figure 4.33. The photocatalytic removal (a), and the degradation kinetics (b) of MB for S1-F3, S1-dip1-F3, and S1-dip2-F3 films under solar simulator (1 Abs. MB, pH 6,  $V_{MB}$  = 10 mL)



The k values calculated for S1-F3 ( $0.0052 \text{ min}^{-1}$ ), S1-dip1-F3 ( $0.00654 \text{ min}^{-1}$ ), and S1-dip2-F3 ( $0.00832 \text{ min}^{-1}$ ) are higher with respect to the k value ( $4.0724\text{E-}4 \text{ min}^{-1}$ ) calculated for the decomposition of MB without using any photocatalyst under same conditions (Figure 4.26). Accordingly, the samples S1-F3, S1-dip1-F3, and S1-dip2-F3 show photocatalytic activity for the decomposition of MB under the solar light. Besides, S1-dip1-F3 and S1-dip2-F3 demonstrate more enhanced photocatalytic activities with respect to S1-F3 as predicted from various analysis techniques.

#### **4.3.3. The Effect of Molar Water Content of the Secondary Growth Gel on the Formation and Photocatalytic Activity of AM-6 Films**

In this section, the effect of water content in the secondary growth gel on film formation and photocatalytic activity of the films by decreasing the molar water amount from 415 to 300, and by increasing it from 415 to 600. Further increase of the molar water amount was also carried out by increasing it from 415 to 700. The other parameters such as seed crystal morphology, reaction time and temperature were kept constant in the secondary growth procedure. Following the hydrothermal treatment procedure, the obtained films were used as photocatalysts for the decomposition of MB under the solar simulator. The obtained films were denoted as S1-F3, S1-F3-W1, S1-F3-W2, and S1-F3-W3 upon the molar water amount as 415, 300, 600, and 700, respectively.

##### **4.3.3.1. Sample Characterization**

The morphological and spatial differences and the thicknesses of S1-F3 and S2-F3 were shown in Figure 4.34. While, Figures 4.34-a, c, e, and g demonstrated the top view FE-SEM images of S1-F3, S1-F3-W1, S1-F3-W2, and S1-F3-W3, respectively; cross-sectional images of S1-F3, S1-F3-W1, S1-F3-W2, and S1-F3-W3 were shown in Figures 4.34-b, d, f, and h, respectively.

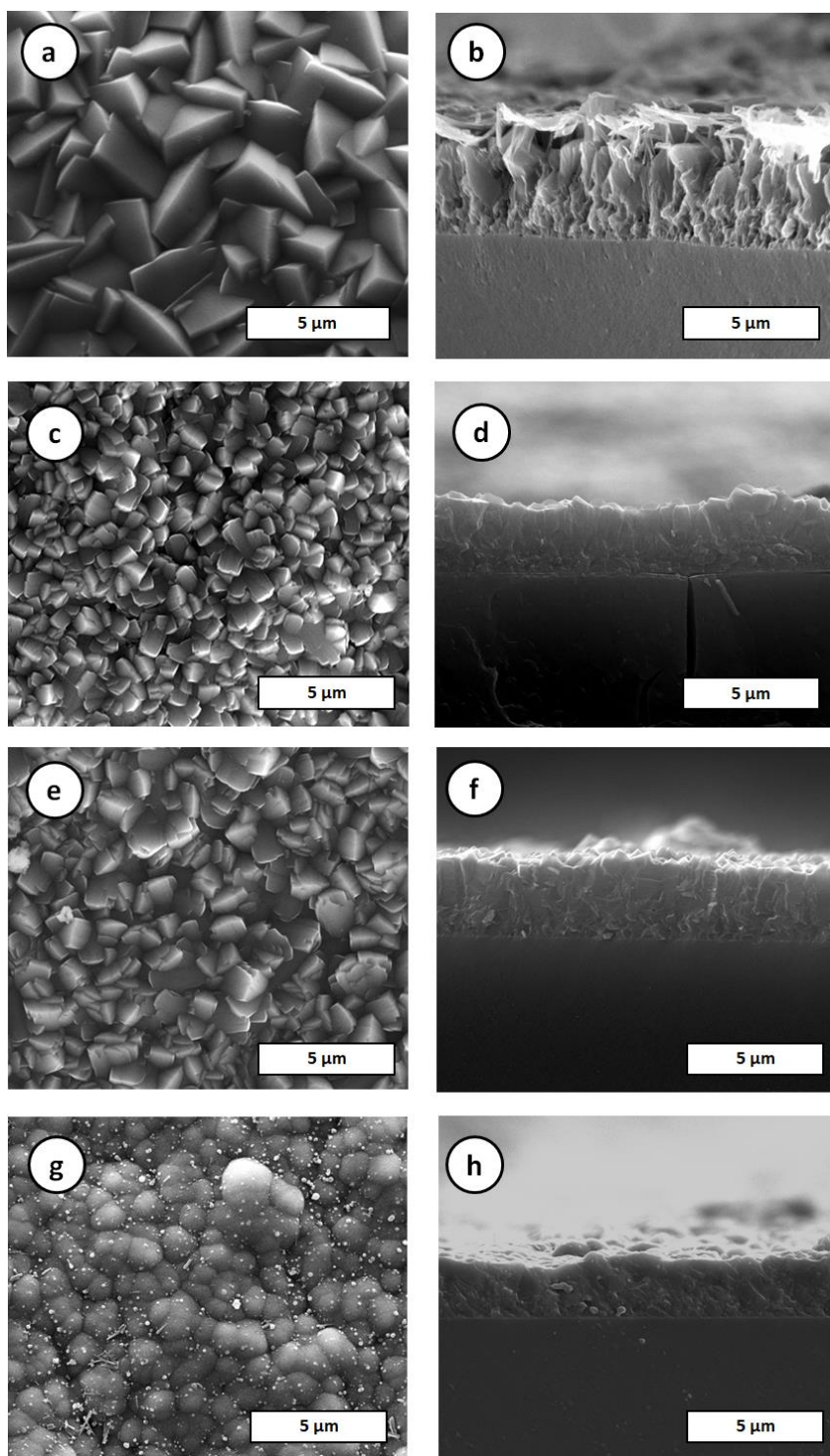


Figure 4.34. Top view and cross-sectional images of S1-F3 (a), (b); S1-F3-W1 (c), (d); S1-F3-W2 (e), (f); S1-F3-W3 (g), (h), respectively

While the crystals of S1-F3 film have truncated bipyramidal morphology as shown in Figure 4.34-a, the crystals of S1-F3-W1 and S1-F3-W2 films (Figure 4.34-c and e) have bipyramidal structure. Morphological differences obtained for the samples may be attributed to different crystal growth rates originated from the different molar water amount of the secondary growth gel formula used for the formation of the films. As shown in Figure 4.34-g, further increase of the molar water amount causes deterioration in the structure of the film. In order to gain a clear understanding the effect of water amount, further analyses were carried out.

XRD analysis technique was used to determine the purity and the crystal orientation of AM-6 films as shown in Figure 4.35. The peak positions of the XRD pattern of AM-6 films fitted with the XRD peak positions defined for AM-6 film formation [98].

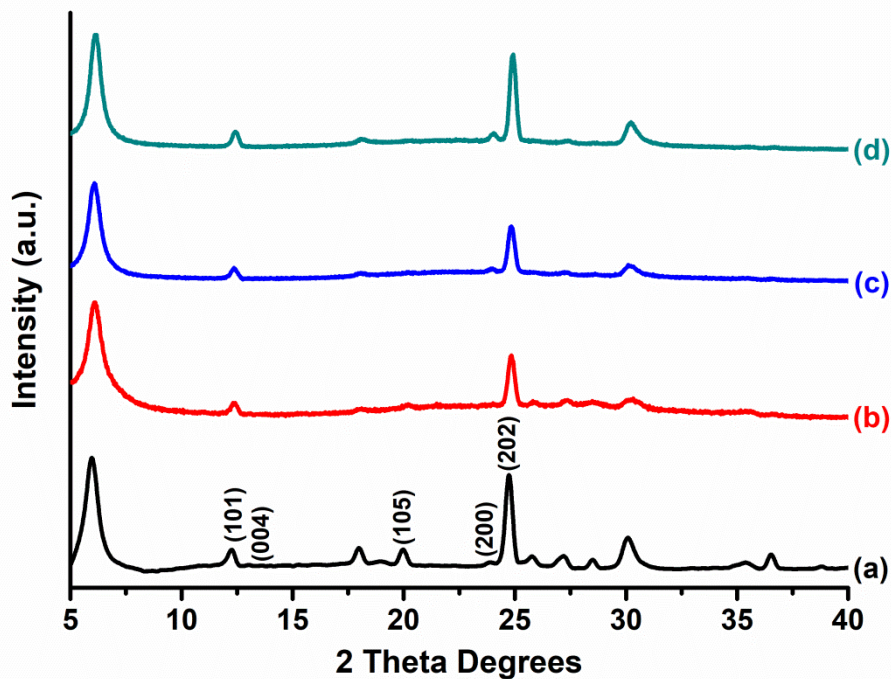


Figure 4.35. X-ray diffraction spectroscopy of the samples S1-F3 (a), S1-F3-W1 (b), S1-F3-W2 (c), and S1-F3-W3 (d)

The peak positions of the XRD data of the samples S1-F3-W1, S1-F3-W2, and S1-F3-W3 well matched with the peak positions of S1-F3 indicating that the obtained films are crystalline and have no impurities. The  $2\theta$  degree of  $\approx 20^\circ$  (i.e., (105) plane) was observable for S1-F3 indicating the tendency of crystals to grow in *c* direction (Figure 4.35). However, this peak loses intensity when the molar amount of water is altered. CPO values were also calculated for the obtained samples to examine the orientation of the crystals.

Integrated intensities of the (105) and (200) planes were identified for S1-F3, S1-F3-W1, S1-F3-W2, and S1-F3-W3 films to calculate CPO values. The equation of  $CPO_{200/105} = \frac{(I_{200}/I_{105})_f - (I_{200}/I_{105})_p}{(I_{200}/I_{105})_p}$  defined for CPO calculation was used based on (200) and (105) reflections for determining the degree of *a(b)*-out-of-plane preferred orientation quantitatively [54,109]. Accordingly, the calculated CPO values are listed in Table 4.10.

Table 4.10. Thickness and CPO values of S1-F3, S1-F3-W1, S1-F3-W2, and S1-F3-W3

Sample	Thickness ( $\mu\text{m}$ )	$CPO_{200/105}$
S1-F3	$4.17 \pm 0.08$	0.39
S1-F3-W1	$2.41 \pm 0.06$	21.98
S1-F3-W2	$2.80 \pm 0.05$	17.22
S1-F3-W3	$2.80 \pm 0.04$	4.05

As shown in Table 4.10, the samples S1-F3-W1 and S1-F3-W2 have the  $CPO_{200/105}$  value of 21.98 and 17.22, respectively indicating the tendency of crystals to grow in  $a(b)$ -out-of-plane orientation. Therefore, it can be implied that the orientation of crystals could be manipulated by altering the molar water amount in the secondary growth gel which is crucial for the photocatalytic activity of the films due to the dependence of photocatalytic activity on crystal orientation [18].

Raman spectroscopy was utilized for further investigation of the samples. Accordingly, characteristic V-O stretching vibration involving coordinated  $V^{4+}$  in AM-6 structure and centered at  $870\text{ cm}^{-1}$  was observed at 871, 868, 870, and  $870\text{ cm}^{-1}$  for the samples S1-F3, S1-F3-W1, S1-F3-W2, and S1-F3-W3, respectively as shown in Figure 4.36.

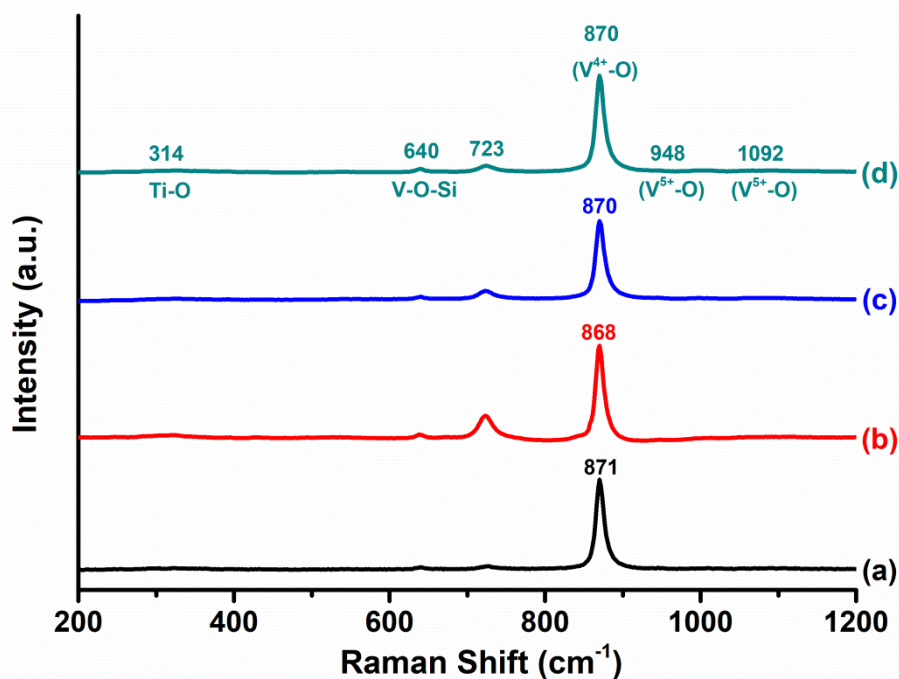


Figure 4.36. Raman spectroscopic analysis of the samples S1-F3 (a), S1-F3-W1 (b), S1-F3-W2 (c), and S1-F3-W3 (d)

Characteristic Raman shifts indicating the formation of the  $V^{5+}$  cation within the  $VO_3^{-2}$  quantum wires in AM-6 crystals centered at around  $950\text{ cm}^{-1}$  and  $1092\text{ cm}^{-1}$  Raman Shift were not significant for the samples [50,112]. Raman shifts observed at around  $314\text{ cm}^{-1}$  and  $723\text{ cm}^{-1}$  are ascribed to Ti-O stretching vibration indicating the presence of ETS-10 crystals [48,49]. The other observable peak centered at  $640\text{ cm}^{-1}$  is attributed to the bridging vibration of V-O-Si [128].

FWHM was also calculated for  $870\text{ cm}^{-1}$  vibration band in Raman spectra to identify the length homogeneity and the quality of the quantum wires in AM-6 crystals [111]. The calculation of FWHM could be a way to determine the defect formation in the  $VO_6$  quantum wires originated from the altering of the molar water content of the secondary growth gel formula which might increase the photocatalytic effectiveness

of the films. FWHM values obtained from the main band of V-O stretching of 870  $\text{cm}^{-1}$  for each film were shown in Table 4.11.

Table 4.11. Raman shift and FWHM (full-width half-maximum) values belonging to V-O stretching of S1-F3, S1-F3-W1, S1-F3-W2, and S1-F3-W3

Samples	V-O Stretching ( $\text{cm}^{-1}$ )	FWHM of V-O stretching
S1-F3	871	$12.27 \pm 0.07$
S1-F3-W1	868	$12.73 \pm 0.04$
S1-F3-W2	870	$13.17 \pm 0.09$
S1-F3-W3	870	$13.04 \pm 0.06$

The sample S1-F3-W2 has the maximum broadening of V-O stretching vibration (i.e.,  $13.17 \pm 0.09$ ). S1-F3-W1 and S1-F3-W3 have also a higher degree of broadening (i.e.,  $12.73 \pm 0.04$  and  $13.04 \pm 0.06$ ) with respect to S1-F3 (i.e.,  $12.27 \pm 0.07$ ). It can be inferred that S1-F3-W2 might be a better candidate for photocatalytic applications under the solar light.

The samples were also analyzed by UV-Vis absorption spectroscopy to determine the optical properties of the samples S1-F3, S1-F3-W1, S1-F3-W2, and S1-F3-W3. Figure 4.37 shows a strong absorption observed in the UV region for all four samples.

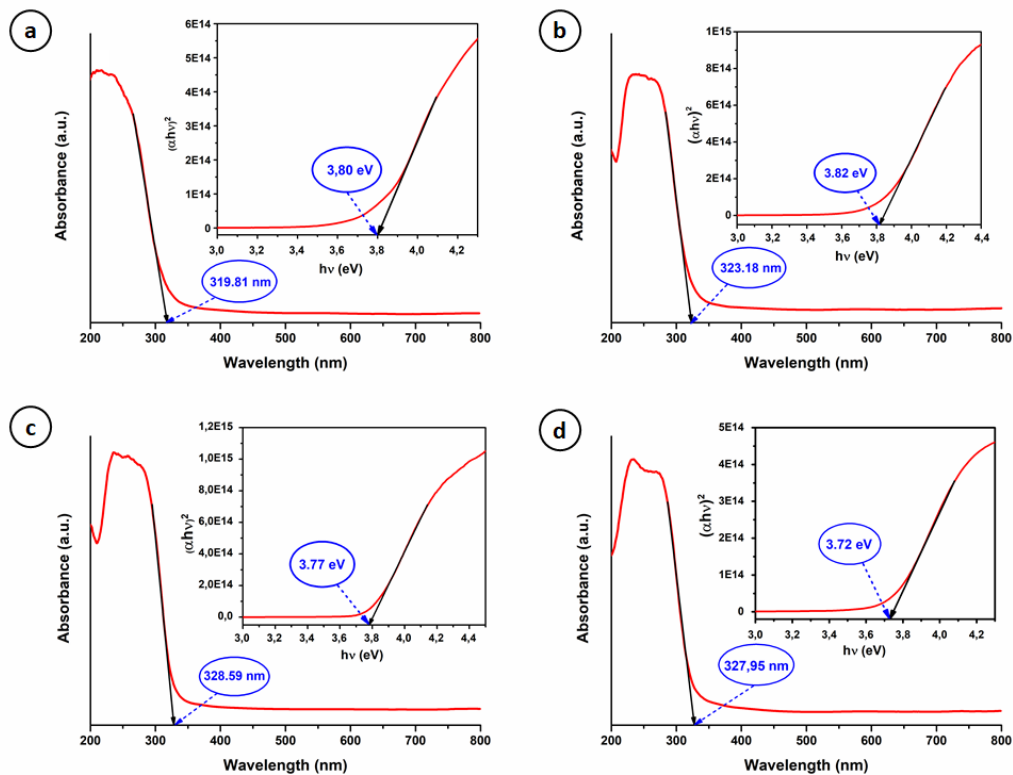


Figure 4.37. UV-Vis absorption spectra and Tauc plot for bandgap calculations for the samples (a) S1-F3, (b) S1-F3-W1, (c) S1-F3-W2, and (c) S1-F3-W3

The absorption maxima ( $\lambda_{\max}$ ) in the UV region were observed at 210 nm, 265 nm, 253 nm and 253 nm for S1-F3, S1-F3-W1, S1-F3-W2, and S1-F3-W3, respectively. It was seen a redshift in the UV-vis absorption spectra of the samples S1-F3-W1, S1-F3-W2, and S1-F3-W3 with respect to S1-F3 which could be due to the defect formation originated from different molar water content of the secondary growth gel formula [99]. The  $\lambda_{\max}$  values observed are similar to the absorption band assigned for O(2p)  $\rightarrow$  V(3d) charge-transfer transition, centered in between 200-350 nm and identified for powder AM-6 [25].

The bandgap energies of the samples were calculated according to the procedure applied by López et al. and obtained as 3.80, 3.82, 3.77, and 3.72 eV for the samples S1-F3, S1-F3-W1, S1-F3-W2, and S1-F3-W3, respectively [105]. The absorption



edge of the absorption spectra was also determined for the samples S1-F3, S1-F3-W1, S1-F3-W2, and S1-F3-W3 as 319.81 nm, 323.18 nm, 328.59 nm, and 327.95 nm, respectively. Accordingly, the energy bandgap values of the samples were calculated using the equation of  $E = \frac{hc}{\lambda}$ , where  $\lambda$  is the absorption edge,  $h$  is Planck constant,  $c$  is velocity of light, and  $E$  is energy. The calculated bandgap energies of the samples were found to be as 3.87 eV, 3.84 eV, 3.77 eV, and 3.78 eV for S1-F3, S1-F3-W1, S1-F3-W2, and S1-F3-W3, respectively. The calculated bandgap energy values obtained using both methods are consistent with the bandgap energy identified for AM-6 structure [25]. The bandgap energies of S1-F3-W2 and S1-F3-W3 are narrower with respect to the bandgap energy of S1-F3. Lower bandgap energy could facilitate electrons to excite to conduction band enhancing the photocatalytic activity [43]. Therefore, S1-F3-W2 and S1-F3-W3 are expected to perform better photocatalytic activity under the solar light.

Different oxidation states of vanadium in the structure of AM-6 films was determined by using XPS analysis technique based on the dependence of binding energy (BE) of the  $Vp_{3/2}$  core level to the oxidation state of V as shown in Figure 4.38 [119]. In order to identify different oxidation states of vanadium (i.e.,  $V^{5+}$  and  $V^{4+}$ ),  $V2p_{3/2}$  level was deconvoluted into two peaks [120,121].

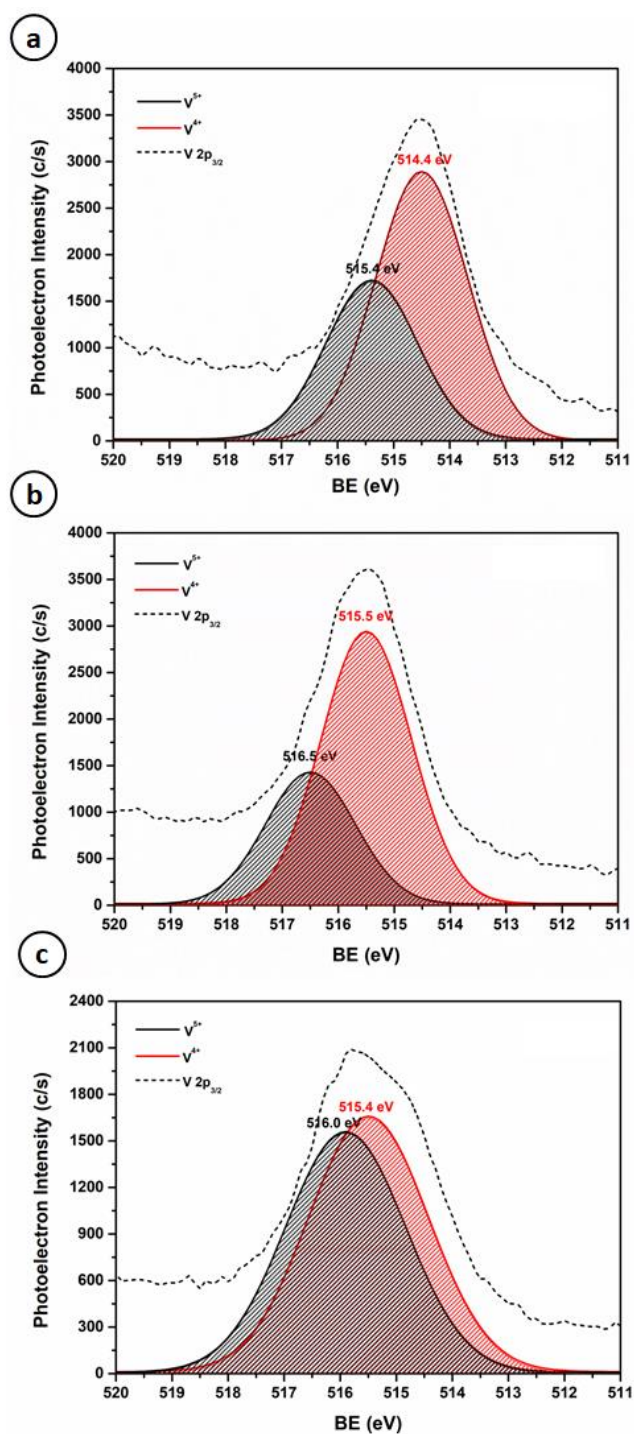


Figure 4.38. XPS high resolution V 2p spectra of S1-F3, S1-F3-W1, S1-F3-W2, and S1-F3-W3. deconvolution of V<sub>2p<sub>3/2</sub></sub> XPS peak of S1-F3 ( $V^{4+}/V^{5+}=1.68$ ) (a), deconvolution of V<sub>2p<sub>3/2</sub></sub> XPS peak of S1-F3-W1 ( $V^{4+}/V^{5+}=2.06$ ) (b), and deconvolution of V<sub>2p<sub>3/2</sub></sub> XPS peak of S1-F3-W2 ( $V^{4+}/V^{5+}=1.06$ ) (c)

Accordingly, V2p<sub>3/2</sub> level of S1-F3 deconvoluted to 514.4 eV and 515.4 eV which have been attributed to V<sup>5+</sup> and V<sup>4+</sup>, respectively. The peaks centered at 516.5eV and 515.5 eV have been attributed to V<sup>5+</sup> and V<sup>4+</sup>, respectively for S1-F3-W1. The peaks with binding energies of 516.0 eV and 515.4 eV have been attributed to V<sup>5+</sup> and V<sup>4+</sup>, respectively for S1-F3-W2. The binding energy values observed for the samples are comparable with the binding energy values identified for V<sup>5+</sup> and V<sup>4+</sup> cations in the literature [99,119,122–124]. Unfortunately, XPS analysis of S1-F3-W3 could not be carried out due to the technical problems related to XPS. Nevertheless, the ratio of V<sup>4+</sup>/V<sup>5+</sup> is expected higher with respect to S1-F3 as can be predicted from other analysis techniques.

The total area of the XPS peaks of V<sup>4+</sup> and V<sup>5+</sup> were accepted as 100 %. Accordingly, the ratio of V<sup>4+</sup>/V<sup>5+</sup> was calculated as 1.68, 2.06, and 1.06 for the samples S1-F3, S1-F3-W1, and S1-F3-W2. Table 4.12 was created using these data obtained from the calculation of the area under each curve.

Table 4.12. XPS spectral parameters for V 2p<sub>3/2</sub> for S1-F3, S1-F3-W1, S1-F3-W2, and S1-F3-W3: Binding energy (eV), and the ratio of V<sup>4+</sup>/V<sup>5+</sup>

Sample	V2p <sub>3/2</sub>		V <sup>4+</sup> /V <sup>5+</sup>
	V <sup>4+</sup> BE (eV)	V <sup>5+</sup> BE(eV)	
S1-F3	514.4	515.4	1.68
S1-F3-W1	515.5	516.5	2.06
S1-F3-W2	515.4	516.0	1.06

The calculated percentage of different oxidation states of vanadium (i.e., V<sup>4+</sup> and V<sup>5+</sup>) based on XPS results and demonstrated in Table 4.12 indicates that the quantity of V<sup>5+</sup> cations is greater in S1-F3-W2 with respect to other samples. Besides, the ratio of V<sup>4+</sup>/V<sup>5+</sup> is increased with a decreasing amount of molar water content of the secondary growth gel formula. It can be deduced that the quantity of V<sup>5+</sup> cations is decreased in S1-F3-W1 which makes this sample unfavorable as a photocatalyst

under visible light irradiation. These results indicate that vanadium exists in two oxidation states ( $V^{4+}$  and  $V^{5+}$ ) and the amount of these oxidation states is different for the samples originated from the utilization of different molar water content for the formation of AM-6 films.

In addition to the observed morphological differences between S1-F3, S1-F3-W1, S1-F3-W2, and S1-F3-W3, it can be inferred that vanadium exists in two different oxidation states in the structure of the films upon the changes induced with the different molar water content of the secondary growth gel. Accordingly, S1-F3-W2 is expected to be more effective as visible light photocatalyst due to its lower ratio of  $V^{4+}/V^{5+}$  based on the fact that visible light photocatalytic activity is dependent on the presence of  $V^{5+}$  cations [50].

#### **4.3.3.2. Evaluation of the Photocatalytic Activity**

The samples S1-F3, S1-F3-W2, and S1-F3-W3 were used as photocatalysts for the decomposition of MB under the solar light. Photocatalysis experiments could not be carried out for S1-F3-W1 due to weak adsorption of AM-6 crystals constituting S1-F3-W1 film. The crystals were peeled off the substrate surface. Dark experiments were also carried out for the samples S1-F3, S1-F3-W2, and S1-F3-W3 to investigate the degree of photodegradation upon adsorption of MB overall photocatalyst films under non-irradiation condition as shown in Figure 4.39-a, c, and e.

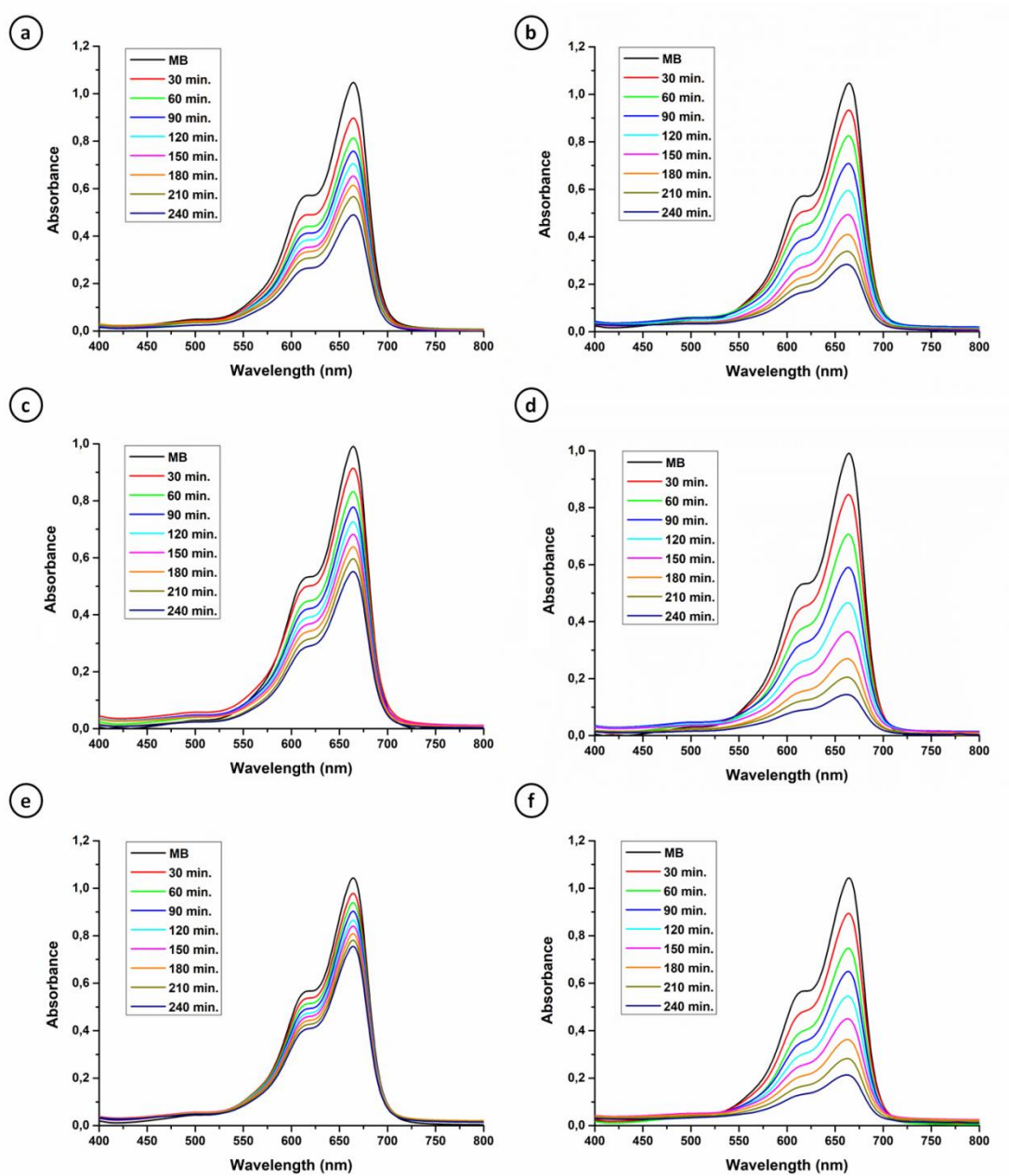


Figure 4.39. Absorbance of MB for S1-F3 in dark (a) and under illumination (b); S1-F3-W2 in dark (c) and under illumination (d); S1-F3-W3 in dark (e) and under illumination (f)

The adsorption of MB was obtained as 50.49 % for S1-F3, 44.29 % for S1-F3-W2, and 26.68 % for S1-F3-W3 after a 240 min period with the highest adsorption

occurring for S1-F3 which might be due to the highly porous structure and rough surface of the samples [20,25].

According to Figures 4.39 and 4.40-a, S1-F3-W2 demonstrates higher photocatalytic activity under the solar light with respect to S1-F3 and S1-F3-W3. 84.98 % removal of MB was observed after 240 min of the solar light illumination when S1-F3-W2 film was used as a photocatalyst. The percent removal of MB was 73.11 for S1-F3 film after 240 min illumination under the solar light which is ~12 % lower with respect to S1-F3-W2. MB degraded 77.78 % when S1-F3-W3 was used as photocatalyst which is ~7 % lower with respect to S1-F3-W2. These results suggest that S1-F3-W2 is more sensitive to the solar light for photocatalytic decomposition with respect to S1-F3 and S1-F3-W3. Another significant result was the increased photocatalytic activity of S1-F3-W2 under the solar light irradiation in comparison with S1-F3 and S1-F3-W3 arising from different amounts of  $V^{5+}$  cations in their structures as predicted from various analysis techniques due to the alteration of the molar water content of the secondary growth gel formula used for the formation of AM-6 films. It was shown that S1-F3-W2 film possessed more  $V^{5+}$  ions than S1-F3 and S1-F3-W3 film. Thus, the photoactivity observed at solar light irradiation could be due to the higher  $V^{5+}$  ions found in S1-F3-W3 films, which is also in correlation with the literature data suggesting  $V^{5+}$  ions to be responsible for the photocatalytic activity under visible light [16,68].

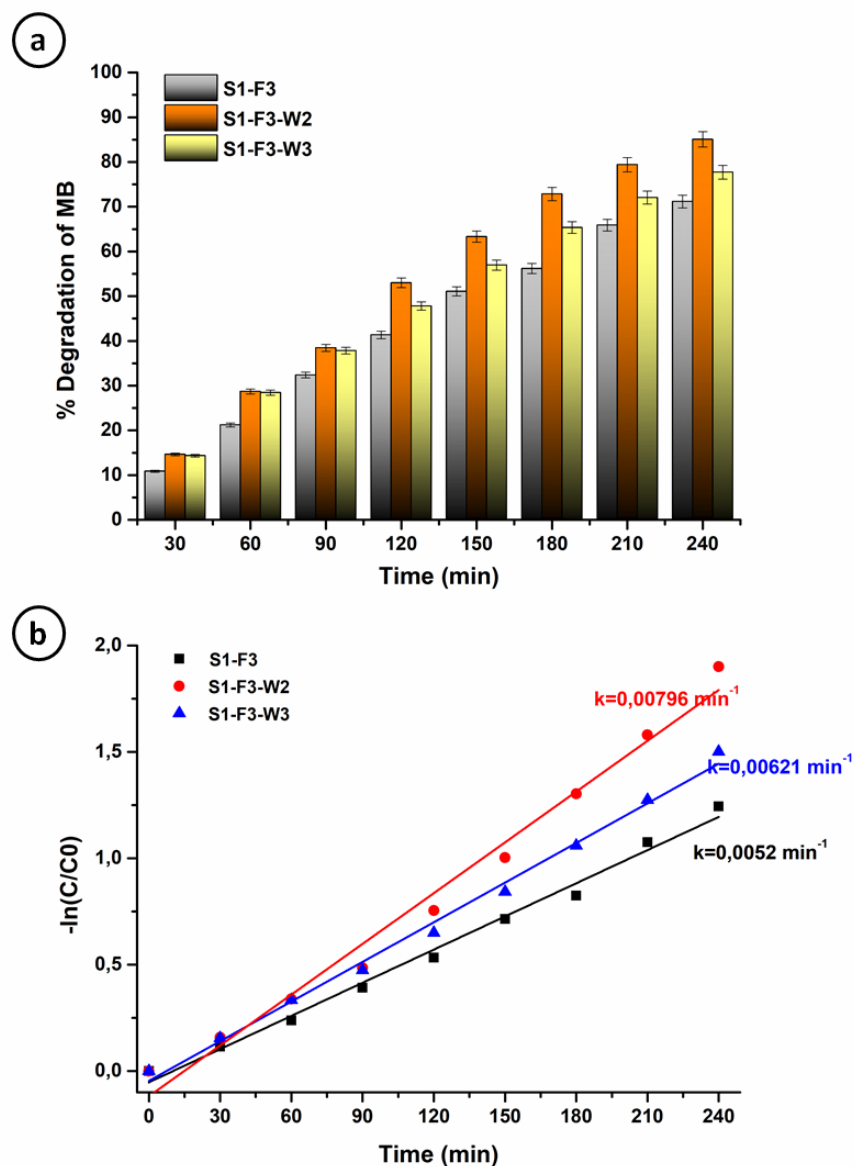


Figure 4.40. The photocatalytic removal (a), and the degradation kinetics (b) of MB for S1-F3, S1-F3-W2, and S1-F3-W3 films under solar simulator (1 Abs. MB, pH 6, VMB= 10 mL)

The pseudo-first-order reaction rate constants ( $k$ ) were calculated based on the photodegradation kinetics as shown in Figure 4.39-b. The  $k$  values calculated for S1-F3 ( $0.0052 \text{ min}^{-1}$ ), S1-F3-W2 ( $0.00796 \text{ min}^{-1}$ ) and S1-F3-W3 ( $0.00621 \text{ min}^{-1}$ ) are higher with respect to the  $k$  value ( $4.0724\text{E-}4$ ) calculated for the decomposition of

MB without using any photocatalyst under same conditions. Accordingly, S1-F3, S1-F3-W2, and S1-F3-W3 show photocatalytic activity for the decomposition of MB under the solar simulator. The photocatalytic activity of S1-F3-W2 was found to be higher with respect to S1-F3 and S1-F3-W3 as also predicted from various analysis techniques.

In order to increase the percent photodegradation of MB up to 100 %, the sample S2-F3 was used as a photocatalyst for the decomposition of MB. The photocatalytic performance of S2-F3 was investigated by evaluating the percent removals of MB dye at every 30 minutes up to 360 minutes under the solar simulator at room temperature. The results were shown in Figure 4.41.



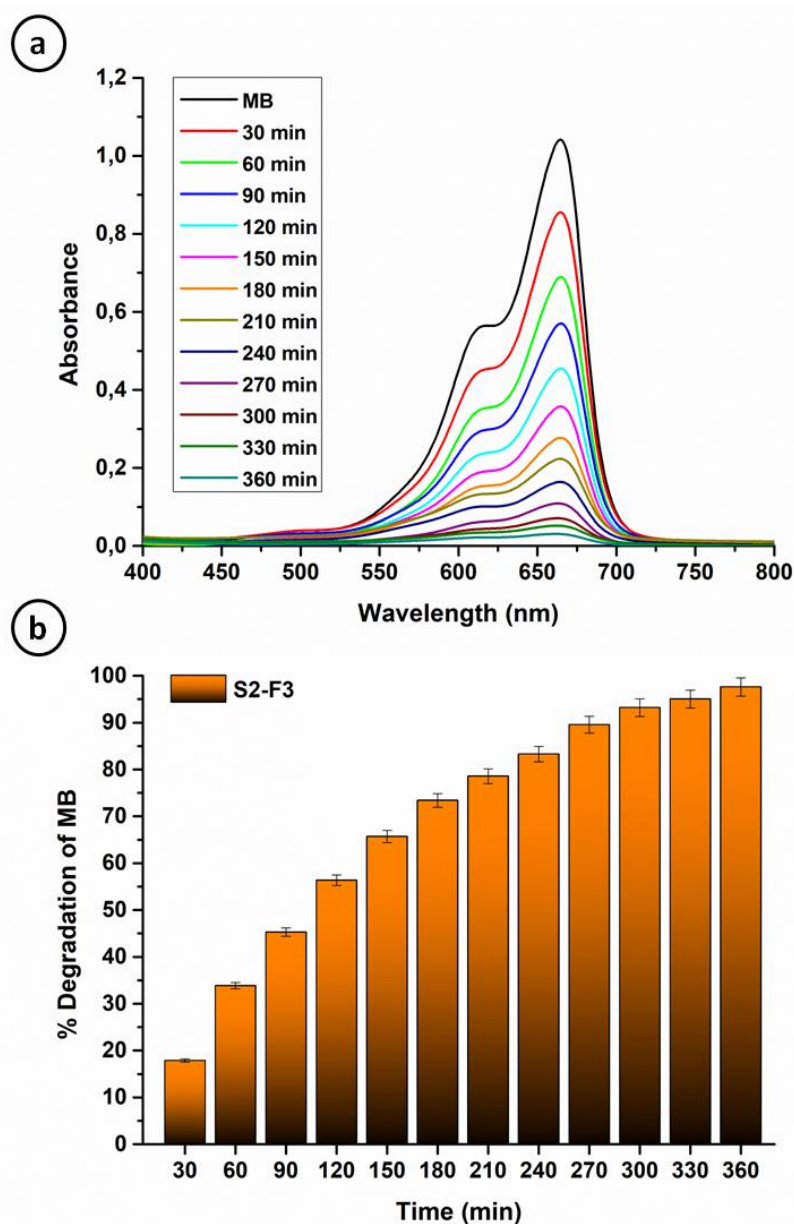


Figure 4.41. Absorbance (a), and percent degradation (b) of MB for S2-F3 film as photocatalyst under solar light (1 Abs. MB, pH 6, VMB= 10 mL)

S2-F3 was selected as a photocatalyst due to its low adsorption capacity in dark and high photodegradation property under the solar light illumination. According to Figure 4.41, 97.6 % degradation of MB was obtained under the solar light after 360 minutes.

CPO,  $V^{4+}/V^{5+}$  ratio, FWHM, and k values of the samples prepared in Section 4.3 were summarized in Table 4.13.

Table 4.13. CPO, FWHM,  $V^{4+}/V^{5+}$ , and k values of AM-6 films

Sample	CPO	$V^{4+}/V^{5+}$	FWHM	k
S1-F2	7.66	1.12	12.17	-
S1-F3	0.39	1.68	12.27	0.00520
S2-F3	14.05	1.17	12.66	0.00749
S1-dip1-F3	3.15	1.108	12.54	0.00654
S1-dip2-F3	3.17	1.101	12.66	0.00832
S1-F3-W1	21.98	2.06	12.73	-
S1-F3-W2	17.22	1.06	13.17	0.00796
S1-F3-W3	4.05	-	13.04	0.00621

According to Table 4.13, chemistry of the secondary growth gel, seed crystal morphology, seed layer coating technique and the molar water content of secondary growth gel are the parameters which are highly effective for AM-6 film formation. It is clear that altering these parameters creates different CPO,  $V^{4+}/V^{5+}$  ratio, FWHM, and k values.

It has been already studied that crystal orientation is effective on photocatalytic activity. Jang et al. synthesized ZnO crystals with different morphologies as photocatalysts for photocatalytic  $H_2O_2$  generation. They claimed that photocatalytic activity is dependent upon a particular crystal plane. They determined the amount of Zn (0001) faces for the synthesized nanoplates, nanorods, microrods, and dumbbell-shaped ZnO crystals. Nanoplates with the highest population of Zn (0001) faces demonstrated the most enhanced photocatalytic activity for  $H_2O_2$  generation. The enhanced photocatalytic activity observed for nanoplates was attributed to the polarity of Zn (0001) face. Oxygen molecules can easily be adsorbed on this face [18]. Similar to this study stated by Jang et al., *a(b)*-out-of-plane orientation can be photocatalytically preferable for our samples. According to Table 4.13, S2-F3 and

S1-F3-W2 have higher CPO values and showed more enhanced photocatalytic activity with respect to S1-F3. CPO represent the degree of  $a(b)$ -out-of-plane orientation. According to Table 4.13, seed layer coating technique do not change CPO, FWHM or  $V^{4+}/V^{5+}$  ratio dramatically. However, k values of S1-dip1-F3 and S1-dip2-F3 were found to be higher with respect to S1-F3. Photocatalytic activity observed for S1-dip1-F3 and S1-dip2-F3 are most probably originated from the adsorption of MB dye due to the thickness of the films.

A broadening observed in FWHM indicates defect formation in the structure due to the fact that FWHM express the quality of  $VO_6$  chains. The ratio  $V^{4+}/V^{5+}$  is crucial for photocatalytic activity due to the fact that  $V^{5+}$  cations are responsible for the photocatalytic activity under visible light irradiation. Therefore, it is expected that the samples with higher amount of  $V^{5+}$  cations or lower  $V^{4+}/V^{5+}$  ratio show enhanced photocatalytic activity under visible light irradiation.

Altering the molar water content of the secondary growth gel affects pH and supersaturation level and consequently film formation. Increasing the molar water content decreases the supersaturation level. Primary nucleation is suppressed and larger crystals are formed. Increased amount of water leads different crystal growth rate and crystallinity resulting in different crystal orientation and photocatalytic activity. Further increase of molar water content can hinder the growth of zeolite crystals. The significance of molar water content for the formation of AM-6 films can be observed from Table 4.13. The adsorption of AM-6 crystals on the substrate surface was weaker for AM-6 films prepared by using decreased amount of water. Therefore, S1-F3-W1 could not be utilized as a photocatalyst. CPO and FWHM values were increased and  $V^{4+}/V^{5+}$  ratio was decreased with increasing amount of water (S1-F3-W2). Accordingly, S1-F3-W2 is expected to perform better photocatalytic activity with respect to S1-F3. Further increase of molar water content caused deterioration in the structure of AM-6 films.

Figure 4.42 demonstrates the relationship between the ratio of  $V^{4+}/V^{5+}$  and photocatalytic reaction rate constant (k) and also CPO values for AM-6 films.

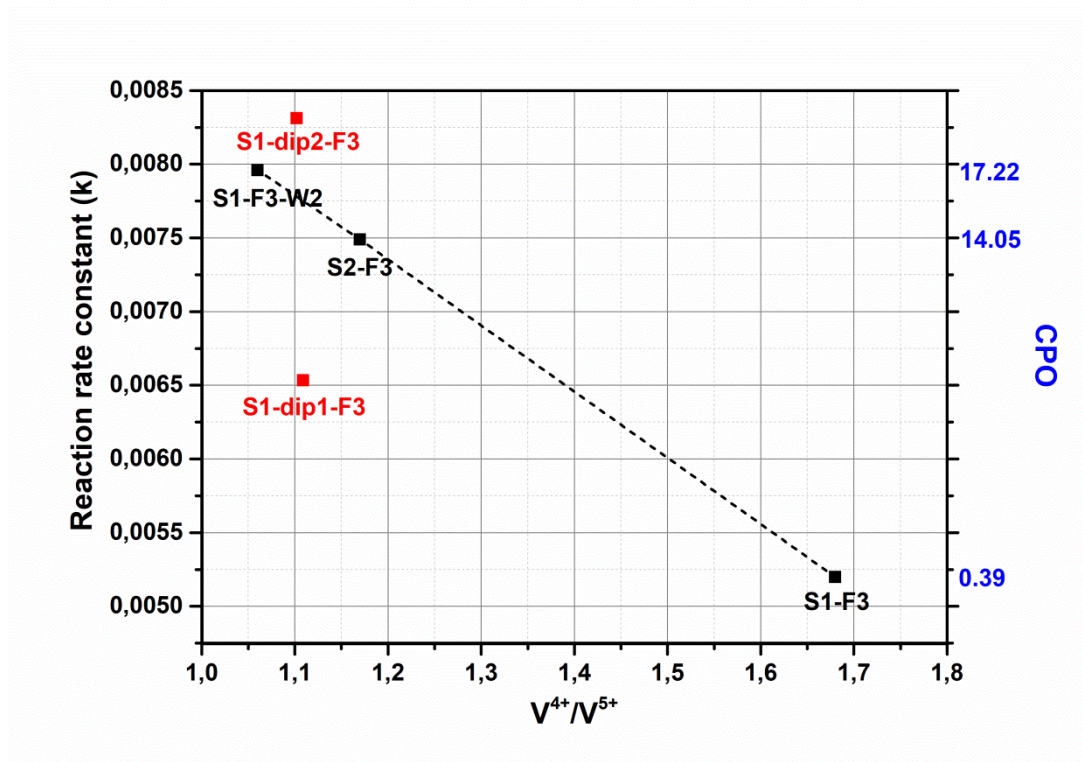


Figure 4.42. CPO vs  $V^{4+}/V^{5+}$  ratio for the samples

The samples S1-F3-W1 and S1-F3-W3 could not be used for creating the Figure 4.42. Photocatalysis experiments could not be carried out for S1-F3-W1 due to weak adsorption of AM-6 crystals constituting S1-F3-W1 film. The crystals were peeled off the substrate surface. Therefore, the photocatalytic reaction rate constant (k) could not be obtained for S1-F3-W1. XPS analysis of S1-F3-W3 could not be carried out due to the technical problems related to XPS. Thus, the ratio of  $V^{4+}/V^{5+}$  could not be calculated for S1-F3-W3. Hereby, the samples S1-F3-W1 and S1-F3-W3 have to be excluded creating the graph shown in Figure 4.42.

CPO and  $V^{4+}/V^{5+}$  values of AM-6 films prepared by using different parameters such as seed crystal morphology, seed layer coating technique, and the molar water content of the secondary growth gel were shown in Figure 4.42. The current results suggest that, lower the  $V^{4+}/V^{5+}$  ratio for the films with identical synthesis solution, higher the photocatalytic activity is obtained. This trend cannot be obtained for thicker films as a function of film thickness. This may be due to the combined effect of adsorption of MB and photocatalytic activity, where more pronounced effect dependent on the adsorption of MB might be occurred. Although one to one correlation cannot be drawn between the CPO and  $V^{4+}/V^{5+}$  values, in the current study  $V^{5+}$  was observed to be increased for the samples with higher CPO values. Therefore, the samples with relatively higher  $a(b)$ -out-of-plane preferred orientation also possessed higher  $V^{5+}$  with enhanced photocatalytic activity as well.

The current thesis study focuses on the methodologies for tailoring the defect sites for hydrothermally grown AM-6 zeo-type films, which was shown to affect the visible light photocatalytic activities. Although it is highly speculative to draw any conclusion among different film parameters such as growth orientation and defect formation, it can be hypothesized that AM-6 thin films with aimed film properties can be optimized for enhanced photocatalytic applications. More detailed studies are necessary to directly draw a conclusion between growth orientation, defect formation and the catalytic performances which were shown to be interrelated in this current thesis study.



## CHAPTER 5

### SUMMARY, CONCLUSION, AND FURTHER SUGGESTIONS

Microporous vanadosilicate AM-6 films were produced on conductive ITO coated glass substrates for the first time by using secondary growth gels with different molar compositions, which were originally for the synthesis of AM-6 powders. It was demonstrated that S1-F3 was the purest film with respect to others having only one oxidation state (i.e.,  $V^{4+}$ ) in its 1-D  $VO_3^{-2}$  quantum wires. According to  $CPO_{200/105}$  values obtained from XRD analyses, S1-F1 and S1-F2 had the tendency to grow in  $a(b)$ -out-of-plane orientation, while S1-F3 in  $c$  direction, which was attributed to the differences between crystal growth rates in different orientations. Moreover, the effect of reaction temperature and the amount of water on morphology and crystal orientation were investigated for S1-F1 films. It was demonstrated that the preferred crystal orientation can be manipulated by changing the amount of water in the secondary growth gel. The increase in water content led to an increase in CPO value. The increase in reaction temperature (i.e., from 503 K to 528 K) led to a decrease in reaction time, resulting in the formation of quartz impurity.

Microporous vanadosilicate AM-6 and microporous titanasilicate ETS-10 samples in thin form were used as photocatalysts for the photocatalytic decomposition of MB. There was no significant difference between the percent removals of MB when the samples were used as photocatalyst under UV irradiation. Vanadosilicate AM-6 thin films produced by using different molar compositions demonstrated different photocatalytic responses under visible light irradiation based upon different oxidation states of vanadium cation (i.e.,  $V^{4+}$  and  $V^{5+}$ ) present in their framework. The different oxidation states of vanadium were indicated by XPS and Raman analysis techniques. It was demonstrated that S1-F2 film with the largest amount of

$V^{5+}$  cation showed increased photocatalytic activity with respect to S1-F3 under visible light irradiation. Therefore, it was shown that vanadosilicate AM-6 thin films as photocatalysts are sensitive to visible light and this sensitivity could be changed using different synthesis conditions during the synthesis of these films. To enhance the photocatalytic activity of S1-F2,  $Ag^0$  nanoparticles were incorporated into S1-F2. The results showed that  $Ag^0$  nanoparticle incorporation provided a slight increase for the photocatalytic activity since  $Ag^0$  nanoparticle incorporation extends the light absorption spectrum into the visible region, hinders the recombination of electron/hole pairs through the electron transfer to the Ag sites, and enhances the surface electron excitation due to surface plasmon resonance effect. However, no significant difference for the photocatalytic decomposition of MB under visible light irradiation was observed. This may be attributed to the structural damage of ...V-O-V-O-V... chains arising from silver nanoparticle incorporation.

To investigate the parameters such as seed morphology, seed layer coating technique, and molar water content of the secondary growth gel on the formation and photocatalytic effectiveness of vanadosilicate AM-6 films, various modifications were studied for preparation of AM-6 films. In this regard, ETS-10 crystals with different morphologies (i.e., bipyramidal and cubic) were synthesized as seed crystals. Vanadosilicate AM-6 films were grown hydrothermally on ETS-10 crystals with different morphologies. The obtained AM-6 films showed differences structurally and had different  $V^{4+}/V^{5+}$  ratio resulting in different photocatalytic activity due to the fact that  $V^{5+}$  cation is responsible for the photocatalytic activity under visible light irradiation. AM-6 films grown on cubic shaped ETS-10 seed crystals demonstrated an enhanced photocatalytic activity. Afterward, different types of seed layer coating techniques were applied to prepare AM-6 films using bipyramidal shaped ETS-10 crystals as a seed layer. AM-6 films obtained by using seed layer coated with different techniques demonstrated structural differences and distinctive photocatalytic activities. AM-6 films produced by using 2 times dip-coated and bipyramidal-shaped ETS-10 crystals showed enhanced photocatalytic



activity with respect to the other samples. Finally, the molar water content of the secondary growth gel formula was altered to investigate the effect of water on the formation and photocatalytic activity of AM-6 films. Decreasing the molar water content caused crystals of AM-6 films to peel off the surface. Therefore, these samples could not be used as photocatalysts. Increasing the molar water content of the secondary growth gel formula has led an increase in the amount of  $V^{5+}$  cation and also photocatalytic activity. Further increase of molar water content caused structural damage and further increase of photocatalytic activity of AM-6 films could not be obtained.

It is believed that AM-6 film formation is crucial for advanced application areas such as electrochromic films, sensors and etc. along with photocatalysis to benefit from the unique properties of microporous vanadosilicate AM-6.



## REFERENCES

- [1] X. Wang, J. Jia, Y. Wang, Enhanced photocatalytic-electrolytic degradation of Reactive Brilliant Red X-3B in the presence of water jet cavitation, *Ultrason. Sonochem.* 23 (2015) 93–99. doi:10.1016/j.ultsonch.2014.10.005.
- [2] O. Mekasuwandumrong, P. Pawinrat, P. Praserttham, J. Panpranot, Effects of synthesis conditions and annealing post-treatment on the photocatalytic activities of ZnO nanoparticles in the degradation of methylene blue dye, *Chem. Eng. J.* 164 (2010) 77–84. doi:10.1016/j.cej.2010.08.027.
- [3] I. Altin, M. Sökmen, Preparation of TiO<sub>2</sub>-polystyrene photocatalyst from waste material and its usability for removal of various pollutants, *Appl. Catal. B Environ.* 144 (2014) 694–701. doi:10.1016/j.apcatb.2013.06.014.
- [4] S.H. Bossmann, C. Turro, C. Schnabel, M.R. Pokhrel, L.M. Payawan, B. Baumeister, M. Wörner, Ru(bpy)<sub>3</sub><sup>2+</sup>/TiO<sub>2</sub>-codoped zeolites: Synthesis, characterization, and the role of TiO<sub>2</sub> in electron transfer photocatalysis, *J. Phys. Chem. B.* 105 (2001) 5374–5382. doi:10.1021/jp002480m.
- [5] S. Da Dalt, A.K. Alves, C.P. Bergmann, Photocatalytic degradation of methyl orange dye in water solutions in the presence of MWCNT/TiO<sub>2</sub> composites, *Mater.Res. Bull.* 48(2013)1845–1850. doi:10.1016/j.materresbull.2013.01.022.
- [6] M.A. Lazar, S. Varghese, S.S. Nair, Photocatalytic Water Treatment by Titanium Dioxide: Recent Updates, *Catalysts.* 2 (2012) 572–601. doi:10.3390/catal2040572.
- [7] H. Kisch, W. Macyk, Visible-light photocatalysis by modified titania, *ChemPhysChem.* 3 (2002) 399–400. doi:10.1002/1439-7641(20020517)3:5<399::AID-CPHC399>3.0.CO;2-H.
- [8] D.I. Petkowicz, R. Brambilla, C. Radtke, C.D.S. da Silva, Z.N. da Rocha, S.B.C. Pergher, J.H.Z. dos Santos, Photodegradation of methylene blue by in situ generated titania supported on a NaA zeolite, *Appl. Catal. A Gen.* 357 (2009) 125–134. doi:10.1016/j.apcata.2008.12.040.
- [9] A. Houas, Photocatalytic degradation pathway of methylene blue in water, *Appl. Catal. B Environ.* 31 (2001) 145–157. doi:10.1016/S0926-3373(00)00276-9.
- [10] M.R. Hoffmann, S. Martin, W. Choi, D.W. Bahnemann, Environmental Applications of Semiconductor Photocatalysis, *Chem. Rev.* 95 (1995) 69–96. doi:10.1021/cr00033a004.
- [11] O. Sacco, V. Vaiano, C. Han, D. Sannino, D.D. Dionysiou, Photocatalytic

- removal of atrazine using N-doped TiO<sub>2</sub> supported on phosphors, *Appl. Catal. B Environ.* 164 (2015) 462–474. doi:10.1016/j.apcatb.2014.09.062.
- [12] A.L. Linsebigler, G. Lu, J.T. Yates, Photocatalysis on TiO<sub>2</sub> Surfaces: Principles, Mechanisms, and Selected Results, *Chem. Rev.* 95 (1995) 735–758. doi:10.1021/cr00035a013.
- [13] S.W. da Silva, C.R. Klauck, M.A. Siqueira, A.M. Bernardes, Degradation of the commercial surfactant nonylphenol ethoxylate by advanced oxidation processes, *J. Hazard. Mater.* 282 (2015) 241–248. doi:10.1016/j.jhazmat.2014.08.014.
- [14] N. Wang, Y. Xu, L. Zhu, X. Shen, H. Tang, Reconsideration to the deactivation of TiO<sub>2</sub> catalyst during simultaneous photocatalytic reduction of Cr(VI) and oxidation of salicylic acid, *J. Photochem. Photobiol. A Chem.* 201 (2009) 121–127. doi:10.1016/j.jphotochem.2008.10.002.
- [15] Z. Ji, M.N. Ismail, D.M. Callahan, E. Pandowo, Z. Cai, T.L. Goodrich, K.S. Ziemer, J. Warzywoda, A. Sacco, The role of silver nanoparticles on silver modified titanosilicate ETS-10 in visible light photocatalysis, *Appl. Catal. B Environ.* 102 (2011) 323–333. doi:10.1016/j.apcatb.2010.12.021.
- [16] X.Z. Li, F.B. Li, Study of Au/Au<sup>3+</sup>-TiO<sub>2</sub> photocatalysts toward visible photooxidation for water and wastewater treatment, *Environ. Sci. Technol.* 35 (2001) 2381–2387. doi:10.1021/es001752w.
- [17] D. Sannino, V. Vaiano, O. Sacco, P. Ciambelli, Mathematical modelling of photocatalytic degradation of methylene blue under visible light irradiation, *J. Environ. Chem. Eng.* 1 (2013) 56–60. doi:10.1016/j.jece.2013.03.003.
- [18] E.S. Jang, J.H. Won, S.J. Hwang, J.H. Choy, Fine tuning of the face orientation of ZnO crystals to optimize their photocatalytic activity, *Adv. Mater.* 18 (2006) 3309–3312. doi:10.1002/adma.200601455.
- [19] M. Yu, J. Li, W. Sun, M. Jiang, F. Zhang, Preparation, characterization, and photocatalytic properties of composite materials of copper(II) porphyrin/TiO<sub>2</sub>, *J. Mater. Sci.* 49 (2014) 5519–5528. doi:10.1007/s10853-014-8132-4.
- [20] D. Gruyter, *Chemical photocatalysis*, 2013.
- [21] U.I. Gaya, *Heterogeneous Photocatalysis Using Inorganic Semiconductor Solids*, Springer US, Kano, Nigeria, 2014. doi:10.1007/978-94-007-7775-0.
- [22] P. Pichat, ed., *Photocatalysis and Water Purification From Fundamentals to Recent Applications*, 2013.
- [23] R.C. Pawar, C.S. Lee, *Heterogeneous Nanocomposite-Photocatalysis for Water Purification*, 2015. doi:10.1016/C2014-0-02650-0.
- [24] J.C. Colmenares, Y.J. Xu, eds., *Heterogeneous Photocatalysis: From*

Fundamentals to Green Applications, Springer US, 2015. doi:10.1007/978-3-662-48719-8\_7.

- [25] SYNTHESIS AND BANDGAP ENGINEERING OF VANADOSILICATE AM-6 FOR PHOTOCATALYTIC APPLICATIONS. A Dissertation Presented by Mariam N . Ismail to The Department of Chemical Engineering In partial fulfillment of the requirements For the degree of Doctor of Philoso, (2011).
- [26] J.C. Ahern, S. Kanan, H.H. Patterson, Heterogeneous Photocatalysis with Nanoclusters of D10 Metal Ions Doped in Zeolites, *Comments Inorg. Chem.* 35 (2015) 59–81. doi:10.1080/02603594.2014.973106.
- [27] M. Tomkiewicz, Scaling properties in photocatalysis, *Catal. Today.* 58 (2000) 115–123. doi:10.1016/S0920-5861(00)00246-7.
- [28] T. Maesen, B. Marcus, The Zeolite Scene - An Overview, *Stud. Surf. Sci. Catal. - Introd. to Zeolite Sci. Pract.* (2001) 1–1062.
- [29] P. Payra, P.K. Dutta, *Handbook of Zeolite Science and Technology*, Marcel Dekker Inc., 2003.
- [30] H. Van Bekkum, E.M. Flanigen, P.A. Jacobs, *Studies in Surface Science and Catalysis* 137 H. van Bekkum, E.M. Flanigen, P.A. Jacobs and J.C. Jansen (Editors) 9 2001 Elsevier Science B.V. All righBekkum, H. Van, Flanigen, E. M., & Jacobs, P. A. (2001). *Studies in Surface Science and Catalysis* 137 H. , *Stud. Surf. Sci. Catal.* (2001) 299–343.
- [31] V. Valtchev, S. Mintova, Synthesis of titanium silicate ETS-10: The effect of tetramethylammonium on the crystallization kinetics, *Zeolites.* 14 (1994) 697–700. doi:10.1016/0144-2449(94)90128-7.
- [32] C. Baerlocher, L.B. McCusker, D.H. Olson, *Atlas of Zeolite Framework Types*, Elsevier, 2007.
- [33] S.E. Sen, S.M. Smith, K.A. Sullivan, Tetrahedron report number 508 Organic Transformations using Zeolites and Zeotype Materials, *Tetrahedron.* 55 (1999) 12657–12698.
- [34] C.C.H. Lin, K.A. Dambrowitz, S.M. Kuznicki, Evolving applications of zeolite molecular sieves, *Can. J. Chem. Eng.* 90 (2012) 207–216. doi:10.1002/cjce.20667.
- [35] L. Lv, F. Su, X.S. Zhao, A reinforced study on the synthesis of microporous titanosilicate ETS-10, *Microporous Mesoporous Mater.* 76 (2004) 113–122. doi:10.1016/j.micromeso.2004.08.004.
- [36] A. Philippou, M.W. Anderson, Aldol-Type Reactions over Basic Microporous Titanosilicate ETS-10 Type Catalysts, *J. Catal.* 189 (2000) 395–400.

doi:10.1006/jcat.1999.2705.

- [37] P.L. Solari, G. Agostini, A. Zecchina, E. Groppo, S. Bordiga, S. Usseglio, M.J. Uddin, C. Prestipino, C. Lamberti, From Isolated Ag<sup>+</sup> Ions to Ag<sup>0</sup> Nanoclusters in Silver-Exchanged Engelhard Titanosilicate (ETS-10) Molecular Sieve: Reversible Behavior, *Chem. Mater.* 21 (2009) 1343–1353. doi:10.1021/cm803216k.
- [38] N.B.K. Magnowski, A.M. Avila, C.C.H. Lin, M. Shi, S.M. Kuznicki, Extraction of ethane from natural gas by adsorption on modified ETS-10, *Chem. Eng. Sci.* 66 (2011) 1697–1701. doi:10.1016/j.ces.2011.01.005.
- [39] Z. Ji, J. Warzywoda, A. Sacco, Titanosilicate ETS-10 thin film preparation on fused silica optical fibers, *Microporous Mesoporous Mater.* 101 (2007) 279–287. doi:10.1016/j.micromeso.2006.10.003.
- [40] S.J. Datta, K.B. Yoon, Synthesis of ideal AM-6 and elucidation of v<sup>4+</sup>-to-O charge transfer in vanadate quantum wires, *Angew. Chemie - Int. Ed.* 49 (2010) 4971–4975. doi:10.1002/anie.200907088.
- [41] M. Guo, G. Li, F. Fan, Z. Feng, C. Li, Enhancement of the visible light absorption intensity of microporous vanadosilicate AM-6, *Chem. Commun.* 48 (2012) 11892. doi:10.1039/c2cc36083g.
- [42] F. Mani, L. Wu, S.M. Kuznicki, A simplified method to synthesize pure vanadium silicate analogue of ETS-10, *Microporous Mesoporous Mater.* 177 (2013) 91–96. doi:10.1016/j.micromeso.2013.02.008.
- [43] M.J. Nash, S. Rykov, R.F. Lobo, D.J. Doren, I. Wachs, V. Pennsylv., Photocatalytic Activity of Vanadium-Substituted ETS-10, (2007) 7029–7037.
- [44] C. Lamberti, Electron-hole reduced effective mass in monoatomic ...-O-Ti-O-Ti-O-... quantum wires embedded in the siliceous crystalline matrix of ETS-10, *Microporous Mesoporous Mater.* 30 (1999) 155–163. doi:10.1016/S1387-1811(99)00022-0.
- [45] G.X.S. Zhao, J.L. Lee, P.A. Chia, Unusual adsorption properties of microporous titanosilicate ETS-10 toward heavy metal lead, *Langmuir.* 19 (2003) 1977–1979. doi:10.1021/la026490l.
- [46] N.B.K. Magnowski, A.M. Avila, C.C.H. Lin, M. Shi, S.M. Kuznicki, Extraction of ethane from natural gas by adsorption on modified ETS-10, *Chem. Eng. Sci.* 66 (2011) 1697–1701. doi:10.1016/j.ces.2011.01.005.
- [47] R.M. Yeates, M.J. Murdoch, P.D. Southon, A.C. Mclaughlin, R.F. Howe, F. Bonino, S. Bordiga, A. Damin, AM-6: a microporous one-dimensional ferromagnet, *Dalt. Trans.* (2009) 8025. doi:10.1039/b908099f.
- [48] M.N. Ismail, N.D. Fraiman, D.M. Callahan, G. Gursoy, E. Viveiros, O.

- Ozkanat, Z. Ji, R.J. Willey, J. Warzywoda, A. Sacco, First unseeded hydrothermal synthesis of microporous vanadosilicate AM-6, *Microporous Mesoporous Mater.* 120 (2009) 454–459. doi:10.1016/j.micromeso.2008.12.020.
- [49] J. Rocha, P. Brandão, Z. Lin, M.W. Anderson, V. Alfredsson, O. Terasaki, The First Large-Pore Vanadosilicate Framework Containing Hexacoordinated Vanadium, *Angew. Chemie Int. Ed. English.* 36 (1997) 100–102. doi:10.1002/anie.199701001.
- [50] M.N. Ismail, U.K. Ibe, T. Chernenko, M. Diem, J. Warzywoda, A. Sacco, Synthesis and characterization of vanadosilicate AM-6 with transition metal ions isomorphously substituted in the framework, *Microporous Mesoporous Mater.* 145 (2011) 118–123. doi:10.1016/j.micromeso.2011.04.030.
- [51] M. Guo, Z. Feng, J.P. Hofmann, B.M. Weckhuysen, F. Fan, C. Li, Synthesis and morphology control of AM-6 nanofibers with tailored -V-O-V- intermediates., *Chemistry.* 19 (2013) 14200–4. doi:10.1002/chem.201301812.
- [52] N.C. Jeong, M.H. Lee, K.B. Yoon, Length-dependent band-gap shift of TiO<sub>2</sub>- molecular wires embedded in zeolite ETS-10, *Angew. Chemie - Int. Ed.* 46 (2007) 5868–5872. doi:10.1002/anie.200701676.
- [53] I. Tiscornia, Z. Lin, J. Rocha, C. Téllez, J. Coronas, J. Santamaría, Molecular Sieves: From Basic Research to Industrial Applications, *Proceedings of the 3rd International Zeolite Symposium (3rd FEZA), Stud. Surf. Sci. Catal.* 158 (2005) 423–430. doi:10.1016/S0167-2991(05)80368-4.
- [54] S. Galioglu, M.N. Ismail, J. Warzywoda, A. Sacco, B. Akata, Preparation and microstructural characterization of oriented titanosilicate ETS-10 thin films on indium tin oxide surfaces, *Microporous Mesoporous Mater.* 131 (2010) 401–406. doi:10.1016/j.micromeso.2010.02.001.
- [55] Z. Wang, Y. Yan, Oriented zeolite MFI monolayer films on metal substrates by in situ crystallization, *Microporous Mesoporous Mater.* 48 (2001) 229–238. doi:10.1016/S1387-1811(01)00357-2.
- [56] X. Lu, Y. Peng, Z. Wang, Y. Yan, Rapid fabrication of highly b-oriented zeolite MFI thin films using ammonium salts as crystallization-mediating agents, *Chem. Commun.* 51 (2015) 11076–11079. doi:10.1039/c5cc02980e.
- [57] Z. Lai, M. Tsapatsis, J.P. Nicolich, Siliceous ZSM-5 membranes by secondary growth of b-oriented seed layers, *Adv. Funct. Mater.* 14 (2004) 716–729. doi:10.1002/adfm.200400040.
- [58] X. Zhang, H. Liu, K.L. Yeung, Influence of seed size on the formation and microstructure of zeolite silicalite-1 membranes by seeded growth, *Mater. Chem. Phys.* 96 (2006) 42–50. doi:10.1016/j.matchemphys.2005.06.031.

- [59] E. Hu, Y.L.W. Huang, Q. Yan, D. Liu, Z. Lai, Synthesis of highly c-oriented AFI membranes by epitaxial growth, *Microporous Mesoporous Mater.* 126 (2009) 81–86. doi:10.1016/j.micromeso.2009.05.023.
- [60] K.B. Yoon, K. Ha, Y.J. Lee, H.J. Lee, Facile assembly of zeolite monolayers on glass, silica, and alumina by employing 3-halopropylsilyl reagents as covalent linkers., *Abstr. Pap. Am. Chem. Soc.* 220 (2000) U238–U238.
- [61] E. Hu, Y.L.W. Huang, Q. Yan, D. Liu, Z. Lai, Synthesis of highly c-oriented AFI membranes by epitaxial growth, *Microporous Mesoporous Mater.* 126 (2009) 81–86. doi:10.1016/j.micromeso.2009.05.023.
- [62] L.C. Boudreau, J.A. Kuck, M. Tsapatsis, Deposition of oriented zeolite A films: In situ and secondary growth, *J. Memb. Sci.* 152 (1999) 41–59. doi:10.1016/S0376-7388(98)00166-5.
- [63] B. Yilmaz, K.G. Shattuck, J. Warzywoda, A. Sacco, Oriented growth of ETS-4 films using the method of secondary growth, *Chem. Mater.* 18 (2006) 1107–1112. doi:10.1021/cm051360u.
- [64] Y. Liu, Y. Li, W. Yang, Effective manipulation of the microstructure of zeolite film by hydrothermal pretreatment, *J. Mater. Sci.* 46 (2011) 3942–3951. doi:10.1007/s10853-011-5319-9.
- [65] T. Sivlim, Ş. Akkan, I. Altın, M. Koç, M. Sökmen, TiO<sub>2</sub> immobilized biodegradable polymer for photocatalytic removal of chlorophenol, *Water. Air. Soil Pollut.* 223 (2012) 3955–3964. doi:10.1007/s11270-012-1163-z.
- [66] X. Lang, X. Chen, J. Zhao, Heterogeneous visible light photocatalysis for selective organic transformations., *Chem. Soc. Rev.* 43 (2014) 473–486. doi:10.1039/c3cs60188a.
- [67] S.H. Bossmann, N. Shahin, H. Le Thanh, A. Bonfill, M. W<sup>^</sup>erner, Synthesis , Characterization , and First Application in Photocatalysis, (2002) 401–407.
- [68] N. Kislov, J. Lahiri, H. Verma, D.Y. Goswami, E. Stefanakos, M. Batzill, Photocatalytic Degradation of Methyl Orange over Single Crystalline ZnO : Orientation Dependence of Photoactivity and Photostability of ZnO Photocatalytic Degradation of Methyl Orange over Single Crystalline ZnO : Orientation Dependence of Photoactivity a, (2009) 3310–3315. doi:10.1021/la803845f.
- [69] G. Begum, J. Manna, R.K. Rana, Controlled orientation in a bio-inspired assembly of Ag/AgCl/ZnO nanostructures enables enhancement in visible-light-induced photocatalytic performance, *Chem. - A Eur. J.* 18 (2012) 6847–6853. doi:10.1002/chem.201103760.
- [70] N. Murakami, T. Chiyoya, T. Tsubota, T. Ohno, Switching redox site of photocatalytic reaction on titanium(IV) oxide particles modified with



transition-metal ion controlled by irradiation wavelength, *Appl. Catal. A Gen.* 348 (2008) 148–152. doi:10.1016/j.apcata.2008.06.040.

- [71] M.J. Nash, R.F. Lobo, D.J. Doren, Photocatalytic oxidation of ethylene by ammonium exchanged ETS-10 and AM-6, *Appl. Catal. B Environ.* 88 (2009) 232–239. doi:10.1016/j.apcatb.2008.10.001.
- [72] A.M. Shough, D.J. Doren, M. Nash, R.F. Lobo, Effects of vanadium substitution on the structure and photocatalytic behavior of ETS-10, *J. Phys. Chem. C.* 111 (2007) 1776–1782. doi:10.1021/jp0662247.
- [73] I. Altin, I. Polat, E. Bacaksiz, M. Sökmen, ZnO and ZnS microrods coated on glass and photocatalytic activity, *Appl. Surf. Sci.* 258 (2012) 4861–4865. doi:10.1016/j.apsusc.2012.01.082.
- [74] L. Mouni, L. Belkhiri, J.C. Bollinger, A. Bouzaza, A. Assadi, A. Tirri, F. Dahmoune, K. Madani, H. Remini, Removal of Methylene Blue from aqueous solutions by adsorption on Kaolin: Kinetic and equilibrium studies, *Appl. Clay Sci.* 153 (2018) 38–45. doi:10.1016/j.clay.2017.11.034.
- [75] M. Rafatullah, O. Sulaiman, R. Hashim, A. Ahmad, Adsorption of methylene blue on low-cost adsorbents: A review, *J. Hazard. Mater.* 177 (2010) 70–80. doi:10.1016/j.jhazmat.2009.12.047.
- [76] G. Chen, J. Pan, B. Han, H. Yan, Adsorption of Methylene Blue on Montmorillonite, *J. Dispers. Sci. Technol.* 20 (2007) 1179–1187. doi:10.1080/01932699908943843.
- [77] H.W.P. Carvalho, A.P.L. Batista, P. Hammer, T.C. Ramalho, Photocatalytic degradation of methylene blue by TiO<sub>2</sub>-Cu thin films: Theoretical and experimental study, *J. Hazard. Mater.* 184 (2010) 273–280. doi:10.1016/j.jhazmat.2010.08.033.
- [78] M.H. Sun, S.Z. Huang, L.H. Chen, Y. Li, X.Y. Yang, Z.Y. Yuan, B.L. Su, Applications of hierarchically structured porous materials from energy storage and conversion, catalysis, photocatalysis, adsorption, separation, and sensing to biomedicine, *Chem. Soc. Rev.* 45 (2016) 3479–3563. doi:10.1039/c6cs00135a.
- [79] F. Achouri, S. Corbel, L. Balan, K. Mozet, E. Girot, G. Medjahdi, M. Ben Said, A. Ghrabi, R. Schneider, Porous Mn-doped ZnO nanoparticles for enhanced solar and visible light photocatalysis, *Mater. Des.* 101 (2016) 309–316. doi:10.1016/j.matdes.2016.04.015.
- [80] S. Guo, J. Bao, T. Hu, L. Zhang, L. Yang, J. Peng, C. Jiang, Controllable synthesis porous Ag<sub>2</sub>CO<sub>3</sub> nanorods for efficient photocatalysis, *Nanoscale Res. Lett.* 10 (2015). doi:10.1186/s11671-015-0892-5.

- [81] S. Cho, J.W. Jang, J.S. Lee, K.H. Lee, Porous ZnO-ZnSe nanocomposites for visible light photocatalysis, *Nanoscale*. 4 (2012) 2066–2071. doi:10.1039/c2nr11869f.
- [82] Y. Jiang, P. Zhang, Z. Liu, F. Xu, The preparation of porous nano-TiO<sub>2</sub> with high activity and the discussion of the cooperation photocatalysis mechanism, *Mater. Chem. Phys.* 99 (2006) 498–504. doi:10.1016/j.matchemphys.2005.11.036.
- [83] A.A. Taha, F. Li, Porous WO<sub>3</sub>-carbon nanofibers: High-performance and recyclable visible light photocatalysis, *Catal. Sci. Technol.* 4 (2014) 3601–3605. doi:10.1039/c4cy00777h.
- [84] S. Galioglu, M. Isler, Z. Demircioglu, M. Koc, F. Vocanson, N. Destouches, R. Turan, B. Akata, Photochromic behavior of silver nanoparticle incorporated titanosilicate ETS-10 films, *Microporous Mesoporous Mater.* 196 (2014) 136–144. doi:10.1016/j.micromeso.2014.05.009.
- [85] Z. Lai, G. Bonilla, I. Diaz, J.G. Nery, K. Sujaoti, M. a Amat, E. Kokkoli, O. Terasaki, R.W. Thompson, M. Tsapatsis, D.G. Vlachos, Microstructural optimization of a zeolite membrane for organic vapor separation., *Science* (80-. ). 300 (2003) 456–460. doi:10.1126/science.1082169.
- [86] S. Mintova, V. Valtchev, V. Engstro, B.J. Schoeman, J. Sterte, Growth of silicalite-1 films on gold substrates, 11 (1997) 149–160.
- [87] S. Mintova, T. Bein, Nanosized zeolite films for vapor-sensing applications, *Microporous Mesoporous Mater.* 50 (2001) 159–166. doi:10.1016/S1387-1811(01)00443-7.
- [88] F. Ying, R.W. Smith, D.J. Srolovitz, The mechanism of texture formation during film growth: The roles of preferential sputtering and shadowing, *Appl. Phys. Lett.* 69 (1996) 3007–3009. doi:10.1063/1.116821.
- [89] B. Yilmaz, K.G. Shattuck, J. Warzywoda, A. Sacco, Controlling crystal orientation in microporous titanosilicate ETS-4 films by secondary growth method, *J. Mater. Sci.* 41 (2006) 3135–3138. doi:10.1007/s10853-006-6453-7.
- [90] J.S. Lee, H.K. Jae, J.L. Young, C.J. Nak, B.Y. Kyung, Manual assembly of microcrystal monolayers on substrates, *Angew. Chemie - Int. Ed.* 46 (2007) 3087–3090. doi:10.1002/anie.200604367.
- [91] Z. Lin, J. Rocha, A. Navajas, C. T??llez, J. Coronas, J. Santamar??a, Synthesis and characterisation of titanosilicate ETS-10 membranes, *Microporous Mesoporous Mater.* 67 (2004) 79–86. doi:10.1016/j.micromeso.2003.10.004.
- [92] F. Qiu, X. Wang, X. Zhang, H. Liu, S. Liu, K.L. Yeung, Preparation and

- properties of TS-1 zeolite and film using Sil-1 nanoparticles as seeds, *Chem. Eng. J.* 147 (2009) 316–322. doi:10.1016/j.cej.2008.11.034.
- [93] J. Li, C. Shi, H. Zhang, X. Zhang, Y. Wei, K. Jiang, B. Zhang, Silicalite-1 zeolite membrane: Synthesis by seed method and application in organics removal, *Chemosphere*. 218 (2019) 984–991. doi:10.1016/j.chemosphere.2018.11.215.
- [94] J. Hedlund, S. Mintova, J. Sterte, Controlling the preferred orientation in silicalite-1 films synthesized by seeding, *Microporous Mesoporous Mater.* 28 (1999) 185–194. doi:10.1016/S1387-1811(98)00300-X.
- [95] W.C. Wong, L.T.Y. Au, C.T. Ariso, K.L. Yeung, Effects of synthesis parameters on the zeolite membrane growth, *J. Memb. Sci.* 191 (2001) 143–163. doi:10.1016/S0376-7388(01)00453-7.
- [96] G. Xomeritakis, A. Gouzinis, S. Nair, T. Okubo, M. He, R.M. Overney, M. Tsapatsis, Growth, microstructure, and permeation properties of supported zeolite (MFI) films and membranes prepared by secondary growth, *Chem. Eng. Sci.* 54 (1999) 3521–3531. doi:10.1016/S0009-2509(98)00515-6.
- [97] Z. Ji, B. Yilmaz, J. Warzywoda, A. Sacco, Hydrothermal synthesis of titanosilicate ETS-10 using  $\text{Ti}(\text{SO}_4)_2$ , *Microporous Mesoporous Mater.* 81 (2005) 1–10. doi:10.1016/j.micromeso.2005.01.006.
- [98] D. Kuzyaka, S. Galioglu, B. Akata, Secondary growth of microporous vanadosilicate AM-6 films, *J. Porous Mater.* (2016) 1–9. doi:10.1007/s10934-016-0191-2.
- [99] H. Liu, F. Shen, M. Xing, J. Zhang, M. Anpo, Synthesis, characterization and photo-activity of vacuum activated  $\text{V}^{4+}$  and  $\text{Ti}^{3+}$  doped  $\text{TiO}_2$ , *Catal. Letters*. 144 (2014) 1494–1498. doi:10.1007/s10562-014-1308-3.
- [100] S. Uma, S. Rodrigues, I.N. Martyanov, K.J. Klabunde, Exploration of photocatalytic activities of titanosilicate ETS-10 and transition metal incorporated ETS-10, *Microporous Mesoporous Mater.* 67 (2004) 181–187. doi:10.1016/j.micromeso.2003.11.003.
- [101] M.N. Ismail, Synthesis and bandgap engineering of vanadosilicate AM-6 for photocatalytic applications - ProQuest, (2011) 197. <http://search.proquest.com/docview/862555775>.
- [102] B. Yilmaz, J. Warzywoda, A. Sacco, Spectroscopic characterization of the quantum wires in titanosilicates ETS-4 and ETS-10, *Nanotechnology*. 17 (2006) 4092–4099. doi:10.1088/0957-4484/17/16/017.
- [103] S.J. Datta, K.B. Yoon, Synthesis of large monodisperse ETS-10 crystals and observation of quantum confinement effects from very long titanate quantum wires, *Catal. Today*. 204 (2013) 60–65. doi:10.1016/j.cattod.2012.08.006.

- [104] F.X. Llabres i Xamena, P. Calza, C. Lamberti, C. Prestipino, A. Damin, S. Bordiga, E. Pelizzetti, A. Zecchina, Enhancement of the ETS-10 titanosilicate activity in the shape-selective photocatalytic degradation of large aromatic molecules by controlled defect production, *J. Am. Chem. Soc.* 125 (2003) 2264–2271. doi:10.1021/ja027382o.
- [105] R. López, R. Gómez, Band-gap energy estimation from diffuse reflectance measurements on sol-gel and commercial TiO<sub>2</sub>: a comparative study, *J. Sol-Gel Sci. Technol.* 61 (2012) 1–7. doi:10.1007/s10971-011-2582-9.
- [106] C. Casado Coterillo, A. María Urtiaga Mendia, I. Ortiz Uribe, *Inorganic Membranes: Synthesis, Characterization and Applications*, 2008. doi:10.1016/S0927-5193(07)13007-2.
- [107] U. Wright, Paul A. (School of Chemistry, St. Andrews University, Fife, Microporous Framework Solids, RCS Publishing, 2008.
- [108] I. Johannes, P. Verduijn, H.C. Anthonis, United States Patent ( 19 ) Ud, (2000).
- [109] H.K. Jeong, J. Krohn, K. Sujaoti, M. Tsapatsis, Oriented molecular sieve membranes by heteroepitaxial growth, *J. Am. Chem. Soc.* 124 (2002) 12966–12968. doi:10.1021/ja020947w.
- [110] A.P. Singh, T. Selvam, Liquid phase oxidation of para-chlorotoluene to para-chlorobenzaldehyde using vanadium silicate molecular sieves, *Appl. Catal. A Gen.* 143 (1996) 111–124. doi:10.1016/0926-860X(96)00074-9.
- [111] S.J. Datta, K.B. Yoon, Length-dependent change of optical, magnetic, and vibrational properties of vanadate (V<sup>IV</sup>O<sub>3</sub><sup>2-</sup>) quantum wire embedded in AM-6 vanadosilicate, *J. Am. Chem. Soc.* 134 (2012) 17202–17211. doi:10.1021/ja307187z.
- [112] S.-H. Lee, H.M. Cheong, M. Je Seong, P. Liu, C.E. Tracy, A. Mascarenhas, J.R. Pitts, S.K. Deb, Microstructure study of amorphous vanadium oxide thin films using raman spectroscopy, *J. Appl. Phys.* 92 (2002) 1893. doi:10.1063/1.1495074.
- [113] M. Guo, Z. Feng, G. Li, J.P. Hofmann, E.A. Pidko, P.C.M.M. Magusin, Q. Guo, B.M. Weckhuysen, E.J.M. Hensen, F. Fan, C. Li, “Extracting” the key fragment in ETS-10 crystallization and its application in AM-6 assembly, *Chem. - A Eur. J.* 18 (2012) 12078–12084. doi:10.1002/chem.201200875.
- [114] T.K. Das, A.J. Chandwadkar, A.P. Budhkar, A.A. Belhekar, S. Sivasanker, Studies on the synthesis of ETS-10 I. Influence of synthesis parameters and seed content, *Microporous Mater.* 4 (1995) 195–203. doi:10.1016/0927-6513(95)00005-T.
- [115] Z. Ji, J. Warzywoda, A. Sacco, Synthesis and morphological control of large

- titanosilicate ETS-10 crystals, *Microporous Mesoporous Mater.* 109 (2008) 1–11. doi:10.1016/j.micromeso.2007.04.019.
- [116] G. Li, E. Kikuchi, M. Matsukata, The control of phase and orientation in zeolite membranes by the secondary growth method, *Microporous Mesoporous Mater.* 62 (2003) 211–220. doi:10.1016/S1387-1811(03)00407-4.
- [117] D. Kuzyaka, S. Galioglu, İ. Altın, M. Sökmen, B. Akata, The effect of microporous vanadosilicate AM-6 thin films as photocatalysts for the degradation of methylene blue, *J. Photochem. Photobiol. A Chem.* 366 (2018) 127–135. doi:10.1016/j.jphotochem.2018.03.041.
- [118] S. Galioglu, M. Zahmakiran, Y. Eren Kalay, S. Özkar, B. Akata, Effect of silver encapsulation on the local structure of titanosilicate ETS-10, *Microporous Mesoporous Mater.* 159 (2012) 1–8. doi:10.1016/j.micromeso.2012.04.015.
- [119] G. Silversmit, D. Depla, H. Poelman, G.B. Marin, R. De Gryse, Determination of the V2p XPS binding energies for different vanadium oxidation states (V5+ to V0+), *J. Electron Spectros. Relat. Phenomena.* 135 (2004) 167–175. doi:10.1016/j.elspec.2004.03.004.
- [120] W. Zhong, T. Qiao, J. Dai, L. Mao, Q. Xu, G. Zou, X. Liu, D. Yin, F. Zhao, Visible-light-responsive sulfated vanadium-doped TS-1 with hollow structure: Enhanced photocatalytic activity in selective oxidation of cyclohexane, *J. Catal.* 330 (2015) 208–221. doi:10.1016/j.jcat.2015.06.013.
- [121] N. Alov, D. Kutsko, I. Spirovová, Z. Bastl, XPS study of vanadium surface oxidation by oxygen ion bombardment, *Surf. Sci.* 600 (2006) 1628–1631. doi:10.1016/j.susc.2005.12.052.
- [122] M.E. Harlin, V.M. Niemi, A.O.I. Krause, Alumina-supported vanadium oxide in the dehydrogenation of butanes, *J. Catal.* 195 (2000) 67–78. doi:10.1006/jcat.2000.2969.
- [123] Y. Suchorski, L. Rihko-Struckmann, F. Klose, Y. Ye, M. Alandjiyska, K. Sundmacher, H. Weiss, Evolution of oxidation states in vanadium-based catalysts under conventional XPS conditions, *Appl. Surf. Sci.* 249 (2005) 231–237. doi:10.1016/j.apsusc.2004.11.083.
- [124] M. Demeter, M. Neumann, W. Reichelt, Mixed-valence vanadium oxides studied by XPS, *Surf. Sci.* 454 (2000) 41–44. doi:10.1016/S0039-6028(00)00111-4.
- [125] A. Fujishima, X. Zhang, D.A. Tryk, TiO<sub>2</sub> photocatalysis and related surface phenomena, *Surf. Sci. Rep.* 63 (2008) 515–582. doi:10.1016/j.surfrep.2008.10.001.

- [126] X. Zhao, Y. Zhu, Synergetic degradation of rhodamine B at a porous ZnWO<sub>4</sub> film electrode by combined electro-oxidation and photocatalysis, *Environ. Sci. Technol.* 40 (2006) 3367–3372. doi:10.1021/es052029e.
- [127] S.G. Kumar, L.G. Devi, Review on modified TiO<sub>2</sub> photocatalysis under UV/visible light: Selected results and related mechanisms on interfacial charge carrier transfer dynamics, *J. Phys. Chem. A.* 115 (2011) 13211–13241. doi:10.1021/jp204364a.
- [128] S.J. Datta, K.B. Yoon, Synthesis of pure VSH-2 in large quantities and its characterization, *Top. Catal.* 53 (2010) 1311–1318. doi:10.1007/s11244-010-9589-2.
- [129] S.M. Lai, L.T.Y. Au, K.L. Yeung, Influence of the synthesis conditions and growth environment on MFI zeolite film orientation, *Microporous Mesoporous Mater.* 54 (2002) 63–77. doi:10.1016/S1387-1811(02)00341-4.

## APPENDICES

### A. Calculation of the Energy Bandgap

UV-Vis absorption spectroscopy and energy bandgap calculation of S1-F3 are shown in Figure A1.

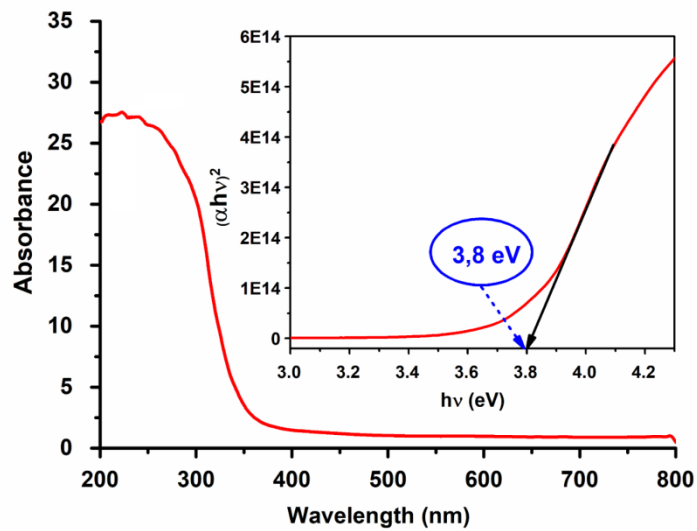


Figure A.1. UV-Vis absorption spectroscopy of S1-F3 and Tauc Plot for energy bandgap calculation

Energy bandgap calculation was carried out by using UV-Vis absorption spectra. Reflectance data was collected and transformed into absorbance data with Kubelka-Munk Function as shown in Equation A.1.

$$Absorbance = \frac{(1-R)^2}{2R} \quad \text{Equation A.1}$$

where R is reflectance.

The absorption coefficient ( $\alpha$ ) of the films was calculated using Equation A.2.

$$\alpha = \frac{\text{Absorption}}{\text{Thickness}} \quad \text{Equation A.2}$$

Energy values of the light source was calculated according to the Equation A.3.

$$\text{Energy} = \frac{hc}{\lambda} \quad \text{Equation A.3}$$

where h is Planck constant, c is speed of light, and  $\lambda$  is wavelength of the light.

Afterward, the value  $(\alpha \times \text{Energy})^2$  was calculated and Tauc Plot was obtained drawing a graph of  $(\alpha \times \text{Energy})^2$  versus Energy. A slope of the graph was drawn and energy bandgap was obtained.



## B. Calculation of the Degradation Kinetics of MB Without Using any Photocatalyst

The calculation of the pseudo-first-order reaction rate constant ( $k$ ) was carried out based on the photodegradation kinetics of MB without using any photocatalysts. Accordingly, MB was also exposed to solar light for 240 minutes uninterruptedly under the solar light. The photocatalytic removal of MB and its photodegradation kinetics are shown in Figure A.2.

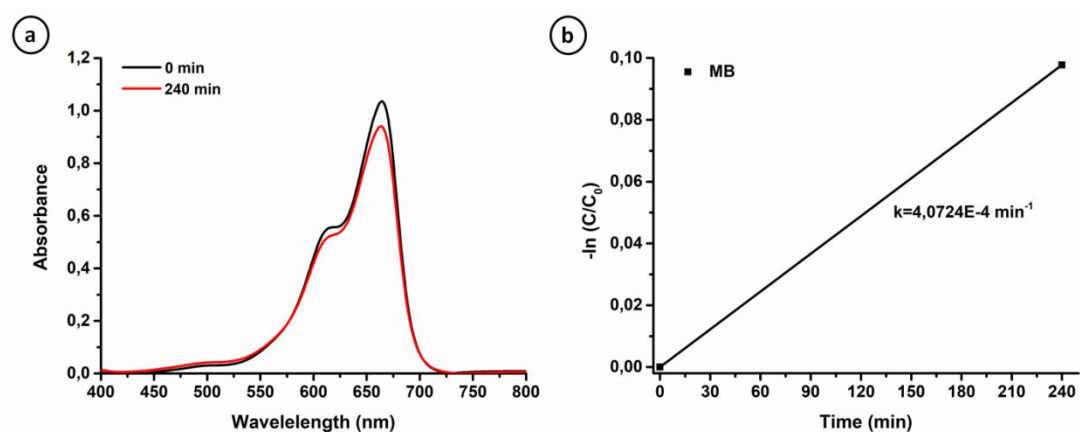


Figure A.2. The photocatalytic removal (a), and the degradation kinetics (b) of MB without using any photocatalysts under solar light (1 Abs. MB, pH 6, VMB= 10 mL)

The pseudo-first-order reaction rate constant ( $k$ ) was calculated following the Equation A.4.

$$\ln\left(\frac{C_t}{C_0}\right) = k \times \text{time}(\text{min.}) \quad \text{Equation A.4}$$

Accordingly, the slope of photodegradation kinetics graph shown in Figure A.2-b was calculated as  $4.0724E-4 \text{ min}^{-1}$  indicating the  $k$  value of MB without using any photocatalysts.

### C. Calculation of the Degradation Kinetics of MB for S1-F3 and S2-F3 as Photocatalyst

The pseudo-first-order reaction rate constants ( $k$ ) based on the photodegradation kinetics of S1-F3 and S2-F3 as shown in Figure A.3.

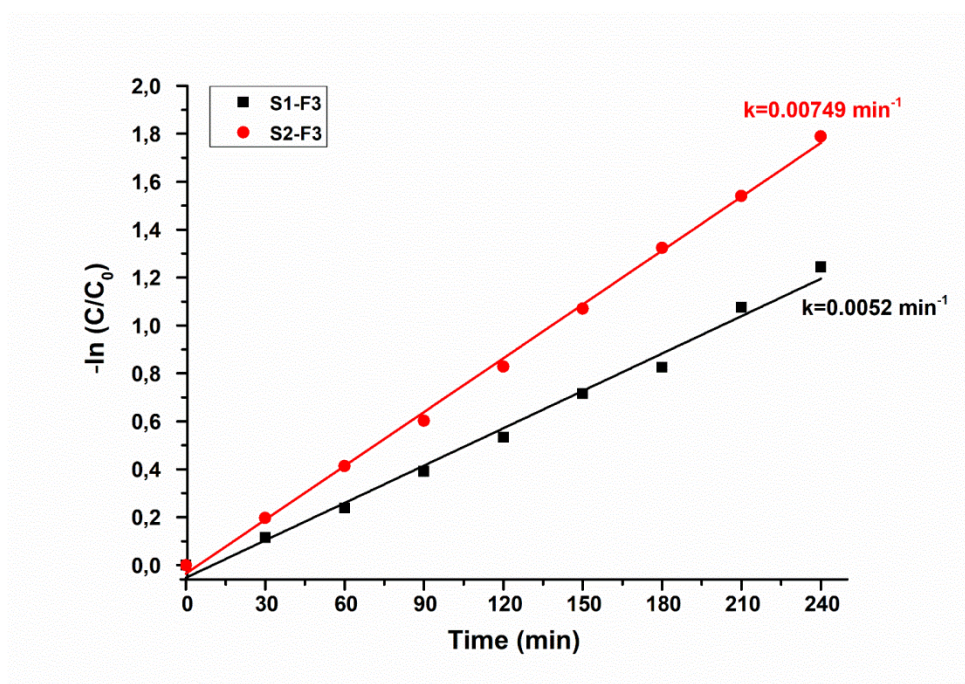


Figure A.3. The photocatalytic removal (a), and the degradation kinetics (b) of MB for S1-F3 and S2-F3 films under solar simulator (1 Abs. MB, pH 6, VMB= 10 mL)

The pseudo-first-order reaction rate constant ( $k$ ) was calculated following the Equation A.4. Accordingly, the slope of photodegradation kinetics graph shown in Figure A.3-b was calculated as  $0.0052 \text{ min}^{-1}$  for S1-F3,  $0.00749 \text{ min}^{-1}$  for S2-F3 indicating the  $k$  values of S1-F3 and S2-F3, respectively. These values are much higher with respect to the  $k$  value of MB signifying S1-F3 and S2-F3 films show photocatalytic activity.

## CURRICULUM VITAE

### PERSONAL INFORMATION

Surname, Name : Kuzyaka, Duygu  
Nationality : Turkish (TC)  
Date and Place of Birth : 23 August 1985, Ankara  
Phone : +90 533 684 77 27  
E-mail : duygu@kuzyaka.com

### EDUCATION

Degree	Institution	Year of Graduation
MS	METU Micro and Nanotechnology	2012
BS	Hacettepe University, Physics Education	2009
High School	Cumhuriyet High School, Ankara	2003

### WORK EXPERIENCE

Year	Place	Enrollment
2017-present	Kastamonu University	Research Assisstant
2010-2010	METU	Research Assisstant

### FOREIGN LANGUAGES

Advanced English

### PUBLICATIONS

#### A. THESIS

[1] **D. Kozanoglu**, Power Conversion Efficiency Enhancement of Organic Solar Cells by Addition of Gold Nanoparticles, M. Sc. Thesis, METU, 2012

## **B. JOURNALS**

- [1] **D. Kuzyaka**, S. Galioglu, İ. Altın, M. Sökmen, B. Akata, The effect of microporous vanadosilicate AM-6 thin films as photocatalysts for the degradation of methylene blue, *Journal of Photochemistry and Photobiology A: Chemistry* 366 (2018) 127-135.
- [2] **D. Kuzyaka**, S. Galioglu, B. Akata, Secondary growth of microporous vanadosilicate AM-6 films, *Journal of Porous Materials* 23 (2016) 1319-1327.
- [3] N. I. Evcimen, S. Coskun, **D. Kozanoglu**, G. Ertas, H. E. Unalan and E. Nalbant Esenturk, Growth of branched gold nanoparticles on solid surfaces and their use as surface-enhanced Raman scattering substrates, *RSC Advances* 5 (2015) 101656-101663.
- [4] M. Kesik, F. Ekiz Kanik, G. Hızalan, **D. Kozanoglu**, E. Nalbant Esenturk, S. Timur, L. Toppare, A functional immobilization matrix based on a conducting polymer and functionalized gold nanoparticles: Synthesis and its application as an amperometric glucose biosensor, *Polymer* 54 (2013) 4463-4471.
- [5] **D. Kozanoglu**, D. Hazar Apaydin, A. Cirpan, E. Nalbant Esenturk, Power conversion efficiency enhancement of organic solar cells by addition of gold nanostars, nanorods, and nanospheres, *Organic Electronics* 14 (2013) 1720–1727.

## **C. CONFERENCE AND MEETING PRESENTATIONS**

- [1] 2019 Materials Research Society (MRS) Fall Meeting and Exhibit, “Humidity Sensing Behavior of Microporous Titanosilicate and Vanadosilicate Thin Films” (Oral Presentation), 1-6 December 2019, Boston, USA.
- [2] International Conference on Chemical Energy and Semiconductor Photochemistry, “Microporous Vanadosilicate AM-6 Thin Films for Photocatalytic Applications” (Oral Presentation), 4-6 September 2019, Trabzon - Turkey.

- [3] 42<sup>nd</sup> Annual Meeting of the British Zeolite Association, “Photocatalytic Performances of Microporous Vanadosilicate AM-6 Thin Films with different amounts of defects in their structures” (Oral Presentation), 11-12 April 2019, Birmingham - UK.
- [4] 14<sup>th</sup> Nanoscience & Nanotechnology Conference (NanoTR-14), “The Effect of Defect Creation in Microporous Vanadosilicate AM-6 Thin Films on Their Photocatalytic Performances” (Oral Presentation), 22-25 September 2018, Çeşme, İzmir - Turkey.
- [5] 2018 Materials Research Society (MRS) Fall Meeting and Exhibit, “The Effect of Defects Created in Microporous Vanadosilicate AM-6 Thin Films in the Photocatalysis” (Oral Presentation), 25-30 November 2018, Boston, USA.
- [6] 34<sup>th</sup> GFZ Congress - Groupe Français des Zéolithes, “The Effect of Microporous Vanadosilicate AM-6 Thin Films as Photocatalysts for the Degradation of Methylene Blue” (Oral and Poster Presentations), 26-29 March 2018, Cabourg - France.
- [7] 6<sup>th</sup> International Conference on Semiconductor Photochemistry, “Effect Of Microporous Vanadosilicate AM-6 Thin Films As Photocatalysts For The Degradation Of Methylene Blue” (Oral and Poster Presentations), 11-14 September 2017, Carl von Ossietzky University Oldenburg - Germany.
- [8] 7<sup>th</sup> FEZA Conference “The ZEOLITES: Materials with Engineered Properties”, “Understanding the Effects of Seed Layer in the Secondary Growth of Microporous Vanadosilicate AM-6 Films” (Poster Presentation), 3-7 July 2017, Sofia - Bulgaria.
- [9] 7<sup>th</sup> FEZA Conference “The ZEOLITES: Materials with Engineered Properties”, “Investigation of Photocatalytic Activities of Vanadium Silicate AM-6 Thin Films” (Poster Presentation), 3-7 July 2017, Sofia - Bulgaria.
- [10] 18<sup>th</sup> International Zeolite Conference, “Secondary Growth of Vanadosilicate Films” (Oral Presentation), 19-24 June 2016, Rio de Janeiro, Brazil.

[11] International porous and powder materials symposium and exhibition PPM 2015, “Secondary Growth of Vanadosilicate Films” (Poster Presentation), 15-18 September 2015, İzmir - Turkey.

[12] 4<sup>th</sup> International Conference on Multifunctional, Hybrid and Nanomaterials, “Secondary Growth of Vanadosilicate Films” (Poster Presentation), 9-13 March 2015, Sitges (near Barcelona) - Spain.

#### **D. RESEARCH ACTIVITIES**

[1] Visiting Researcher, CNRS à l’Institut des Sciences Analytiques de l’Université Claude Bernard-Lyon 1, Lyon, France, April-June, 2014.

[2] Visiting Researcher, Department of Bioengineering, McGill University, Montréal, Quebec, Canada, September-December, 2015.

#### **E. CERTIFICATES**

[1] Scanning Electron Microscopy User Certificate, Certificate Number: ODT.S190018.556, Central Laboratory, Middle East Technical University.

#### **HOBBIES**

Scuba diving, Tango, Movies, Reading